CRBRP-ARD-0108

ap. 3

[redacted]

CLINCH RIVER BREEDER REACTOR PLANT

11:1 SCALE WIRE WRAPPED ROD BUNDLE AIR FLOW TEST, INTERIOR SUBCHANNELS

JANUARY, 1977

TOPICAL REPORT

Full release per David Harris 9/19/2012

WESTINGHOUSE ELECTRIC CORPORATION
ADVANCED REACTORS DIVISION

Prepared for Project Management Corporation and the U.S. Energy Research and Development Administration Under Contracts 49-18-12-3 and EY-76-C-15-2395

TECHNICAL INFORMATION CENTER
UNITED STATES ENERGY RESEARCH AND DEVELOPMENT ADMINISTRATION

NOTICE

Available from USERDA Technical Information Center, P. O. Box 62, Oak Ridge, TN 37830

Price: Paper Copy $6.75 (domestic)

Printed in the United States of America
USERDA Technical Information Center, Oak Ridge, Tennessee

CRBRP-ARD-0108
Distribution Category UC-79e

CLINCH RIVER BREEDER REACTOR PLANT

11:1 SCALE WIRE WRAPPED ROD BUNDLE AIR FLOW TESTS

INTERIOR SUBCHANNELS

TOPICAL REPORT

T.G. BARTHOLET
R.M.ROIDT
L.J. HARPER

Prepared for Project Management Corporation and the U.S. Energy Research and Development Administration under Contracts 49-18-12-3 and EY-76-C-15-2395

Westinghouse Electric Corporation
Advanced Reactors Division
P.O. Box 158
Madison, Pennsylvania 15663

TABLE OF CONTENTS

TABLE OF CONTENTS

(Cont'd)

PAGE

ACKNOWLEDGEMENT

The authors gratefully acknowledge their indebtedness to F. C. Engel of the Advanced Reactors Division, who initiated overall coordination of this experimental program.

LIST OF FIGURES

LIST OF FIGURES

(Cont'd)

LIST OF FIGURES

(Cont'd)

LIST OF FIGURES

(Cont'd)

LIST OF TABLES

1.0 EXPERIMENTAL PROGRAM

1.1 Summary of Results

This document is a report of experimental work conducted with the 10.87 to 1 scale air flow test facility at the Westinghouse Research Laboratories for the Energy Research and Development Administration under contract AT(11-1)-2395. The purpose is to obtain new data for subchannel analysis code developers to improve the accuracy of their calculational techniques for wire wrapped rod bundles.

The large scale rod bundle offers a unique opportunity to make detailed measurements of mixing and flow behavior within the rod bundle. The experimental results described here cover identification of flow development characteristics, tracer gas mixing tests, gap crossflow determination, and detailed axial flow measurements for interior subchannels of a wire wrapped rod bundle.

Interpretations of the data obtained are also offered in view of how the data may be applied to code development.

1.2 Background

An LMFBR core is composed of a parallel array of cylindrical fuel rods through which the coolant flow axially. A typical cross section of such an arrangement is shown in Figure 1-1. Molecular and turbulent transport of mass, momentum, and energy take place laterally through the clearance gaps as well as in the axial direction which results in transverse distributions of these quantities; distributions which are of considerable importance with respect to core design.

To design an economically feasible LMFBR, it is necessary to reliably predict through analytical computer codes the thermal and hydrodynamic behavior of the coolant within the reactor core. Knowledge of the uncertainty in the output of the codes as well as detailed information concerning flow within the core fuel assemblies is essential. Since it would be quite difficult to obtain such information in an actual rod bundle, due to cost and instrumentation problems, a large scale, geometrically similar model was fabricated to use air as the working fluid. With flow velocities on the order of 100 ft/sec, the Mach number is small enough so that only Reynolds number similarity is required for proper hydrodynamic modeling. Thus, velocity distributions, turbuelnce, and other phenomena governed strictly by the fluid momentum equations, which are obtained in the scaled experiment, should be directly applicable to an analysis of the actual fuel rod bundle.

The "wire wrap" fuel element support and spacer has been selected for the initial core loadings of the Clinch River Breeder Reactor Plant (CRBRP). Fabrication of this type of support involves the spiral wrapping (on an 11.9 inch spiral pitch) of each 0.230 inch diameter fuel rod with an 0.056 inch diameter wire. Two hundred and seventeen of these wrapped fuel rods, with wire wraps all "in phase" are inserted into the subassembly sketched in Figure 1-2. This figure also outlines the segment of the subassembly modeled in the 10.87:1 scale air flow model used in this experiment.

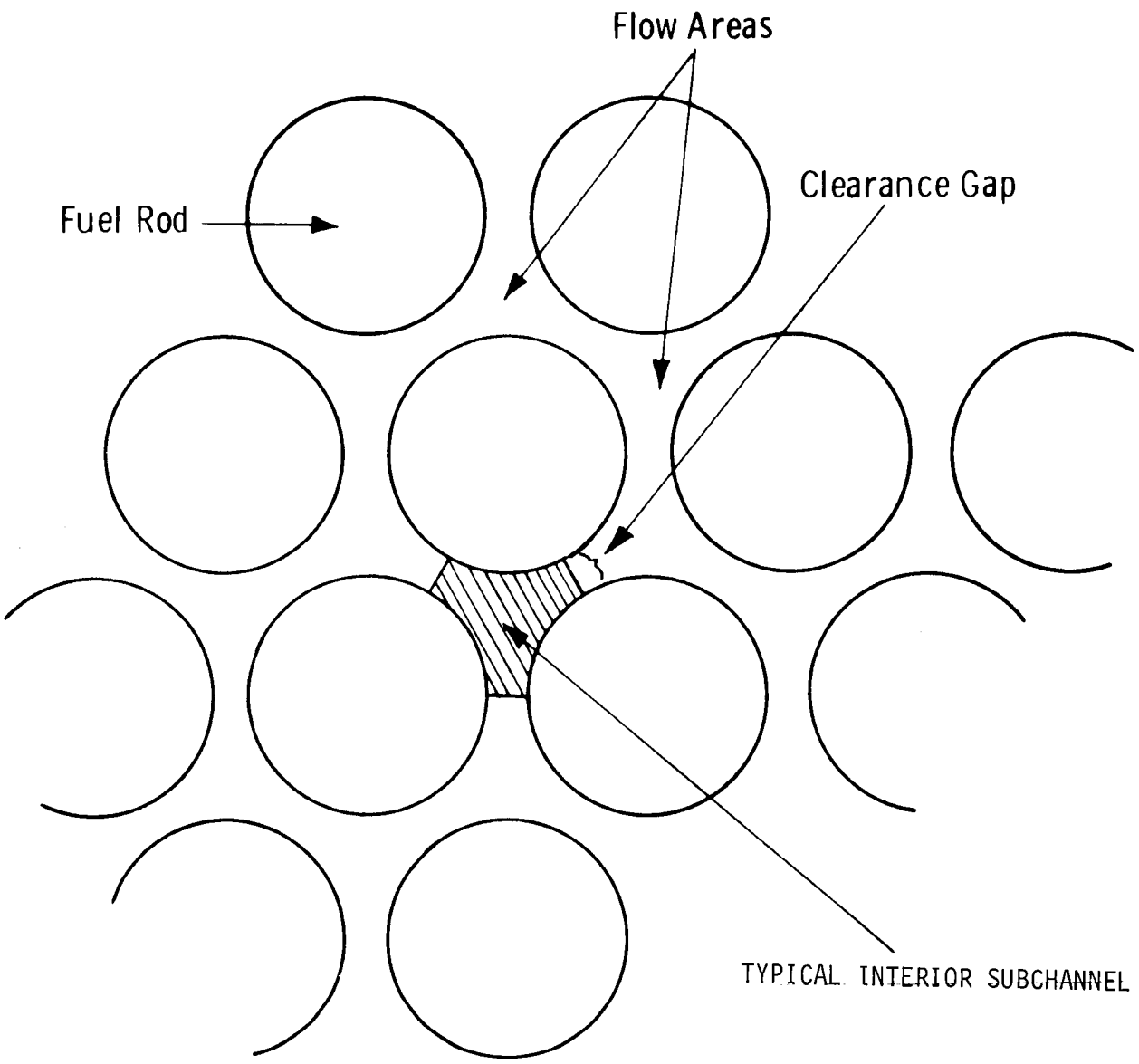

Fig. 1-1—Rod bundle cross-section with triangular geometry

Dwg. 6354A30

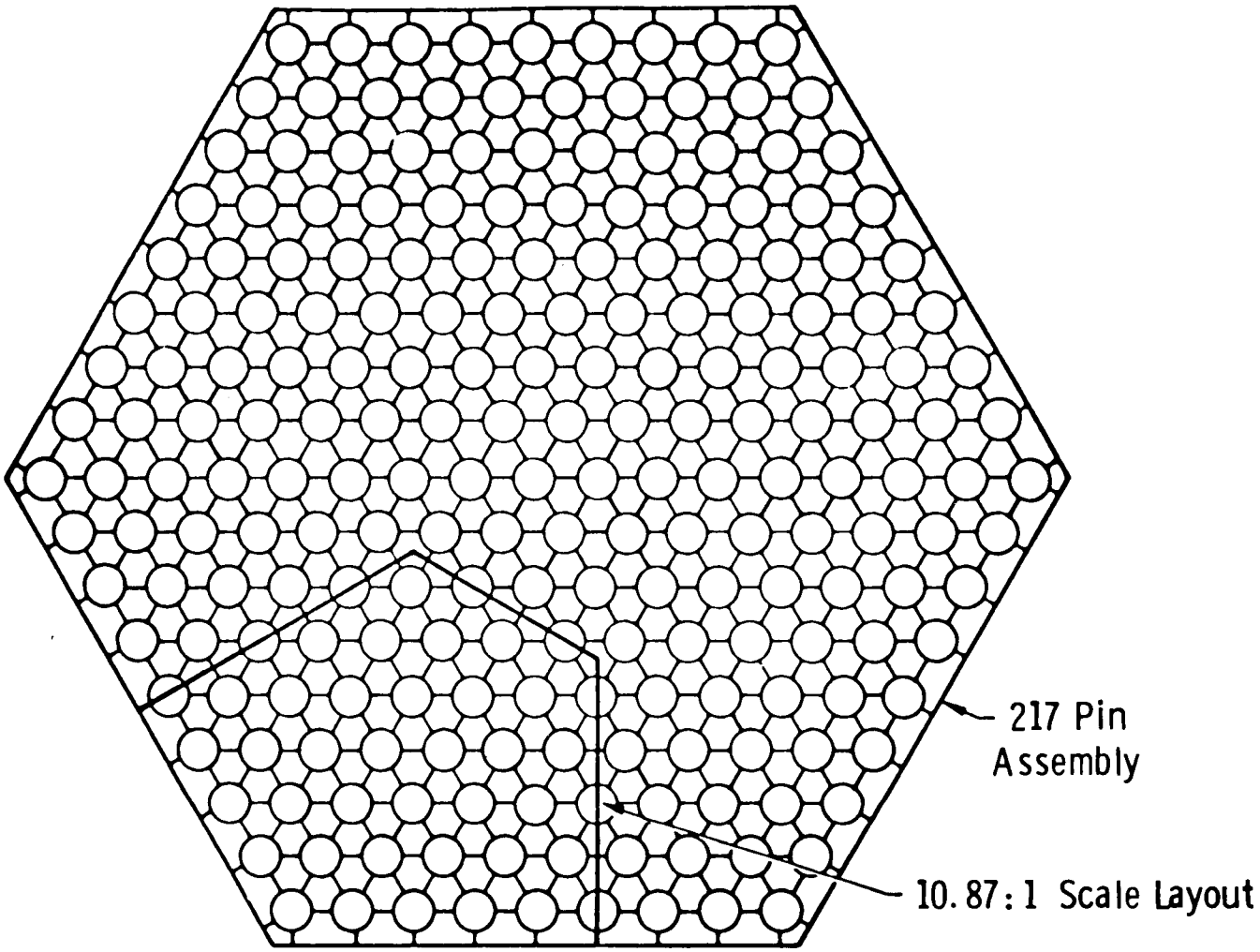

Fig. 1-2—217 Pin fuel assembly with 10.87:1 scale model cross section super-imposed

1.3 Pretest Predictions

Prior to operation of the test section, pretest predictions were made with the CØBRA subchannel analysis code. Axial flow and crossflow rates were predicted using the CØBRA-IIIB code[1] after incorporating the wire wrap subroutine FØRCE from CØBRA-IIIC[2]. Air properties shown in Table 1-1 replaced those of sodium.

Based on the experimental facility as previously used for gridded rod bundle flow measurements[3] and modified to include a clockwise wire wrap; the as-built geometric dimensions reported in Figure 2-5 for rod diameters and Figure 2-7 for gap widths were used in the analytical model. Average values were used for those not specified. Nominal values for wire wrap lead (129.4 inches) and wire wrap diameter (0.625 inches) were also used.

For modeling purposes, the duct cross section was divided into the subchannels shown in Figure 1-3. Computer code limitations on the number of subchannels (60) and inter-subchannel gaps (92) made necessary the use of composite subchannels around the periphery of the duct cross section. These were positioned on the periphery in order to maintain the most precise divisions in the vicinity of the rods to be instrumented. The subchannel divisions as shown resulted in 56 subchannels and 86 gaps.

Several input parameters were chosen for the computer model. Values for subchannel flow areas and wetted perimeters were based on the dimensions already described. The friction factor correlation[4]

$$f = 0.316\ M\ Re^{-0.25}$$

where

$$M = \left\{\frac{1.034}{(P/D)^{0.124}} + \frac{29.7(P/D)^{6.94}\,Re^{0.086}}{(H/D)^{2.239}}\right\}\ 0.885$$

and

$$P/D = \frac{2.504 + 0.643}{2.504} = 1.257$$

$$H/D = \frac{129.4}{2.504} = 51.68$$

$$Re = 73{,}000$$

TABLE 1-1

ADOPTED AIR PROPERTIES

Temperature	75°F
Pressure	15 psia
Density	0.0744 lb/ft^3
Viscosity	0.04728 lb/ft/hr

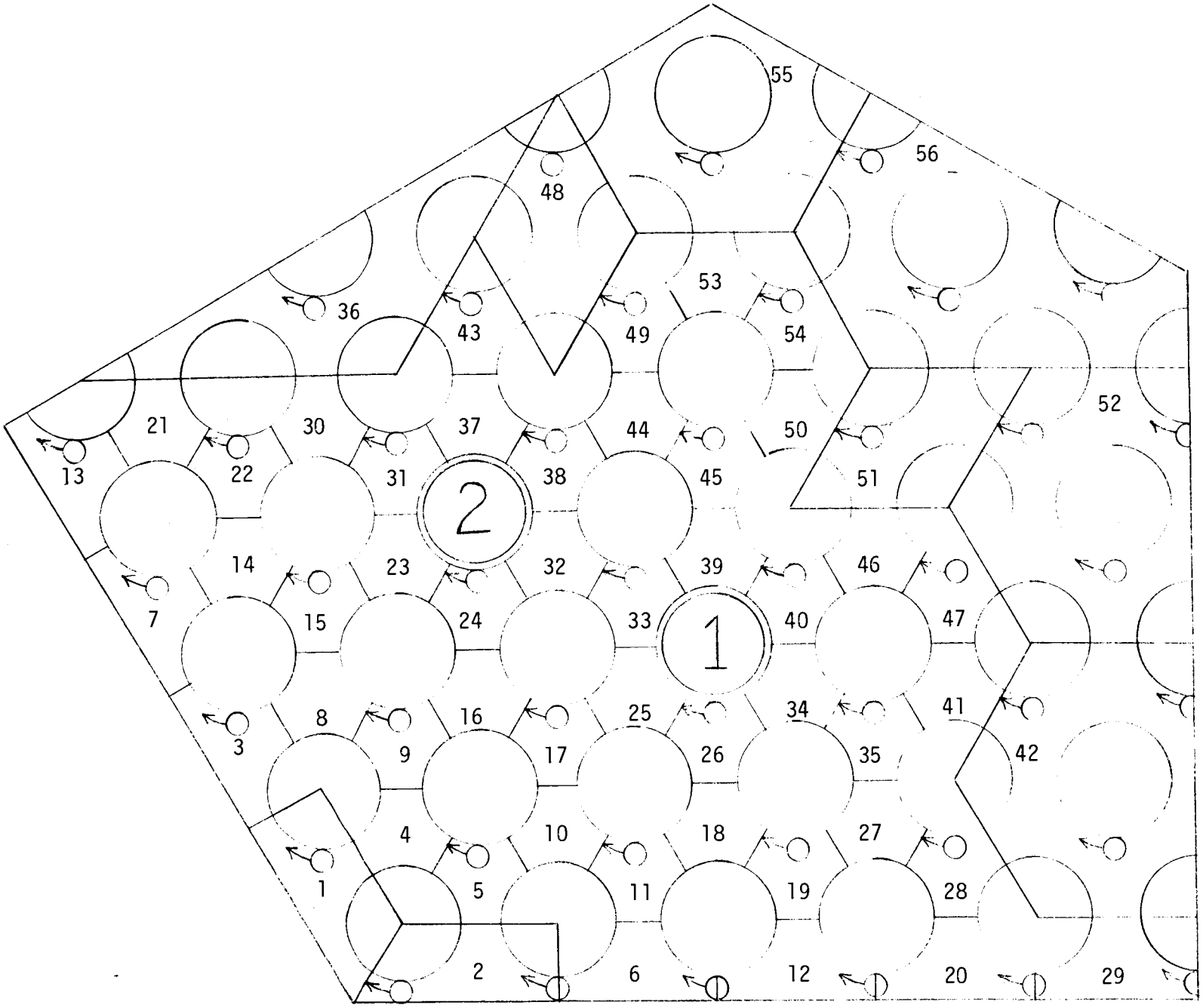

FIGURE 1-3

SUBCHANNEL DIVISIONS FOR COMPUTER MODELING

was applied, resulting in

$$f \simeq 0.333\ Re^{-0.25} \text{ or } f \simeq .0203.$$

The following code parameters were based on the previous bare and gridded rod experiments using the same test assembly[3]:

Crossflow Resistance	0.001 ft.
Turbulent Momentum Factor	0.0
Subcooled Mixing Parameter (Beta)	0.02

Total flow through the test assembly was calculated on the basis of a nominal flow rate of 112.6 ft^3/sec. The resultant mass flow rate of 3.0159×10^4 lb/hr was used in the modeling.

Initial positions of the wire wrap in the subchannels were as indicated in Figure 1-3. This veiw is looking downstream from the test assembly inlet. The effective fractions of wire wrap pitch length forcing crossflow through a gap were arbitrarily chosen as follows:

Interior-to-Interior Subchannel Gap	0.10
Peripheral-to-Interior Subchannel Gap	0.12
Peripheral-to-Peripheral Subchannel Gap	0.14

The series of figures shown in Appendix A represent the results of this pretest analysis in terms of subchannel axial flow (lb/hr) and inter-subchannel crossflow (lb/sec/ft) for the subchannels and gaps surrounding instrumented rod number 2 (Figure 1-3) and the gaps between subchannels 25 and 33 (gap g-g in Figure 4-1) and subchannels 32 and 33 (gap h-h in Figure 4-1). For comparison, axial flow and crossflow plots are also shown for some selected peripheral and near-peripheral subchannels.

Axial variations in axial flow calculated for interior subchannels show a regularly repeating behavior phased with the wire wrap. The use of composite subchannels in the modeling seems not to have affected the results since subchannels adjacent to and distant from the composite subchannels show identical results, i.e., Figure A-1 and Figure A-4. Figures A-1 through A-6 represent all the subchannels surrounding the instrumented rod labeled "2" in Figure 1-3.

By comparison, axial flow patterns shown in Figures A-7 and A-8 for peripheral subchannels display radically different behavior. Consistently, the near-peripheral subchannels (Figures A-9 and A-10) demonstrate an axial flow pattern somewhat in between the patterns of the interior and peripheral subchannels.

Axial variations in crossflow between the subchannels surrounding instrumented rod "2" are shown in Figures A-11 through A-16. Crossflow in gaps g-g and h-h of Figure 4-1 are given in Figures A-17 and A-18, respectively. For comparison, Figures A-19 through A-21 show the crossflow calculated for peripheral and near-peripheral gaps.

2.0 DESCRIPTION OF EXPERIMENTAL APPARATUS

2.1 General Description of Duct and Method of Placing the Model Wire Wraps

The major dimensions of the test facility cross section are indicated in Figure 2-1. The test assembly consists of 35 model fuel rods nominally 2.5 inches in diameter with eight half-rods mounted around part of the circumference. The double circled rods numbered 1 and 2 in this figure represent rods which may be moved axially in and out of the duct as well as circumferentially. These instrumented rods house adjustable flow measuring or sampling devices.

The overall configuration of the rod bundle internals are best illustrated by photographs taken during its assembly. These are shown in Figures 2-2a, 2-2b, 2-3a and 2-3b. A schematic of the axial layout of the duct is shown in Figure 2-4. During operation, air enters the duct from the laboratory through a curved (6 inch radius) inlet flange shown clearly in Figure 2-3a. It passes through the test section to a downstream cylindrical plenum and then moves upward through an 18.04 by 20.07 inch rectangular duct located above the test section. After moving through a 40 HP radially bladed blower, it passes an adjustable throttling plate before it is exhausted through the laboratory roof to the outside.

Two hundred and forty inch long sections of 0.625 inch diameter copper pipe (full hard) were used as model wire wraps. After scribe lines 0.625 inches apart were centered over four alignment points, the copper tube was centered between these lines and C-clamped into position, the C-clamps at each end being placed near the ends of the two foot rod extensions. Six 6-32 machine screw tap sized holes were then drilled through the wrap and model rod, two 12 inches apart at each end of the rod and one each at the 129.3 and 64.7 inches marks. The model wrap was then removed and each tap size hole in the wrap enlarged to a 6-32 clearance while the outside hole was drilled to accept a 6-32 Allen head cap screw. After tapping the holes in the model rod, the wrap was replaced and fastened with machine screws. Adhesive aluminum foil was used to cover the outside holes in the wire wrap which was then cut at the mark four inches from the downstream end at a point protruding three inches past the upstream end.

Dwg. 6354A29

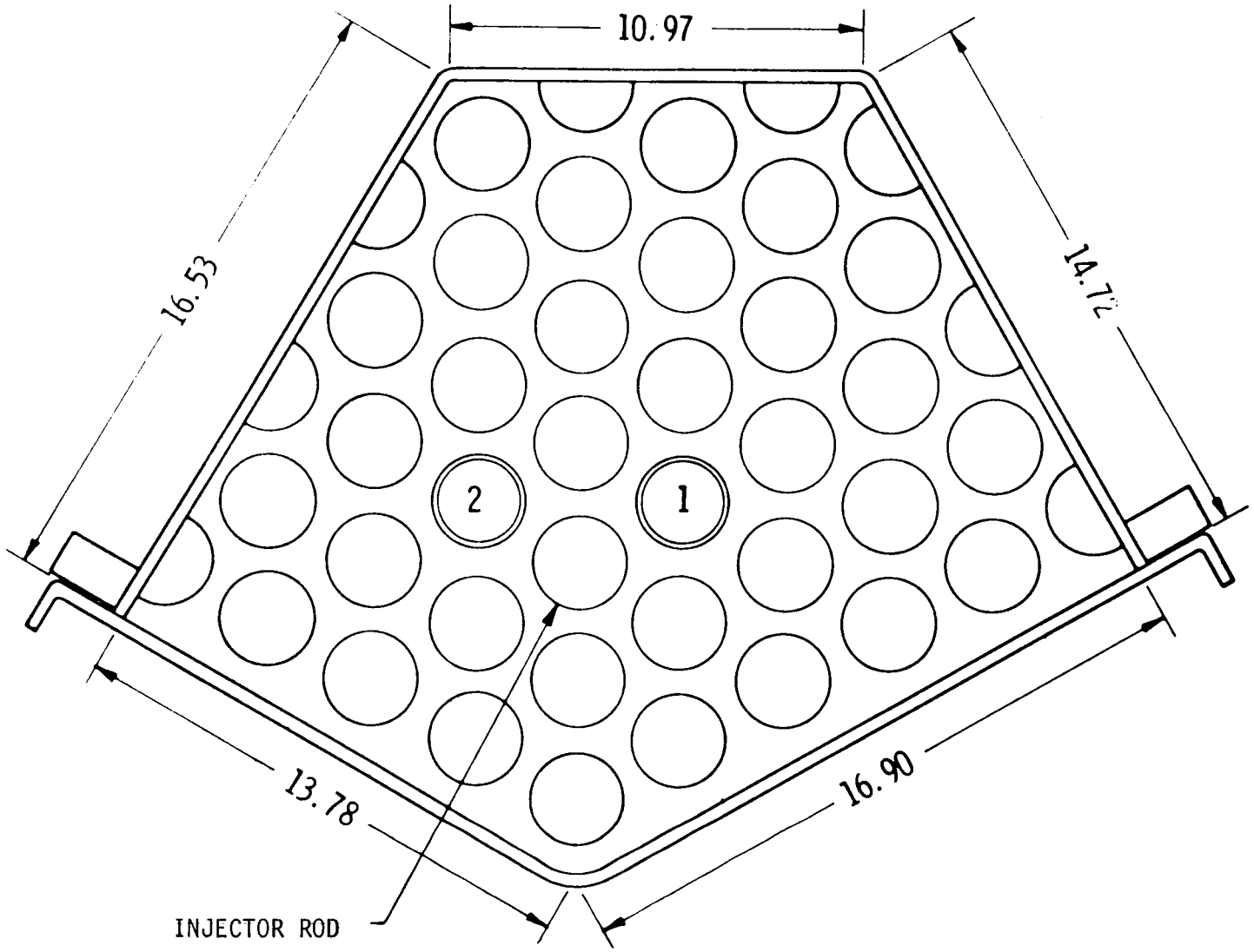

Fig. 2-1—Cross-section of test section (dimensions in inches)

a

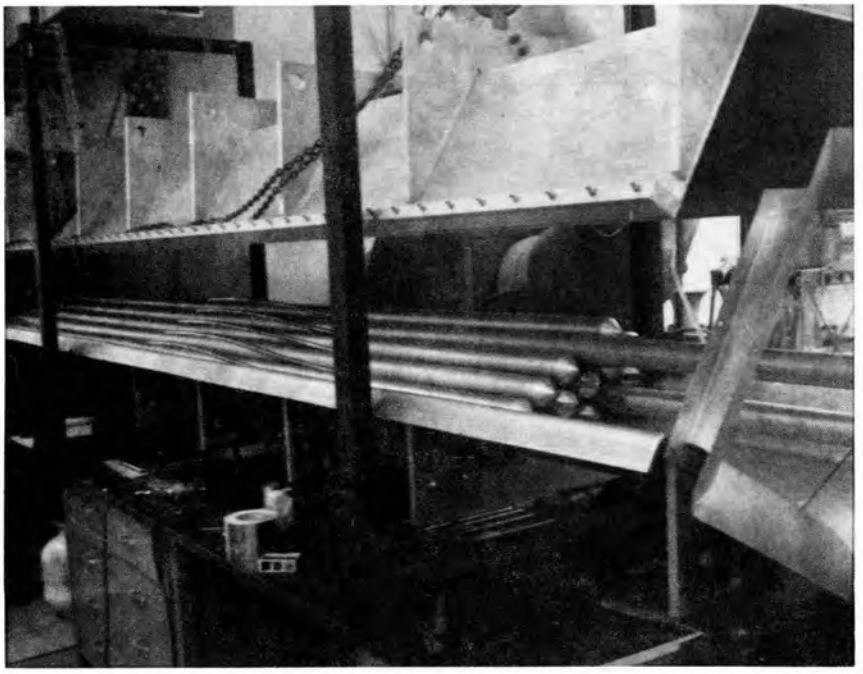

b

Figure 2-2. Test Section During Assembly

7689-2

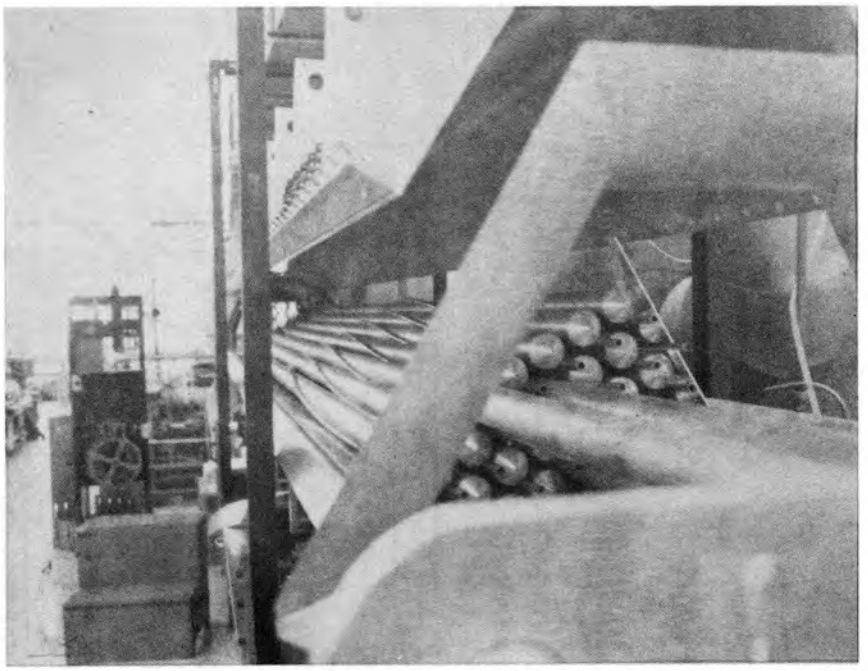

a

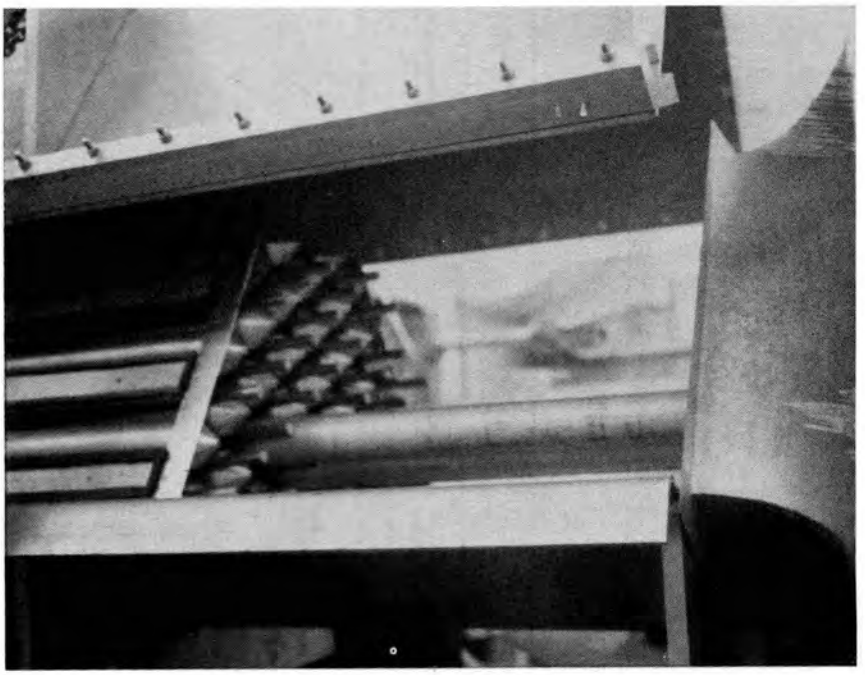

b

Figure 2-3. Test Section During Assembly

7689-1

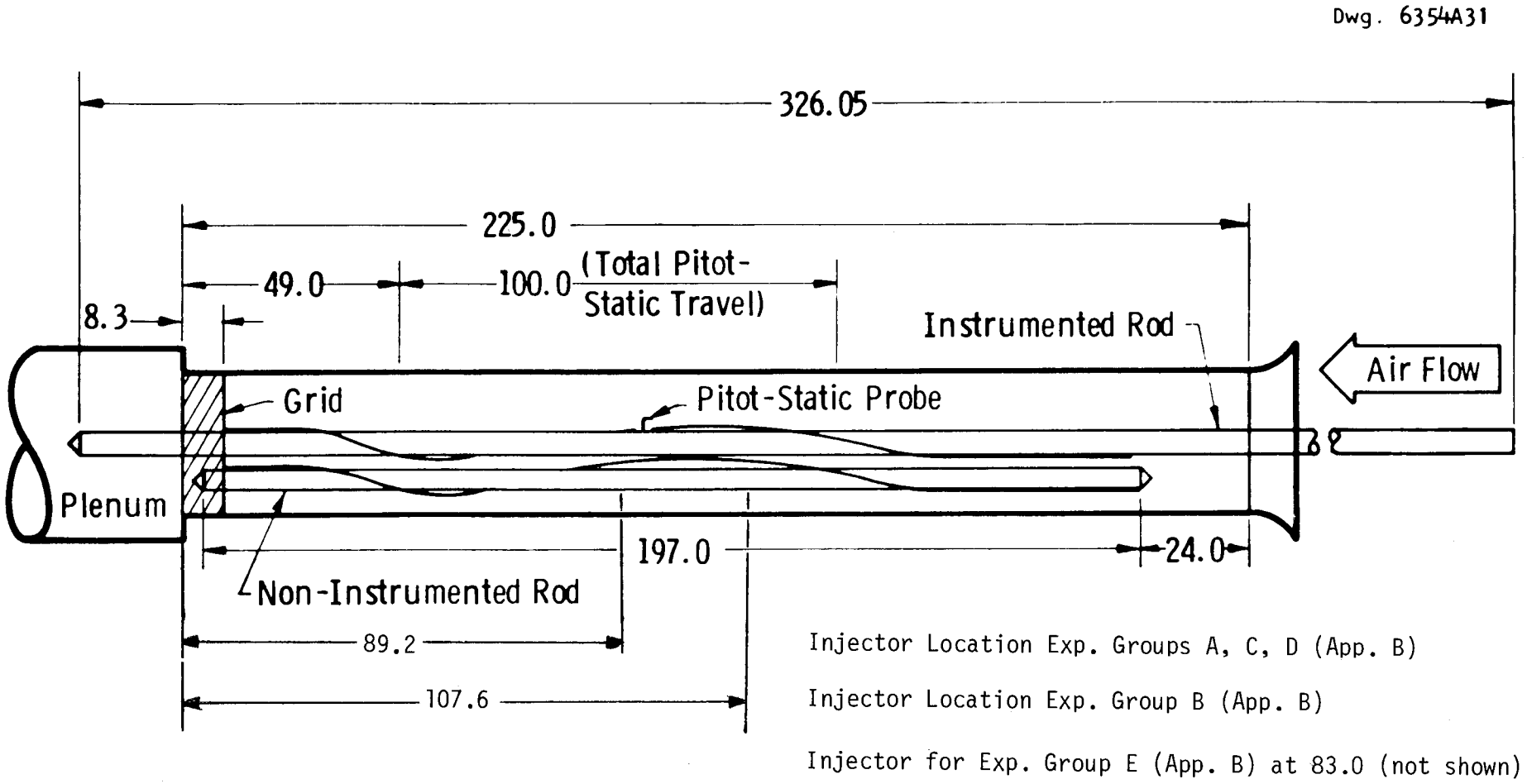

Fig. 2-4—Axial layout of test section (dimensions in inches)

To insure the spiral wraps remained in phase during their emplacement in the duct as in Figure 2-2a, the following procedure was used. At a position 113.6 inches from the downstream end of the duct, a straight edge was placed along the top of the model rods. The rods, with attached wire wraps were then rotated until the straight edge was tangent to all rods and model wraps. Machine screws were then used, through the duct wall, to hold the wire wraps and rods in place at the entrance to the test section. Each succeeding layer of rods was aligned at the same point and fastened with small wooden wedges in the grid to prevent rotation.

Provision had to be made to allow for axial motion and rotation of the two instrumented rods as well as the tracer injection rod and to this end the model wraps for each of these had to be fastened to the adjoining stationary rods. This was accomplished by placing a "regular" or non-instrumented rod and aligning it as indicated above. Then all rods except those immediately adjacent to this rod were removed. Where the wire wrap contacted these remaining adjacent rods, a 6-32 machine screw tap drill was drilled through the rods and into the wire wrap. The model rod and wire wrap were then removed and taken apart. The same procedure was then used for fastening the wire wrap to adjacent rods as was used to fasten the wire wrap to the model rod surface except that it was the wire wrap that was tapped. After the required three rods were thus treated, assembly of the rod bundle continued as indicated in Figure 2-3a.

During assembly of the duct, measurements of the "as-built" dimensions were made at three positions with respect to clearance gaps and at one position for the true rod diameters. These measurements are shown in Figures 2-5, 2-6, 2-7 and 2-8.

After all the "full rods" were in place, the half-rods were mounted by fastening with machine screws at the grid and to metal strips at the duct inlet such as is shown in Figure 2-3b. The wire wrap was fixed to the half-rods by putting two of them back to back and using the same procedure as for wrapping the full rods. The wraps were then cut along the plane joining the two halves.

Dwg. 257C121

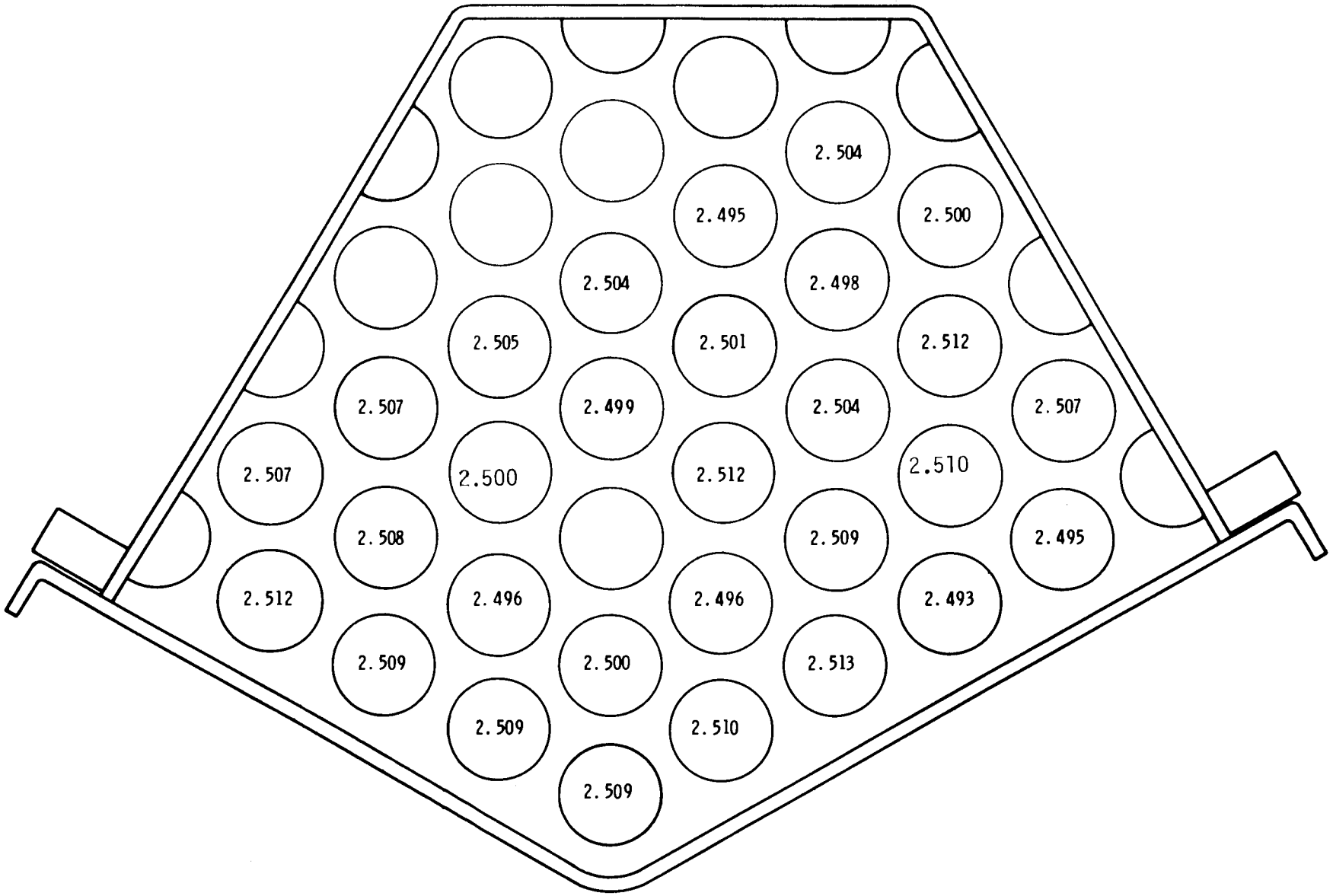

Fig. 2-5—Measured model rod diameters 93.5 inches from downstream end of test section

Dwg. 257C124

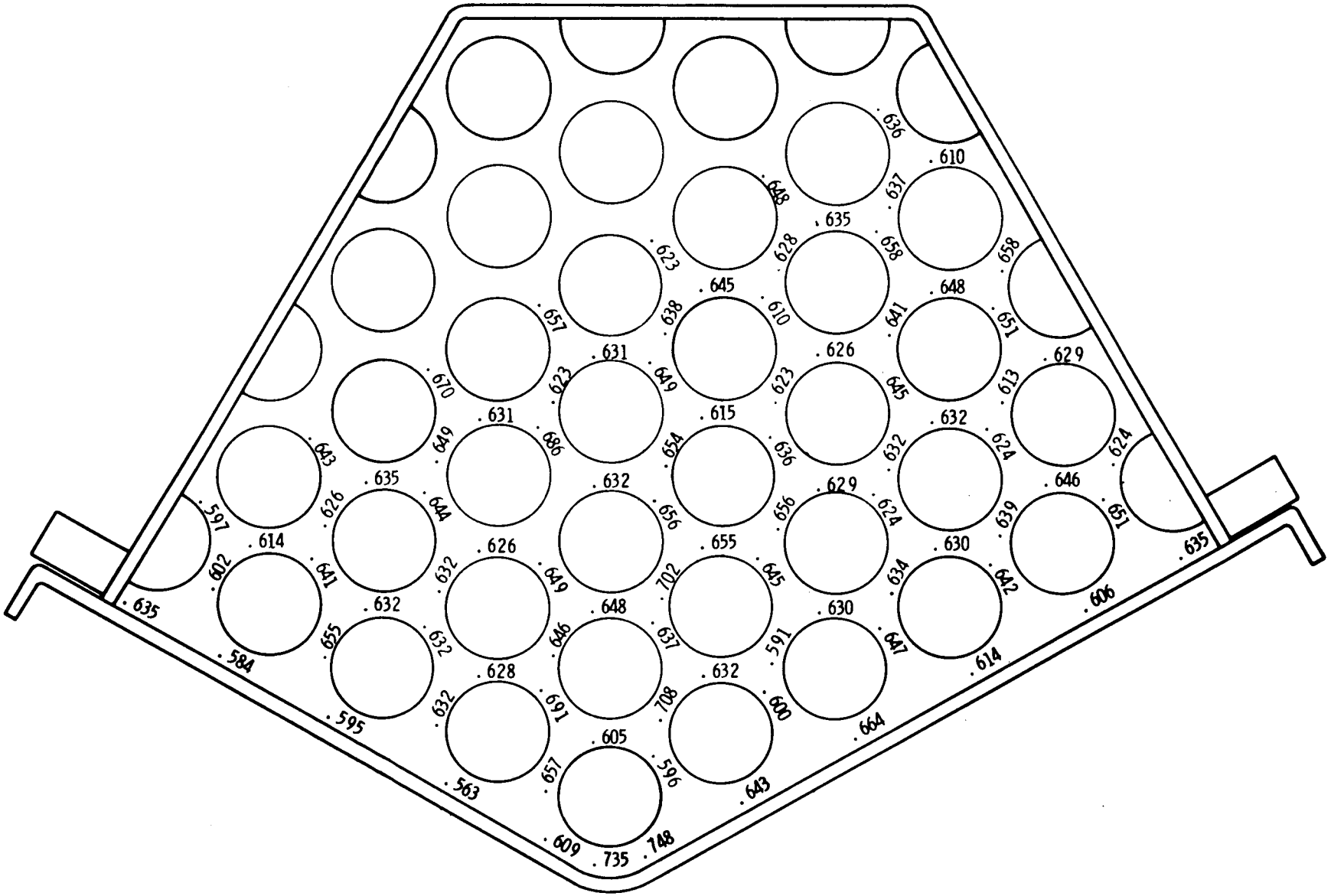

Fig. 2-6—Clearance gap spacings 55.0 inches from downstream end of test section

Dwg. 257C123

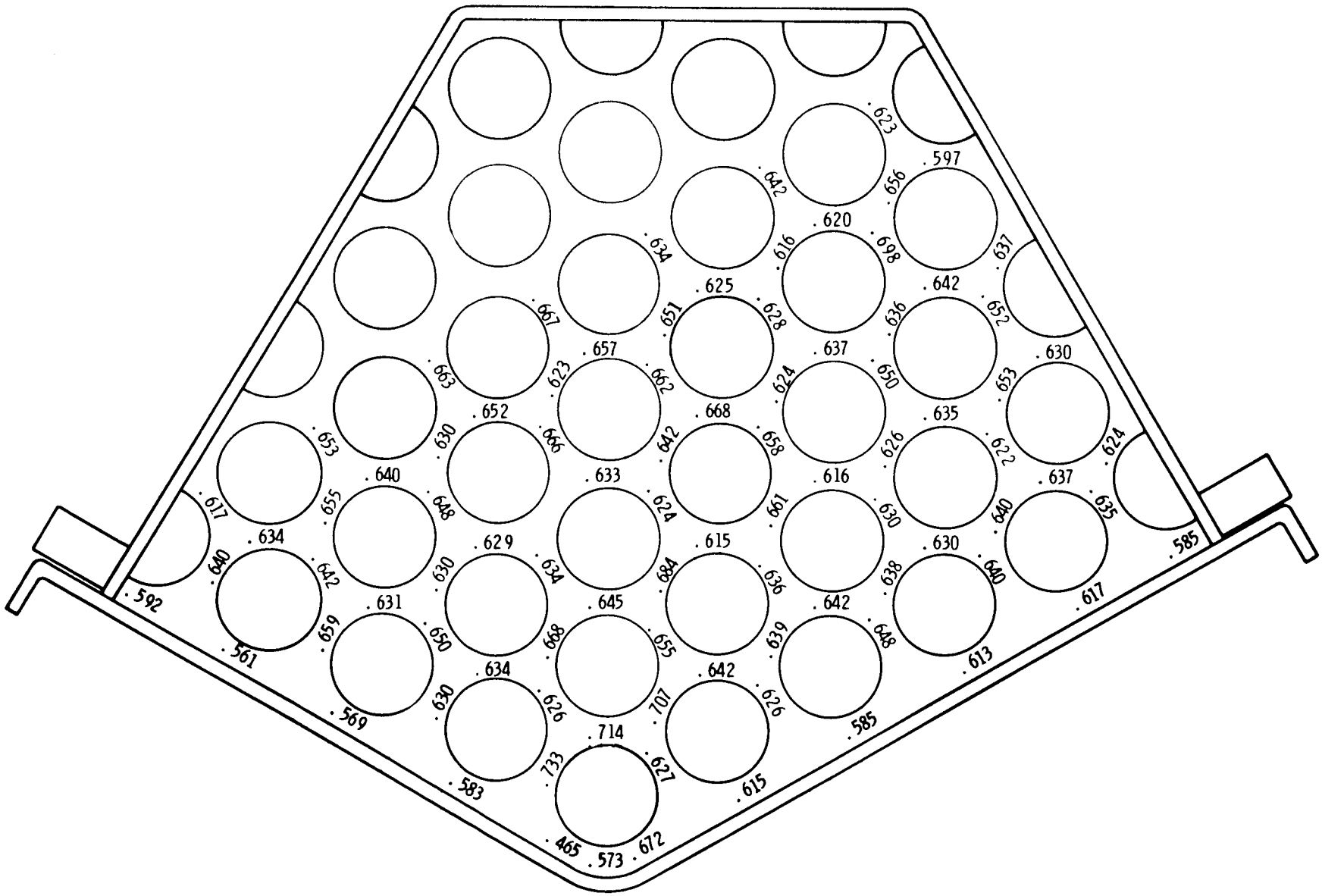

Fig. 2-7—Clearance gap spacings 93.5 inches from downstream end of test section

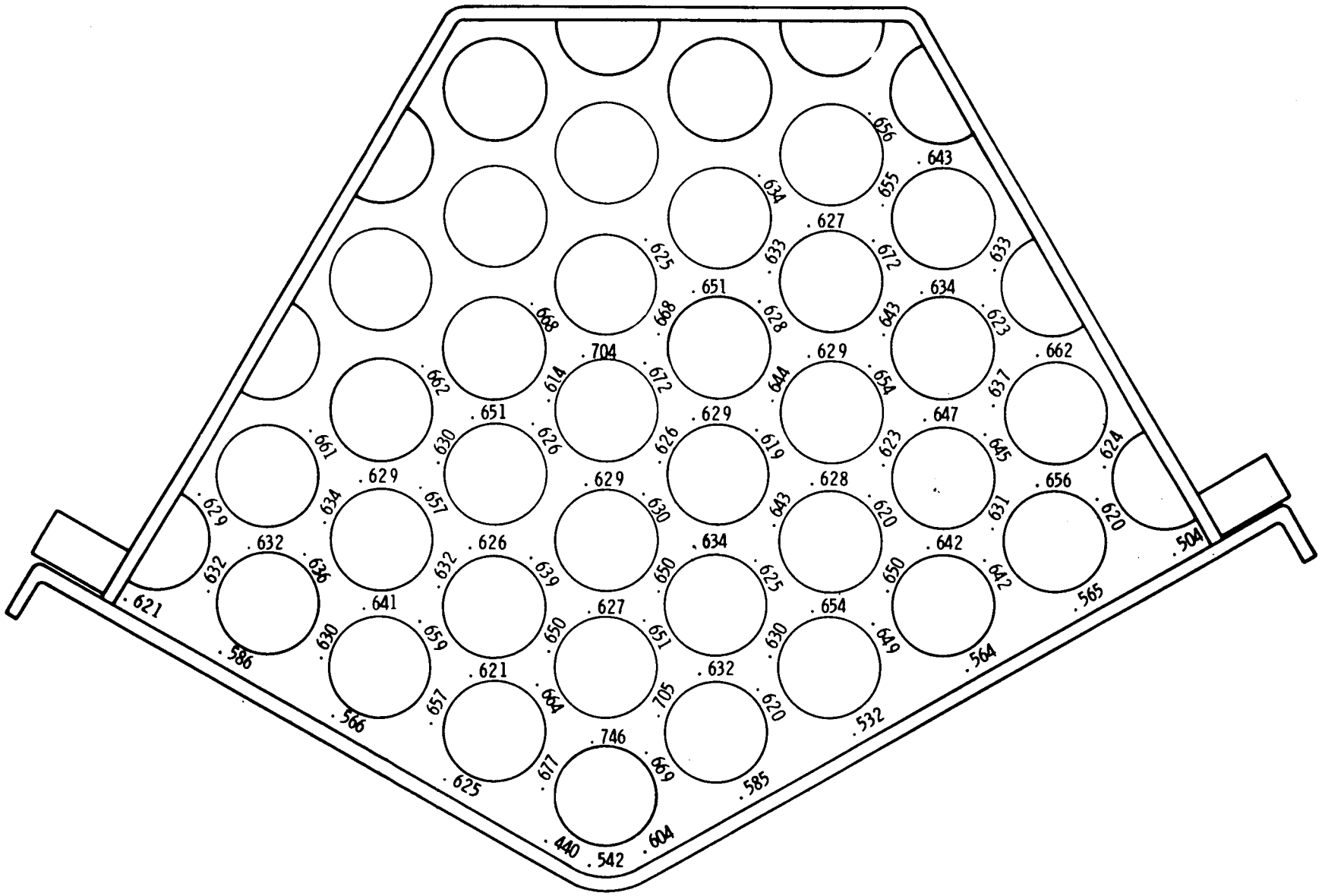

Fig. 2-8—Clearance gap spacings 132.0 inches from downstream end of test section

The cover was then lowered over the assembly and measurements made of the spacing between the half-rods and the cover. Strips of foamed rubber one-half inch wide were fastened to the outside of the half-rods to close off this region (which measured about 7/16 inches thick) to flow. These strips may be seen in Figure 2-3b. The cover was then lowered into place and the test section completed by putting small corks in the model wire wraps at the test section inlet.

2.2 The Duct Cross-Section

For the proper determination of duct Reynolds number and for verification of pre-test predictions, it was important to have an accurate measure of the total flow area. The major dimension to be measured was the area of the overall duct with no rods or wire wrap in place. The calculated area, based upon the dimensions in Figure 2-1 is 354.54 in^2. However, the uncertainty in the various angles lead to consideration of an alternative method of area determination.

Pencil lead was rubbed over the front edges of the duct and a sheet of heavy (0.6878 grams/in^2) cardboard was pressed against these edges. This outline was then cut out and weighed. The total weight of the original cardboard sheet was 849.9 grams for the 1235.63 in^2 of cardboard. After the cross section was removed, 601.8 grams remained; ratioing the difference resulted in an overall duct area of 360.7 in^2. Weighing the cut out section and noting the difference yielded a measure of the inaccuracies due to the weighing procedure. This section weighed 247.8 grams implying an area of 360.26 in^2 or an uncertainty of about 0.1 percent due to weighing. Errors in duct outline, cutting out procedure, and cardboard density variations could not have caused more than about $\pm$ 1.0 in^2 difference so that the value of 360.7 in^2 was used rather than the calculated value of 354.54 in^2 for the overall duct area. This 1.7 percent difference could easily be accounted for in the uncertainties associated with the various measured angles and lengths in Figure 2-1. Although the above difference seemed quite small, when the (known) areas of the rods and half-rods were subtracted to obtain a net flow area, a considerable difference between the calculated and "experimental" areas, i.e., 4.6 percent, was found.

As a starting point for determining the areas of the internal parts of the duct assembly, it was noted, from Figure 2-5, that the average diameter of the model fuel rods was 2.505 inches as opposed to the nominal value of 2.5 inches. The total area for flow through the duct was calculated by subtracting the total rod area,

$$39 \times \frac{\pi}{4} (2.505)^2 \text{in}^2$$

the total wire wrap area,

$$39 \times \frac{\pi}{4} (.625)^2 \text{in}^2$$

and the area blocked by the rubber pads on the half-rods,

$$8 \times \frac{7}{16} \times 2.5 \text{ in}^2$$

or a total of 212.9 in^2, from the duct area of 360.7 in^2 to find a test section flow area of 147.6 in^2. The total wetted perimeter of the duct was 421.6 inches resulting in an overall hydraulic diameter of 1.400 inches. The hydraulic diameter for a "standard" triangular subchannel was 1.322 inches or 5.42 percent below that for the entire duct.

2.3 Instrumentation

Two of the rods in the duct cross section, noted by the numbers 1 and 2 in Figure 2-1, housed adjustable pitot-static probes, 0.0625 inches in diameter. The instrumented rods extended upstream through the duct inlet, through an alignment plate and were fastened, with respect to axial motion, in a carriage. This carriage was moved axially over a total displacement of 100.0 inches by a chain belt driven, double lead screw arrangement. The instrumented rods were long enough so that with the pitot-static probes as far upstream as possible, there were no "holes" in the downstream end of the rod matrix which might adversely affect the flow distributions within the subchannels upstream of the grid support shown in Figure 2-4.

The axial motion carriage held protractors which allowed angular positioning of the pitot tubes within the duct by rod rotation. On the end of the instrumented rods were mounted 4.0 inch displacement dial indicators which were correlated with the radial displacement of the pitot tubes. These dial indicators measured the axial position of a screw actuated push-pull rod which, through a yoke, drove a wedge that radially positioned the pitot tube.

A linkage was incorporated to maintain the pitot tube parallel to the rod surface against the torques of the plastic tubing leading out the upstream end of the instrumented rod. These two concentric tubes ducted the dynamic and static pressures to a battery of four foot long manometer tubes inclined at an angle of 15.0° to the horizontal and using 0.834 S.G. manometer oil.

2.4 Flow Rate Determination

Since there was no section of ducting long enough to satisfy the necessary lead-in conditions for a standard flow measuring orifice, the total flow rate was determined from nine pitot-static probes located in the rectangular flow return section above the duct. These pitot tubes of 0.0625 inch diameter, (Type PDA-12-F-10-KL, manufactured by the United Sensor and Control Corporation) were arranged on Gaussian quadrature coordinates as shown in Figure 2-9. The pressures were read upon an inclined manometer with increments of 0.005 inches of water. This manometer was checked against a differential micromanometer, accurate to $\pm$ 0.0002 inches of alcohol. The two readings were in agreement to within 0.6 percent over the range of interest in the present work and to within 0.8 percent overall. These variations were not systematic so that no correction factor could be determined.

Using Gaussian multipliers, the average velocity was determined for pitot-static probes, 11, 21, and 31 in Figure 2-9 and applied over the area designated by the width A and similarly for the other two regions. The same procedure was followed then in the transverse direction and the average of the two results was used as the mean velocity. The only judgement factor entering into the flow rate determination was the relative area assigned to each average velocity; i.e., the quantities A/L and B/L where L = 20.0

DWG. 6186A67

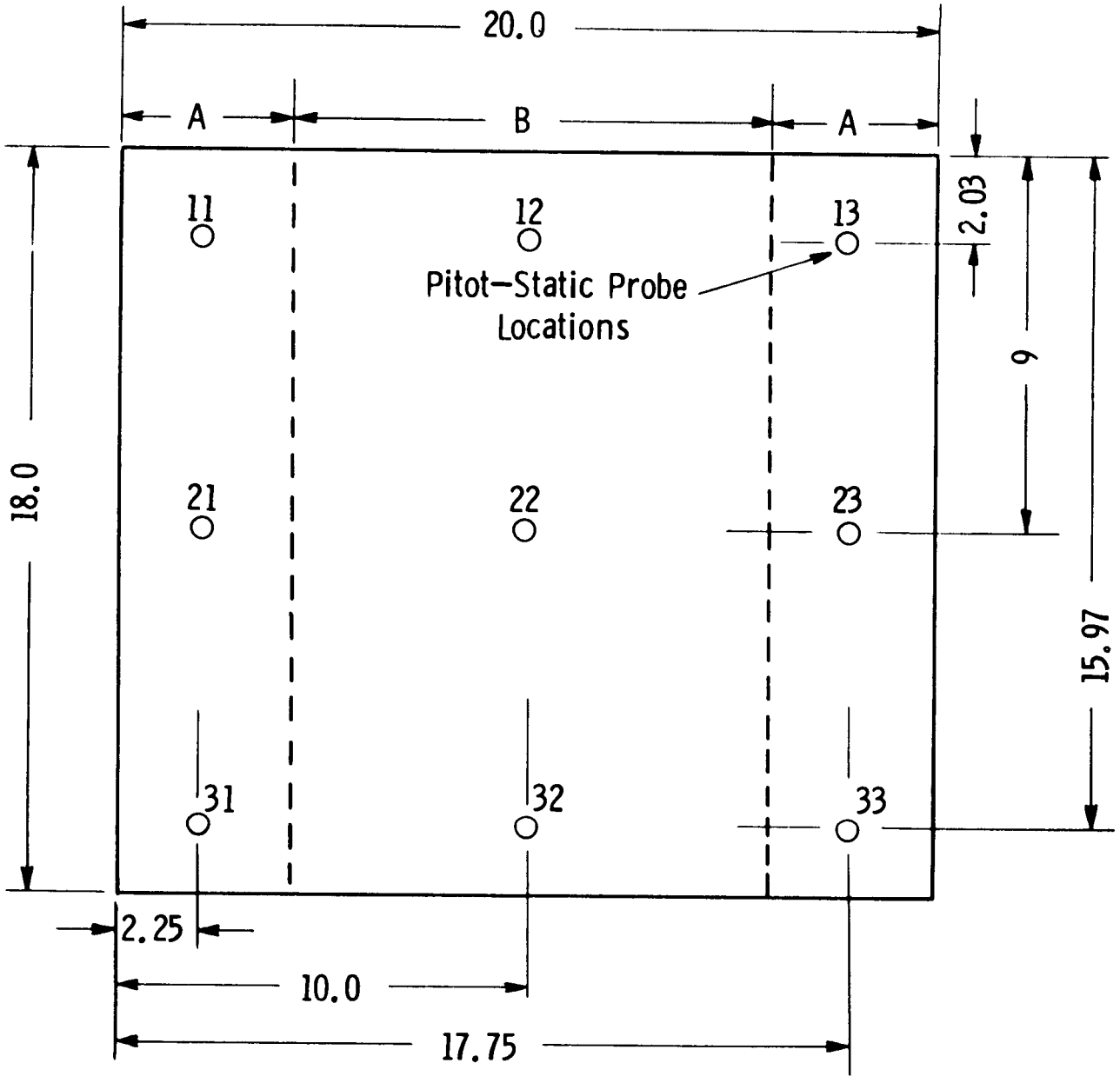

Fig. 2-9 – Layout of flow measuring pitot-static probes
(dimensions in inches)

inches for vertical integration and 18.0 inches for the transverse sum. (The actual values for the internal dimensions of the rectangular duct were 20.07 inches by 18.04 inches). The A/L and B/L ratios were varied for the same input data with the following results.

TABLE 2-1

COMPARISON OF FLOW RATE RESULTS
WITH DIFFERENT INTEGRATION AREAS

	Direction of Integration	Flow Rate (ft^3/sec)	Average Flow Rate
Case I			
A/L = .225	Transverse	99.376	99.157
B/L = .550	Vertical	98.940	
Case II			
A/L = .333	Transverse	98.752	98.983
B/L = .333	Vertical	99.214	
Case III			
A/L = .300	Transverse	98.944	99.037
B/L = .400	Vertical	99.130	

From Table 2-1, it may be noted that the maximum difference due to integration area choice was less than 0.5 percent while the average flow rates differed by less than 0.2 percent.

3.0 PRELIMINARY EXPERIMENTS

3.1 Introduction

During check out of the test facility, certain measurements were made which are of interest to report and these are discussed before the mixing experiments are considered. Throughout all testing, the flow was held constant at a volumetric rate of 112.6 ft^3/sec in the rectangular duct. This yielded an average velocity in the test section of 109.8 ft/sec and a test section Reynolds number of 73,000 based upon 75°F air.

Measurements of the volumetric flow rate over long periods of time showed maximum variations of up to $\pm$ 4.0 percent, but swings on the order of $\pm$ 2.0 percent were more common.

3.2 Wire Wrap Angular Positioning

Figure 3-1 shows the subchannels and gaps near the instrumented rods and injector rod which were studied in this work. The zero angular reference from which the angle of the wire wrap was measured was arbitrarily taken as that corresponding to the wire wrap centered in gap g-g of the figure. After duct assembly, the first operation was to determine whether the angular alignment of a wire wrap was adequate.

The pitot-static probes discussed in Section 2.3 were electrically insulated from the duct and when contact was made between the probe and any part of the duct, a red light and buzzer warning system was activated. Using this buzzer system as a wire wrap locating system, i.e., extending the pitot static probe and rotating it until the wire wrap is touched, resulted in the curve shown in Figure 3-2 for the wrap surrounding the number 1 instrumented rod (the wrap marked as "B" in Fig. 3-1).

Dwg. 6354A32

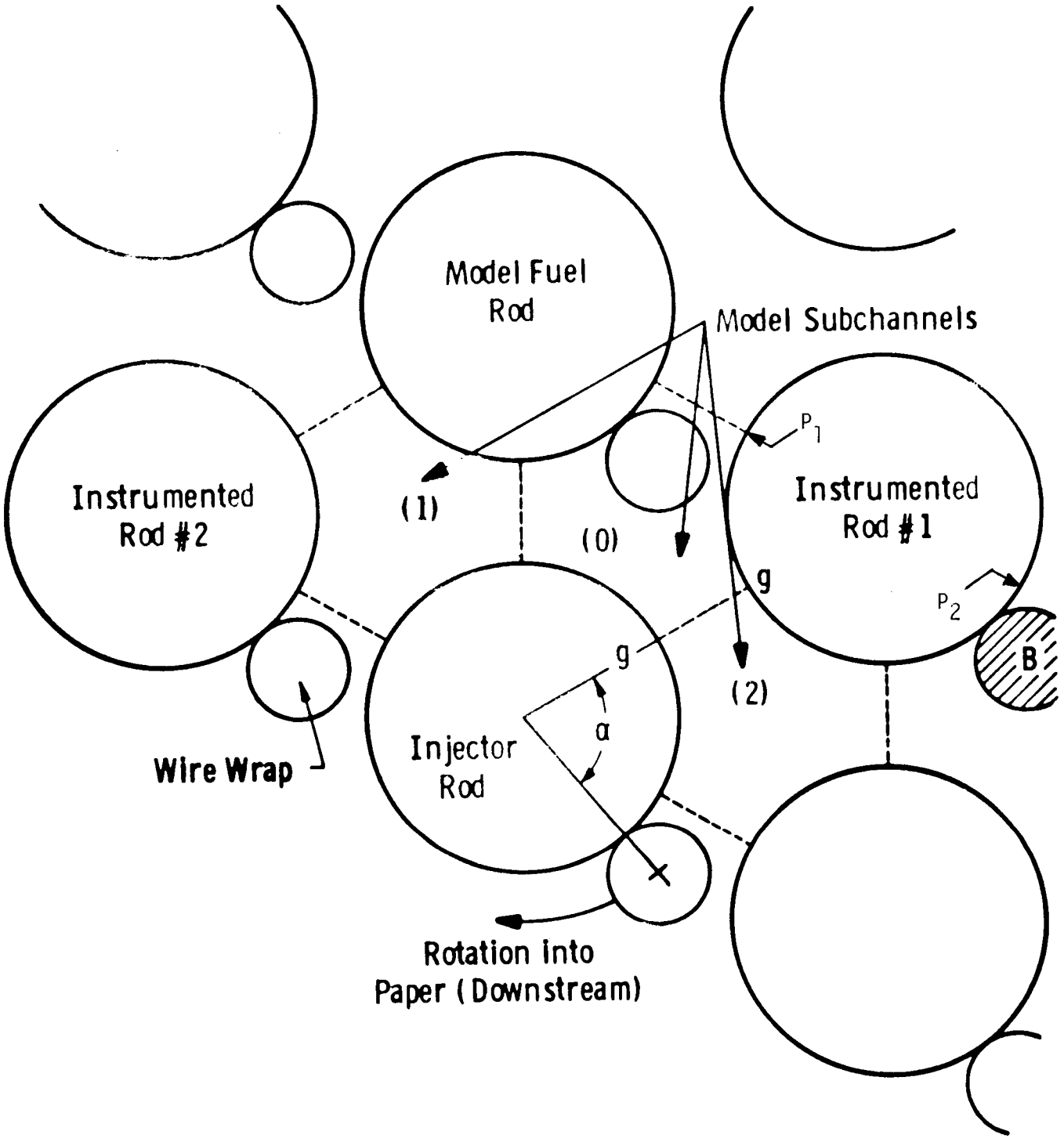

Fig. 3-1—Internal wire wrap configuration

The vertical coordinate corresponds to the angle α in Figure 3-1 and the axial distance along the horizontal coordinate is measured in the upstream direction from the point of maximum pitot-static probe penetration in Figure 2-4. It may be noted that the "curvature" of this wire wrap increased somewhat with axial distance into the duct starting at about 2.54 degrees/inch at the upstream end and increasing to 2.78 degrees/inch at the exit. These values are -3.5 percent and +6.0 percent respectively from the average rate of 2.63 degrees/inch. Since this model wire wrap was suspended from adjacent rods, its angular positioning is among the worst in the test-section. However, the linearity of the curve in Figure 3-2 appears acceptable and the rest of the test section was expected to be at least as good.

3.3 Flow Development

During verification of the wire wrap location described in the previous section, axial flow measurements were made with the pitot-static tube along the subchannel axis at a uniform 50 degrees clockwise from the wire wrap. These velocities are shown in Figure 3-3. Since the wire wrap moved only through a little more than one half a rotation about the instrumented rod in the distance traversed in this experiment, it should be noted that it "passes through" three gaps during each half rotation. Thus, the probe moved through four gaps in this experiment to yield a reasonable picture of developing flow.

Since the measurements were away from the wall surfaces in the subchannels, velocities were expected to be somewhat greater than the overall duct average of 109.8 ft/sec and this seems to be the case in Figure 3-3. The overall picture appeared to indicate the usual type of flow development with slug type flow at speed $\overline{U}$ at the entrance gradually developing as the boundary layer built up to yield a fully developed profile. However, it was noted that the last experimental point is 108 hydraulic diameters into the duct, a point at which one would normally anticipate relatively completely developed flow, and there appeared to be some small amount of change in the axial direction.

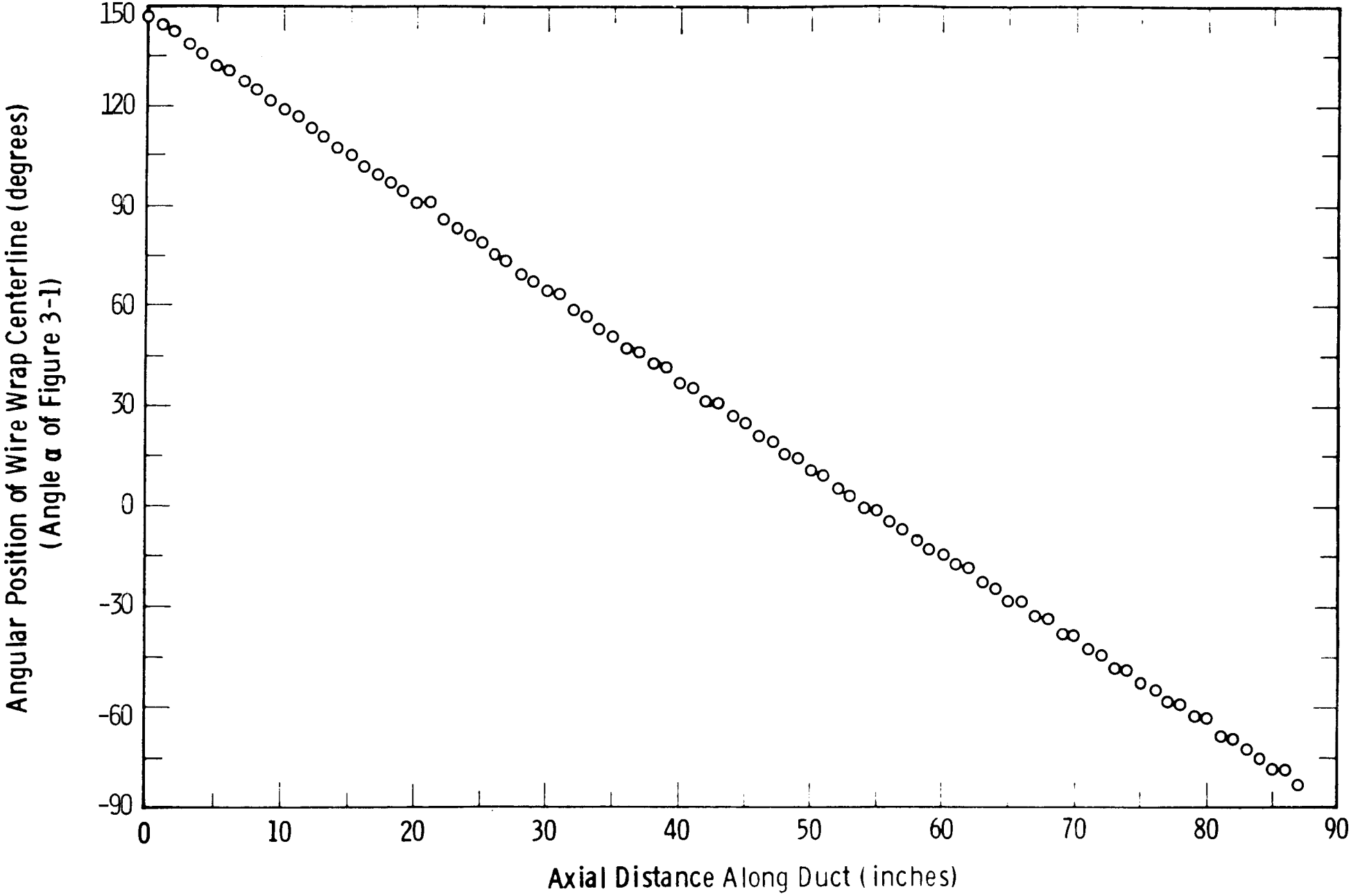

Fig. 3-2—Experimental determination of angular location of center of wire wrap

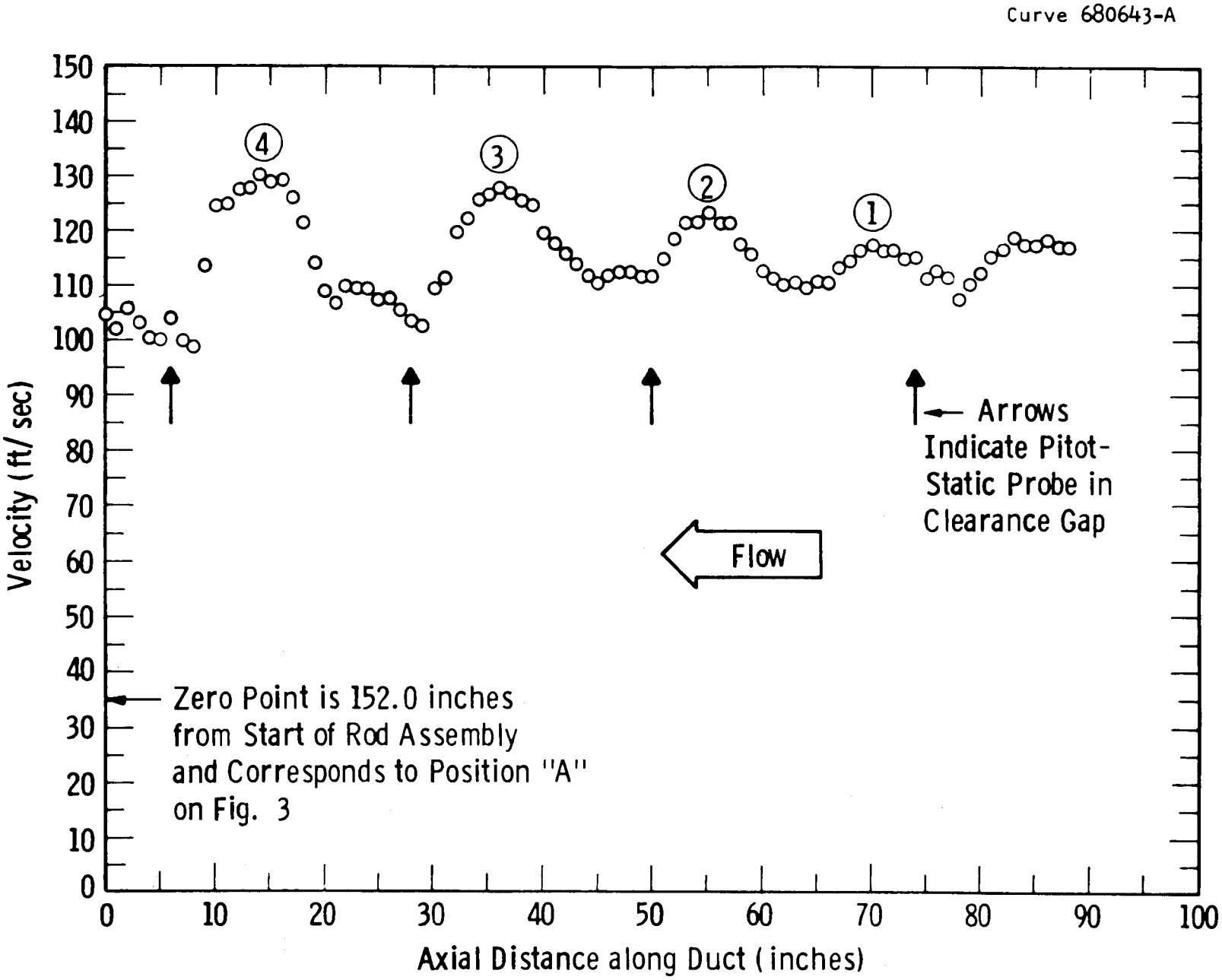

Fig. 3-3 —Velocity development in duct

Due to the normal asymptotic approach to full flow development and the small percentage changes shown from peak-to-peak in Figure 3-3, it is impossible to make a definitive statement for the downstream end of the test assembly with regard to the fullness of flow development on the basis of these data alone. The next section, however, does provide more definitive data.

3.4 Friction Factor Calculation

Several static pressure profiles were taken over the length of the test section, one of which is shown in Figure 3-4 and corresponds to the type of experiment described in the previous section. Let the friction factor, f, be defined by (*)

$$\frac{\Delta P}{\Delta L} = \frac{f}{d_h} \frac{1}{2} \frac{\rho}{g} \bar{u}^2 \qquad (1)$$

where ΔP = pressure drop due to friction over ΔL;
ΔL = increment in axial length;
d_h = hydraulic diameter;
ρ = density of air;
g = gravitational constant;
$\bar{u}$ = average axial flow.

Then f = 0.0206, corresponding to the straight line in the figure. Reasonably complete flow development is indicated over the last 40 inches of pitot tube travel by this value of f in that it agrees within 1.5 percent with the value calculated in Section 1.3. That calculated value is based on the assumption of fully developed flow.

One further experiment was performed using simple 0.0625 inch diameter static pressure holes flush with the instrumented rod surface at the positions marked P_1 and P_2 in Figure 3-1. This technique results in a pressure drop profile along the axis of a gap. In this case the rod was not rotated but drawn straight out with P_1 and P_2 readings taken at each gap. These results are shown in Figure 3-5 and indicate a slight increase in the

(*) The friction factor is based on the Blasius rather than the Fanning correlation.

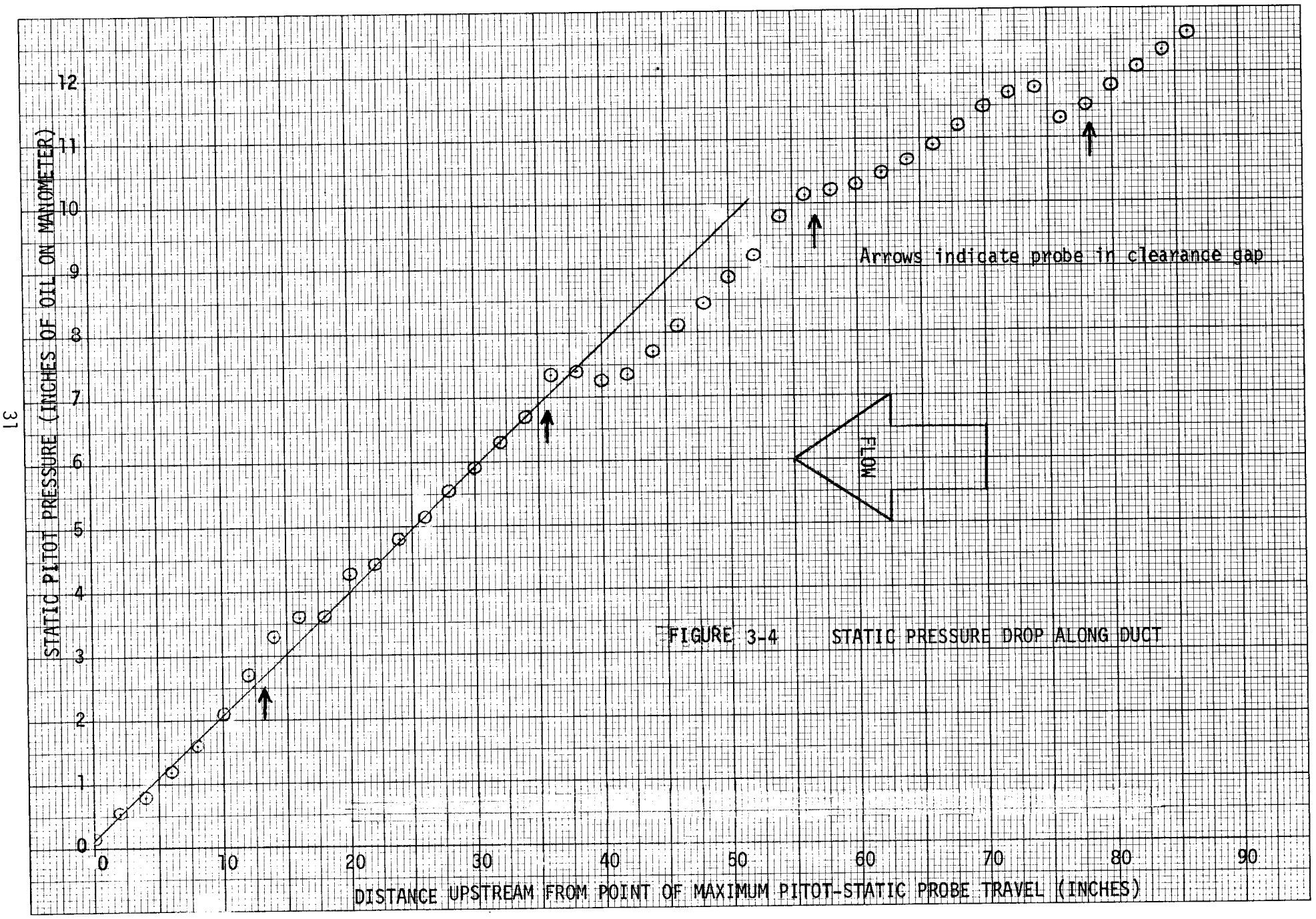

FIGURE 3-4 STATIC PRESSURE DROP ALONG DUCT

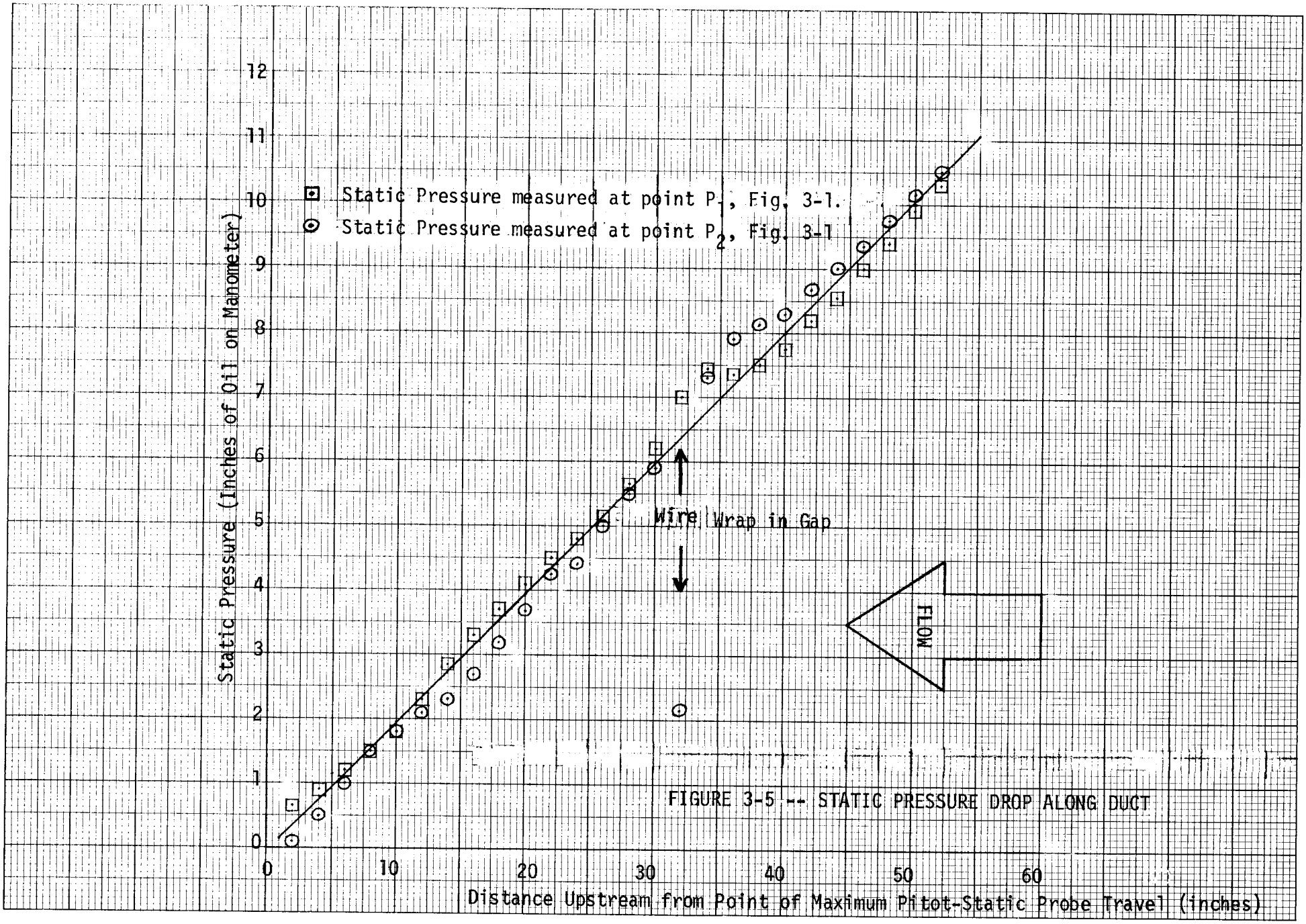

FIGURE 3-5 -- STATIC PRESSURE DROP ALONG DUCT

static pressure just upstream of the wire wrap as it enters the gap. The very low point at 32 inches indicates there may have been some leakage of the flow between the rod and wrap at that point. The proper straight line to draw for friction factor calculations is not quite so clear in this case as in the previous case. The line shown in the figure yields f = 0.0220 but is somewhat questionable since a considerable portion of it is based in the developing region of the flow.

4.0 TRACER GAS MIXING EXPERIMENTS

4.1 Introduction

The various computer codes used to analyze internal flows through rod bundles generally rely upon a lumped parameter approach which treats the interstitial spaces between the rods as discrete subchannels connected with adjacent subchannels through the three surrounding clearance gaps. Transport of mass, energy, and momentum takes place through the gaps to cause transverse variations in the distributions of these parameters. It is important to have a sound physical basis for such inter-subchannel transport terms in order to properly predict the core operating conditions. The purpose of this work is to obtain such a basis.

4.2 Tracer Sampling and Injection Systems

The general approach was that of injecting a small amount of tracer gas into a subchannel and, by taking downstream concentration distributions, noting how the marked fluid was transported from one subchannel into those adjacent to it. The dynamic pressure taps of the pitot-static probes mounted on the instrumented rods (numbered 1 and 2 in Figure 2-1) were used as gas sampling ports. The lines through which the samples were drawn exited from the instrumented rods outside the upstream end of the test facility where the sample gas passed through a dessicant before entering a MSA Model 300 Infra-Red Analyzer. The tracer gas used in these experiments was Ethane (C_2H_6), since its molecular weight of 30.07 is close enough to that of air to render buoyancy effects negligible. The Infra-Red Analyzer was factory calibrated to read 0 to 2000 ppm ethane at atmospheric pressure with a maximum scale non-linearity of 2.5 percent.

The test facility was operated at subatmospheric pressures so that a vacuum pump was necessary to draw the sample gas through the analyzer. To speed up the sample withdrawal rate, the specimen chamber was held at 22.2 inches of Hg below atmospheric pressure. The exhaust from the vacuum pump was piped back into the experiment just ahead of the blower.

The ethane was metered into the injector model rod by passing through a 0.043 inch diameter orifice with a 0.834 S.G. oil manometer differentially mounted across the orifice. The ethane volumetric flow rate was determined by calibrating the orifice pressure drop against a precision volumetric displacement type wet test meter.

The tracer gas entered the injector rod at the upstream end of the model rod bundle and exited into the flow inside the test section through a 0.0625 inch I.D. tube epoxyed in a hole in the side of the rod. The 0.0625 inch tube was filed flush with the rod surface.

4.3 Method of Analyzing Experimental Results

Before proceeding with a discussion of the experimental results, the method of data reduction should be mentioned since this has a considerable bearing upon the accuracy required of the data.

The axial flux of tracer within a subchannel may be written:

$$\int_{A_s}\int u\, C\, dA_s \qquad (2)$$

where

u = axial velocity of the flow in the subchannel

C = molecular concentration of the tracer gas

A_s = subchannel cross-sectional area.

If the circumferential velocity, v, induced about the rod wire wrap is considered as the main intersubchannel transport mechanism, the tracer flux into a particular subchannel per unit axial distance is:

$$\sum_{j=1}^{3} \int_{S_{gj}} v\, C\, dS_{gj} \qquad (3)$$

where,

v = circumferential velocity component

S_{gj} = distance across the jth gap

dS_{gj} = differential element of length normal to both rod surfaces and across the jth gap.

The axial rate of change of subchannel tracer flux in Eq. (2) will be given by Eq. (3) so that

$$\frac{d}{dx} \int\int_{A_s} u\, C\, dA_s = \sum_{j=1}^{3} \int_{S_{gj}} v\, C\, dS_{gj} \qquad (4)$$

where x represents the axial coordinate.

In the present experiment, neither u nor v distributions are known so that mean values, $\bar{u}$ and $\bar{v}$, will be assumed applicable over the subchannel and gap cross-sections, respectively, and thus

$$\frac{d}{dx} \int\int_{A_s} C\, dA_s \simeq \sum_{j=1}^{3} \frac{\bar{v}_j}{\bar{u}} \int_{S_{gj}} C\, dS_{gj} \qquad (5)$$

If zero concentration levels occur in two of the subchannel gaps, $\bar{v}/\bar{u}$ may be obtained in the third gap from

$$\frac{\bar{v}}{\bar{u}} = \frac{\frac{d}{dx} \int\int_{A_s} C\, dA_s}{\bar{C}_g\, S_{gj}} \qquad (6)$$

where,

$$\bar{C}_g\, S_{gj} = \int_{S_{gj}} C\, dS_{gj} \qquad (7)$$

Equation (6) may well be more applicable to lumped parameter computer application than precise expressions obtained by integration of Eqs. (2) and (3) since only $\bar{v}$ and $\bar{u}$ are calculated in most programs.

4.4 Experimental Results and Calculations

The initial mixing experiment was performed to find out how much of the flow in a particular subchannel would be swept out ahead of a wire wrap as the wrap passed through the sixty degrees corresponding to the angle subtended by the subchannel. To this end, the sampling probe from rod number 1 was located at the center of the subchannel marked as (0) in Figure 4-1 at an axial position such that wire wrap "A" was just entering the gap marked j-j. The injector flow rate, angular position, and axial position were varied until readings were obtained on the infrared analyzer. Then, using a grid similar to that shown in Figure 4-2, a concentration field was mapped.

The grid of Figure 4-2 was not used as an absolute positioning scheme since often the tracer field would be rather compact so that, once the position of the tracer fluid had been located, interpolative readings were made to yield the requisite mapping data. These readings were entered directly on a 5:1 scale drawing of the subchannel being studied. Then, using graph paper, these readings were plotted versus angle in the circumferential direction and versus radius in the radial direction along constant radius lines or constant angle lines, respectively. Smooth curves drawn through these plots allowed determination of intercepts at arbitrary intervals to yield plots such as that shown in Figure B-1 of Appendix B. A total of twenty-one distributions were determined. These were divided into five data sets according to the five different injector positions and are shown in Figures B-1 through B-21. Two percent concentration contours are shown for only the more diffuse mappings where more definition is needed. The uncertainty, however, at that concentration is relatively high.

The procedure for determination of the average rod clearance gap circumferential velocities is given below. If all the wire wraps are assumed to have angle versus length curves such as that shown in Figure 3-1, an angular rate of change of 2.67 degrees/inch is found over the test section region. Thus, an axial distance of six inches corresponds to a 16-degree

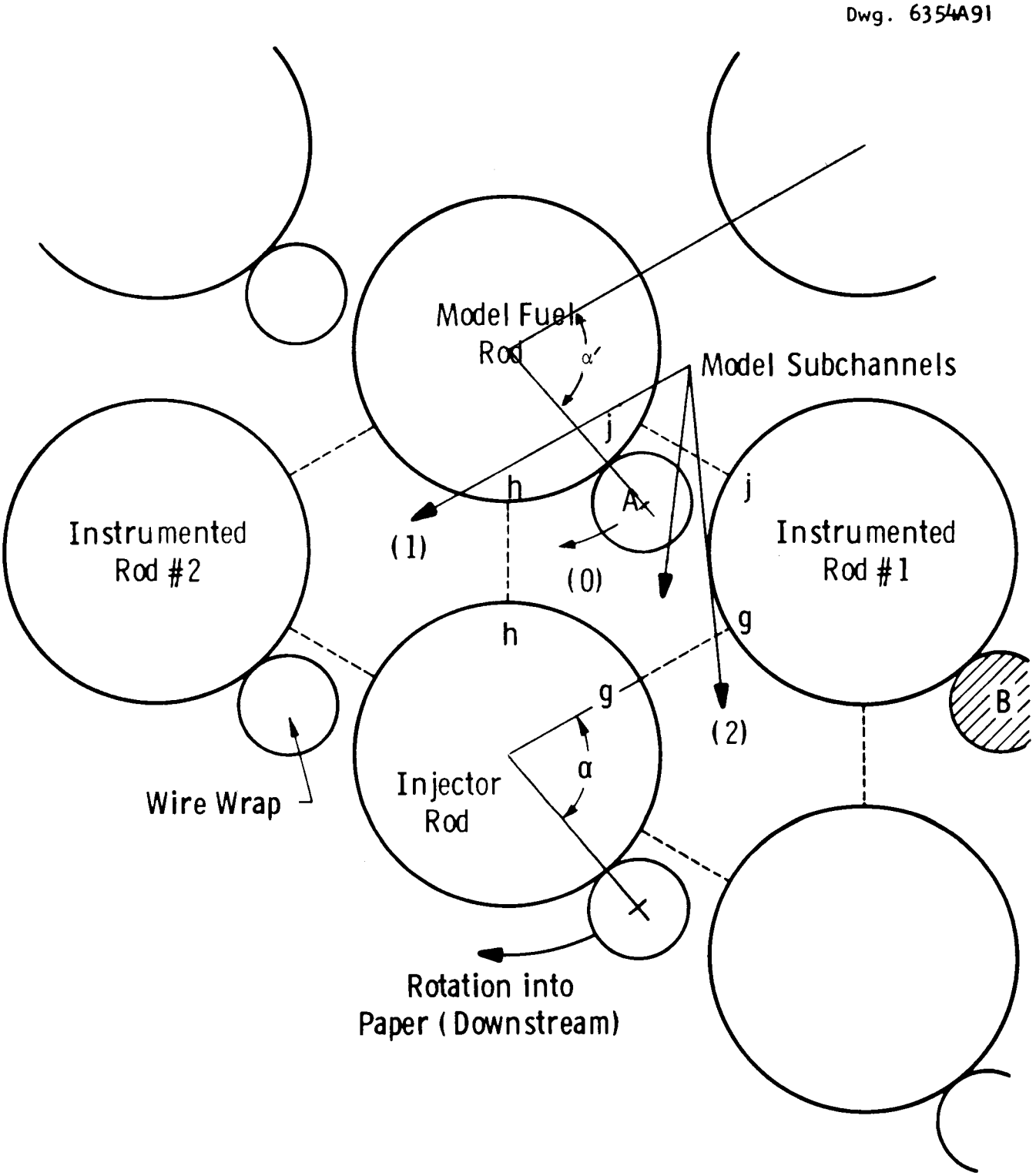

Fig. 4-1—Internal wire wrap configuration

Dwg. 6175A65

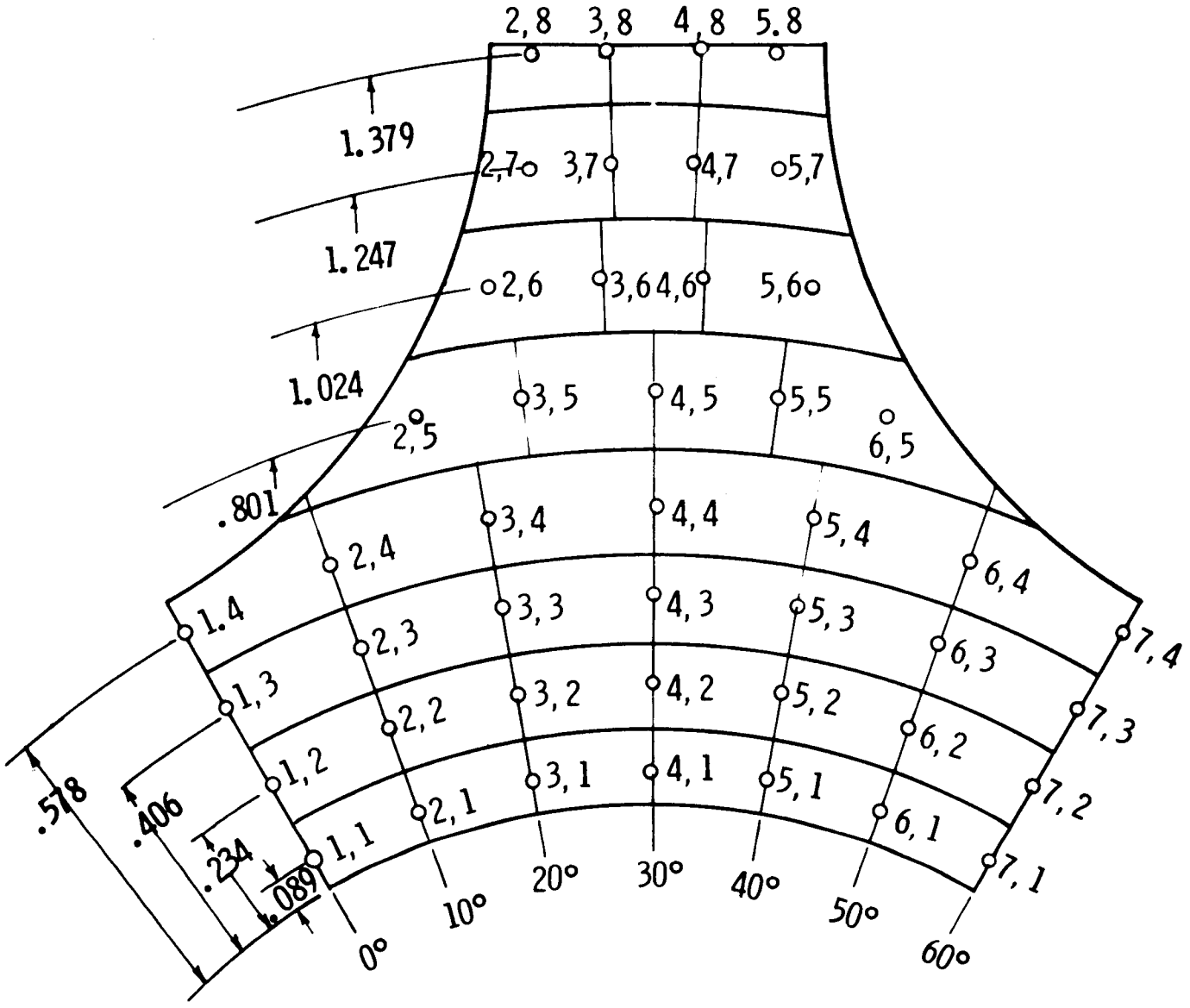

Fig. 4-2—Inboard subchannel (dimensions in inches)

wrap angle change. The six inch distance is required to obtain a distinct change in the concentration distributions and hence allow accurate evaluation of any differences. For the purposes of data reduction, Equation (6) is written:

$$\frac{\bar{v}}{\bar{u}} = \frac{\frac{d}{dx}\int_{A_s}\int C\, dA_s}{\bar{C}_g\, S_g} \simeq \frac{\left[\int_{A_s}\int C\, dA_s\right]_{x+\Delta x} - \left[\int_{A_s}\int C\, dA_s\right]_x}{\bar{C}_g\, S_g\, \Delta x} \tag{8}$$

The integrals in the last term of the above equations are evaluated by the approximation

$$\int_{A_s}\int C\, dA_s \simeq \sum_{i=1}^{N} C_i\, \Delta A_i \tag{9}$$

where the concentration C_i and corresponding elemental areas ΔA_i are taken as those lying between the contours of the concentration profiles in Appendix B. For example, in Figure B-1 the areas between the 10 and 20 concentration levels are taken as ΔA_{10} where there is a ΔA_{10} for both the (0) and (1) subchannels (see Figure 4-1). The summation in Equation (9) was evaluated by tracing the 5:1 scale distributions on heavy cardboard, cutting along the contours and weighing the cardboard cutouts for each region in each subchannel. Thus, for subchannel (0) in Figure B-1,

$$\sum_{i=1}^{N} C_i\, \Delta A_i = 10\, \Delta A_{10} + 20\, \Delta A_{20} + \cdots + 80\, \Delta A_{80} \tag{10}$$

For consistency (and simplicity), the average concentration in the gap, $\bar{C}_g$ of Eq. (8), was determined by plotting C_g across the gap on cardboard, cutting out, and weighing. The scale upon which the weighing was performed was accurate to within 0.1 milligram - much more refined than the procedure and interpolations required. The various pertinent results are tabulated in Table 4-1. An explanation of this table follows.

TABLE 4-1

SUMMARY OF EXPERIMENTAL MIXING RESULTS

1	2	3	4	5	6	7	8	9	10	11	12	13	14	15
			$\sum_i C_i \Delta A_i$ (grams)				Average Gap Concentrations							
	Exp. No.	Wrap Angle(°)	Subch. (0)	Subch. (1)	Subch. (2)	Total	$\bar{C}_{0-1}$	$\bar{C}_{0-2}$	Axial Position In Duct	Distance Below Injector	$\bar{\alpha}$	$\phi_{0-2}(\bar{\alpha})$	$\bar{\alpha}$	$\phi_{0-1}(\bar{\alpha})$
Experimental Set "A" Ethane Flow Rate of 0.236 lb/hr Injector at 40.25" Cardboard at 44.193 grams/ft^2	1	62°	96.92	6.11	0.0	103.03	13.34	0.0	31.9	8.3	70°	Note A	130°	-.691 to .086
	2	78°	79.24	4.00	0.75	83.99	9.08	3.78	25.9	14.3	86°	.389 to 1.316	146°	-1.085 to .239
	3	94°	58.20	1.01	8.12	67.33	2.45	13.57	19.9	20.3	102°	.624 to .893	162°	Note B
	4	110°	28.05	4.50	26.76	59.31	1.96	13.78	13.9	26.3	118°	-.230 to .144	178°	Note B
	5	126°	26.59	12.00	30.55	69.14	2.00	10.26	7.9	32.3				
Experimental Set "B" Ethane Flow Rate of 0.236 lb/hr Injector at 58.6" Cardboard at 44.193 grams/ft^2	6	12°	79.0	0.0	0.212	79.21	0.0	0.745	50.6	8.0	20°	Note C	80°	Note A
	7	28°	32.44	0.0	33.14	65.58	0.0	25.52	44.6	14.0	36°	.247 to .263	96°	Note A
	8	44°	21.18	0.0	44.15	65.33	0.0	16.31	38.6	20.0	52°	.265 to .570	112°	Note A
	9	60°	13.60	0.0	60.54	74.14	0.0	10.04	32.6	26.0	68°	.161 to .353	128°	Note A
	10	76°	7.34	0.0	63.40	70.74	0.0	6.22	26.6	32.0				
Experimental Set "C" Ethane Flow Rate of 0.214 lb/hr Injector at 40.2" Cardboard at 44.189 grams/ft^2 (same for "D" & "E")	11	77°	27.69	0.0	32.69	60.38	0.0	20.87	26.2	14.0	85°	.208 to .470	145°	Note A
	12	93°	9.46	0.0	40.74	50.20	0.0	14.62	20.2	20.0	101°	.381 to .413	161°	Note A
	13	109°	0.64	0.0	48.88	49.52	0.0	4.96	14.2	26.0	117°	Note B	177°	Note A
	14	125°	0.097	0.0	38.63	38.73	0.0	1.41	8.2	32.0				
Experimental Set "D" Ethane Flow Rate of 0.214 lb/hr Injector at 40.2"	15	61°	0.0	62.55	0.0	62.55	0.0	0.0	32.2	8.0	69°	Note A	129°	Note A
	16	77°	0.897	60.26	0.0	61.16	4.93	0.0	26.2	14.0	85°	Note A	145°	-.196 to .251
	17	93°	3.39	62.2	0.0	65.59	4.15	0.0	20.2	20.0				
Experimental Set "E" Ethane Flow Rate at 0.214 lb/hr Injector at 34"	18	78°	12.13	39.39	0.0	51.52	18.41	0.0	26.0	8.0	86°	Note A	146°	.292 to .452
	19	94°	30.53	27.52	0.0	58.05	18.86	1.12	20.0	14.0	98°	Note A	158°	.040 to .200
	20	102°	31.72	21.60	1.09	54.41	8.32	2.68	17.0	17.0	106°	Note D	166°	Note D
	21	110°	---	23.23	---	23.23	---	---	14.0	20.0				

Note "A" Zero gap concentrations upstream from experimental plane do not permit calculation of $\bar{C}g$.
Note "B" Large fractions of gap or subchannel concentrations at low concentrations with associated large uncertainties.
Note "C" Wire Wrap in gap prevents calculation of $\bar{C}g$.
Note "D" Position of wire wrap prevents determination of ΔC.

The first column lists the experimental data set, i.e., those concentration profiles corresponding to a given injector setting and tracer flow rate. The injector for set "A" was located 40.25 inches upstream of the maximum downstream pitot-static probe travel as indicated in Figure 2-4. Column 10 in the table, "Axial Position in Duct" gives the distance of the experimental plane upstream from the same reference point. The eleventh column then gives the distance of the experimental plane downstream from the injector position. The angular position of the injector outlet is indicated in the corresponding figures in Appendix B.

The second column gives the number of the experiment while the third indicates the value of α of Figure 4-1 at the test plane. The fourth, fifth, and sixth columns give the values of the sum in Equation (10) for subchannels (0), (1), and (2), respectively, and the seventh column is the combined sum. Columns 8 and 9 have the average values of the gap concentrations, $\overline{C}_{0-1}$ and $\overline{C}_{0-2}$, for the gaps between subchannels (0) and (1), and (0) and (2).

To facilitate understanding of the flow sweeping phenomenon in the wire wrapped configuration, the variable $\overline{v}/\overline{u}$ was divided by the tangent of the angle between the wire wrap centerline and the axis of the model rod, $\Theta = 4.33°$, so that

$$\overline{\phi}\ (\alpha) = \frac{\overline{v}(\alpha)}{\overline{u}\ \tan\ \Theta} \qquad (11)$$

Thus, when $\overline{\phi}\ (\alpha) = 1.0$, the circumferential flow is following the wire wrap exactly. This approach brings the very small values of $\overline{v}/\overline{u}$ to a more reasonable scale. Since $\overline{u}$ has been assumed constant, $\overline{\phi}(\alpha)$ indicates relative crossflow velocity from one axial location to the next.

The method of presenting the data from this experiment was to choose a clearance gap (gap g-g in Figure 4-1) and determine $\overline{\phi}(\alpha)$ at that particular gap as the wire wrap angle, α, varied. Such an output could then be applied to any internal clearance gap and explicit expressions for subchannel crossflows determined.

The final form of Equation (6) is:

$$\bar{\phi}(\bar{\alpha}) = \frac{\left[\sum_i C_i \Delta A_i\right]_{X+\Delta X} - \left[\sum_i C_i \Delta A_i\right]_X}{\bar{\bar{C}}_g \, S_A \, \Delta_X \, S_g \, \tilde{w}} \qquad (12)$$

where S_g = gap distance = 0.656/12 feet

S_A = area scale factor for cardboard = 25

$\tilde{w}$ = weight/unit area of cardboard = 44.193 gm/ft^2

ΔX = increment in axial length = 0.5 ft.

The difference in the numerator on the right side of the equation is the difference between the values of $\Sigma_i C_i \Delta A_i$ for a subchannel over the axial distance ΔX. The symbol $\bar{\bar{C}}_g$ represents the mean value of the average gap concentration over the same ΔX. The average angle of the wire wrap between the positions X and X + ΔX is represented by $\bar{\alpha}$.

From Equation (12), $\bar{\phi}_{0-2}$ and $\bar{\phi}_{0-1}$ in columns 13 and 15 are calculated for $\bar{\alpha}$ as listed in columns 12 and 14, respectively. This relationship assumes that the change in $\Sigma_i C_i \Delta A_i$ takes place through only one gap. Therefore, in the case of ϕ calculated over ΔX between experiments numbered two and three in Table 4-1, $\bar{\phi}_{0-2}$ and $\bar{\phi}_{0-1}$ are determined by combining first subchannels (0) and (1) and then subchannels (0) and (2) into composite subchannels to make the respective ϕ calculation. Crossflow of tracer gas into surrounding, unmeasured subchannels is assumed zero.

The values for $\bar{\phi}_{0-1}$ and $\bar{\phi}_{0-2}$ as functions of $\bar{\alpha}$ are represented in Figure 4-3 as a single function $\bar{\phi}$ for the (0)-(2) or g-g gap shown in Figure 4-1 with positive $\bar{\phi}$ indicating crossflow from subchannel (0) to (2). This is made possible by noting that as wire wrap "A" moves from gap j-j to gap h-h, the $\bar{\phi}(\alpha')$ values for gap h-h correspond to those obtained through gap g-g as α varies from 300° to 360° where the angle α' is also shown in Figure 4-1. Thus

$$\bar{\phi}_{h-h} \; (60° \leq \alpha' \leq 120°) = \bar{\phi}_{g-g} \; (300° \leq \alpha \leq 360°) \qquad (13)$$

or in general,

$$\bar{\phi}_{h\text{-}h}\ (\alpha') = \bar{\phi}_{g\text{-}g}\ (\alpha + 240°) \qquad (14)$$

and $\alpha' = \alpha$ since they are both measured from the same base direction.

The data are also represented as bars rather than points. The method for calculating $\bar{\phi}$ as just described can use the change in $\sum_i C_i \Delta A_i$ over ΔX from either side of the gap being considered. If the experimental procedure and data reduction technique were completely free of uncertainties and approximations, either choice would yield the same result. This, of course, was not the case. The end points of the data bars in Figure 4-3 are the values calculated for both choices. The various bar lengths are, then, an indication of the experimental uncertainty. They are not a measure of total uncertainty, however, in that an estimate of random error can not be made.

Despite the significant uncertainties indicated, a trend is apparent in Figure 4-3. The variable $\bar{\phi}$ seems relatively constant for $30° \leq \alpha \leq 90°$, experiences a crossflow reversal in the vicinity of $\alpha = 120°$ and returns to positive values for $\alpha > 120°$. Such a pattern is consistent with the relationship

$$\bar{\phi}\ (\alpha + 120°) = \bar{\phi}\ (\alpha + 60°) - \bar{\phi}\ (\alpha) \qquad (15)$$

where $\lim_{\alpha \to 0°} \bar{\phi}\ (\alpha) = 1.0.$

This equation describes the effect of phased, volumnless wire wraps and does not take into account the effects of volumetric displacement of sodium or obstruction of gap widths and flow areas by a physically real wire wrap, while variations in the mean axial velocity are assumed negligible. The detailed derivation of the equation is shown in Appendix C and specifically states the underlying assumptions and meaning of terms.

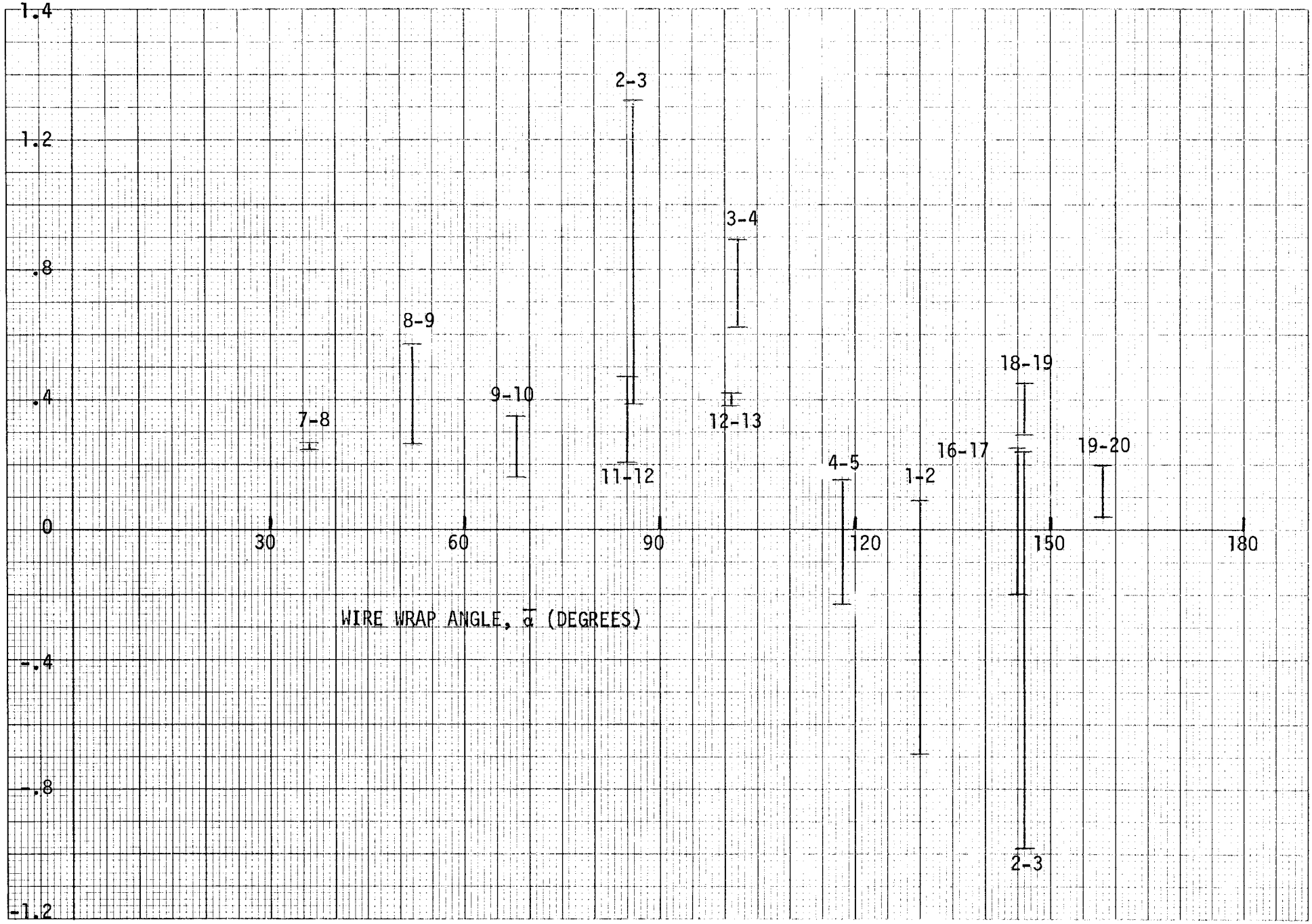

FIGURE 4-3 ϕ DETERMINED BY TRACER GAS DATA

5.0 CØBRA PROBE EXPERIMENTS

5.1 Introduction

The subchannel gap transport inferred from the tracer measurements in the previous section provided an indication of the behavior of this crossflow. Study of the various tracer concentration distributions should yield information on "dwell times" in a given subchannel as well as local estimates of internal mixing. However, the averaging required for reduction of data introduces a considerable amount of uncertainty so that more precise measurements would be desirable. The pitot-static probe in an instrumented rod (number 1) was replaced by a two-dimensional Cobra type probe, United Sensor Corporation, Type CA-120-12-CD. This probe has a central dynamic pressure tap with an angled tap on each side such that the pressure difference between the angled taps yields a measure of the flow angle across the probe.

The basic idea required placing the probe in the clearance gap such that the flow angle through the gap could be determined, and from this flow angle, $\phi(\alpha)$ values calculated at a local position rather than averaged over a particular length.

5.2 Cobra Probe Calibration

The initial calibration of the cobra probe was set up to determine the relationship between the flow angle and the cobra probe outer pressure tap differences. To accomplish this calibration, the apparatus shown in Figure 5-1 was assembled. For different dynamic pressures (measured by a pitot tube at the same flow tube cross section as the cobra probe), the cobra probe pressure tap differences were recorded as a function of β, the flow angle, over the range $-6° \leq \beta \leq 6°$. This data is shown in Figure 5-2. A least squares straight line was used as the calibration curve.

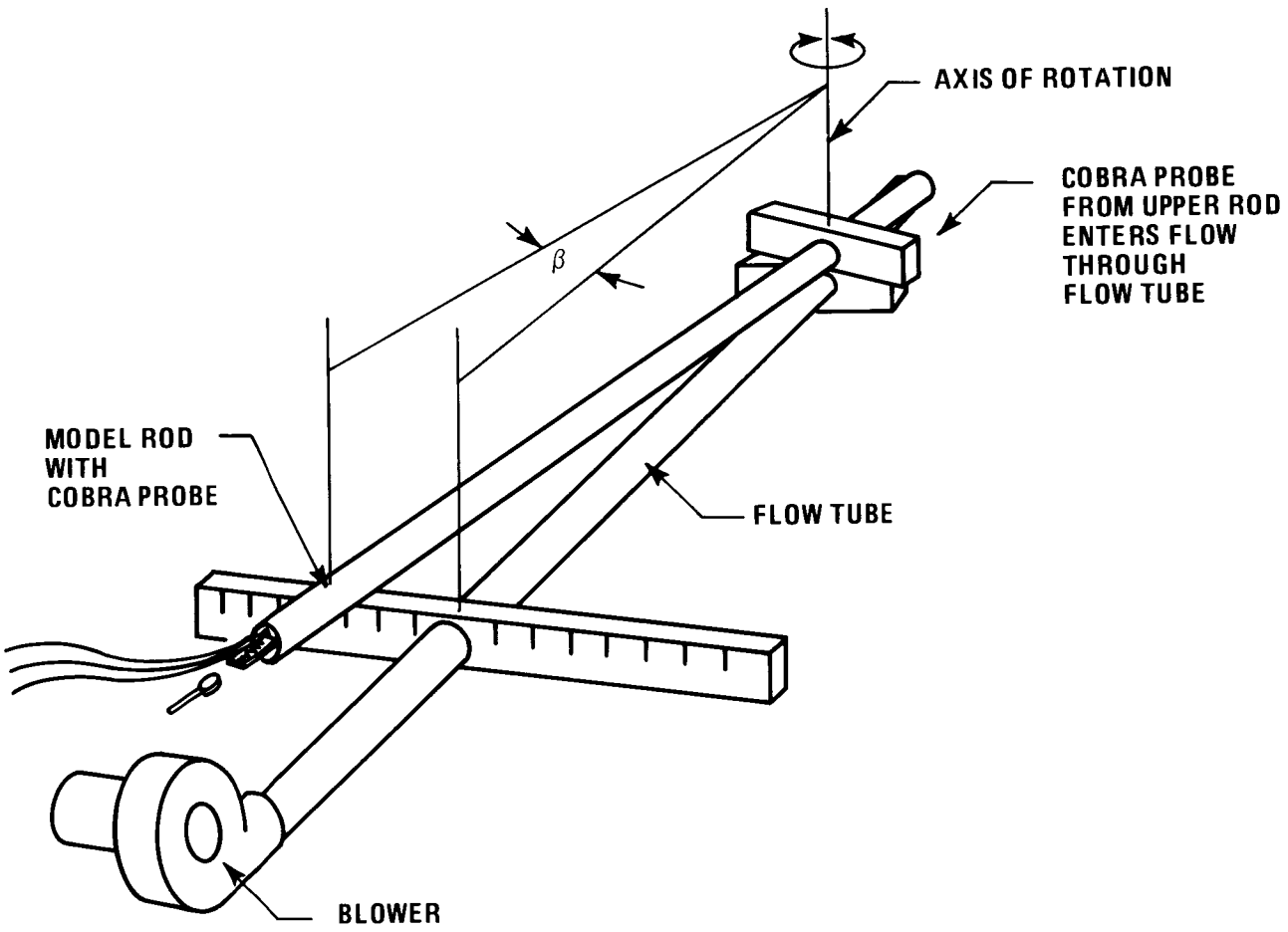

Figure 5-1 Schematic of Cobra Probe Calibration Procedure

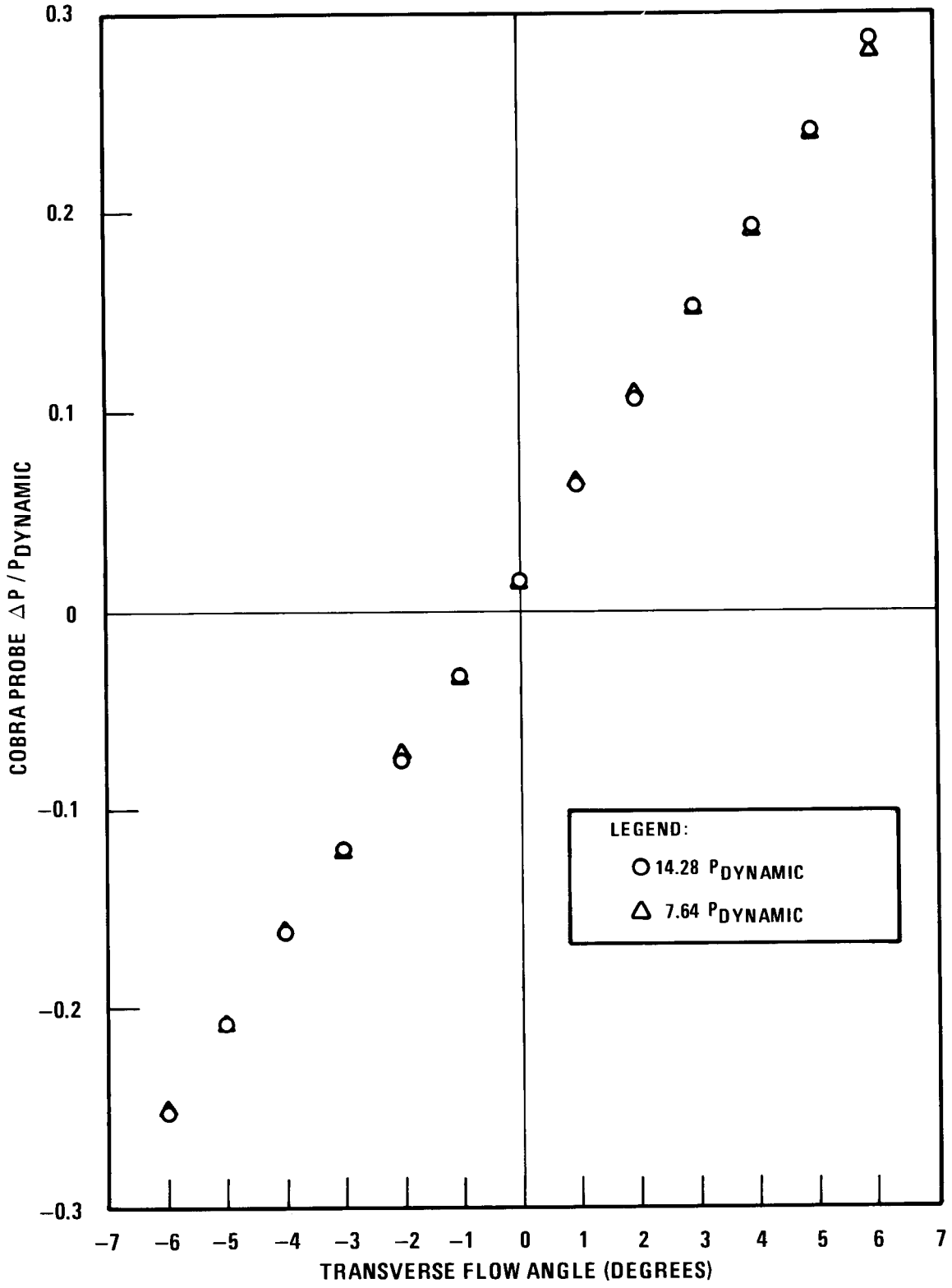

Figure 5-2 Cobra Probe Calibration Curve: Cobra Probe $\Delta P / P_{Dynamic}$ Vs. Transverse Flow Angle

7686-25

A second calibration was made after completing the testing in the model rod bundle to check the original calibration and to investigate a systematic translation that the Cobra probe may have undergone. Using the same calibration apparatus as before, it was found that the angle between the Cobra probe and the instrumented rod varied with probe height as shown in Figure 5-3. The curve is offset a small amount, $\delta = 0.18°$, from the original calibration (which was carried out at only one probe height). It was felt that the best data reduction procedure would utilize the curve of Figure 5-3 with an error band of $\pm 2\delta$.

5.3 Experimental Results

The instrumented rod with the Cobra probe was inserted into the model fuel rod bundle and measurements of the flow angle, β, were made in a clearance gap. Profiles of ϕ (α) were generated using β values from an 11-point traverse across the gap. Nineteen ϕ-profiles were measured over a range $9.66° \leq \alpha \leq 144.33°$. These are presented in Appendix D. The average value of ϕ (α) for each profile is shown in Figure 5-4 as a function of the wire wrap angle, along with the error band previously discussed. The solid curve of Figure 5-4 represents a trial and error fitting of the continuity equation written as

$$\overline{\phi}\ (\alpha) = \overline{\phi}\ (\alpha + 60°) - \overline{\phi}\ (\alpha + 120°).$$

The experimental results from the Cobra probe tests not only confirm the flow pattern indicated by the tracer gas data but also provide a more precise definition of that behavior. In fact, using the fact that

$$\overline{\phi}\ (\alpha) = -\overline{\phi}\ (\alpha + 180°),$$

the results are extended for the full range $0 \leq \alpha \leq 360°$. This is shown in Figure 5-5. In essence, these last two figures show more crossflow behind the wire wrap than in front of it. Interpretation must be made by recognizing that $\overline{\phi}$ was calculated with a constant value for axial velocity, 109.8 ft/sec. The value $\overline{\phi}$ therefore, indicates relative crossflow velocity from one axial location to the next.

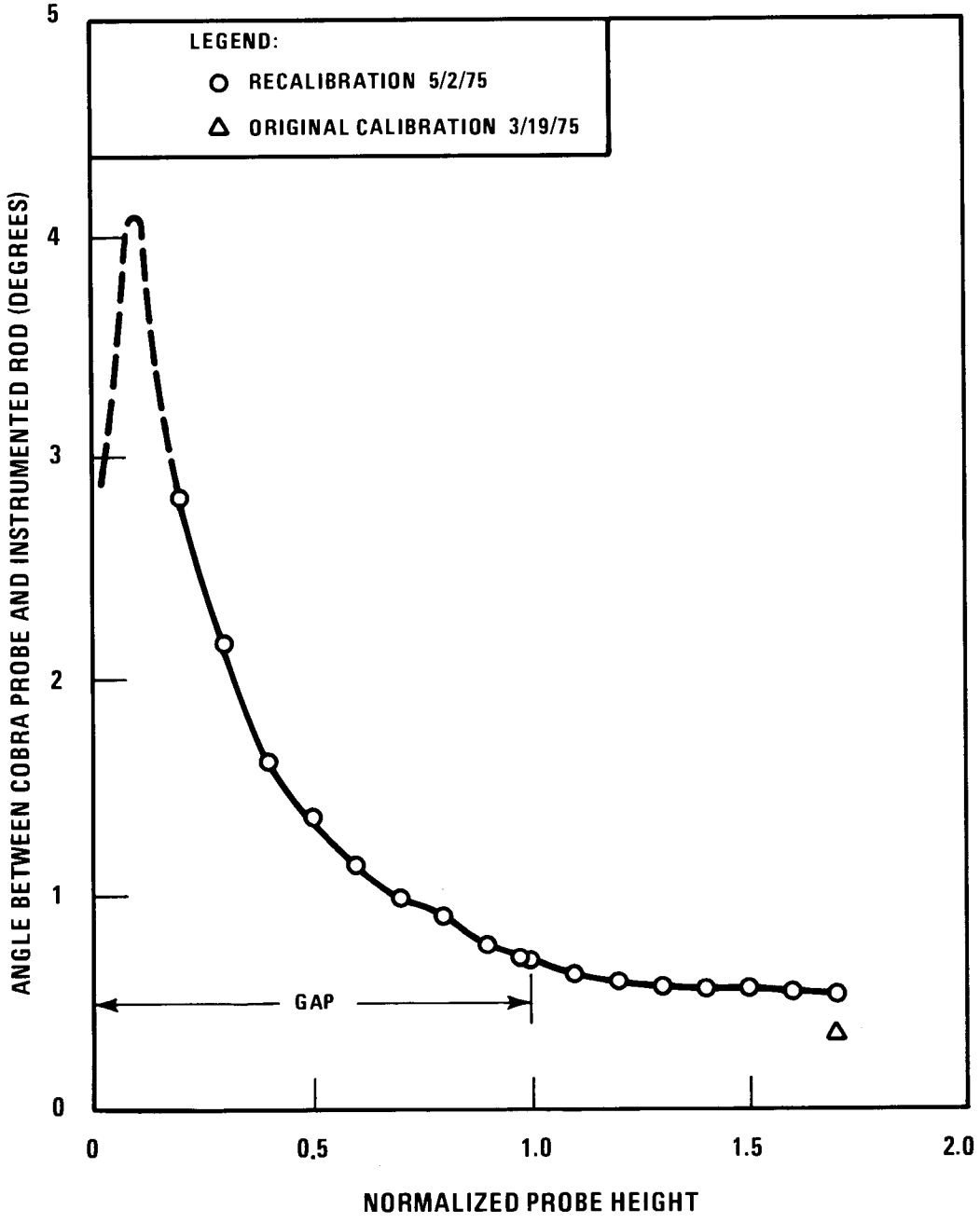

Figure 5-3 Angle Between Cobra Probe and Instrumented Rod as a Function of Probe Height

7686-26

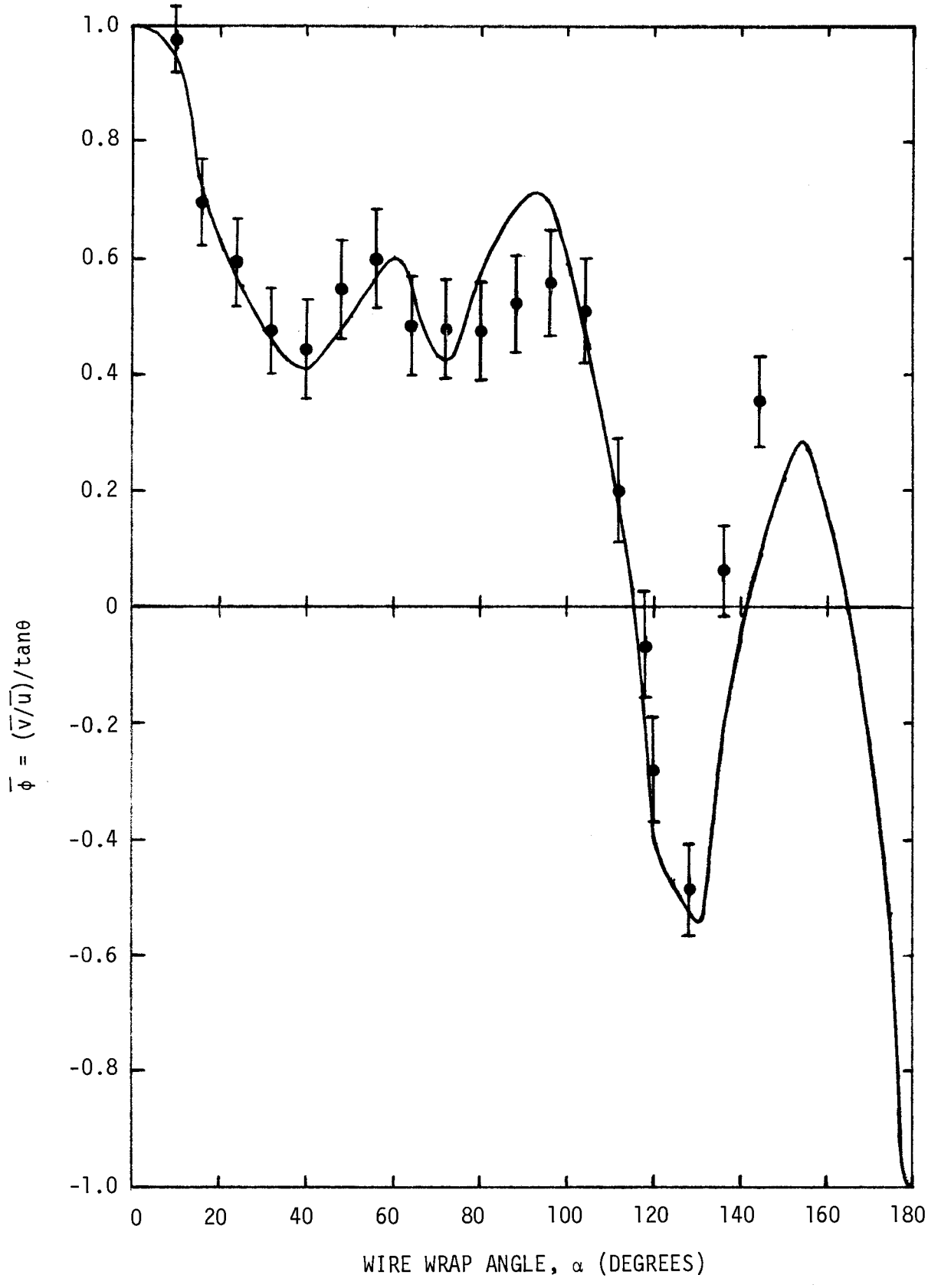

FIGURE 5-4 AVERAGE ϕ IN THE GAP PLOTTED VERSUS α, THE WIRE WRAP ANGLE (REVISED)

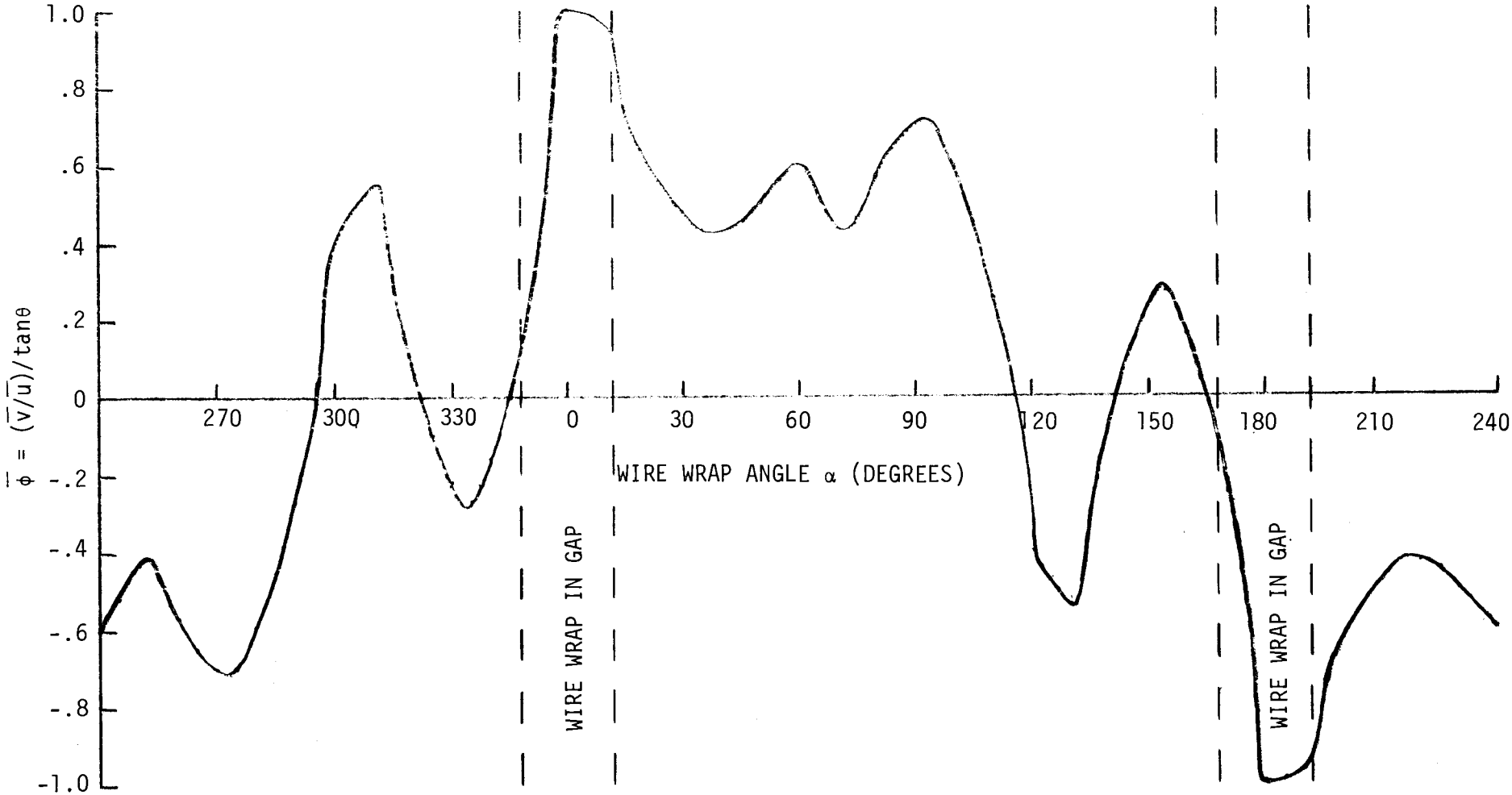

FIGURE 5-5 AVERAGE ϕ OVER EXTENDED RANGE OF THE WIRE WRAP ANGLE (REVISED)

The gap crossflow profiles used to calculate experimental values for $\overline{\phi}$ could only be measured when no part of a wire wrap was in the gap concerned. Certainly the continuity equation for $\overline{\phi}$ derived on the basis of a volumnless wire wrap cannot be used directly to calculate crossflow when a physically real wire wrap is present in the gap.

The significance of the trial and error fit of the continuity of mass correlation for $\overline{\phi}(\alpha)$ is best illustrated by comparison to the subchannel analysis code CØBRA as used in making pretest predictions. The curve plotted for $\overline{\phi}(\alpha)$ in Figures 5-4 and 5-5 could be used as a replacement for the forcing function f(x/P) in Subroutine FØRCE of CØBRA-IIIC[2]. The curve for $\overline{\phi}(\alpha)$, however, depicts forced crossflow with respect to the gap, whereas the CØBRA forcing function f(x/P) defines crossflow with respect to a wire wrap passing through the gap. The fact that extensive cross-flow does take place in the gap even when the wire wrap is relatively far removed from it, indicates that the wire wraps in adjacent gaps also influence crossflow. At present, the crossflow forcing function in CØBRA assumes that only the wire wrap passing through the gap leads to forced crossflow and only when in the immediate vicinity of the gap.

Inter-subchannel mass transfer calculations, however, must also account for both the volumetric displacement of fluid and variation of flow areas due to the presence of the wire wrap. In the CØBRA code, this may be done in a manner similar to that presently incorporated in Subroutine FØRCE of CØBRA-IIIC[2]. The fact that the continuity of mass correlation for $\overline{\phi}(\alpha)$ based on a volumnless wire wrap fits so well to the experimental crossflow data indicates that these effects are minor when the wire wrap is not intersecting the gap itself.

Because the nature of the experimental crossflow behavior is fundamentally different from the current CØBRA model, no attempt to modify or calibrate the pretest predictions is justified. The code itself needs to be modified by its developers. These results may also be similarly applied to other subchannel analysis codes incorporating wire wrap forced crossflow by their developers.

6.0 AXIAL FLOW EXPERIMENTS

6.1 Procedure

Axial flow measurements were made using a pitot-static tube mounted in rod number 2 (see Figure 4-1). The measurements were made in five axial planes in the surrounding subchannels at locations of 33, 27, 21, 15 and 9 inches from the downstream end of allowable pitot tube travel. In each subchannel, data were taken at 40 to 50 points based on the grid pattern shown in Figure 4-2. Variations from that pattern were made when the wire wrap interfered with the measurements or when flow patterns indicated more measurements in a particular region were needed for better definition of those patterns.

The pitot-static tube measurements were used to calculate the dynamic pressure head as follows:

$$\Delta P_{dynamic} = P_{static} - P_{total}.$$

This subtraction was reversed from the normal order since measurements were taken in a suction. The axial velocity was then calculated from this pressure head.

The results are shown in Figures 6-1 through 6-5 as contour lines of constant velocity throughout the surrounding subchannels. These contour lines were determined by interpolating radially and circumferentially between data points. The viewpoint is looking downstream with gap h-h (see Figure 4-1) indicated on the right for proper orientation. The subchannels are also designated A through F for convenient reference.

The six subchannels were divided into two groups according to similar wire wrap position and direction. Subchannels B, F and D formed one group while subchannels A, E and C formed the second. For all six subchannels, area-weighted, average axial velocities were calculated at the different axial locations with one exception. At 21 inches, from the downstream end of pitot tube travel, the wire wrap position in subchannels F, B and D precluded measurements throughout these subchannel areas so no subchannel

Dwg. 257C517

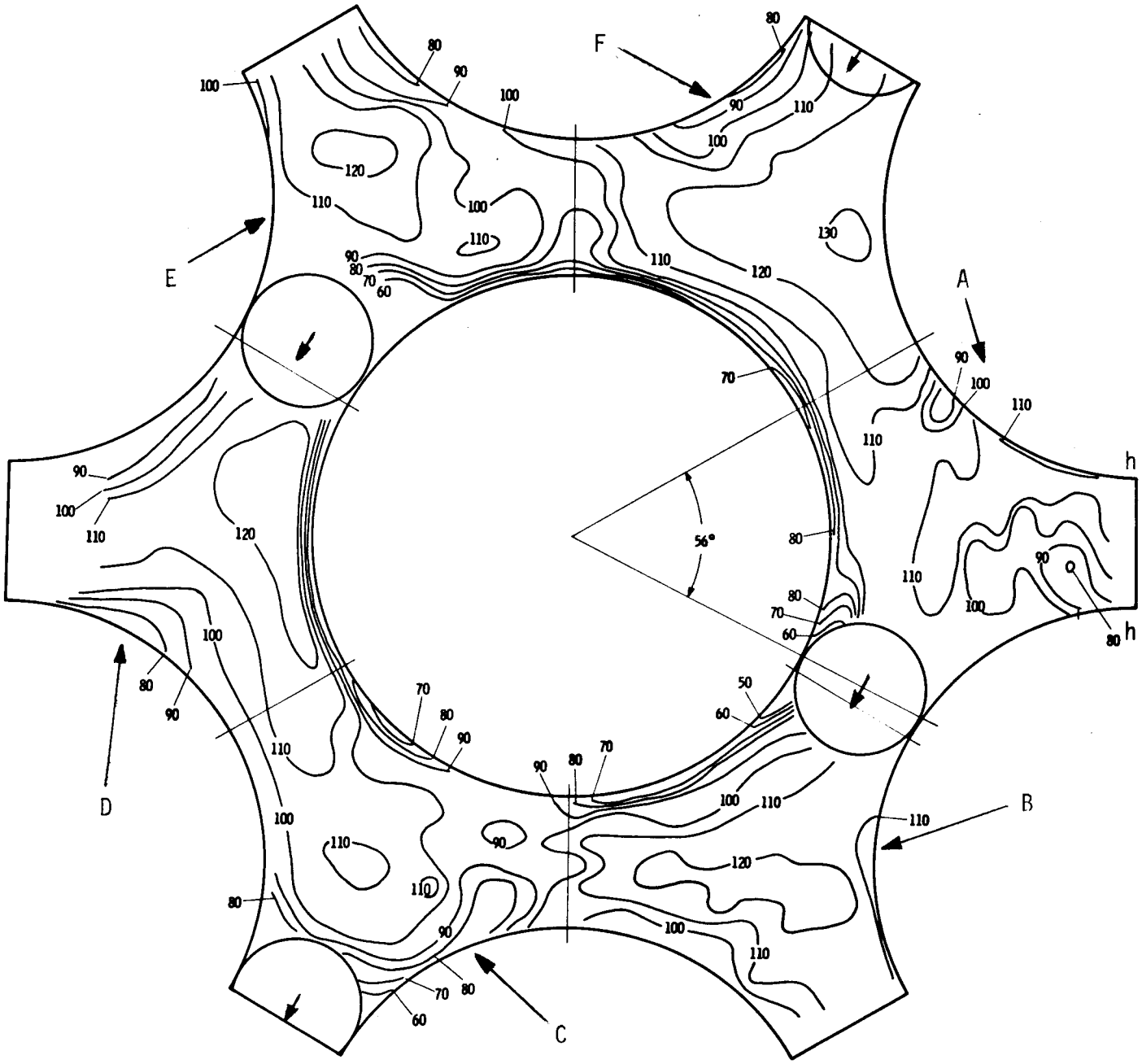

FIGURE 6-1

Axial Velocity Distribution (Ft/Sec) 33 Inches
from Downstream End of Pitot Tube Travel

Dwg. 257C518

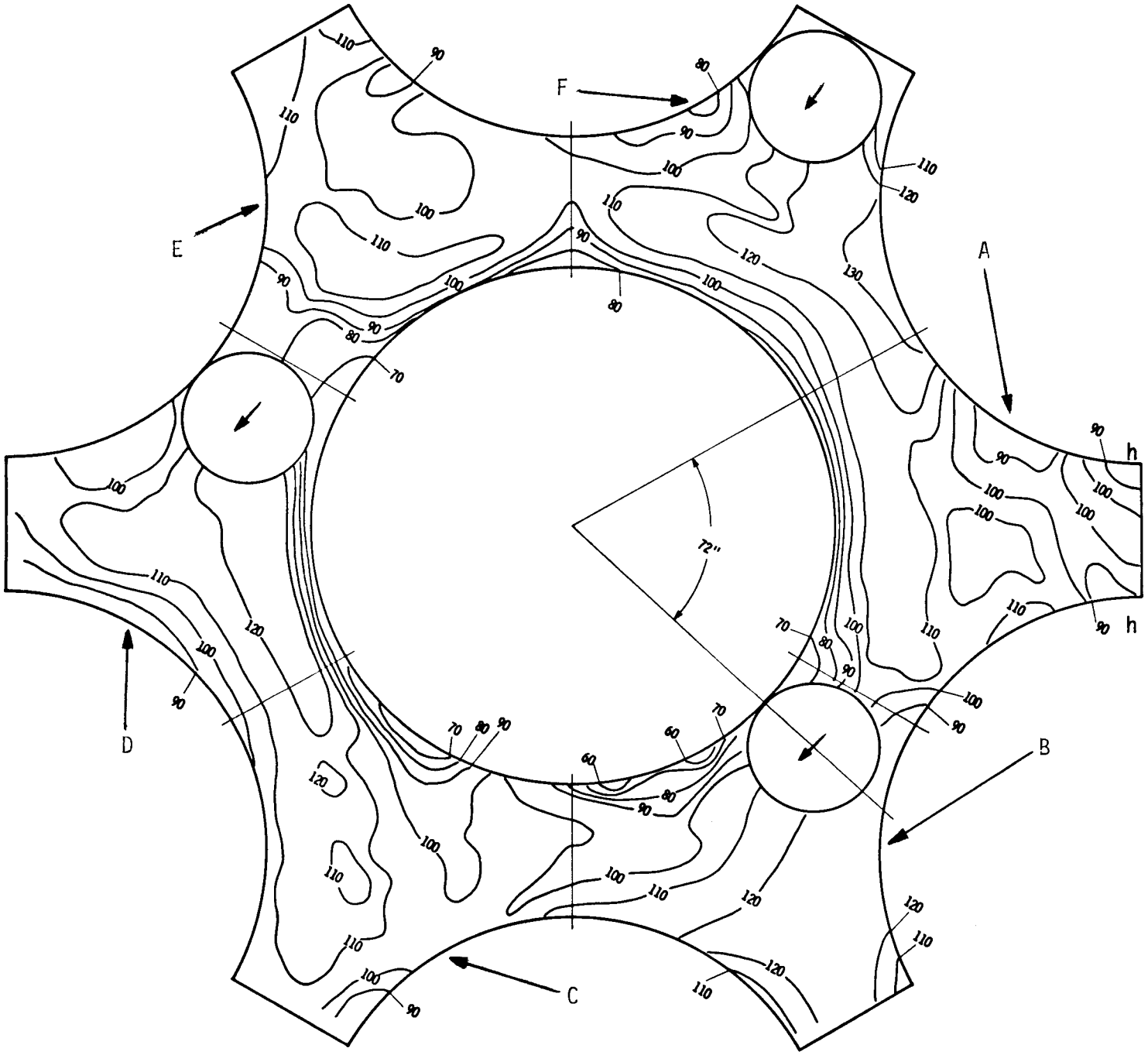

FIGURE 6-2

Axial Velocity Distribution (Ft/Sec) 27 Inches
from Downstream End of Pitot Tube Travel

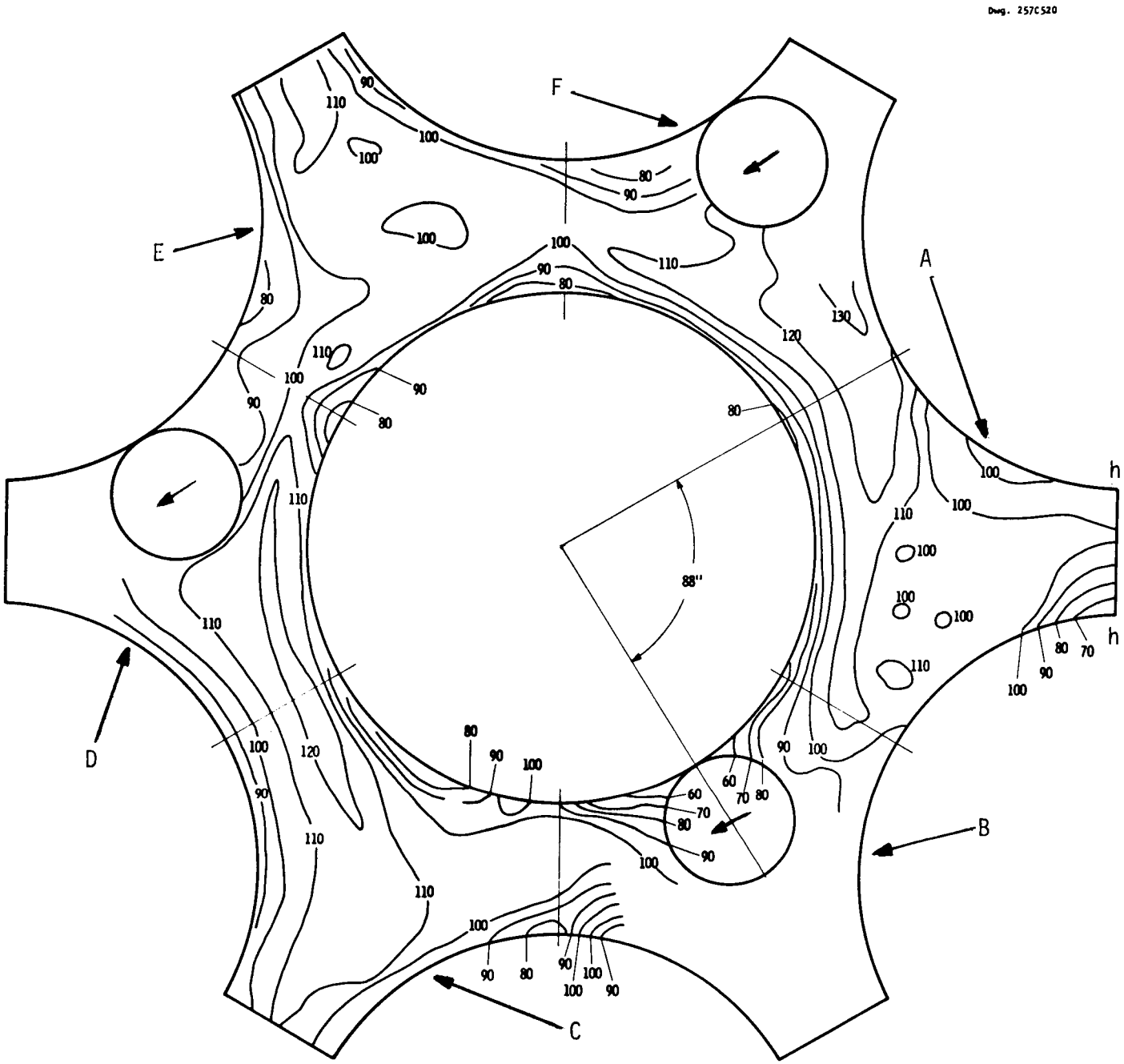

FIGURE 6-3

Axial Velocity Distribution (Ft/Sec) 21 Inches
from Downstream End of Pitot Tube Travel

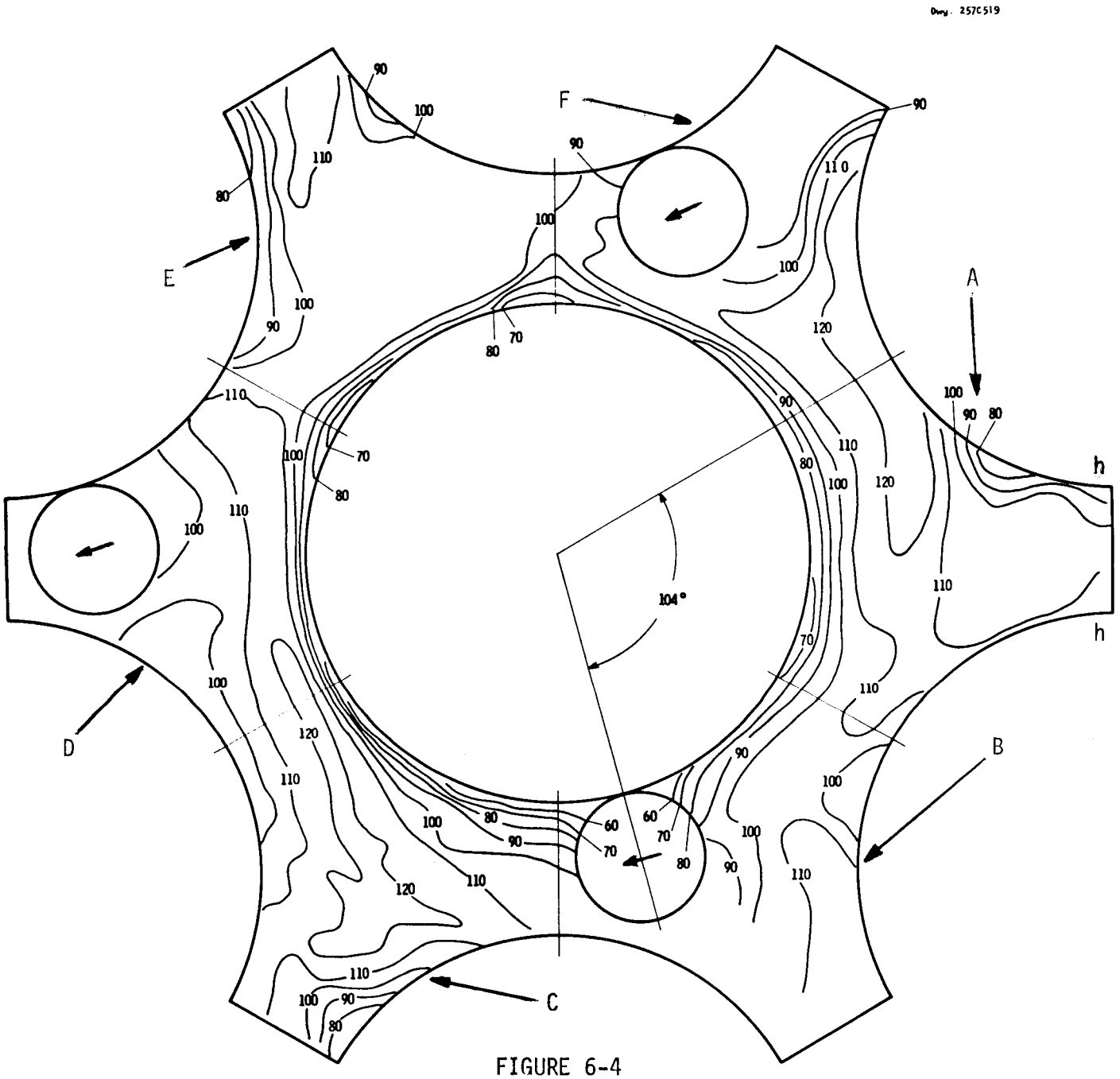

FIGURE 6-4

Axial Velocity Distribution (Ft/sec) 15 Inches

from Downstream End of Pitot Tube Travel

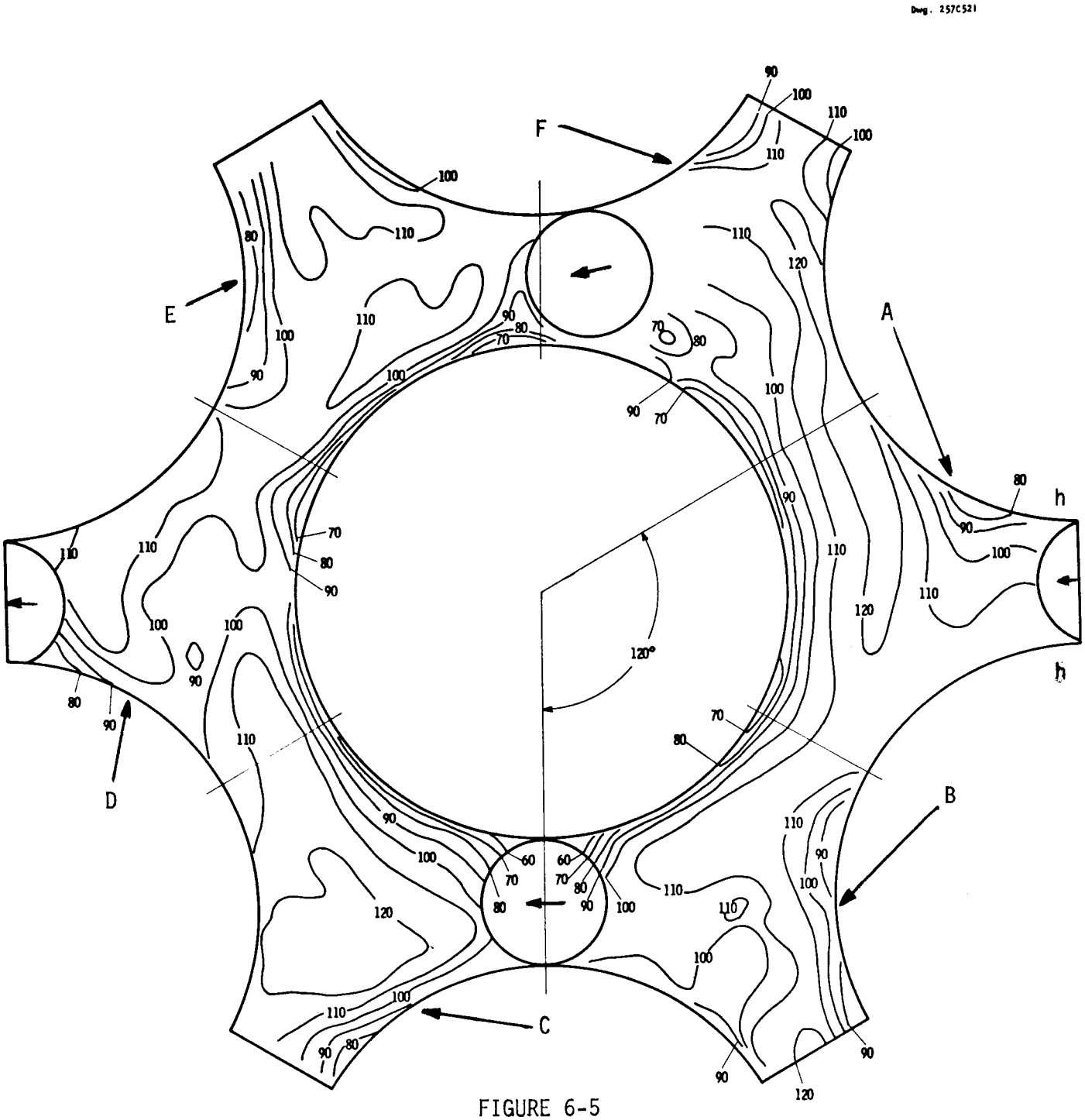

FIGURE 6-5

Axial Velocity Distribution (Ft/Sec) 9 Inches
from Downstream End of Pitot Tube Travel

average was calculated. The subchannel average velocities as functions of axial location have been plotted for the two subchannel groups in Figures 6-6 and 6-7.

6.2 Interpretation of Experimental Results

The subchannels in each of the two groupings show consistent flow patterns. An overall asymmetry potentially attributable to test assembly asymmetry or circumferential swirl flow is not observed. This is important for interpretation of the data since the test assembly itself is not symmetric and represents only a portion of a full hexagonal assembly. The nature of the overall test assembly apparently has not affected the distribution of flow among the interior subchannels. The relatively minor asymmetry that is observed may be caused by two factors. First, the subchannel geometries are not perfectly symmetric. Gap widths and rod diameters vary as shown in Figures 2-5 through 2-8. The resulting subchannel areas also must vary. The wire wraps are shown in Figures 6-1 through 6-5 as located by contact with the pitot tube; they are not perfectly in phase. The second factor is that the ability to position the pitot tube accurately varies throughout the subchannel areas. The accuracy decreases as the pitot tube is extended. For this reason, detailed observations at the outer periphery of the subchannels are impossible, and the steep velocity gradients representing boundary layer flow around the non-instrumented rods could not be measured. For this reason, they are not shown in Figures 6-1 through 6-5.

Each of the two subchannel groups provide three subchannels of one type, oriented 120 degrees with respect to one another. For example, the instrumented rod surface in subchannel C is the same as the upper, outer rod surface of subchannel A. Also, the instrumented rod surface of subchannel E is the same as the lower, outer rod surface of subchannel A. A similar argument can be made for subchannels B, D and F.

Due to the geometric similarity and the fact that no overall flow asymmetry was detected, the inner third of the three subchannels in each group was oriented and combined to give a composite subchannel at each axial location.

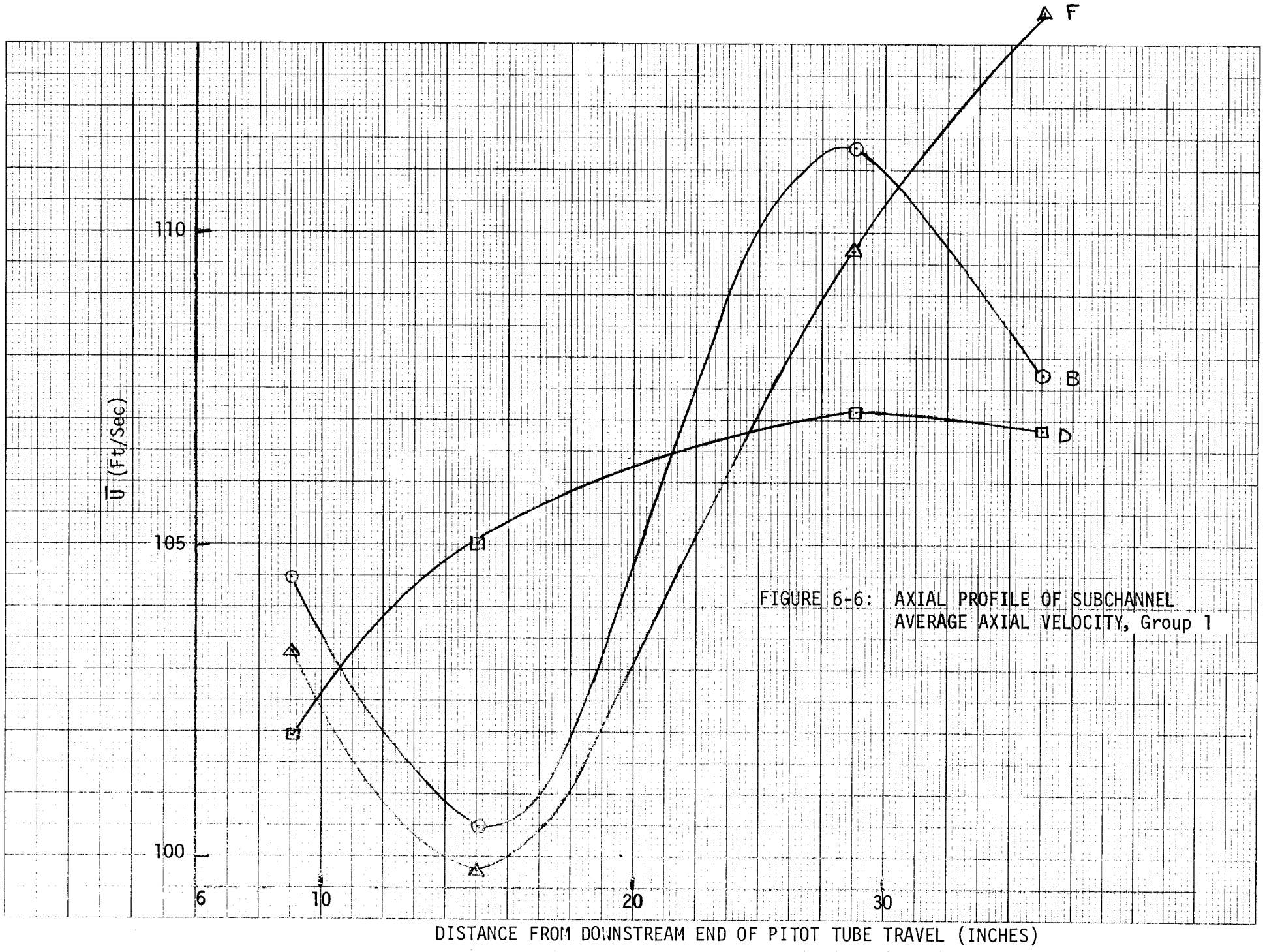

FIGURE 6-6: AXIAL PROFILE OF SUBCHANNEL AVERAGE AXIAL VELOCITY, Group 1

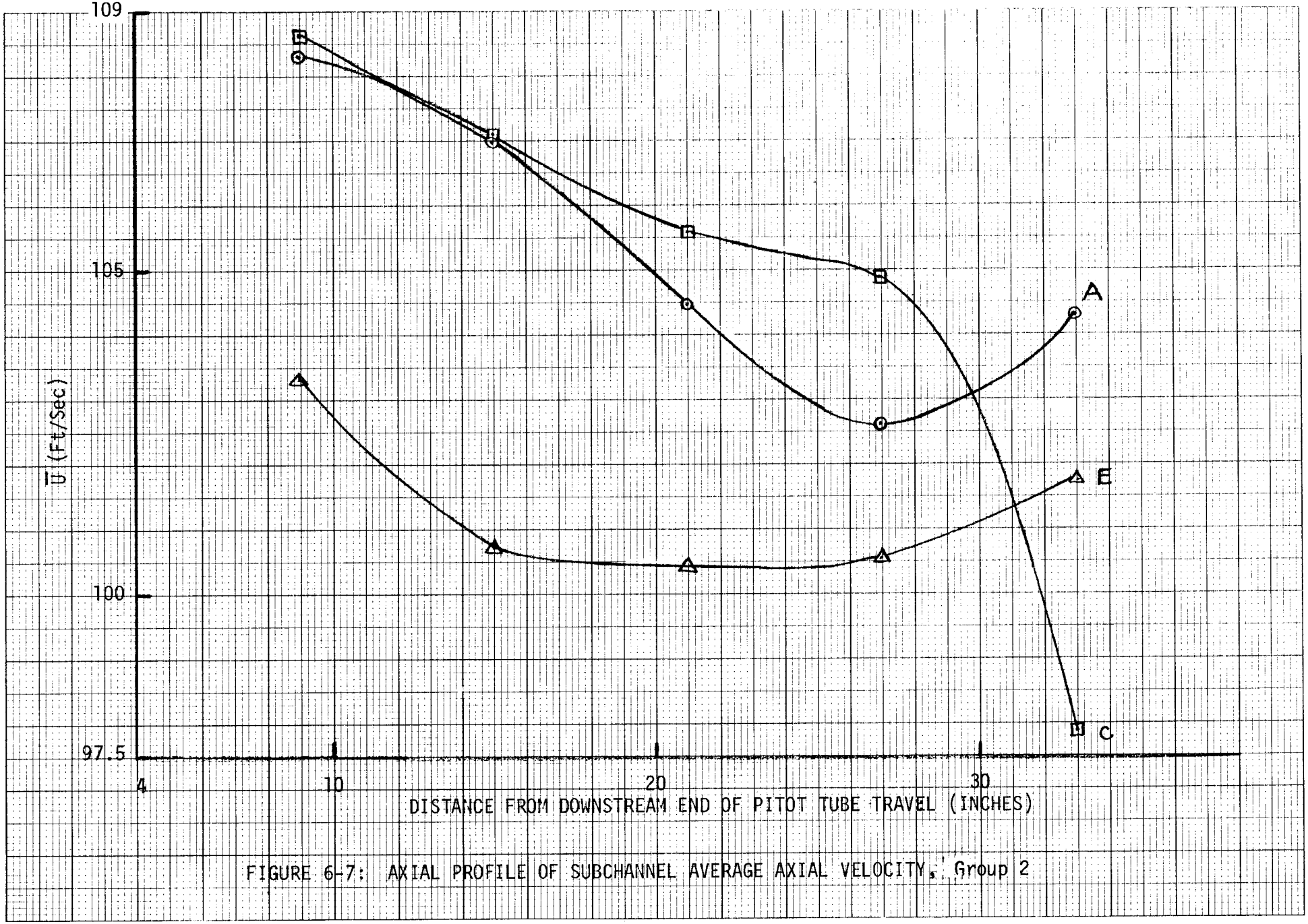

FIGURE 6-7: AXIAL PROFILE OF SUBCHANNEL AVERAGE AXIAL VELOCITY, Group 2

This was done by reproducing the boundary layer flow patterns out to the 100 fps contour line or even the 110 fps line where it closely followed the boundary layer contours. For the central regions of the individual subchannels, contour lines of constant velocity showed considerable variation but estimates of the general patterns were made by overlaying the three subchannels and sketching in approximate contours with due regard to known symmetry. The results are offered in Figures 6-8 and 6-9 for the five axial locations as an interpretative guide to the general axial flow patterns found in interior subchannels. In each of these figures, the upper, right hand gap (II) and lower, left hand gap (III) match due to symmetry as do the lower, right hand gap (IV) and upper, left hand gap (I).

Three pronounced low axial velocity centers were observed in these diagrams. They occurred: 1) immediately preceding the wire wrap; 2) immediately following the wire wrap; and 3) behind the wire wrap but adjacent to the opposing rod surface. The third low velocity region disappeared (Figure 6-8(c)) as the wire wrap left the gap and moved away from the opposing rod surface, but reformed (Figure 6-9(b)) as the wire wrap approached the next opposing rod surface. On the other hand, the highest axial velocity region lay ahead of the wire wrap but then slipped through the gap not traversed by the wire wrap into the adjoining subchannel to be ahead of the wire wrap moving into that subchannel.

Comparison of these flow patterns with axial progression revealed a cyclic behavior. The flow patterns in the two types of composite subchannels at 33 inches from the downstream end of pitot tube travel (Figure 6-8(a)) gradually developed until they were just reversed at 9 inches from the downstream end of pitot tube travel (Figure 6-9(b)). This cyclic behavior offered a predictability which makes extension of the flow patterns to adjoining subchannels possible at each of the axial locations. Furthermore, since the five axial locations cover the complete transit of a wire wrap through a subchannel, the entire axial cycle of axial flow distribution is shown.

Average axial velocities were calculated for the two composite subchannels at each of the five axial locations. These are shown in Figure 6-10. Axial

FIGURE 6-8

Axial Velocity Profiles (Ft/Sec) in Composite Subchannels

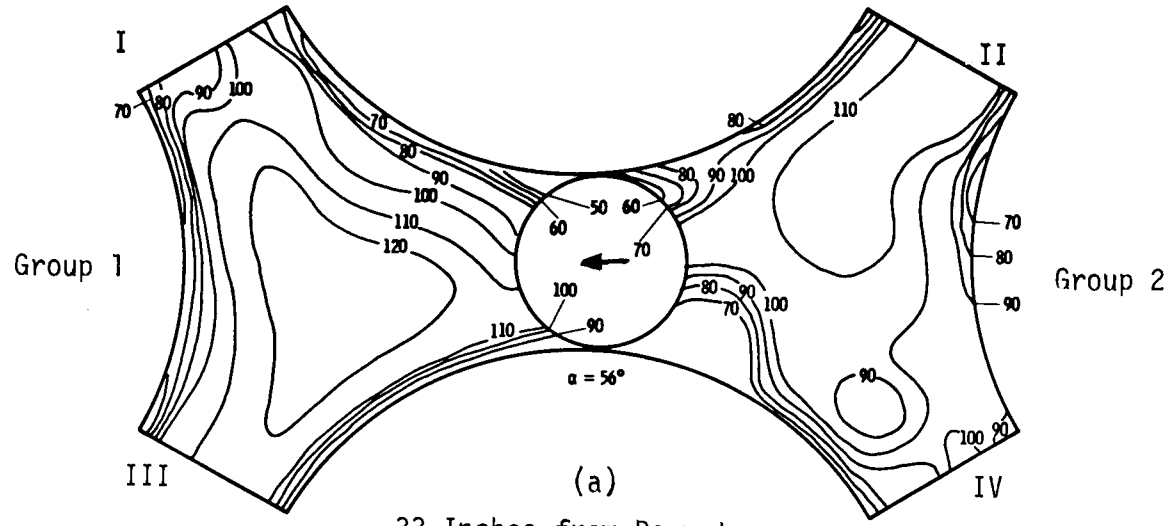

(a)

33 Inches from Downstream

End of Pitot Tube Travel

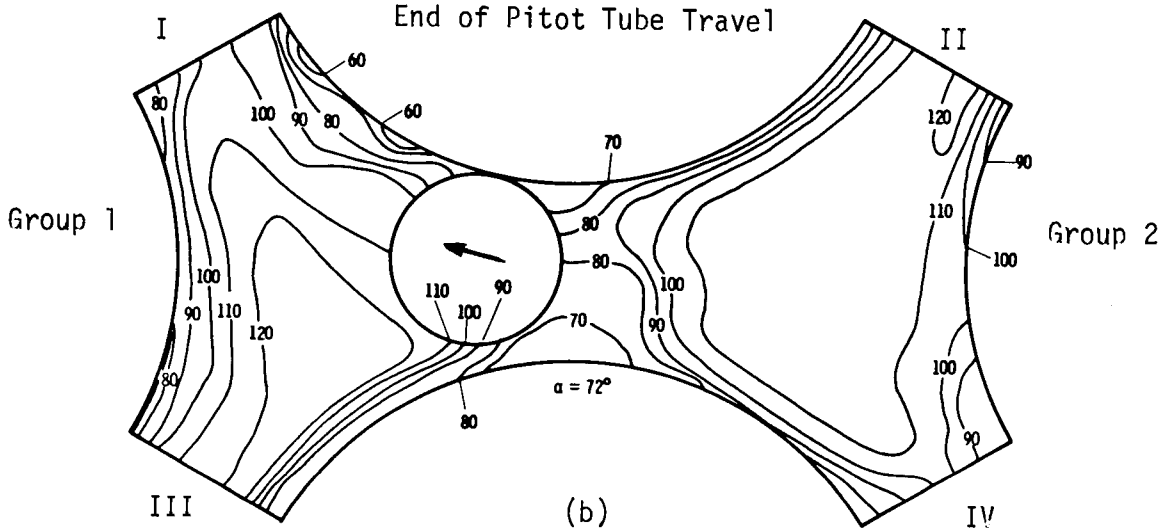

(b)

27 Inches from Downstream

End of Pitot Tube Travel

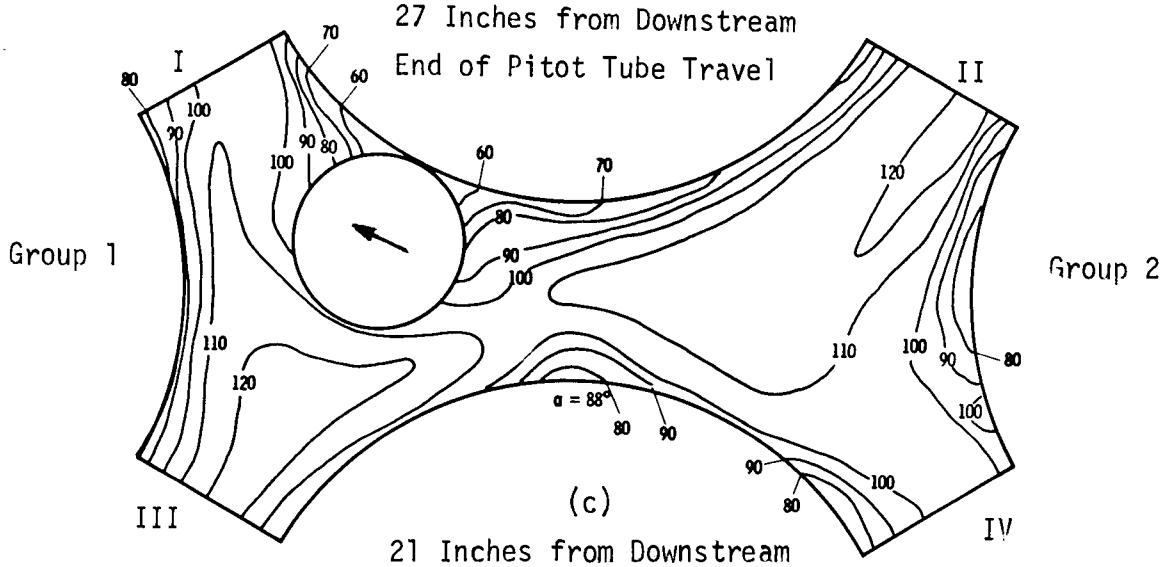

(c)

21 Inches from Downstream

End of Pitot Tube Travel

FIGURE 6-9

Axial Velocity Profiles (Ft/Sec) in Composite Subchannels

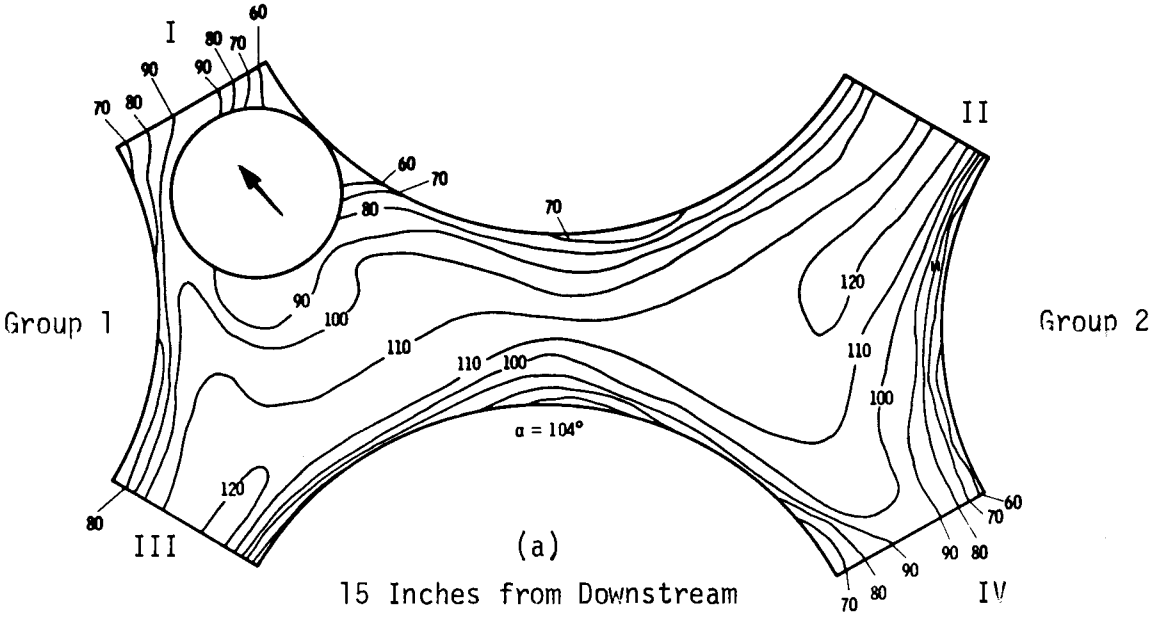

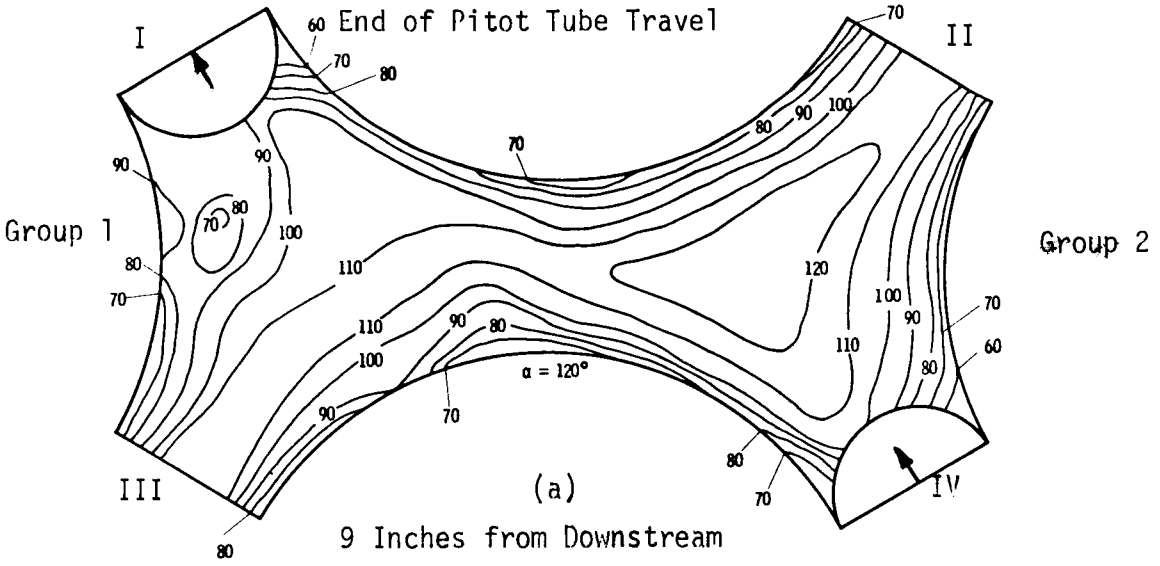

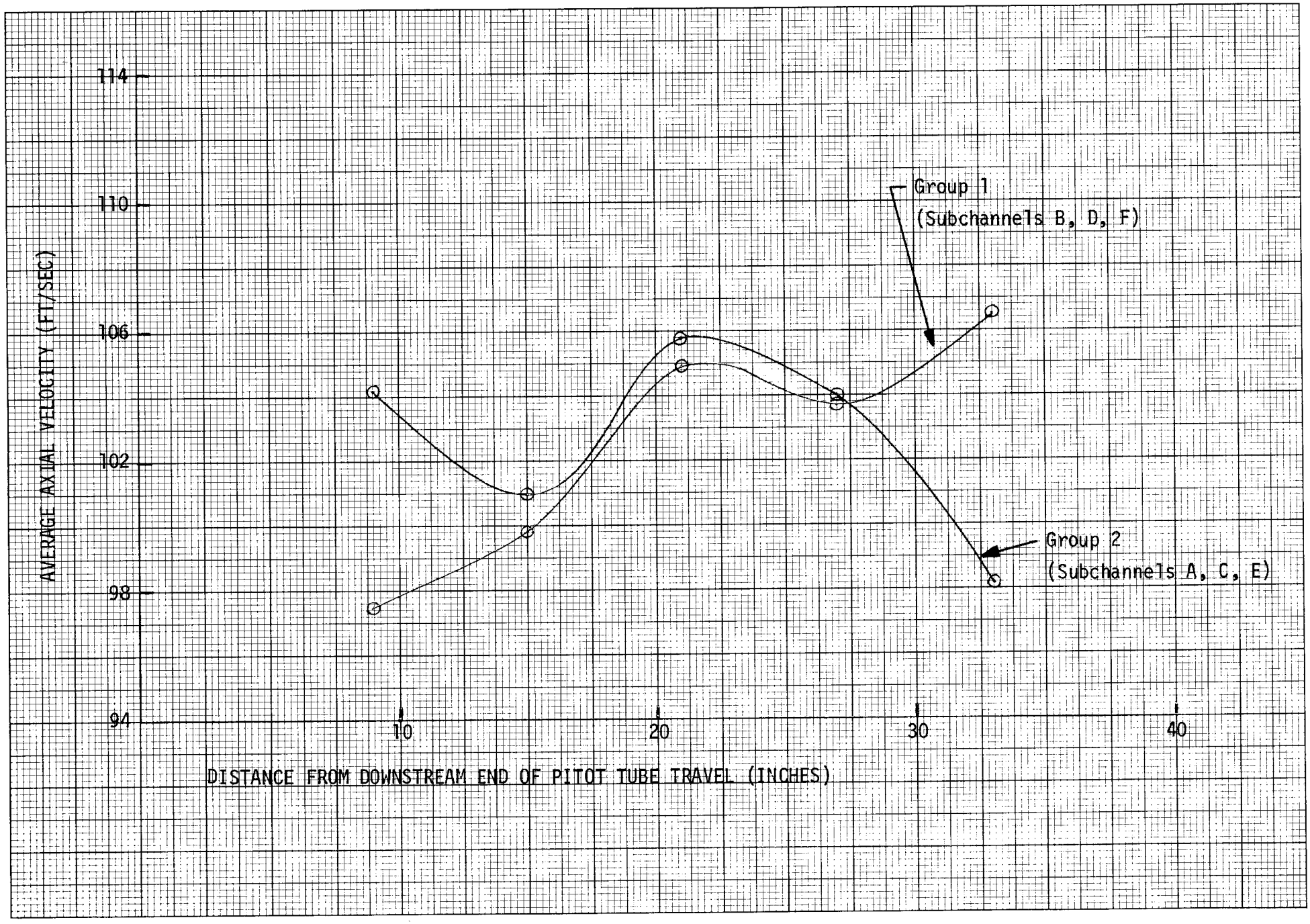

FIGURE 6-10: AXIAL PROFILE OF COMPOSITE SUBCHANNEL AVERAGE AXIAL VELOCITY

variation of the average axial velocities for the two composite subchannels is not completely consistent with the complementary nature of the two subchannel types. The derivatives of the two curves should be equal and opposite at all axial locations if mass is to be conserved. Nowhere is this completely true, and in the central region, the curves are first simultaneously increasing then decreasing. This fact again points out the interpretative nature of Figures 6-8 and 6-9. It must be noted, however, that the maximum variations from an overall average of 102.6 ft/sec are +3.9 to -4.9 percent. The fact that the average for the two subchannels is lower than the assembly-wide value of 109.8 ft/sec by 6.6 percent should also be noted. Side subchannels may possibly have a higher average axial velocity to account for this difference; however, at this moment, side subchannel data are still unavailable. Discussion on the variation of axial velocities will be resumed, if necessary, when side channel testing is completed.

6.3 Application of Axial Flow Data

The axial flow contours shown in Figures 6-1 through 6-5 can be correlated with the gap crossflow data represented in Figure 5-4. A detailed derivation in Appendix E shows how axial flow in an interior subchannel can be represented as an empirical function of wire wrap angle normalized to the average axial velocity in the measured subchannels. The result is

$$U(\alpha) = \frac{u(\alpha)}{\bar{u}} = \frac{1}{A_c(\alpha)} \{C + \frac{P\tan\theta}{2\pi} \cdot \int_0^{\alpha} [\sum_{j=1}^{3} \tilde{\phi}_j(\alpha) Sg_j(\alpha)] d\alpha\} \quad (16)$$

where α = angular displacement of wire wrap, radians

$U(\alpha)$ = normalized axial flow in subchannel

$u(\alpha)$ = axial flow in subchannel

$\bar{u}$ = average axial flow in measured subchannels, 1254 in/sec (104.5 ft/sec)

$A_c(\alpha)$ = cross-sectional area of interior subchannel

C = evaluated constant of integration, 1.648 in^2 or 90.5% of the maximum cross-sectional area

P = wire wrap lead, 129.4 in.

θ = constant angle of wire wrap centerline from rod bundle axis, 4.33°

$\tilde{\phi}_j(\alpha)$ = as-measured gap crossflow in j^{th} gap

$Sgj(\alpha)$ = unobstructed gap width of j^{th} gap.

The function $U(\alpha)$ is plotted in Figure 6-11. Average dimensions for the subchannel were used from the local area of measurements in evaluating the function. Peak axial velocities are obtained while a wire wrap is in the subchannel. In this repeating cycle, axial velocities vary from 0.93 to 1.08 times the average axial velocity of 104.5 ft/sec determined by the average of all subchannel average axial velocities calculated from Figures 6-1 through 6-5. Additional features of the cycle are small, axial flow perturbations as a wire wrap enters and leaves the subchannel. Their nature is consistent with the corresponding increase and decrease of the wetted perimeter of the subchannel.

By multiplying the function $U(\alpha)$ by the function for the varying cross-sectional subchannel area, the normalized axial mass flow is determined as a function of wire wrap angular displacement, α. The result is given in Figure 6-12 where the greatest axial mass flow occurs just after the wire wrap has left the subchannel and the least just after a wire wrap has entered the subchannel.

The net mass crossflow rate between subchannels forced by the wire wrap is then calculated by taking the derivative of the curve in Figure 6-12. This is shown in Figure 6-13. The most intense gain in axial mass flow rate takes place as a wire wrap leaves the subchannel while the greatest loss rate occurs as a wire wrap enters the subchannel. This curve, of course, does not reflect gross mass interchange or mixing between subchannels, but rather net gain or loss in the axial mass flow rate as a function of wire wrap angle. Total mass exchange between subchannels could be calculated by summing over the open width of the gap the absolute values of the product

$$\rho \cdot P \cdot \bar{u} \cdot \tan\theta \cdot \tilde{\phi}(\alpha, Sg) \cdot dSg \cdot \frac{d\alpha}{2\pi}$$

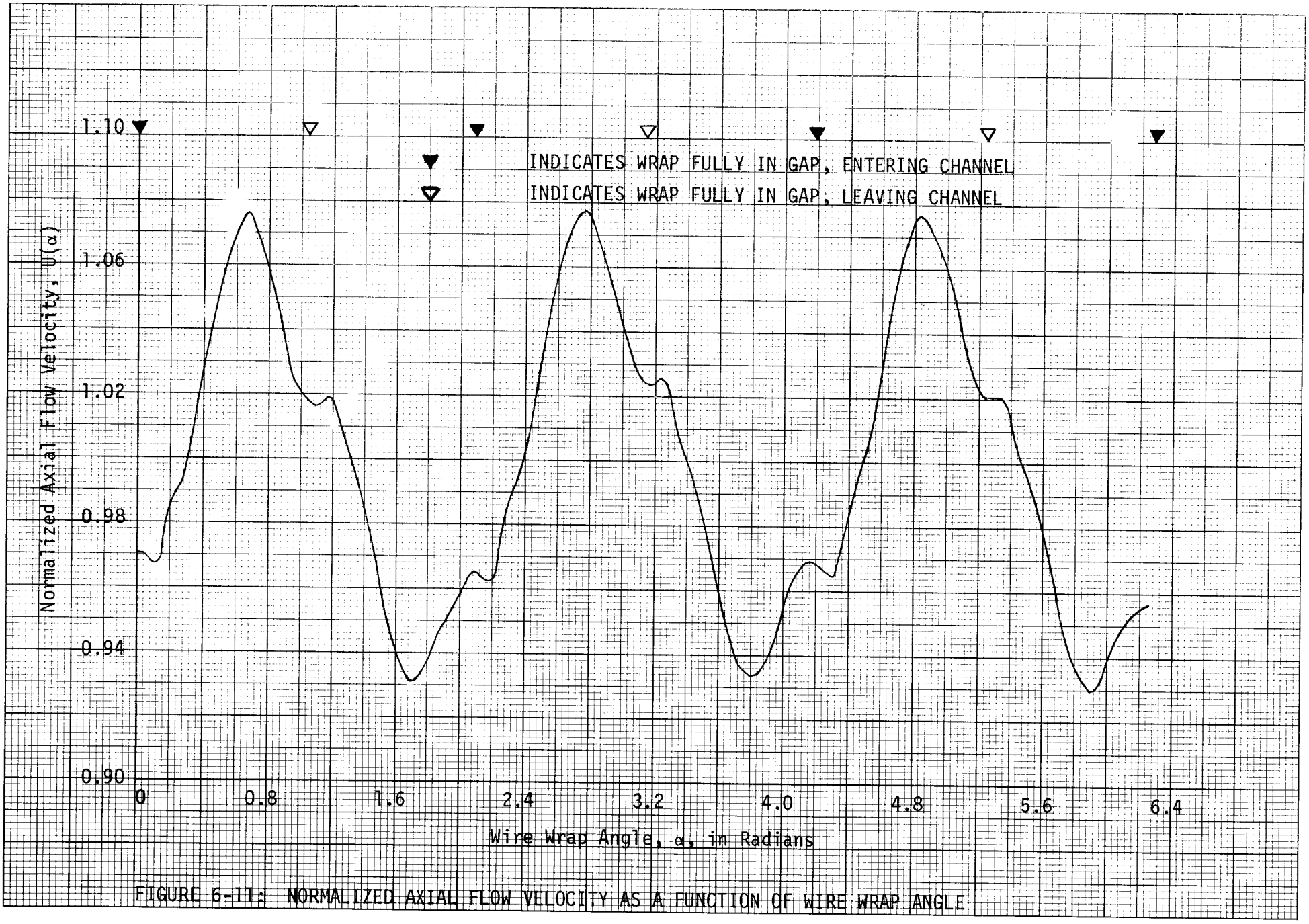

FIGURE 6-11: NORMALIZED AXIAL FLOW VELOCITY AS A FUNCTION OF WIRE WRAP ANGLE

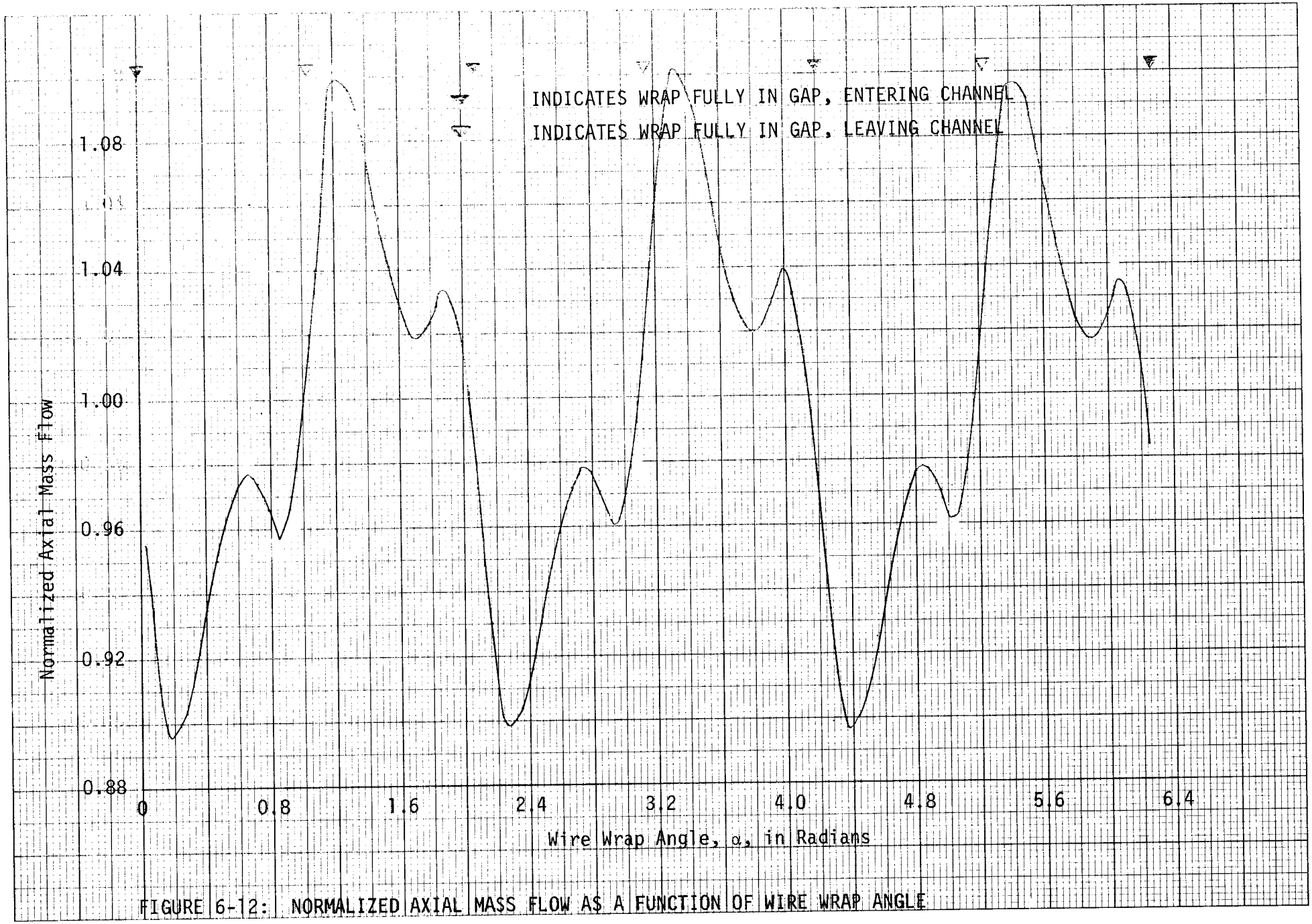

FIGURE 6-12: NORMALIZED AXIAL MASS FLOW AS A FUNCTION OF WIRE WRAP ANGLE

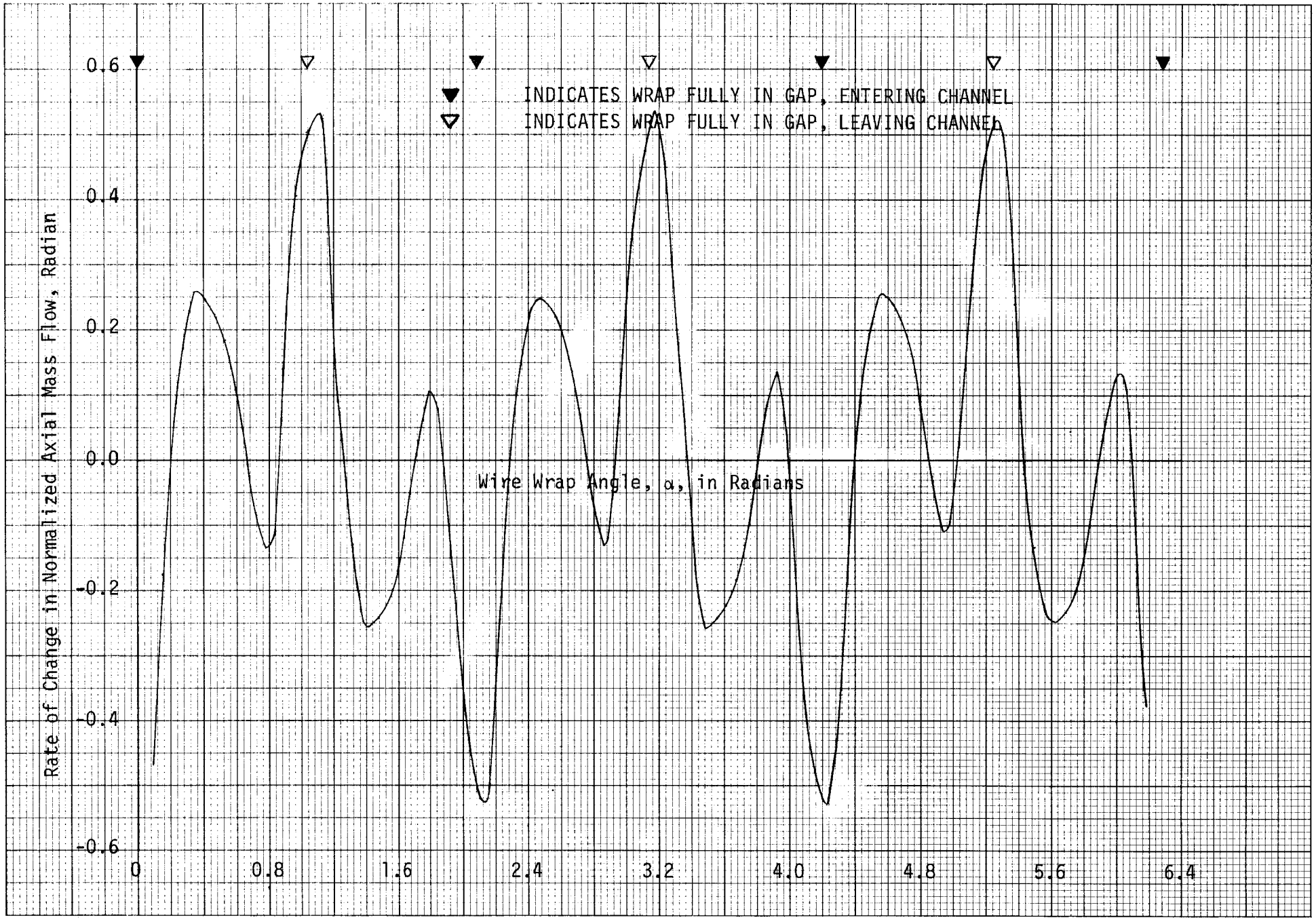
INDICATES WRAP FULLY IN GAP, ENTERING CHANNEL
INDICATES WRAP FULLY IN GAP, LEAVING CHANNEL
Rate of Change in Normalized Axial Mass Flow, Radian
Wire Wrap Angle, α, in Radians
0.6
0.4
0.2
0.0
-0.2
-0.4
-0.6
0
0.8
1.6
2.4
3.2
4.0
4.8
5.6
6.4

for each gap. This would be important for determining energy transfer between subchannels in a heated rod bundle.

The function $U(\alpha)$ represents one empirical correlation of the experimental data. Others may be possible or, perhaps, even desirable for further development of specific subchannel analysis codes. Lastly, it must be noted that the function $U(\alpha)$ and the resultant correlations for axial mass flow are empirical and not absolute. They do incorporate the uncertainties of the experimental data which they represent.

7.0 CONCLUSIONS

The experimental results obtained through this series of interior subchannel tests demonstrate excellent consistency within a valid region of flow development. An axial fluid pressure profile within the wire wrapped rod bundle results in a friction factor value within 1.5 percent of that calculated for fully developed flow (Section 3.4). The trial-and-error fit of a continuity of mass relationship for crossflow (Section 4.4) to the detailed gap crossflow data (Section 5.3) is supported by the tracer gas mixing data despite large uncertainties in that data (Section 4.4). Finally, detailed axial flow contours within the interior subchannels (Section 6.1) indicate that the most extensive, low axial velocity region occurs behind the wire wrap as it passes through a gap (Section 6.2). This is consistent with the gap crossflow data which shows the most extensive forced crossflow taking place under the same conditions (Section 5.3).

Representative interpretations of the data are offered to illustrate the potential use of the data. The gap crossflow data, for example, leads to a radically different wire wrap forcing function in the CØBRA subchannel analysis code (Section 5.3). The axial flow data for six adjoining, interior subchannels can be combined into two composite, complementary subchannels to reveal flow distributions which may be extended to all other interior subchannels free from peripheral flow effects and which cover the entire axial cycle of axial flow (Section 6.2). Finally, an empirical correlation for normalized axial velocity as a function of wire wrap angle is derived which incorporates both the axial flow and gap crossflow data (Section 6.3).

In summary, detailed experimental flow data of excellent quality have been obtained within the interior subchannels of a wire wrapped rod bundle. Representative interpretations of the data have been offered as an indication of the potehtial applicability of the data in refining analytical techniques for fluid flow within a wire wrapped rod bundle.

REFERENCES

1. D. S. Rowe, "CØBRA-III: A Digital Computer Program for Steady State and Transient Thermal-Hydraulic Analysis of Rod Bundle Nuclear Fuel Elements", BNWL-B-82 (Interim Report), July, 1971.

2. D. S. Rowe, "CØBRA-IIIC: Digital Computer Program for Steady State and Transient Thermal-Hydraulic Analysis of Rod Bundle Nuclear Fuel Elements", BNWL-1695, March, 1973.

3. M. J. Pechersky, R. M. Roidt, B. J. Vegter and R. A. Markley, "11:1 Scale Rod Bundle Air Flow Tests - Parts 1 through 7", WARD-OX-3045-6, February, 1974 (Availability - U.S. ERDA Technical Information Center).

4. E. H. Novendstern, "Turbulent Flow Pressure Drop Model for Fuel Rod Assemblies Utilizing a Helical Wire Wrap Spacer System", Nuc. Eng. Des., 22, pp. 19-27 (1972).

APPENDIX A

PRETEST PREDICTIONS

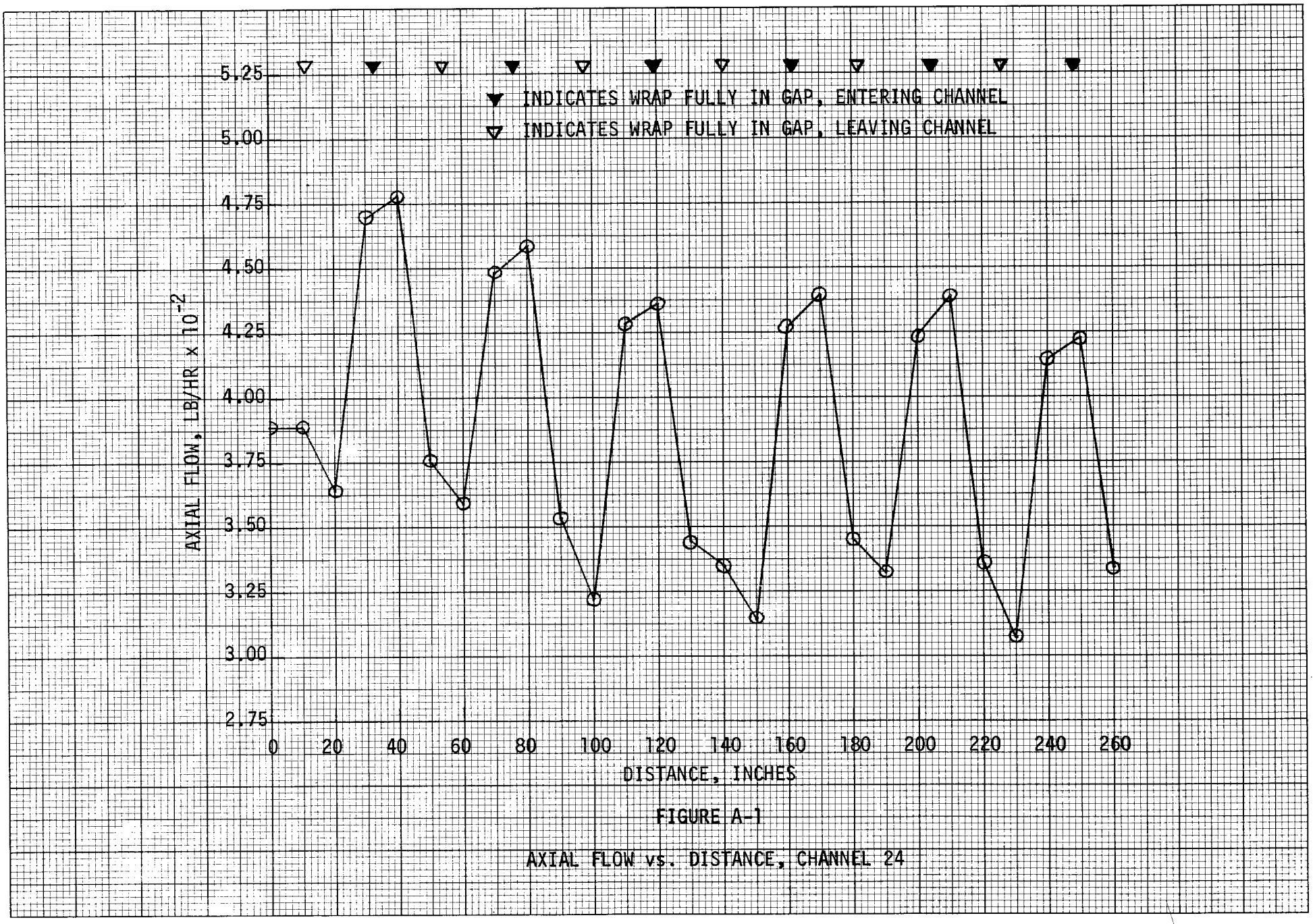

FIGURE A-1

AXIAL FLOW vs. DISTANCE, CHANNEL 24

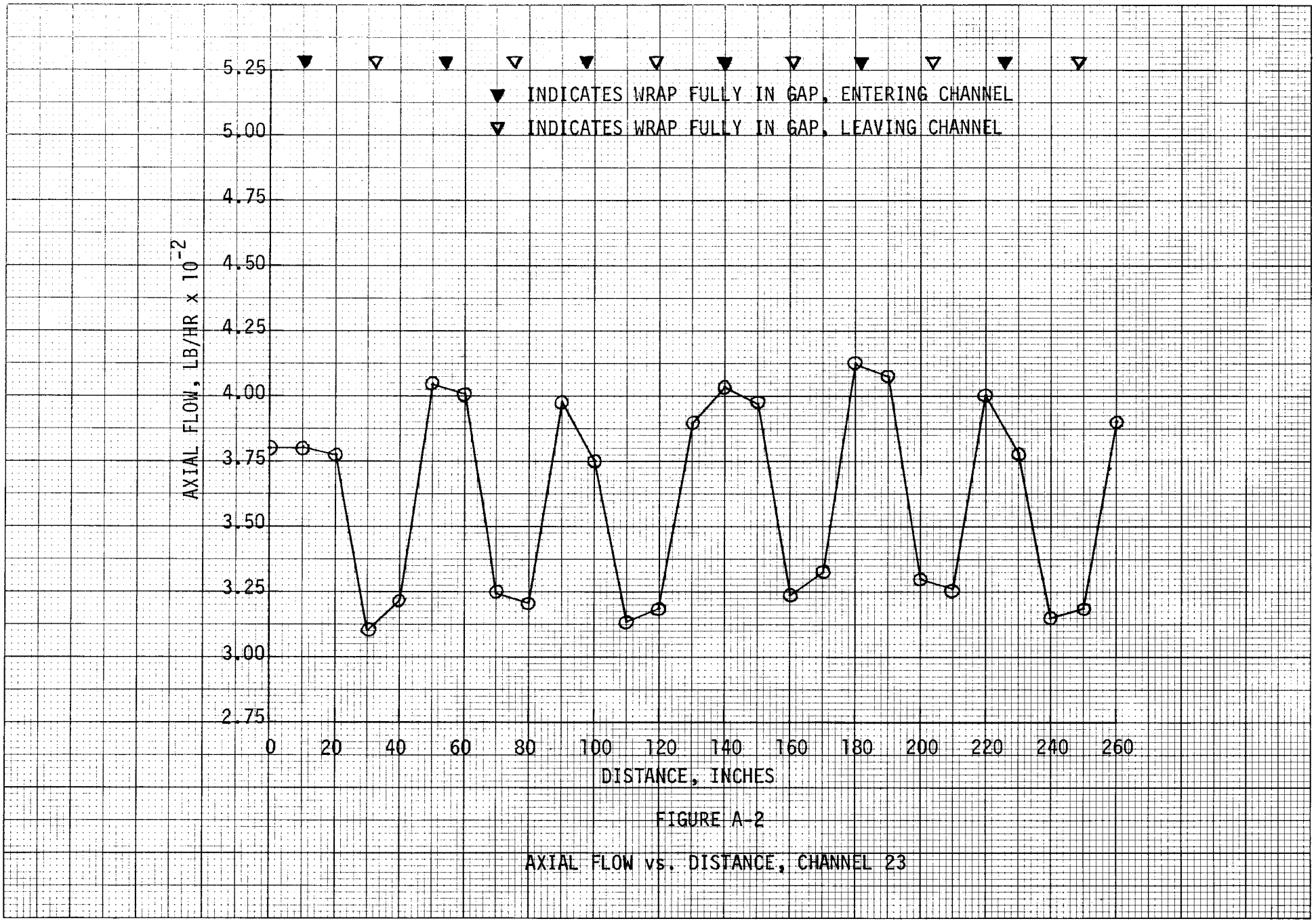

FIGURE A-2

AXIAL FLOW vs. DISTANCE, CHANNEL 23

FIGURE A-3

AXIAL FLOW vs. DISTANCE, CHANNEL 31

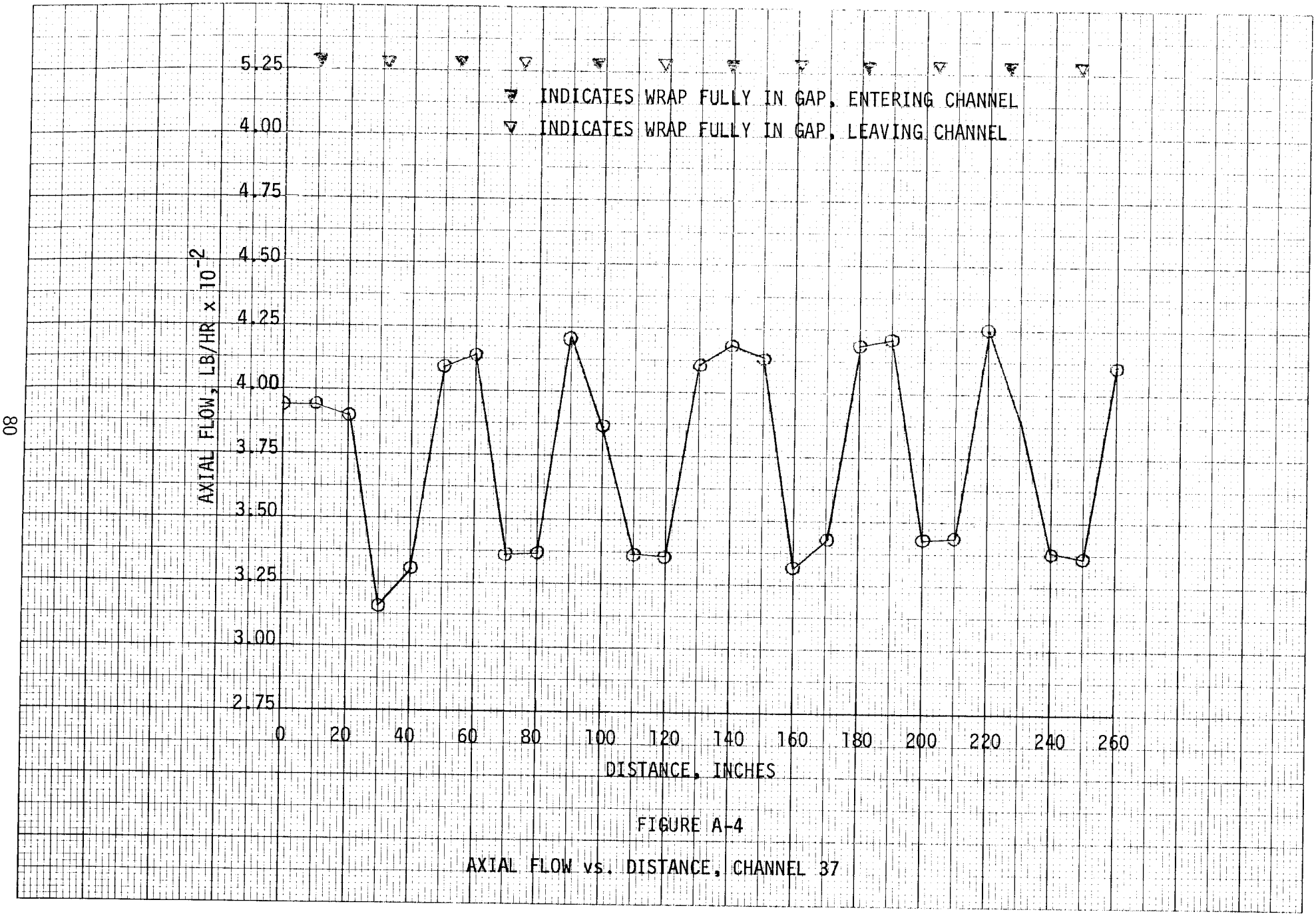

FIGURE A-4

AXIAL FLOW vs. DISTANCE, CHANNEL 37

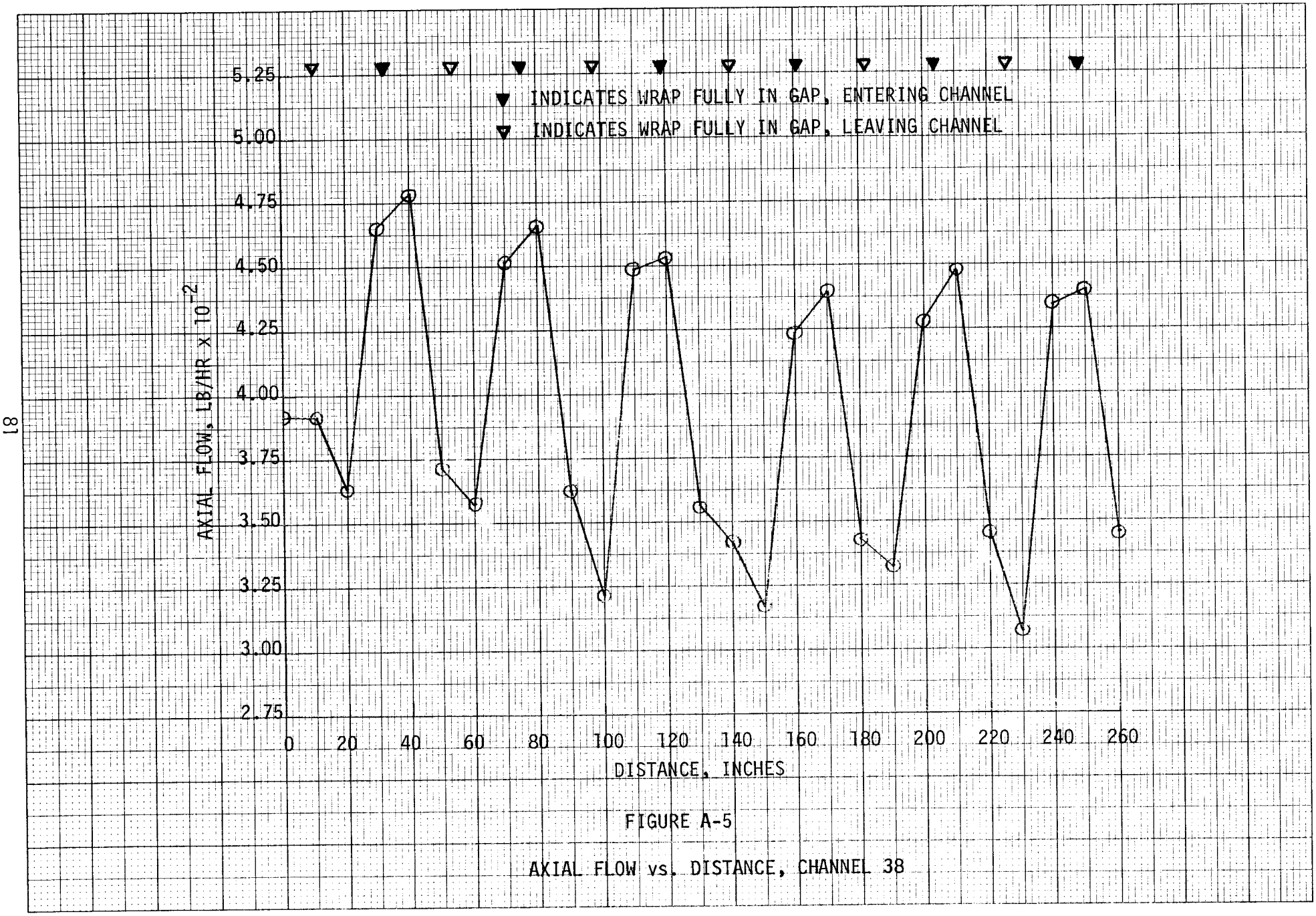

FIGURE A-5

AXIAL FLOW vs. DISTANCE, CHANNEL 38

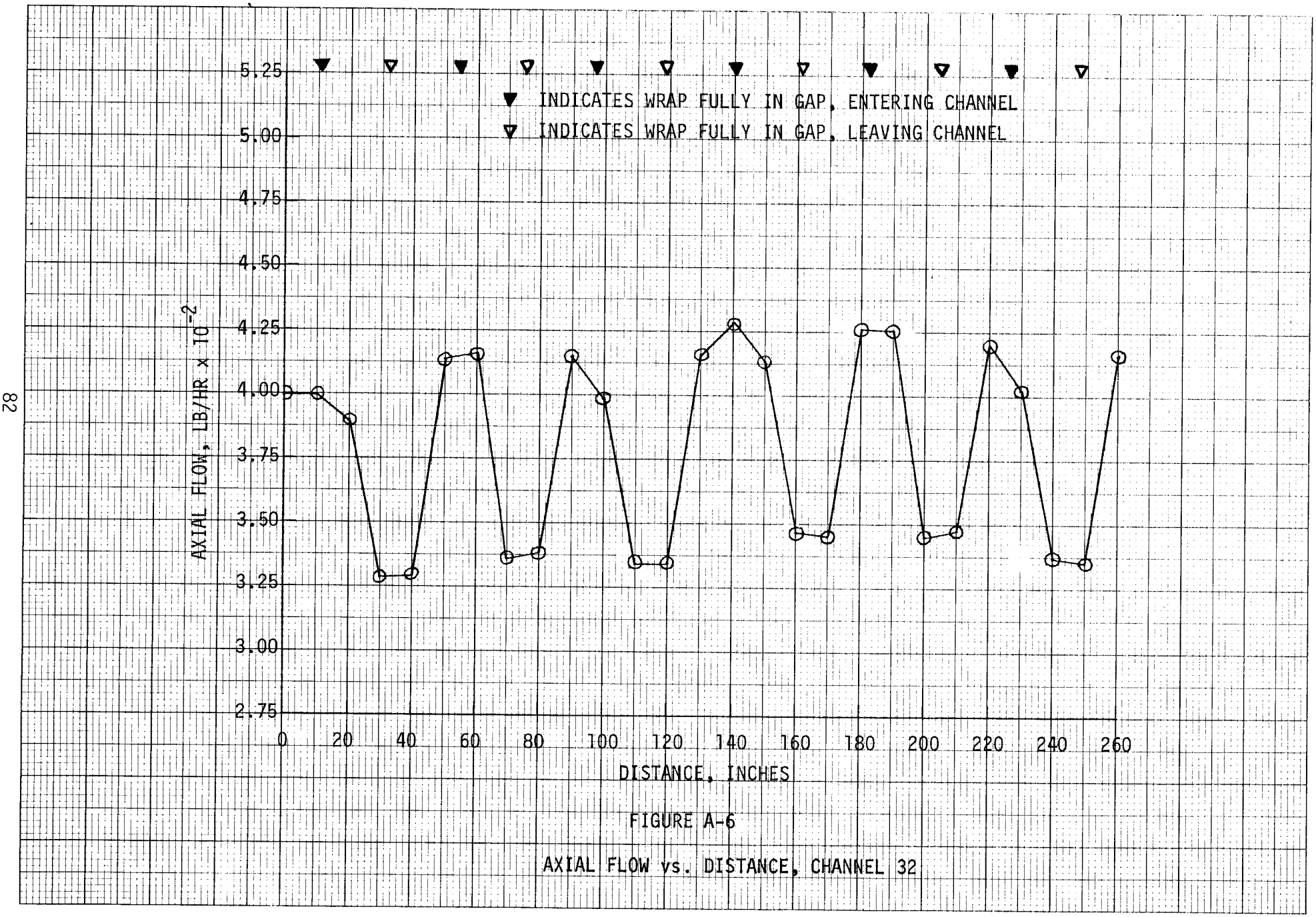

FIGURE A-6

AXIAL FLOW vs. DISTANCE, CHANNEL 32

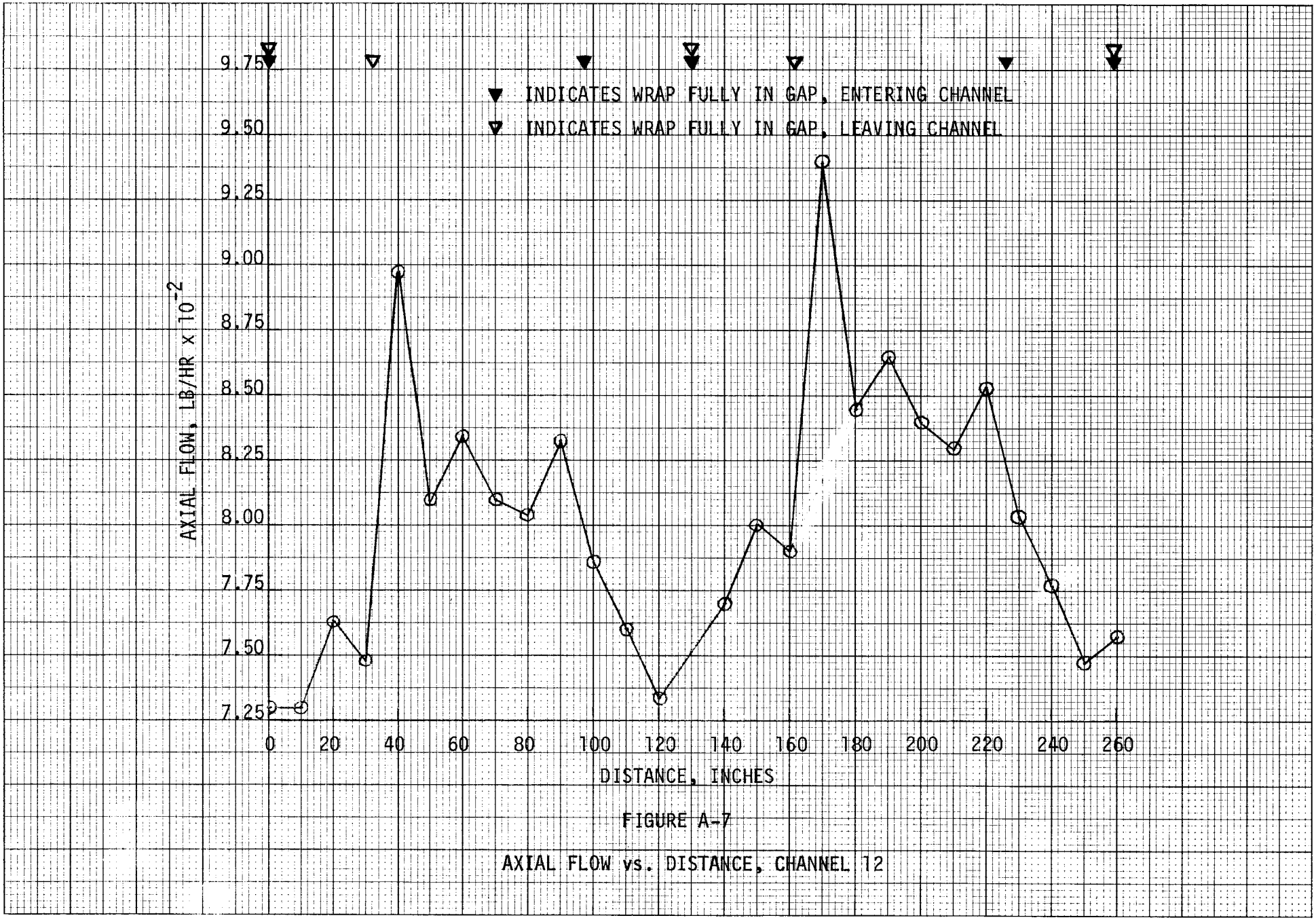

FIGURE A-7

AXIAL FLOW vs. DISTANCE, CHANNEL 12

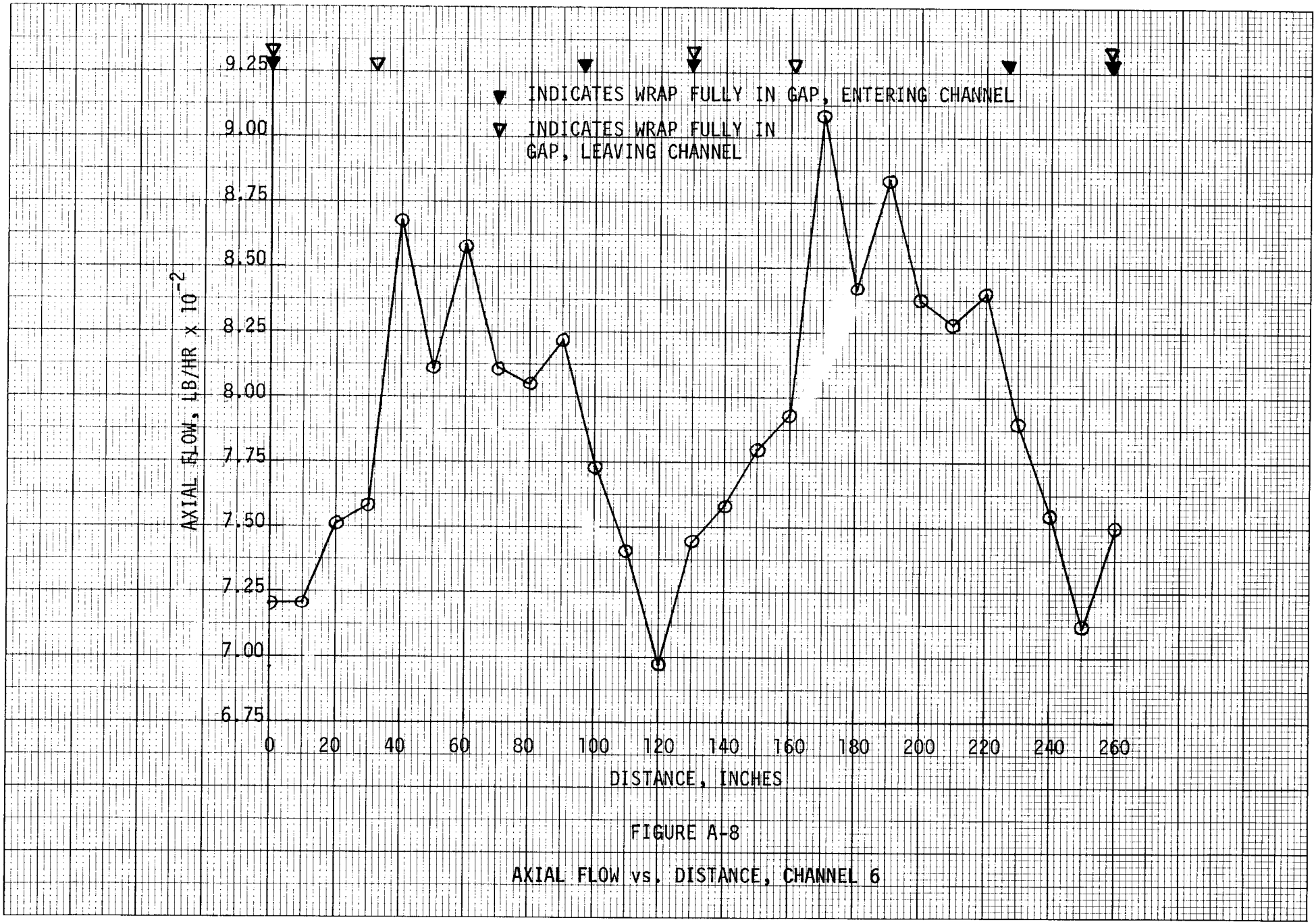

FIGURE A-8

AXIAL FLOW vs. DISTANCE, CHANNEL 6

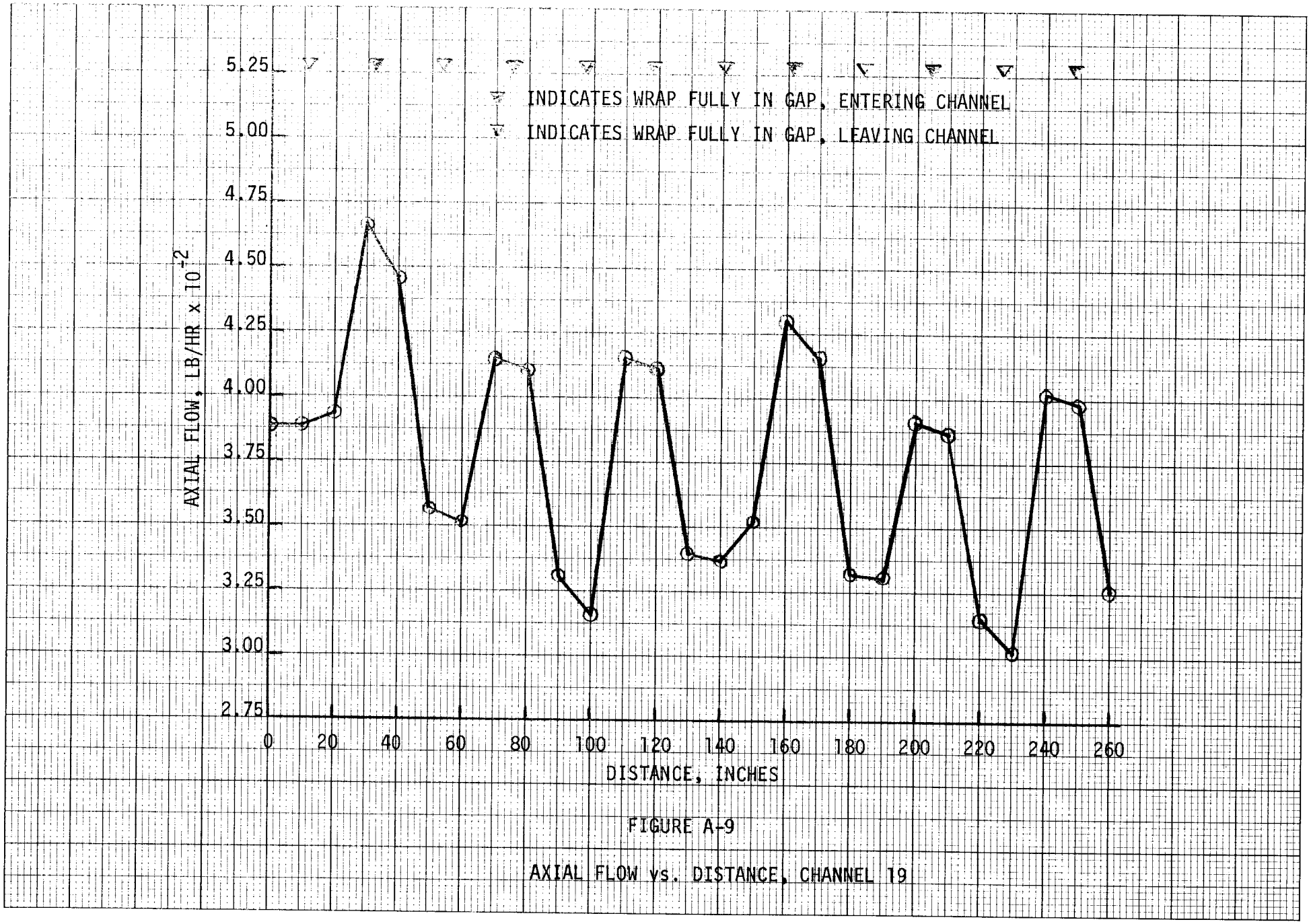

FIGURE A-9

AXIAL FLOW vs. DISTANCE, CHANNEL 19

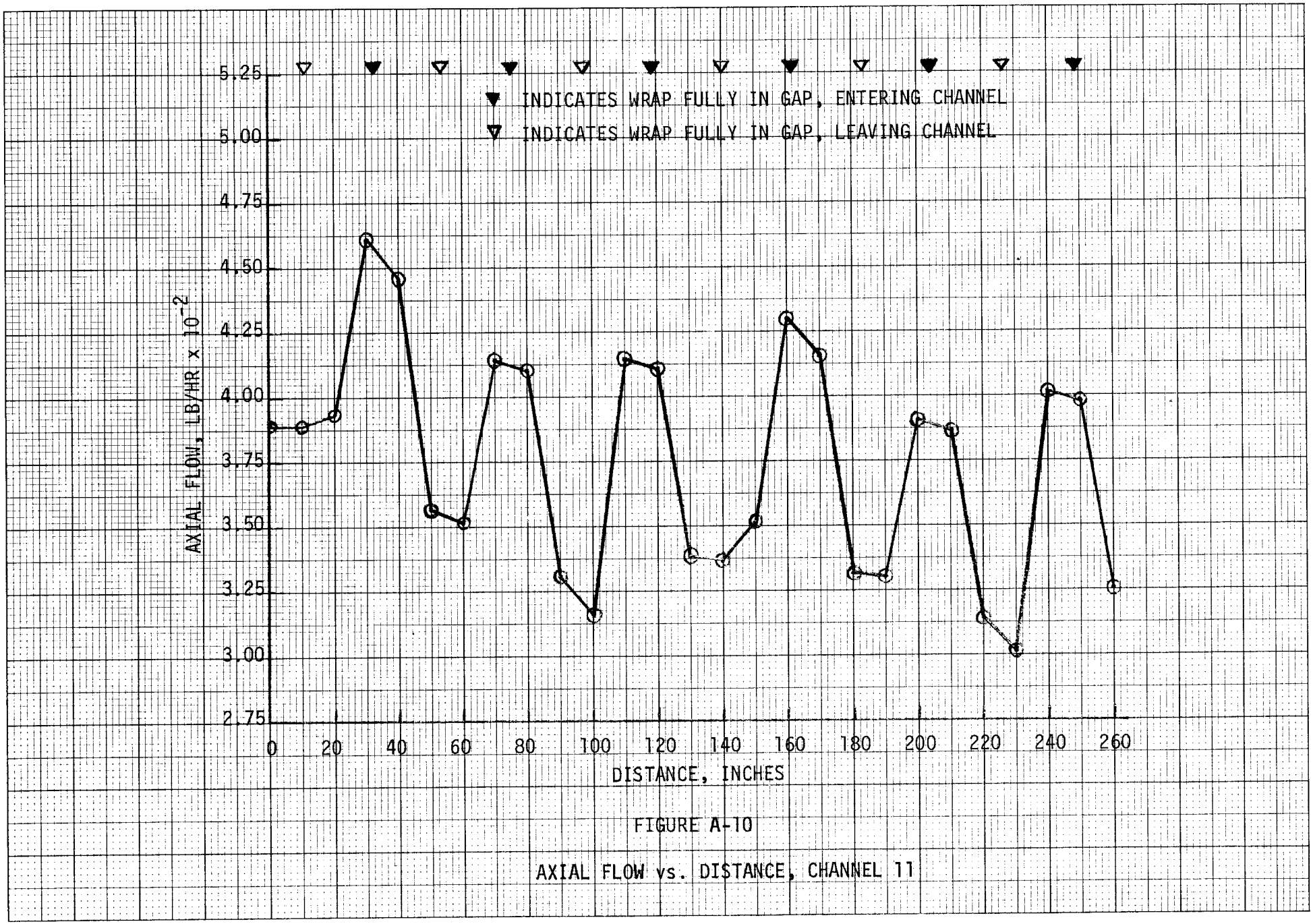

FIGURE A-10

AXIAL FLOW vs. DISTANCE, CHANNEL 11

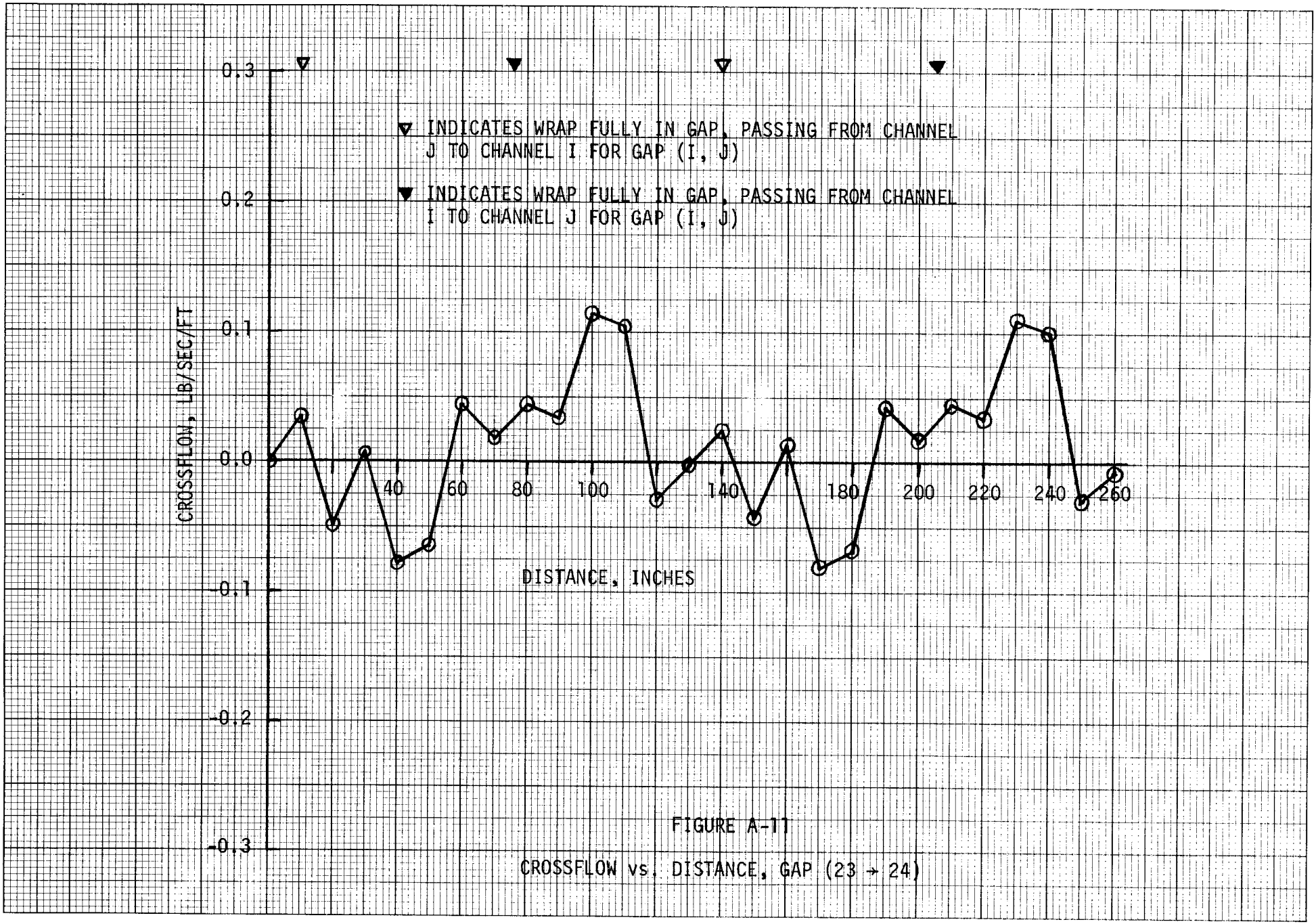

FIGURE A-11

CROSSFLOW vs. DISTANCE, GAP (23 → 24)

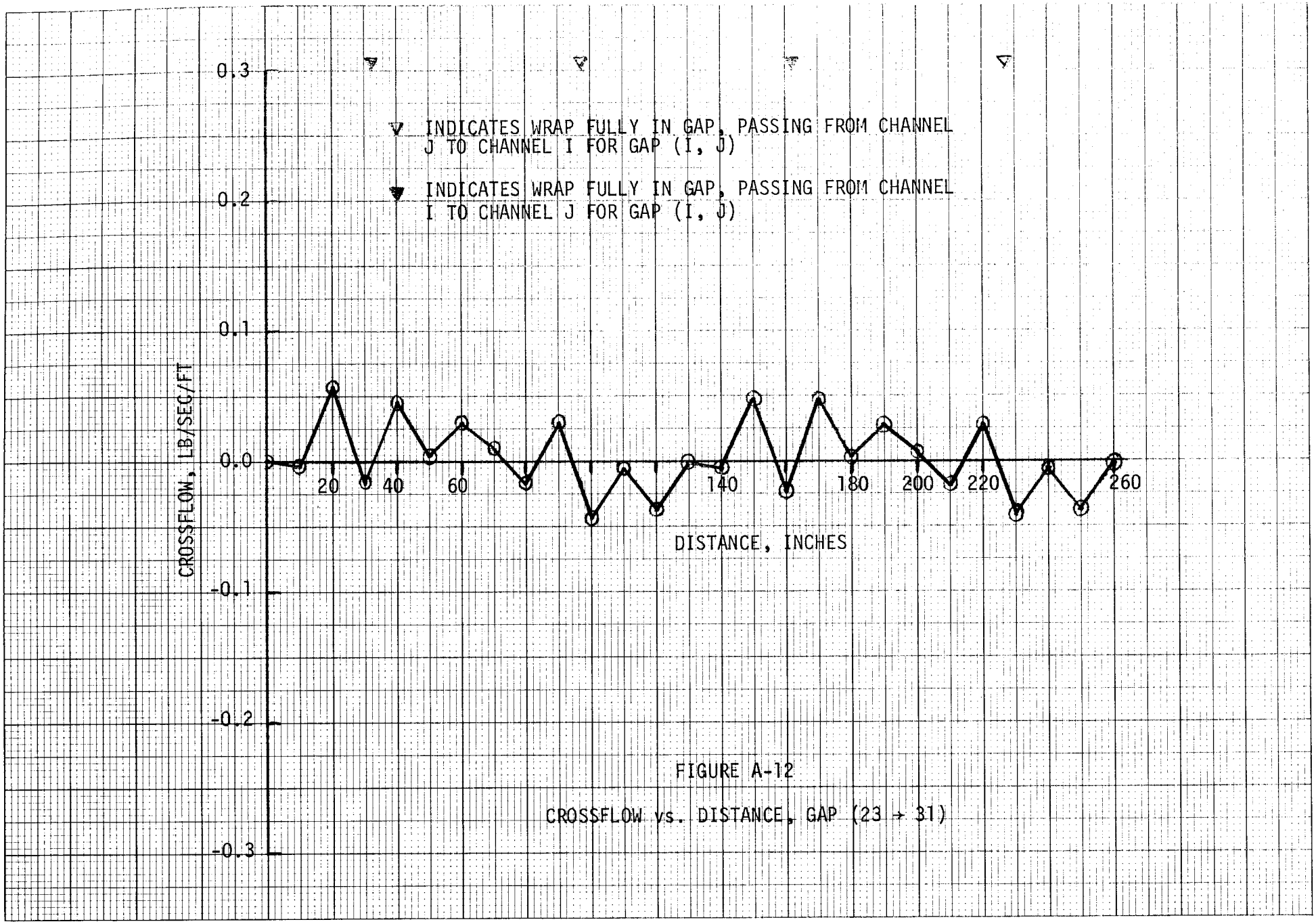

FIGURE A-12

CROSSFLOW vs. DISTANCE, GAP (23 → 31)

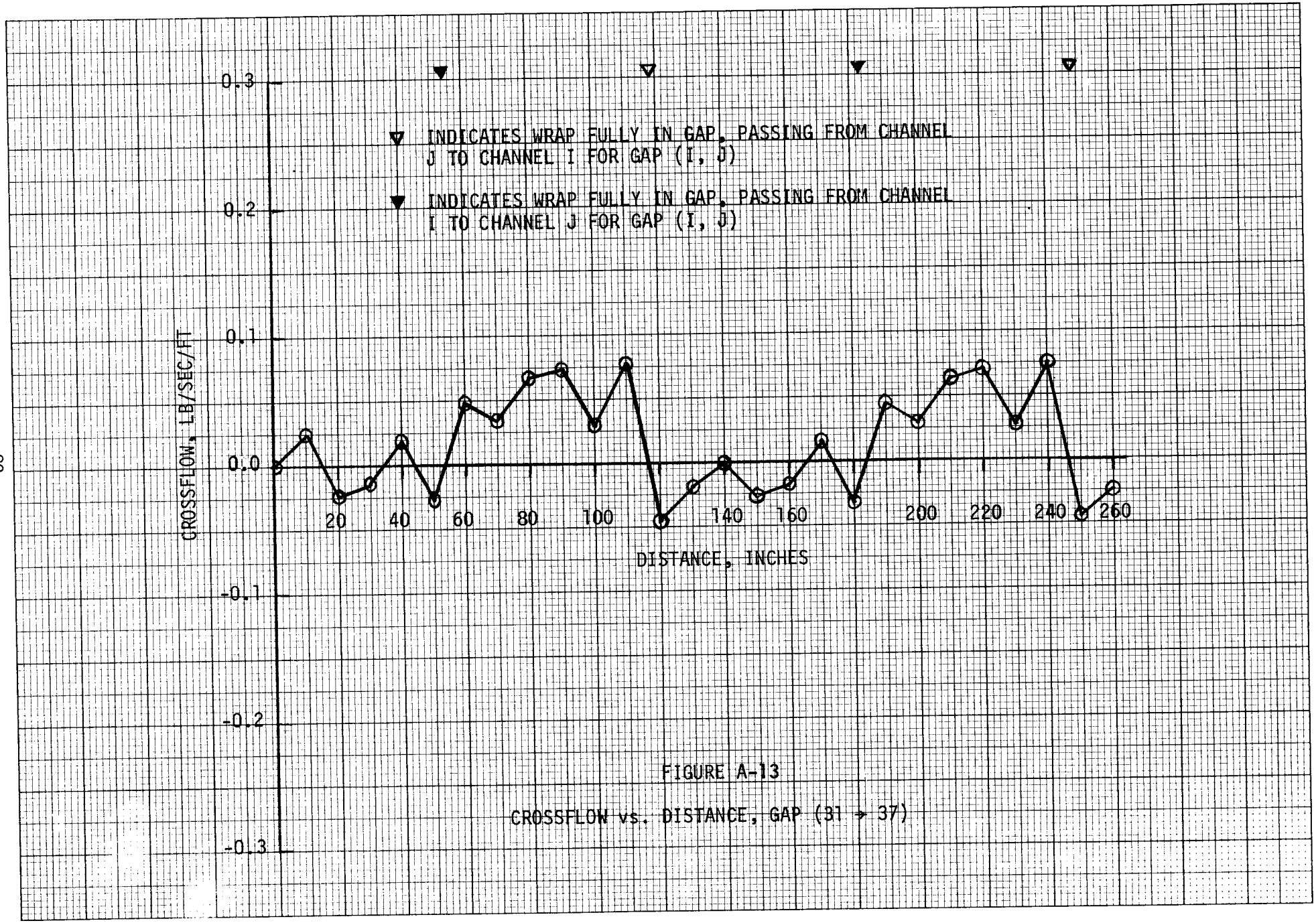

FIGURE A-13

CROSSFLOW vs. DISTANCE, GAP (31 → 37)

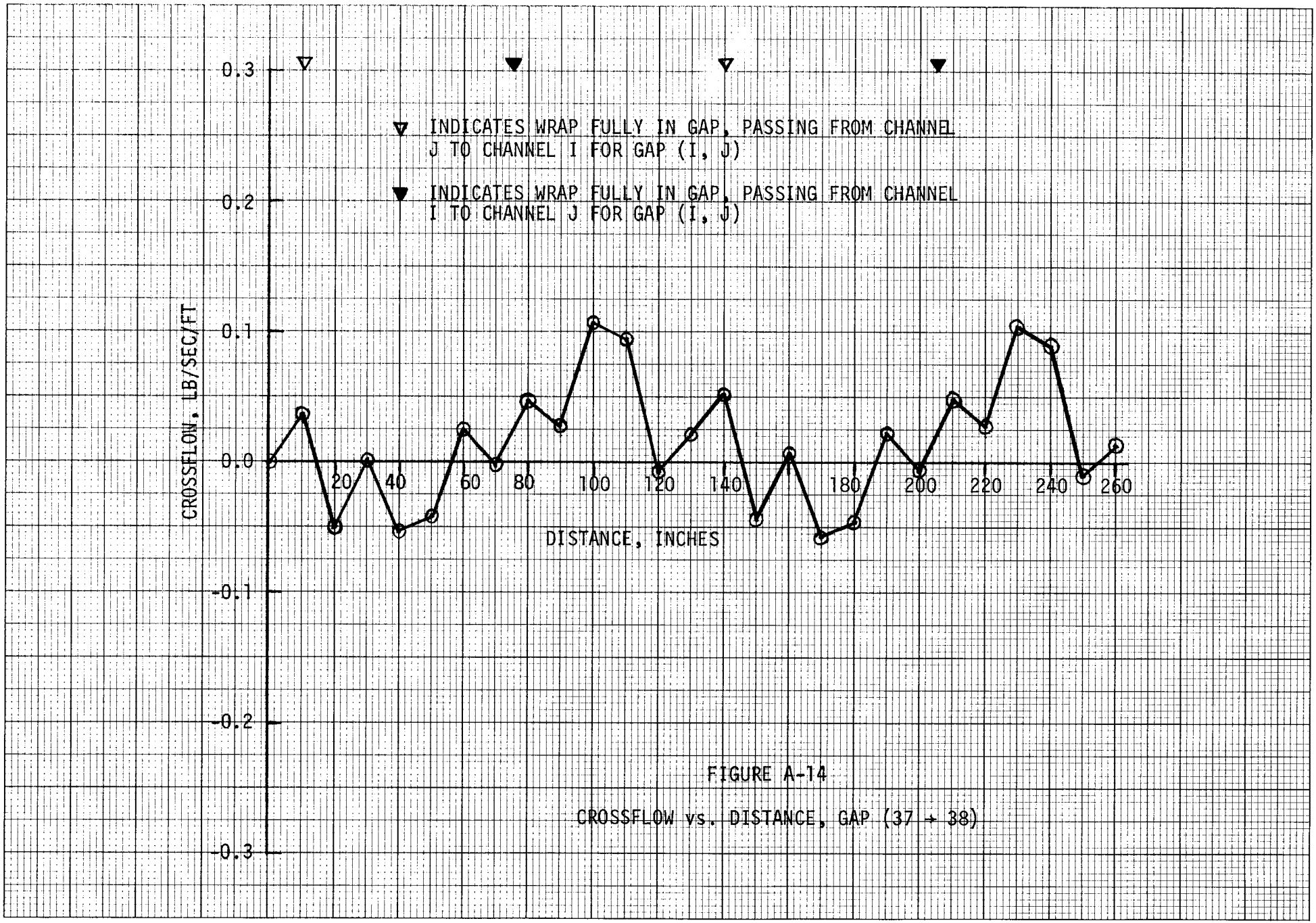

FIGURE A-14

CROSSFLOW vs. DISTANCE, GAP (37 → 38)

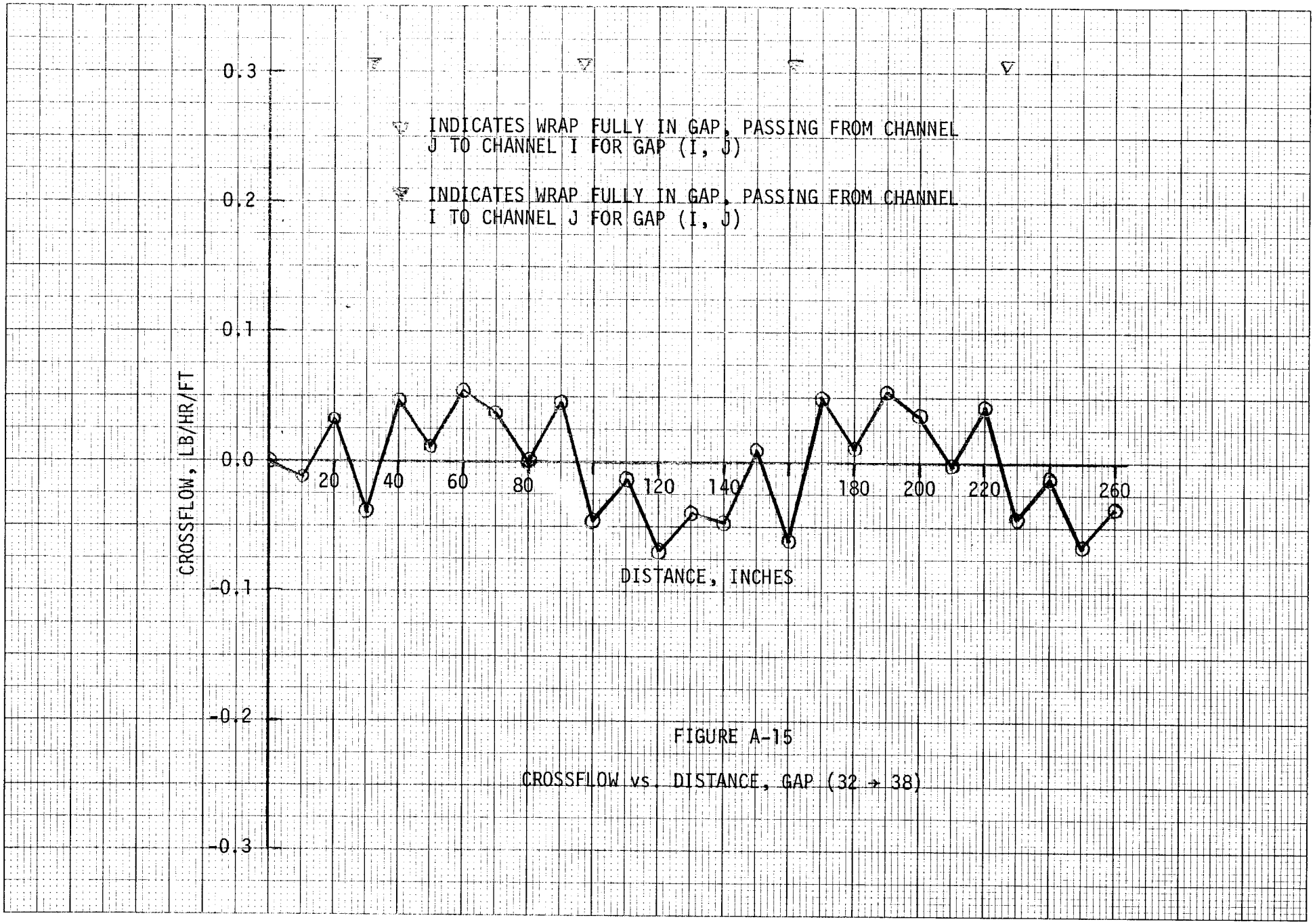

FIGURE A-15

CROSSFLOW vs. DISTANCE, GAP (32 → 38)

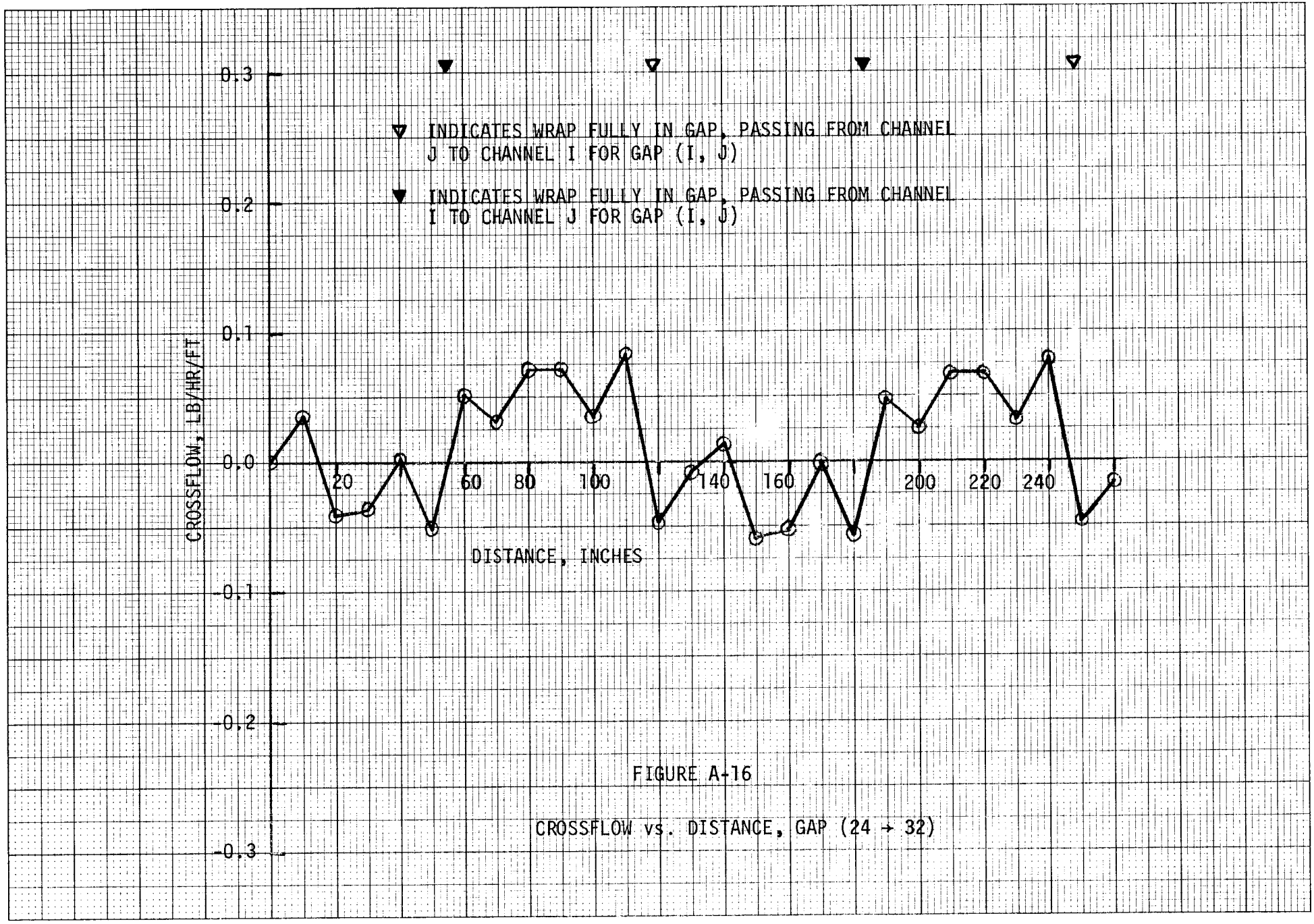

FIGURE A-16

CROSSFLOW vs. DISTANCE, GAP (24 → 32)

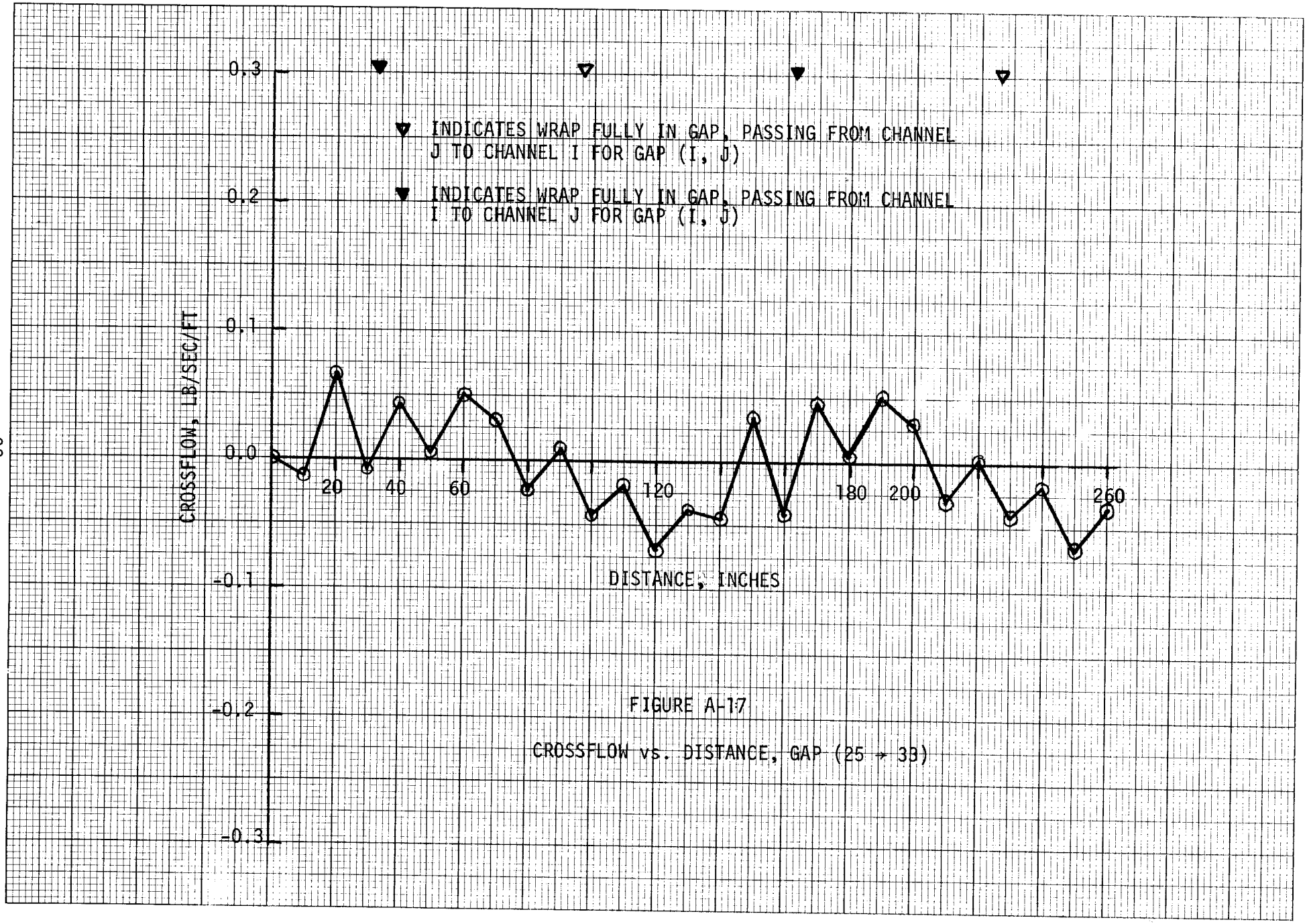

FIGURE A-17

CROSSFLOW vs. DISTANCE, GAP (25 → 33)

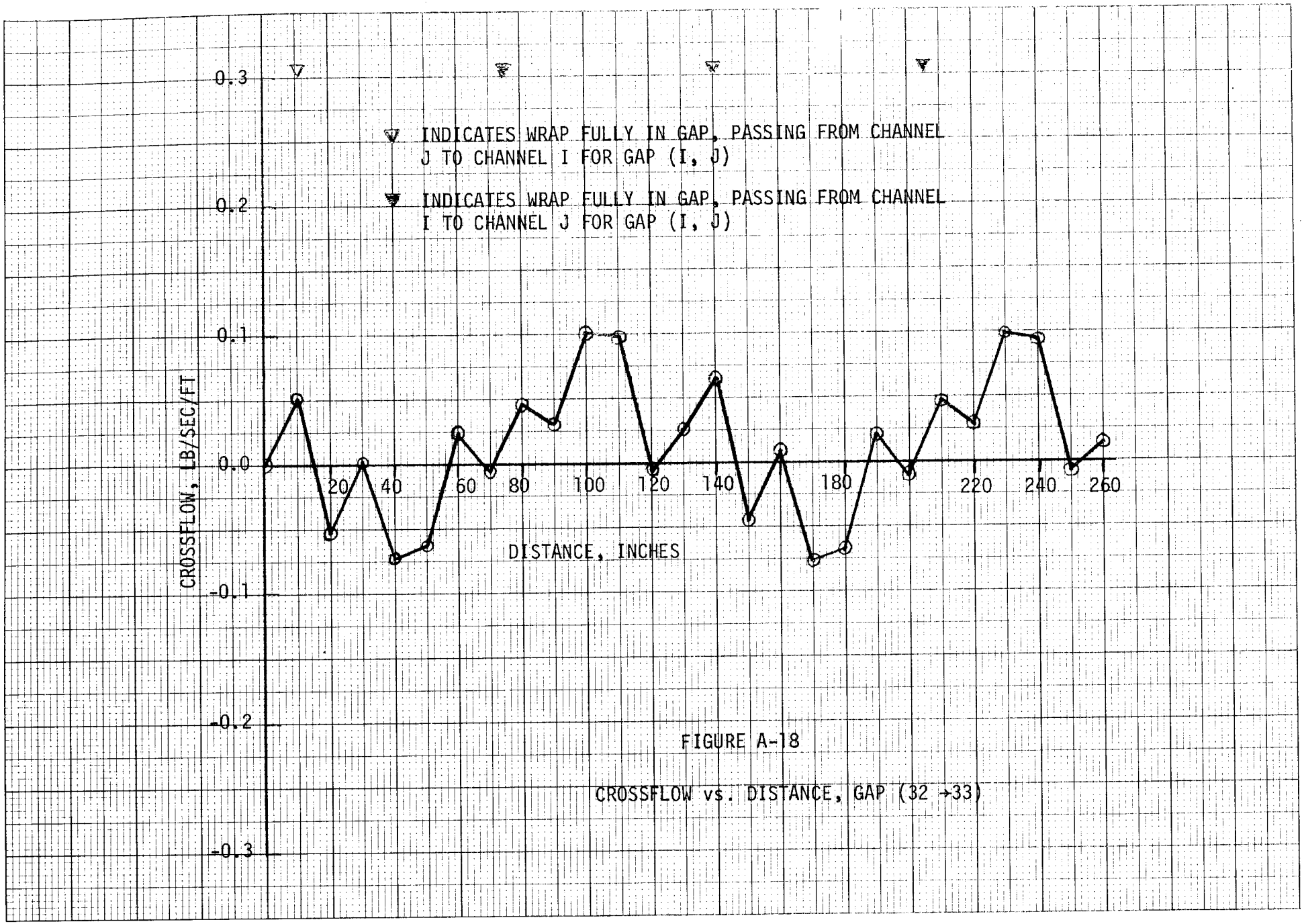

FIGURE A-18

CROSSFLOW vs. DISTANCE, GAP (32 →33)

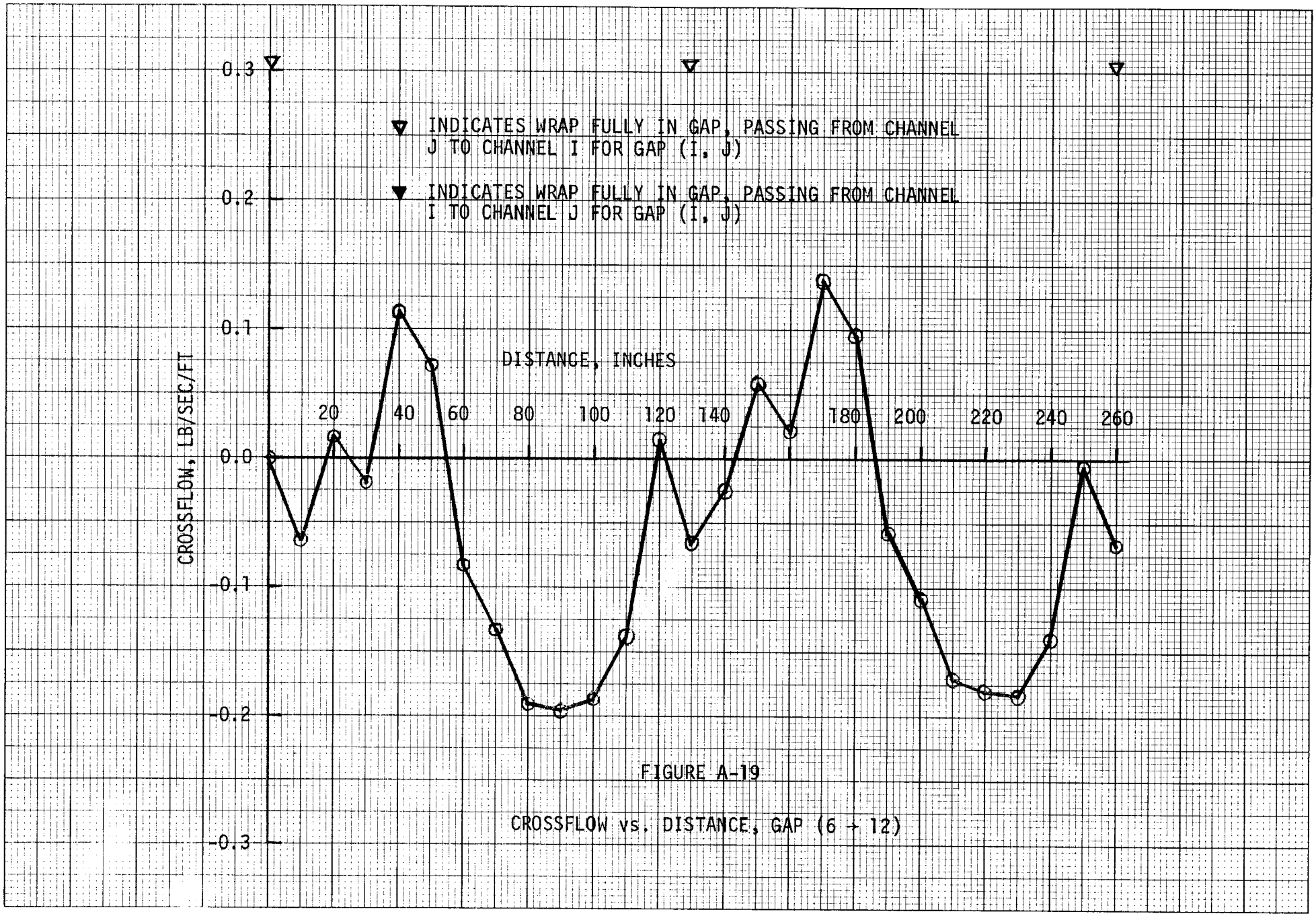

FIGURE A-19

CROSSFLOW vs. DISTANCE, GAP (6 → 12)

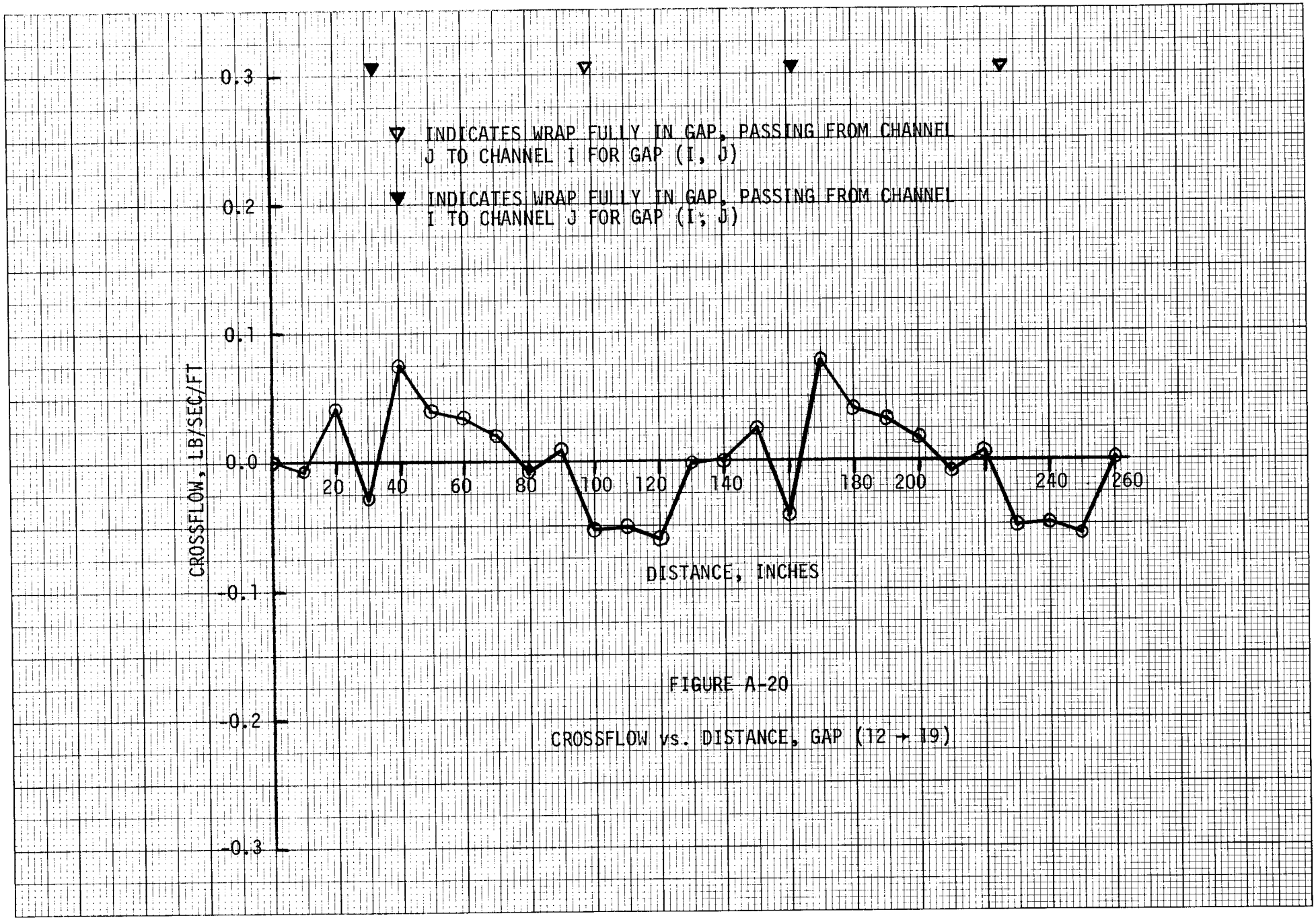

FIGURE A-20

CROSSFLOW vs. DISTANCE, GAP (12 → 19)

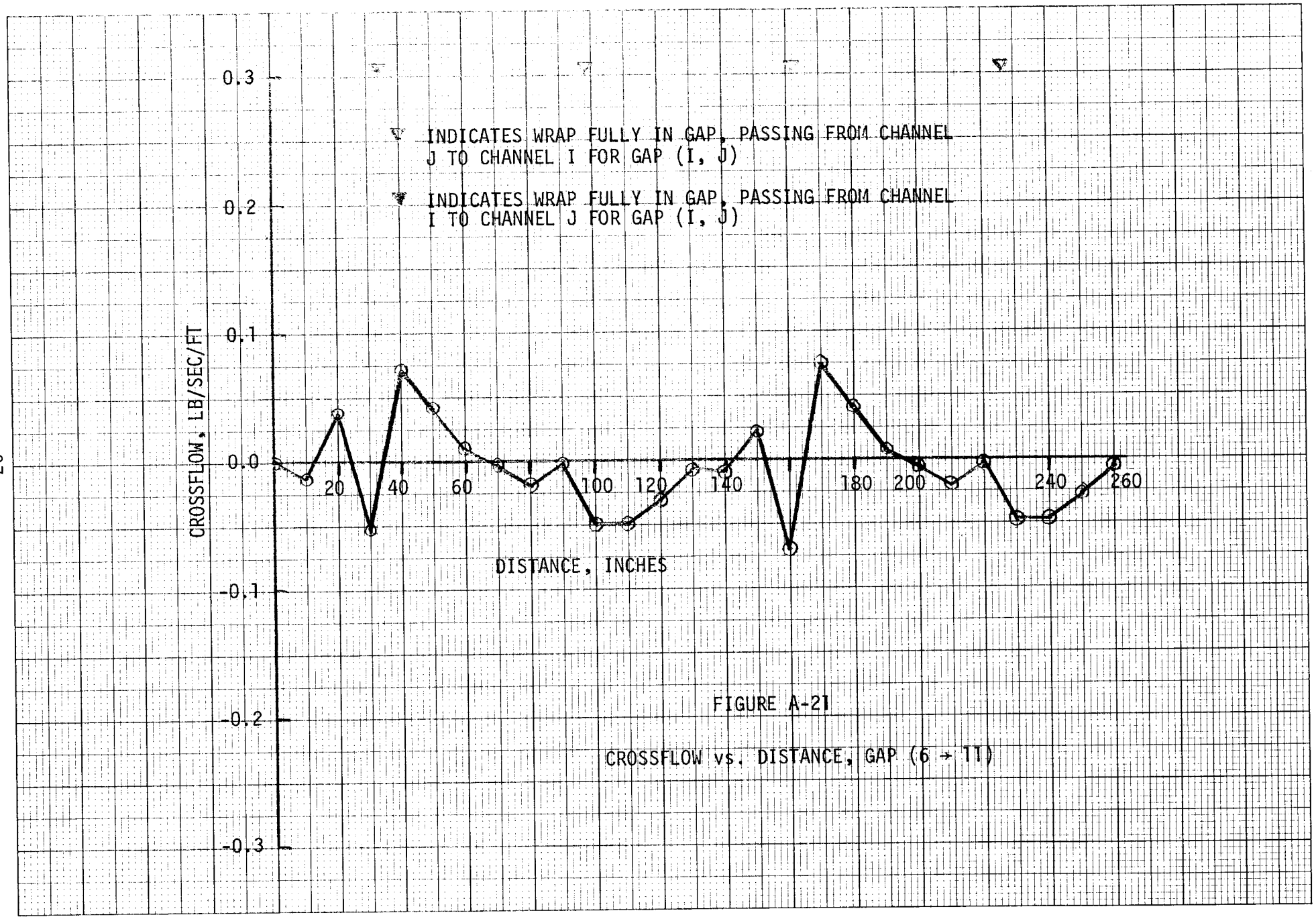

FIGURE A-21

CROSSFLOW vs. DISTANCE, GAP (6 → 11)

APPENDIX B

TRACER GAS DISTRIBUTION PROFILES

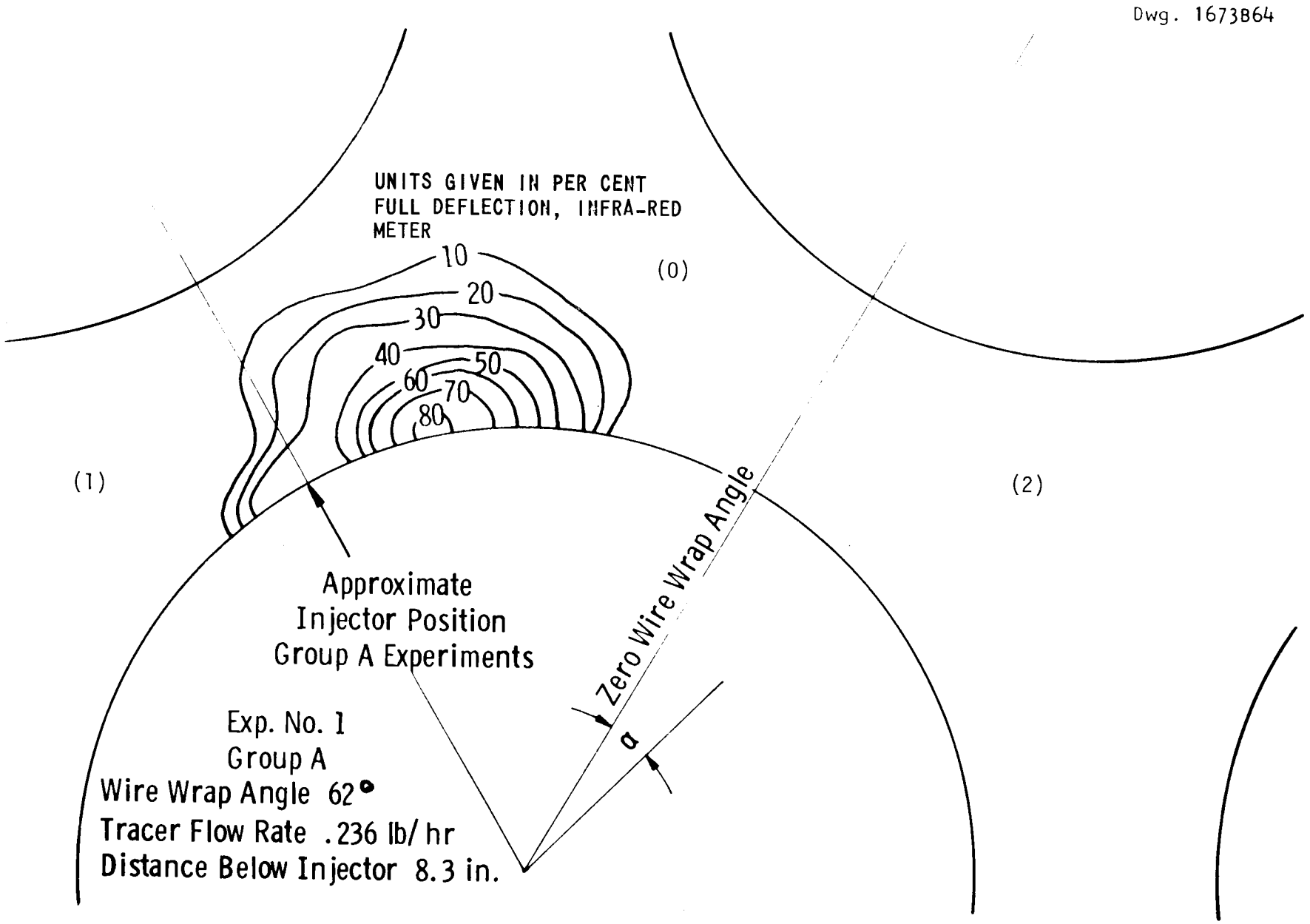

Fig. B-1—Tracer distribution no. 1

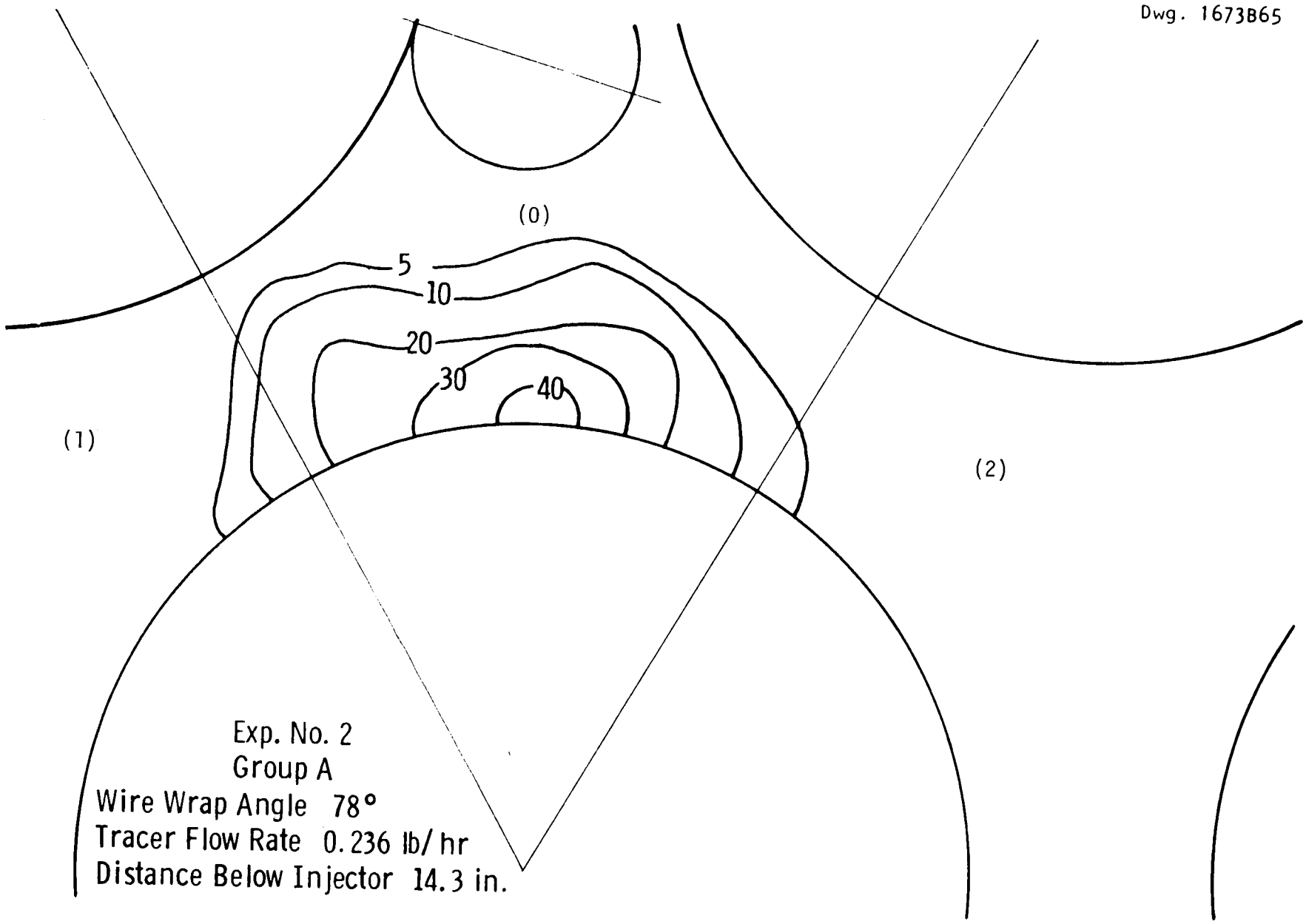

Fig. B-2—Tracer distribution no. 2

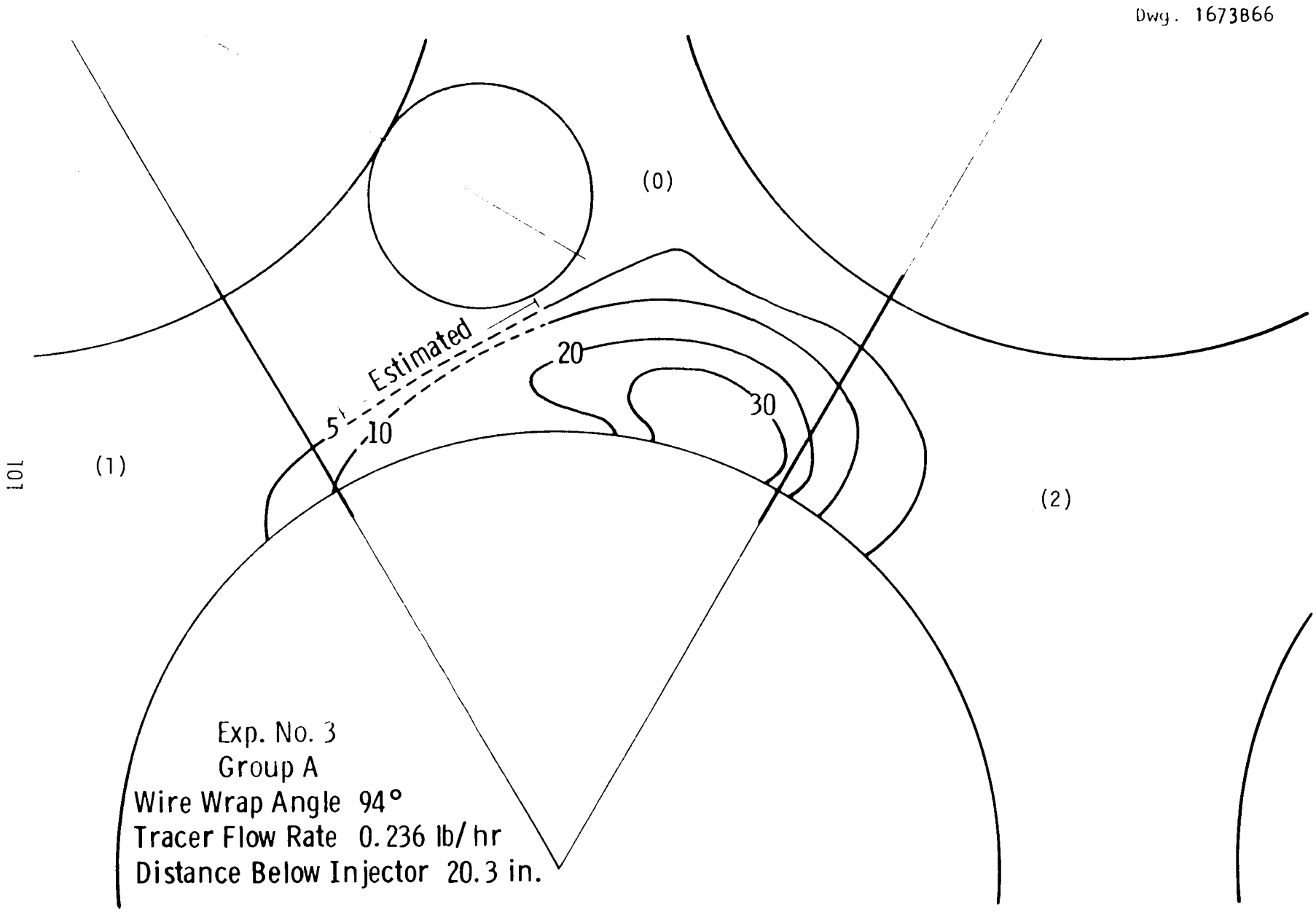

Fig. B-3—Tracer distribution no. 3

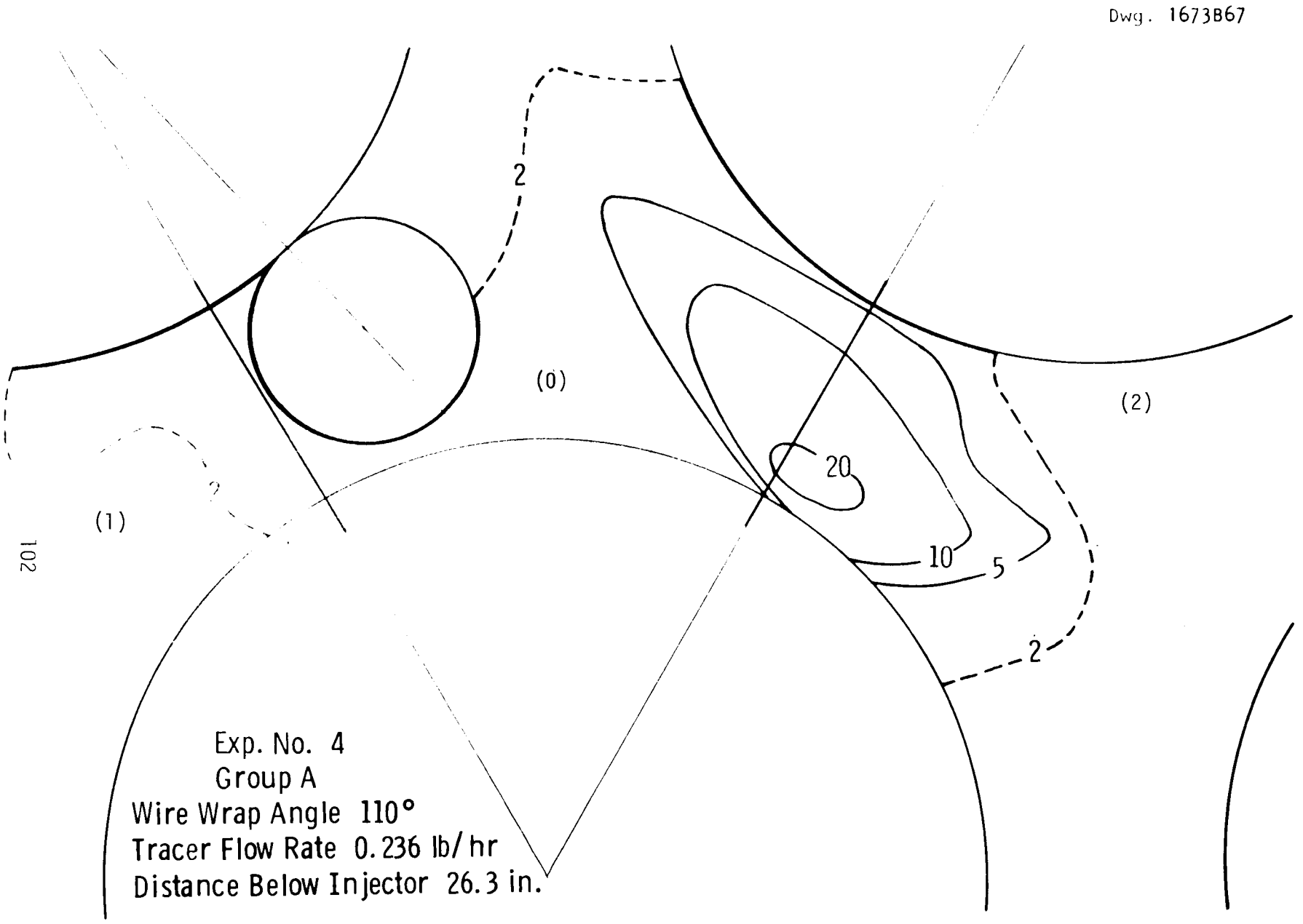

Fig. B-4—Tracer distribution no. 4

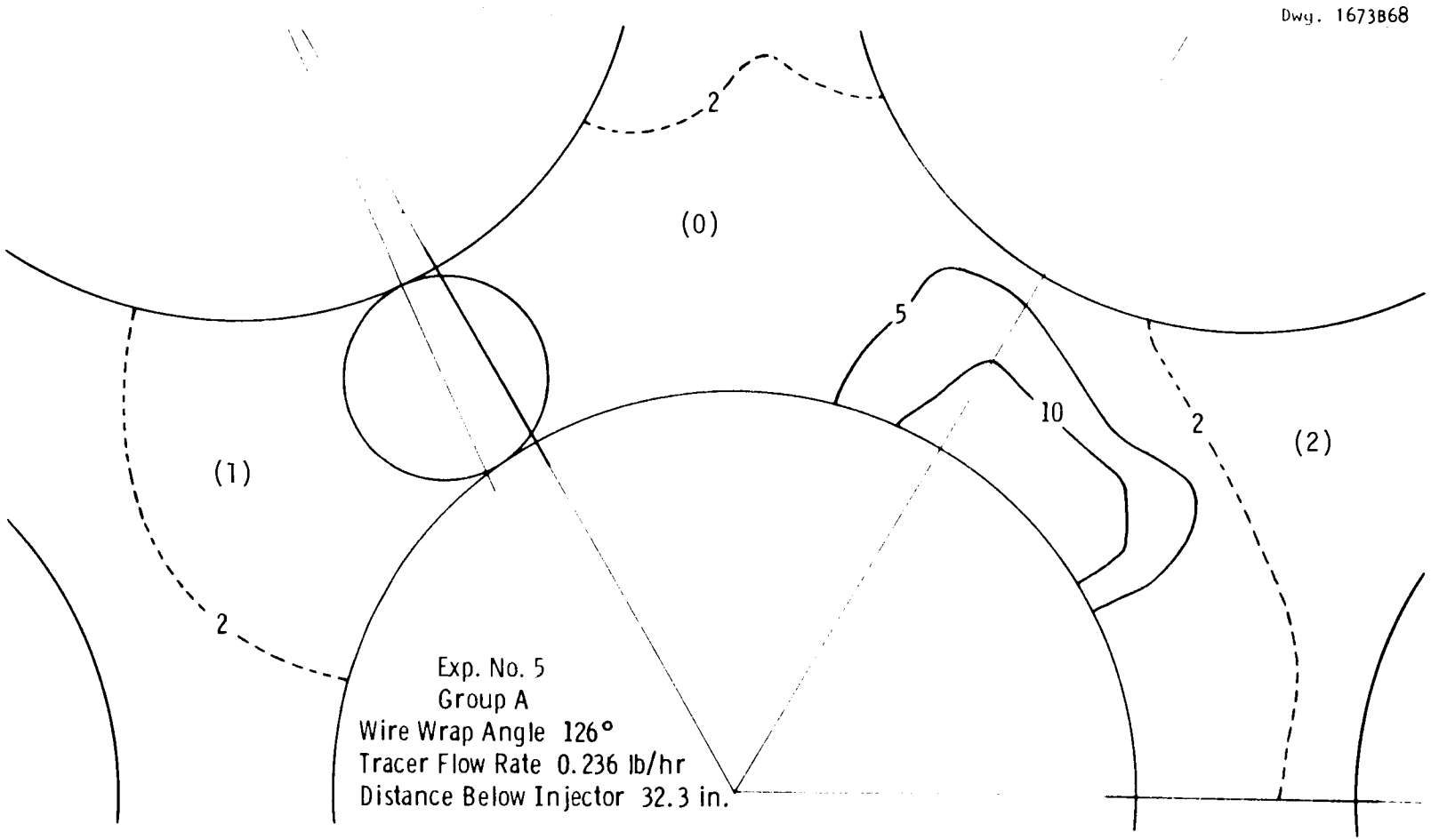

Fig. B-5—Tracer distribution no. 5

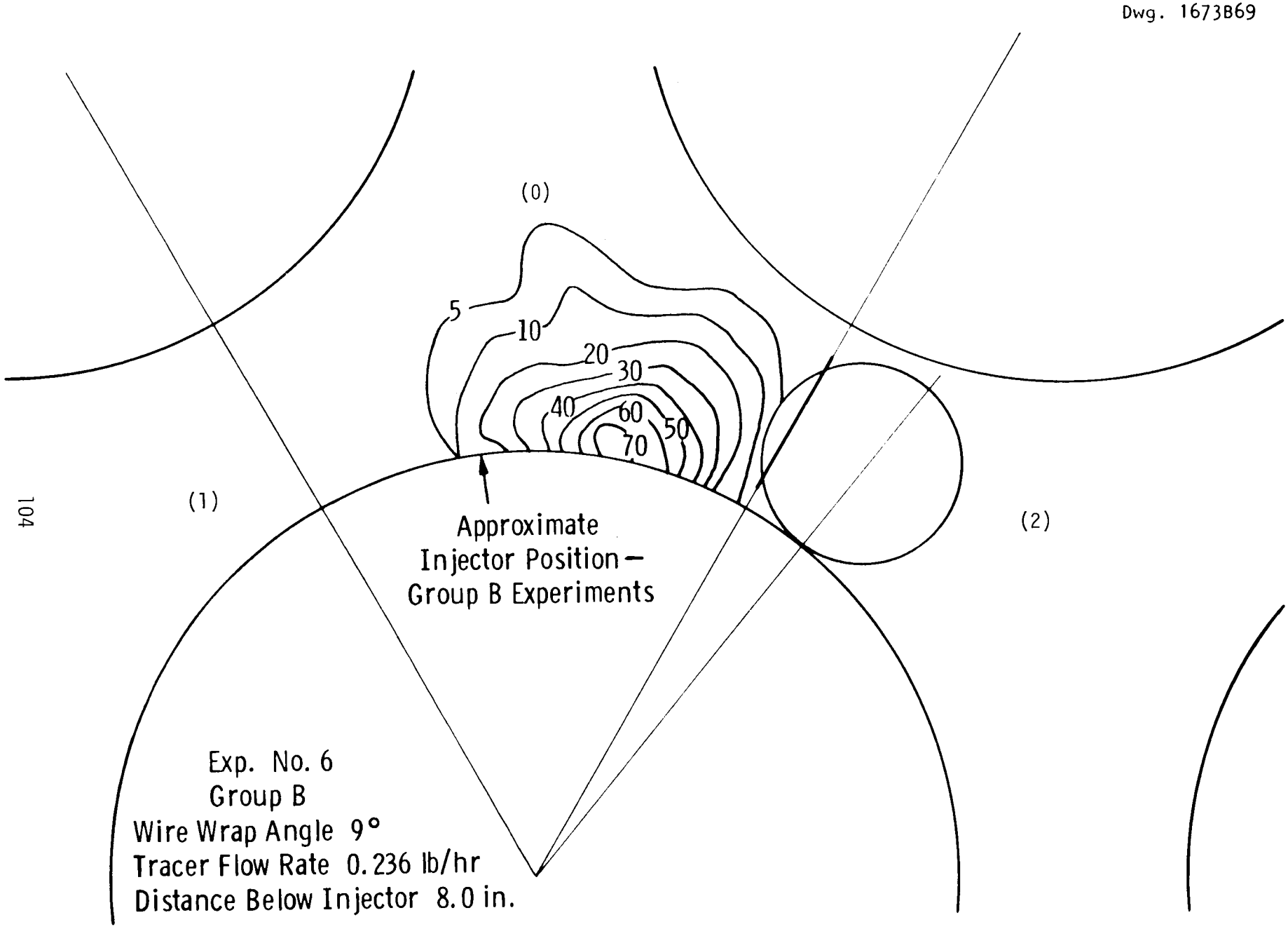

Fig. B-6—Tracer distribution no. 6

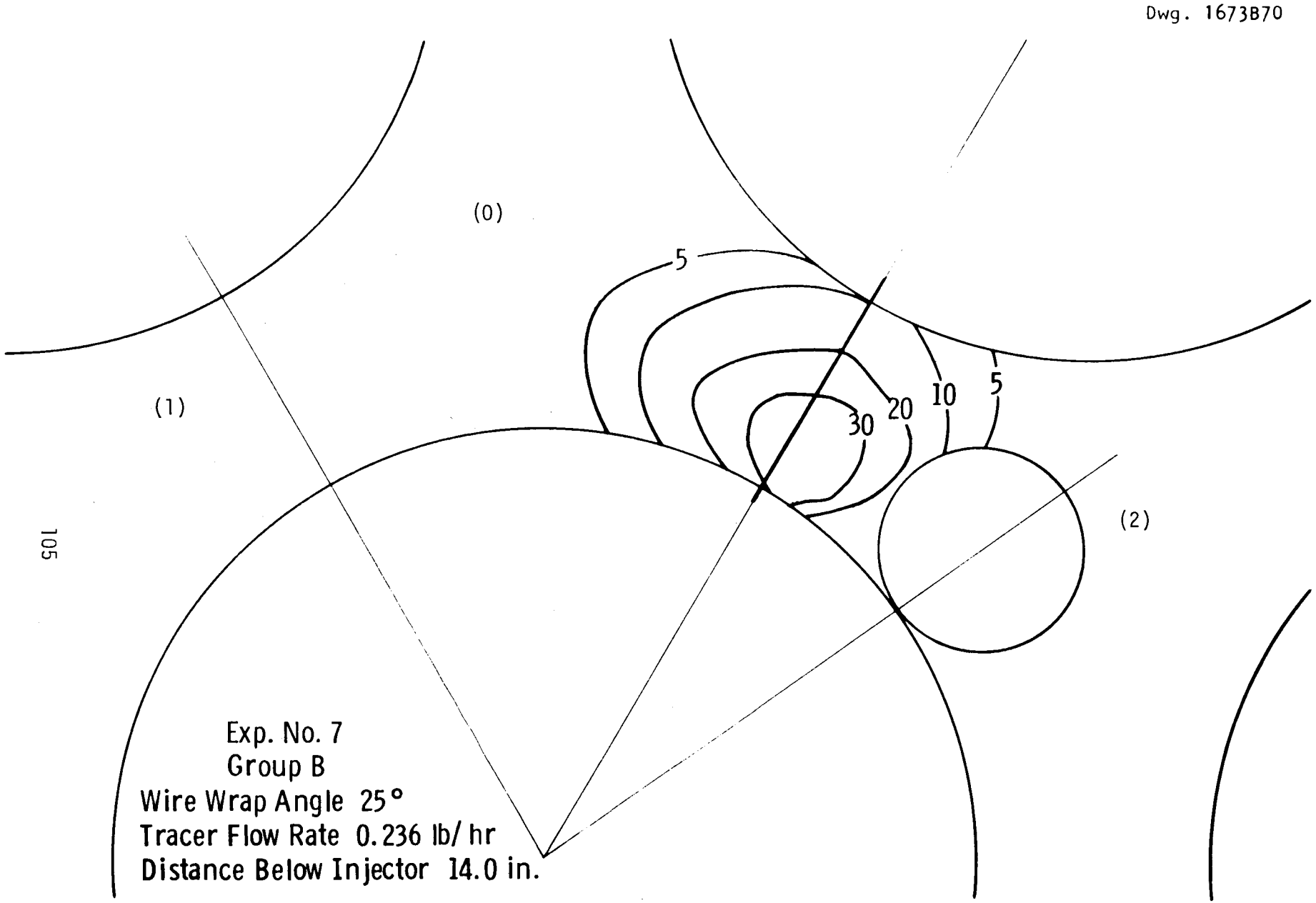

Fig. B-7—Tracer distribution no. 7

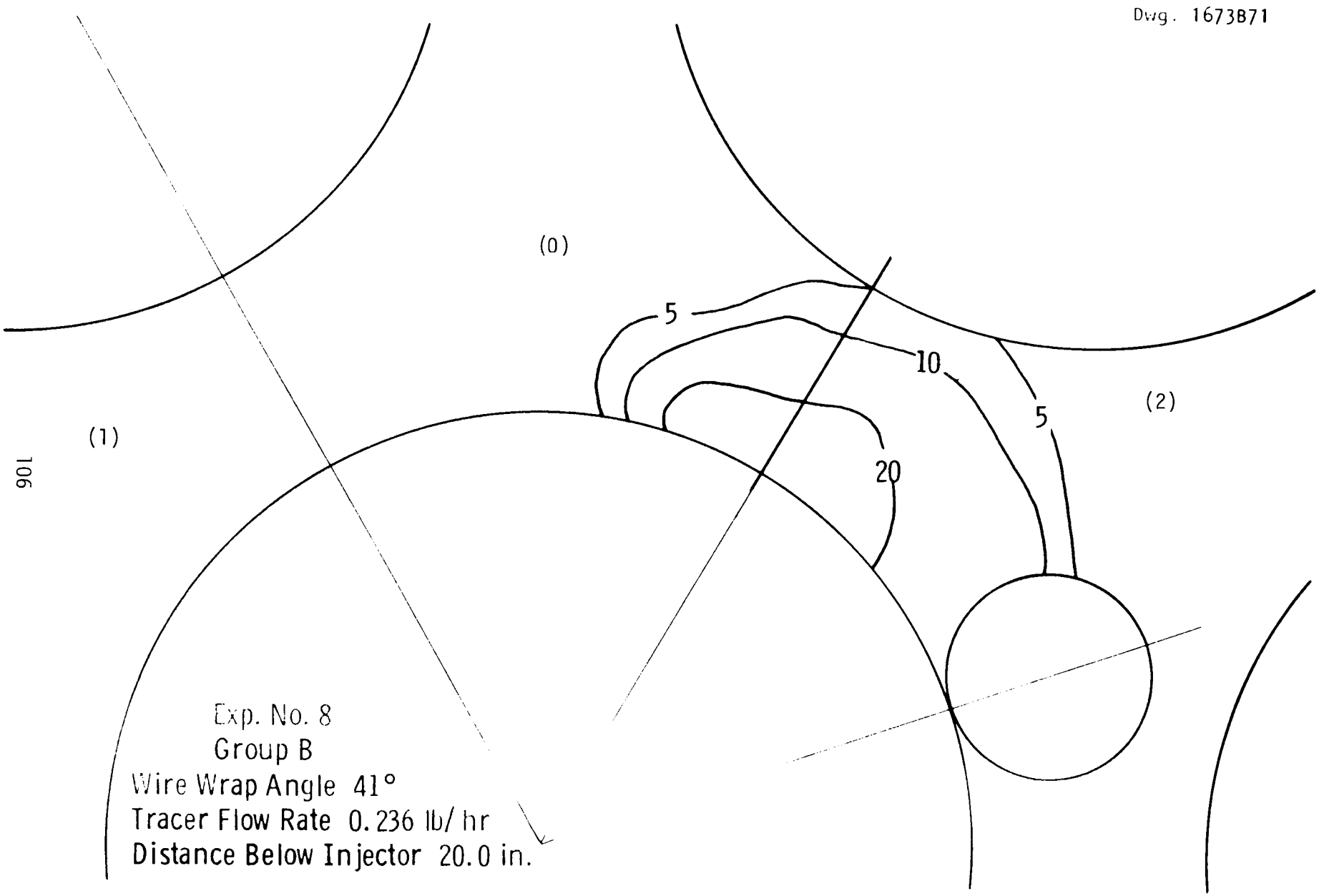

Fig. B-8—Tracer concentration no. 8

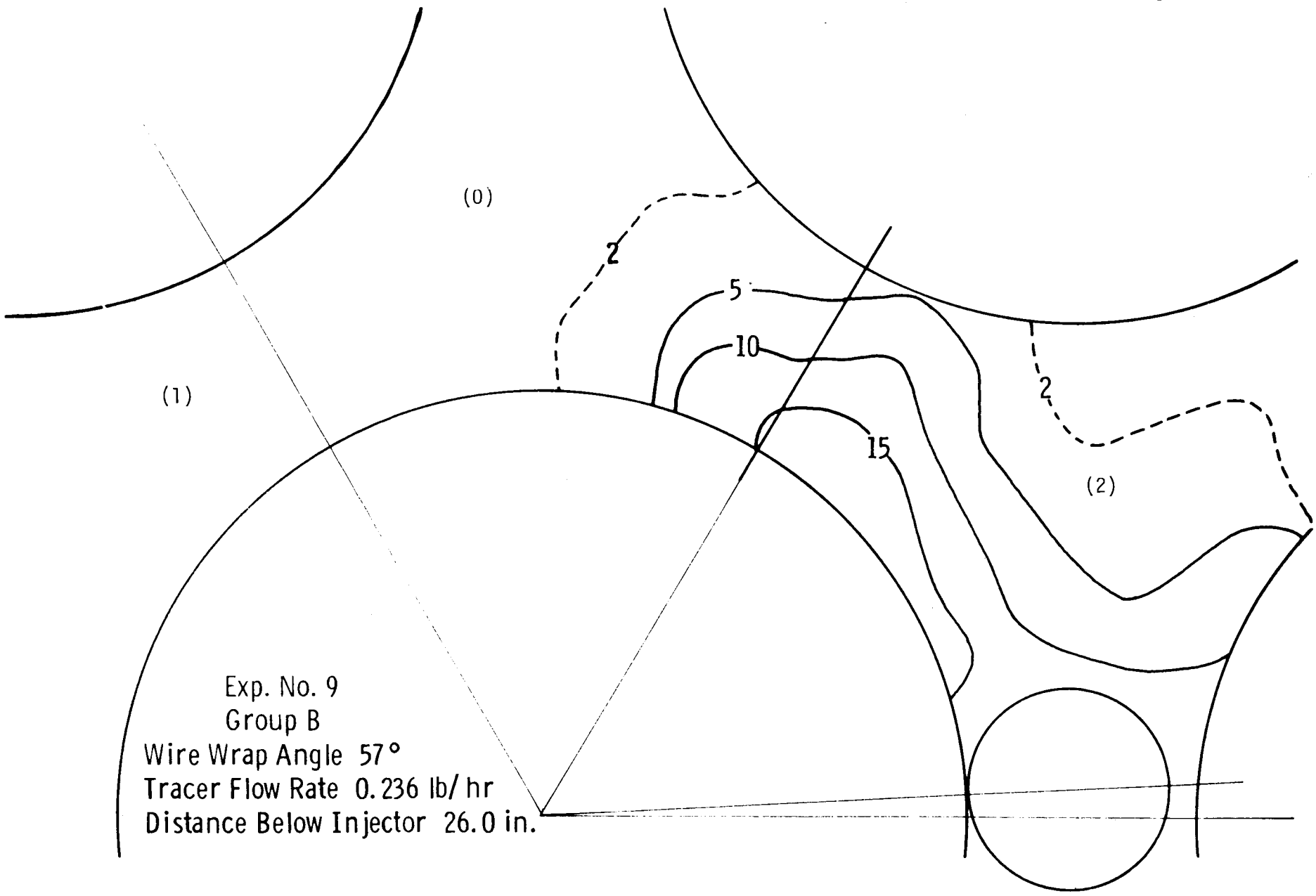

Fig. B-9—Tracer distribution no. 9

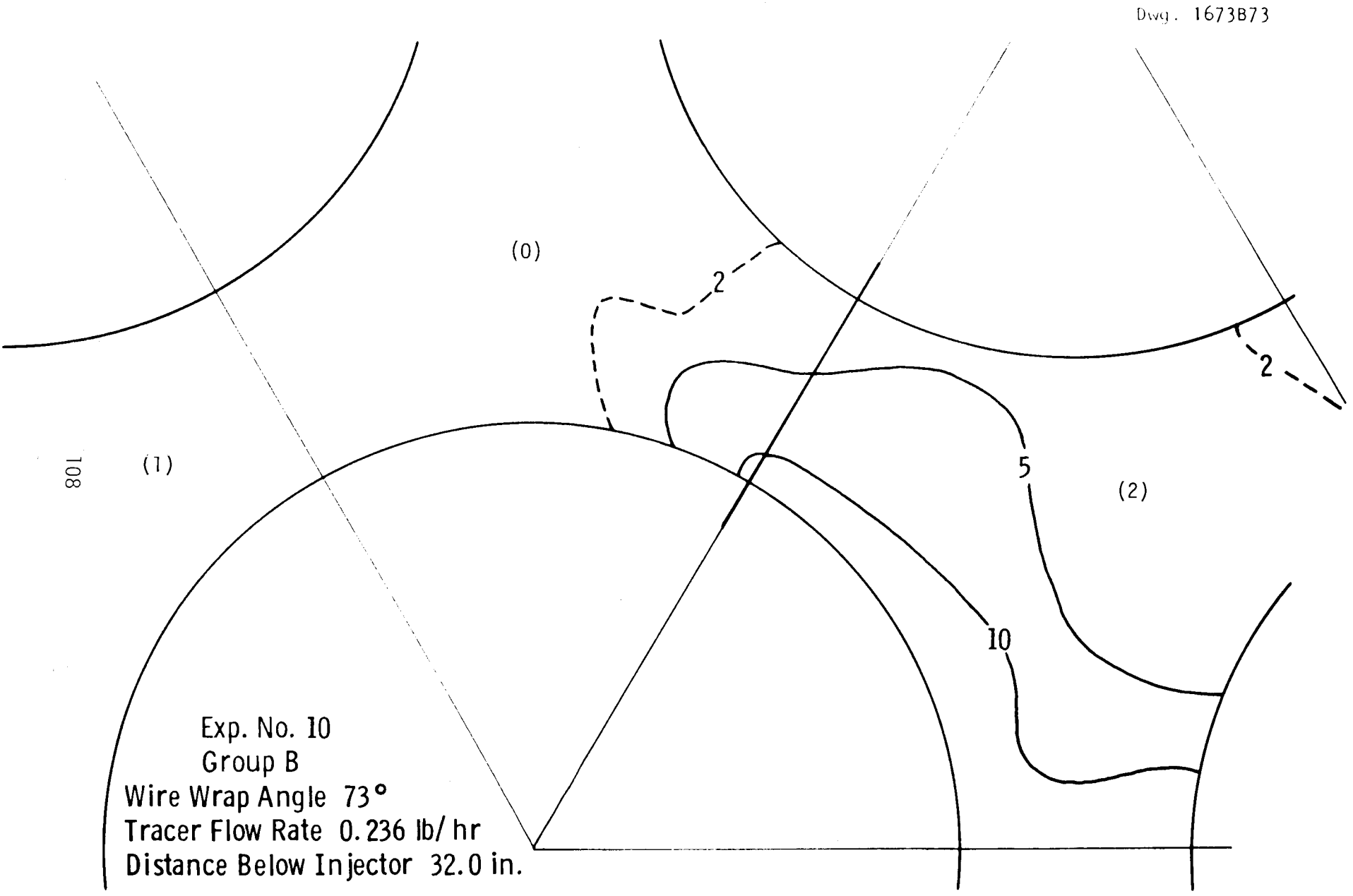

Fig. B-10—Tracer distribution no. 10

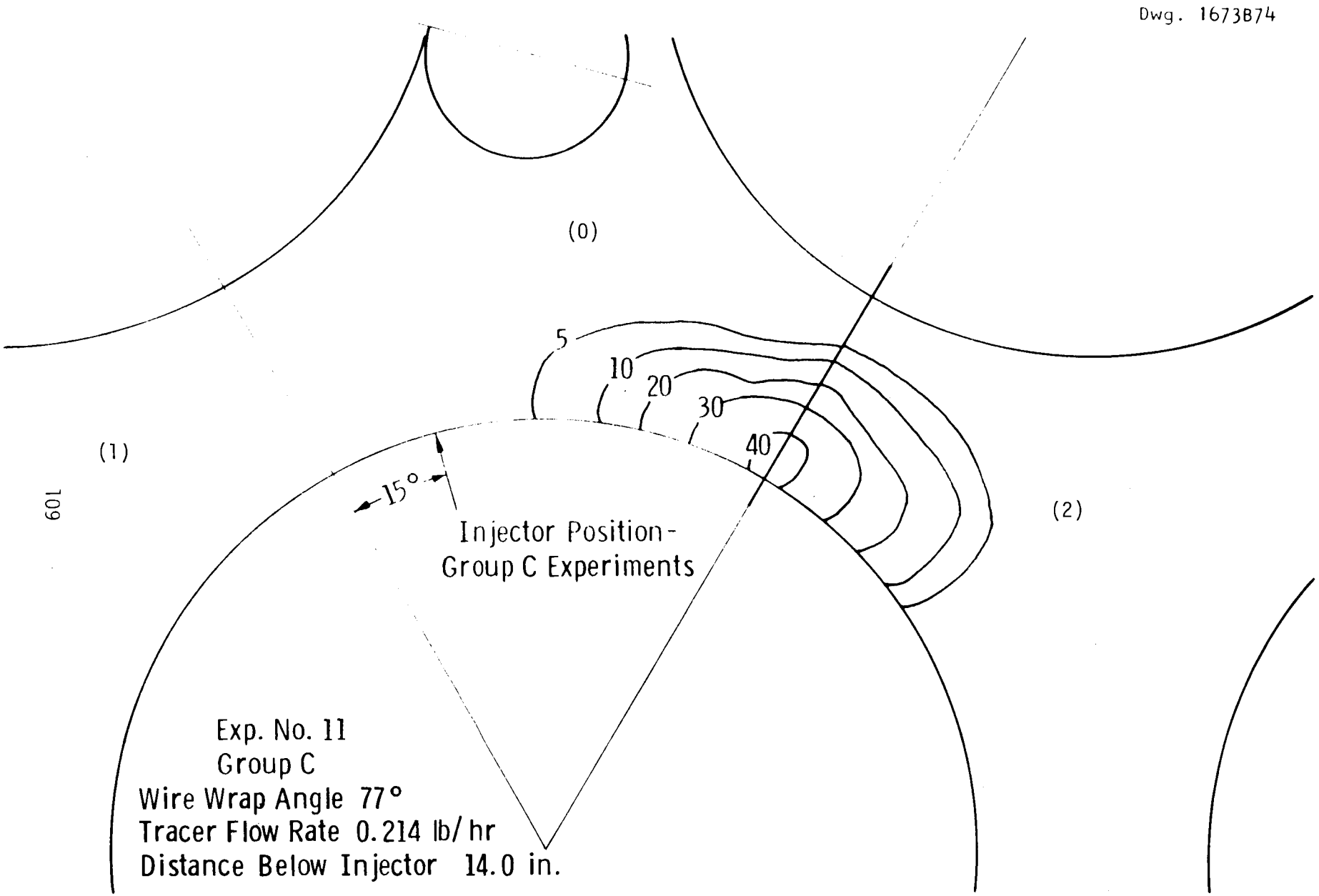

Fig. B-11—Tracer distribution no. 11

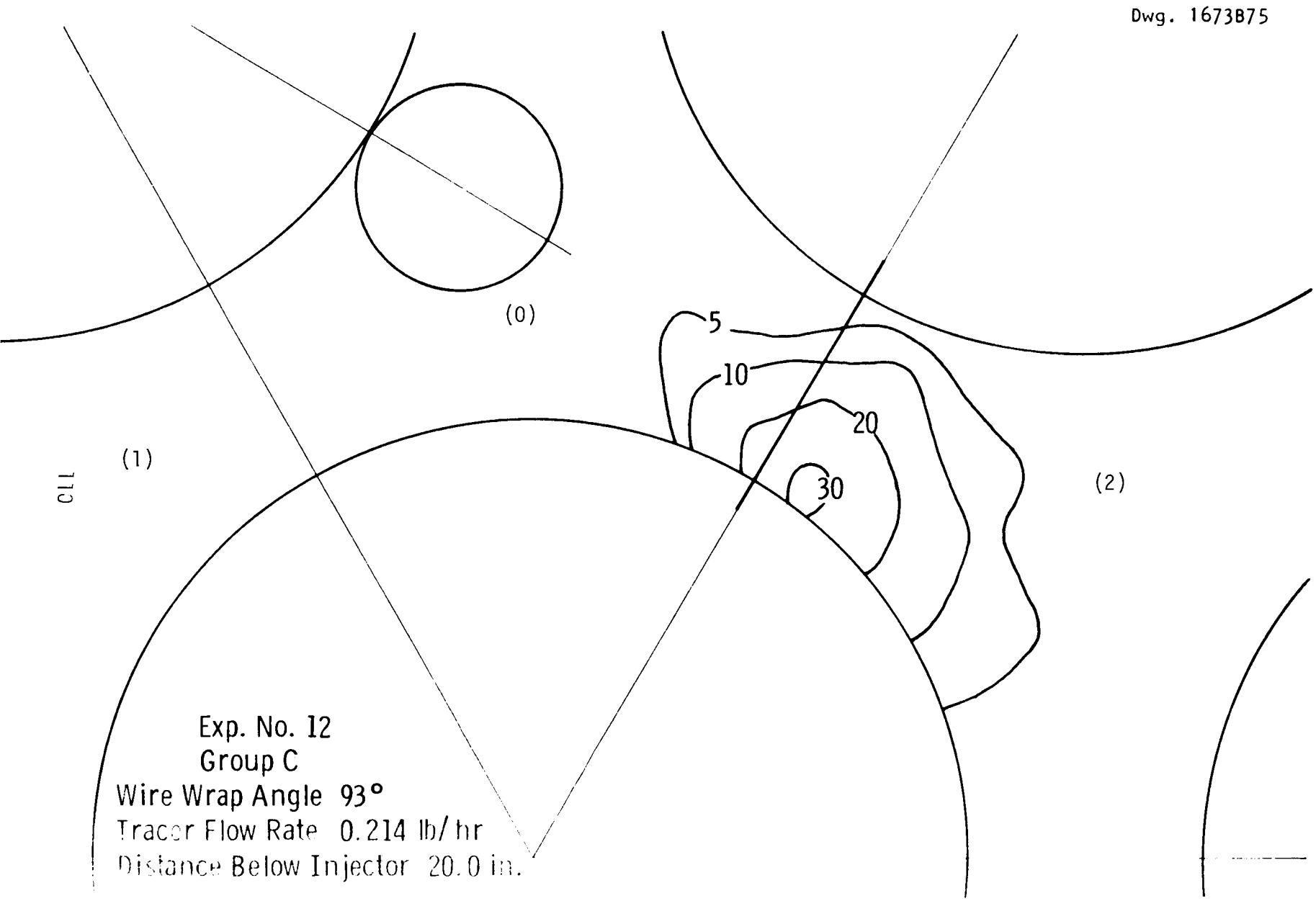

Fig. B-12—Tracer distribution no. 12

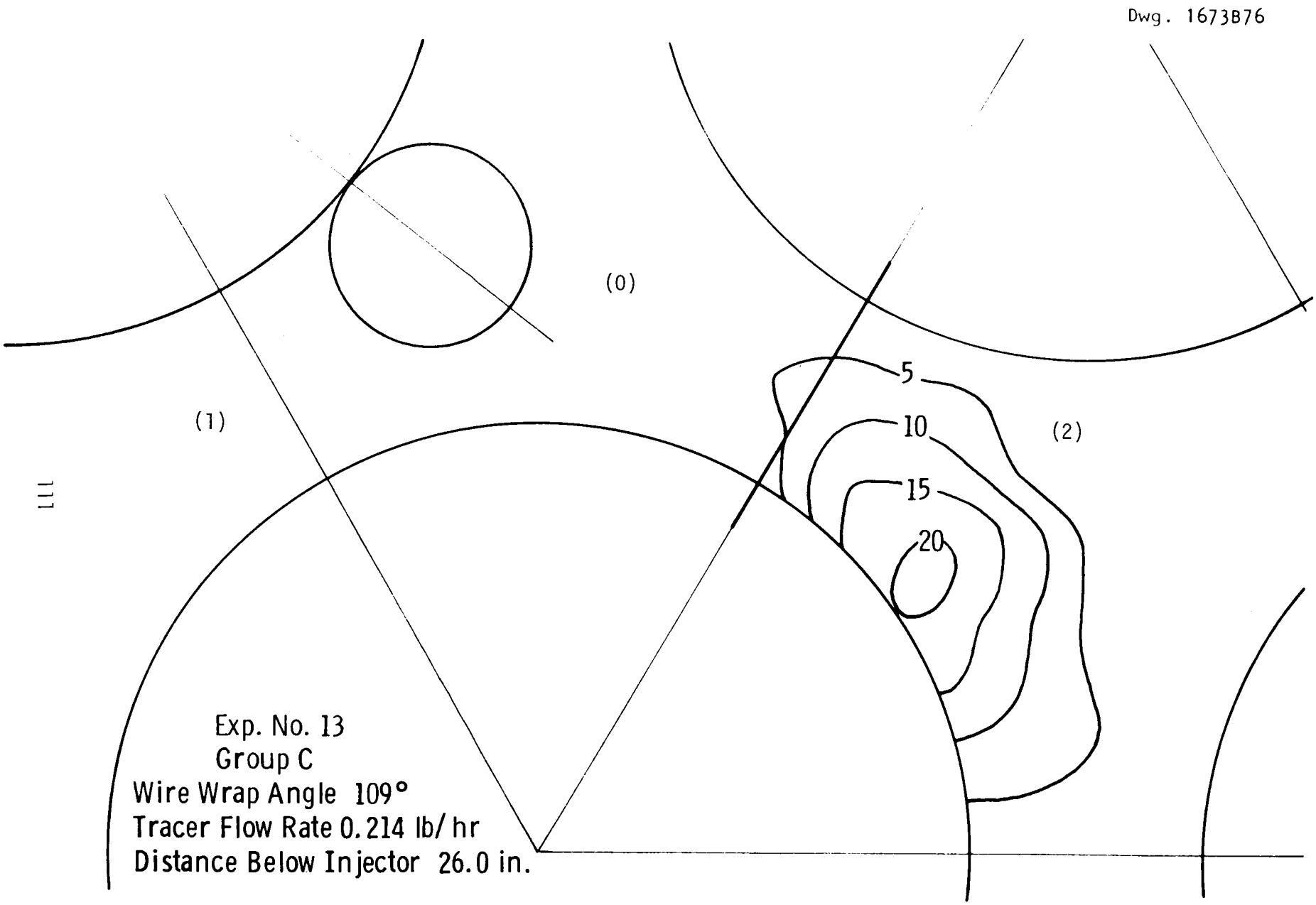

Fig. B-13—Tracer distribution no. 13

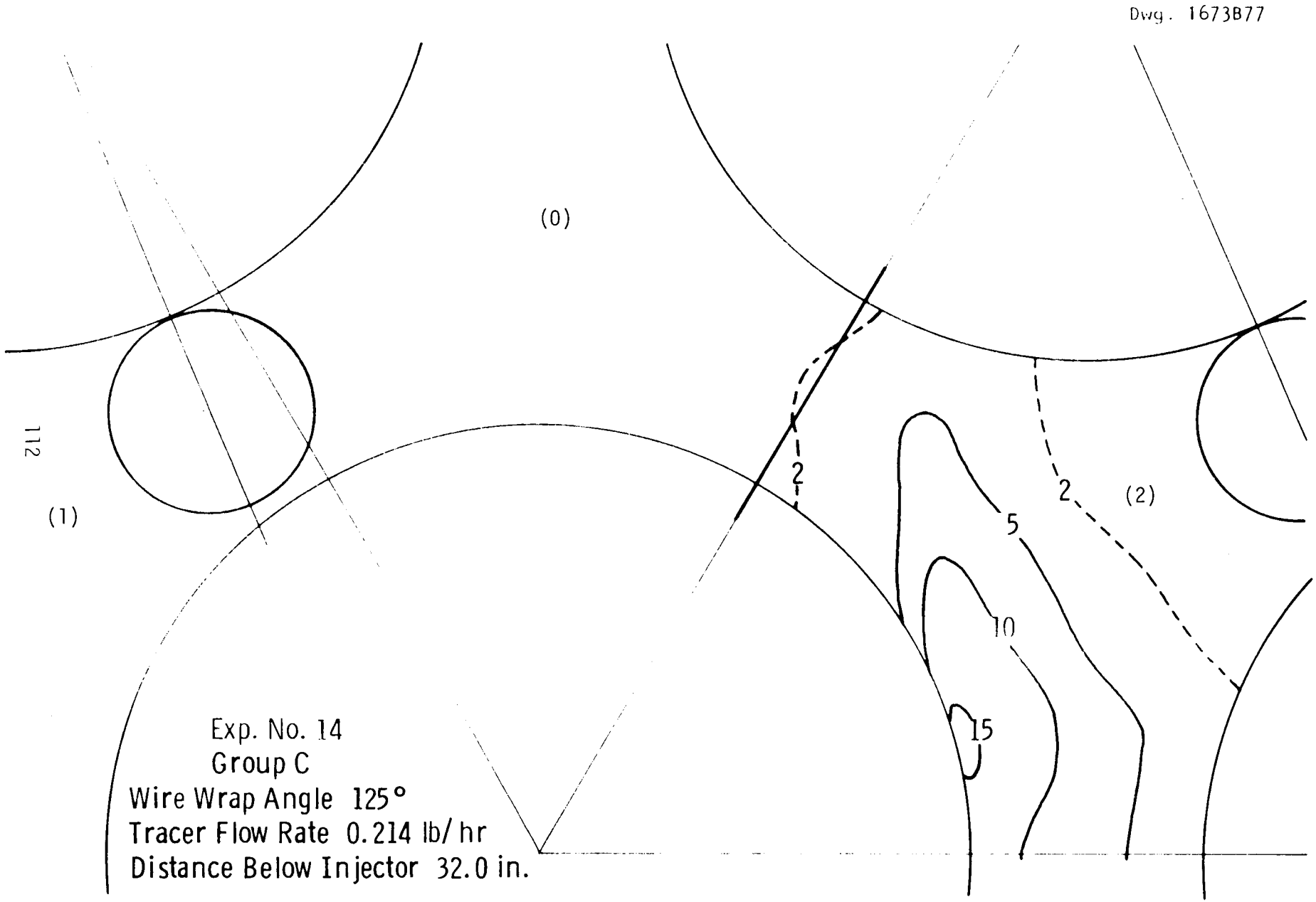

Fig. B-14—Tracer distribution no. 14

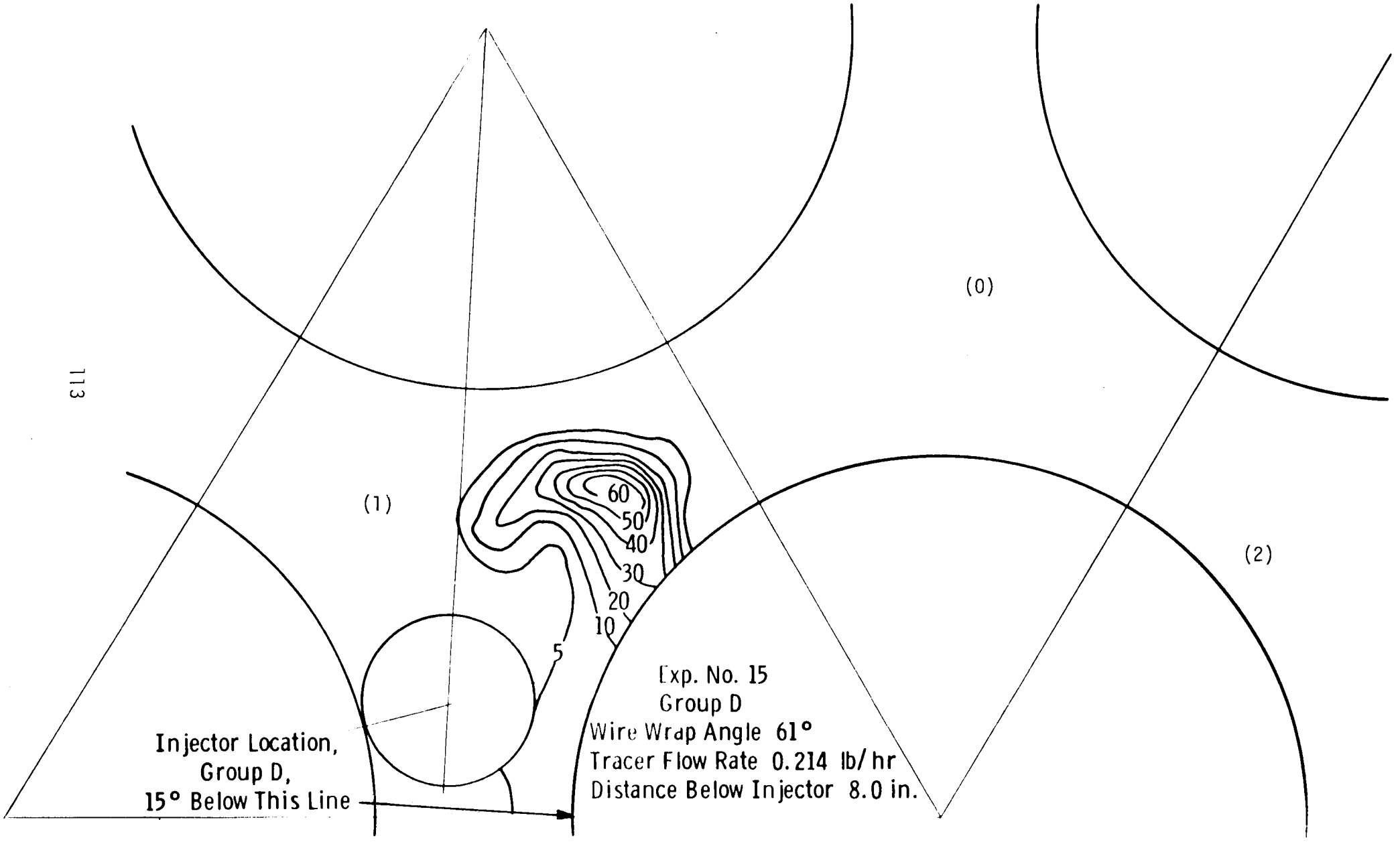

Fig. B-15—Tracer distribution no. 15

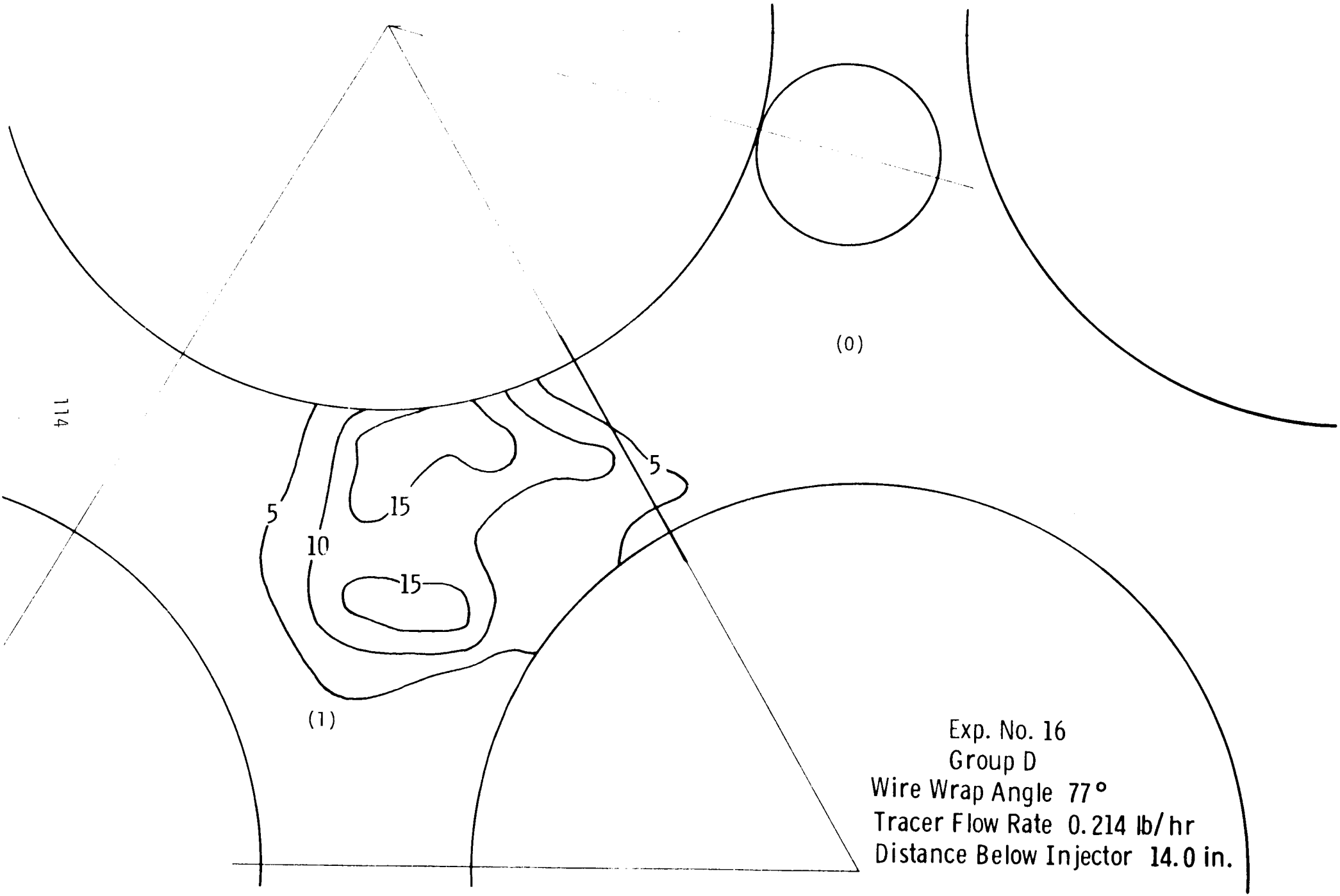

Fig. B-16—Tracer distribution no. 16

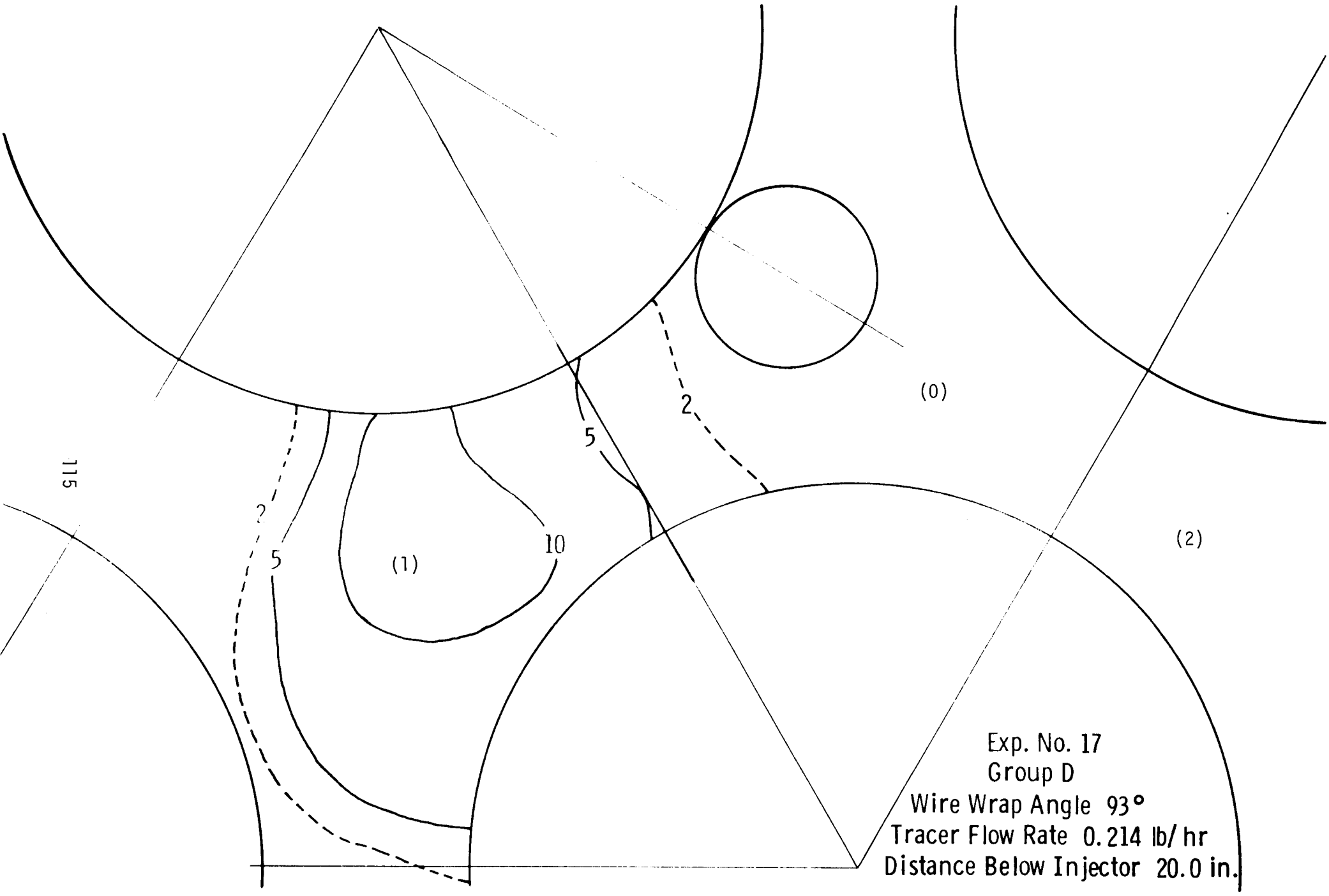

Fig. B-17—Tracer distribution no. 17

Dwg. 1673B80

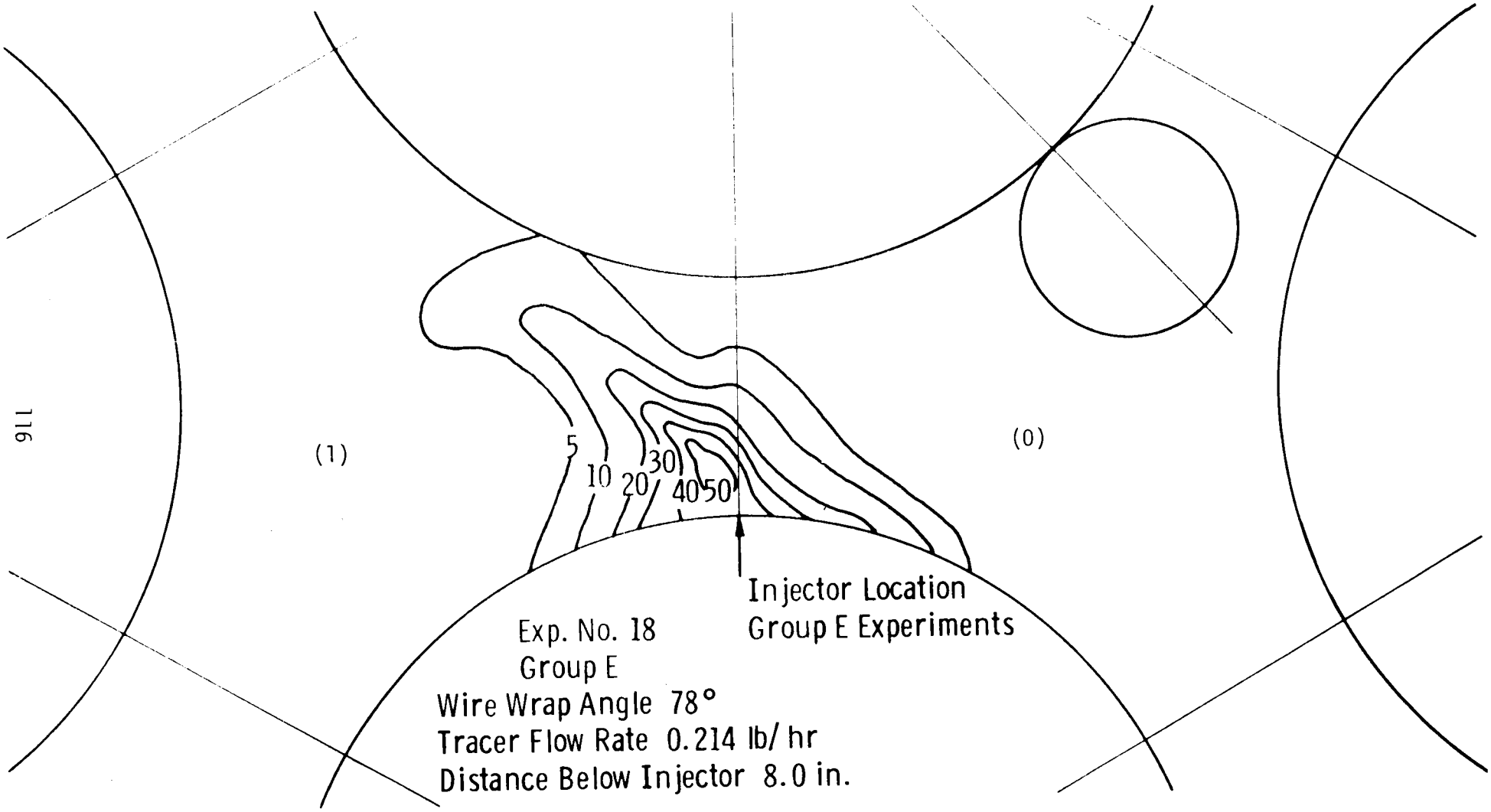

Fig. B-18—Tracer distribution no. 18

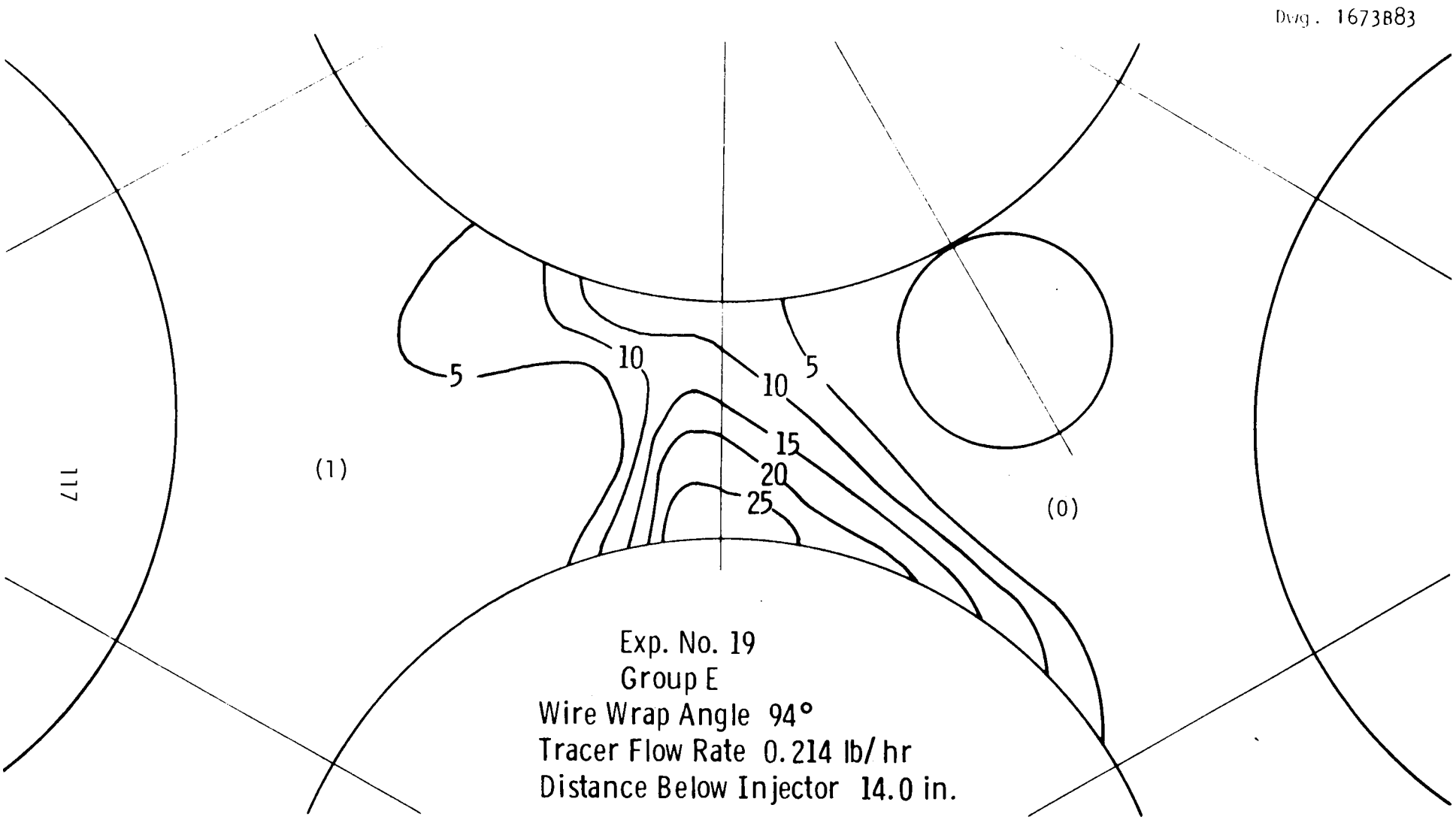

Fig. B-19—Tracer distribution no. 19

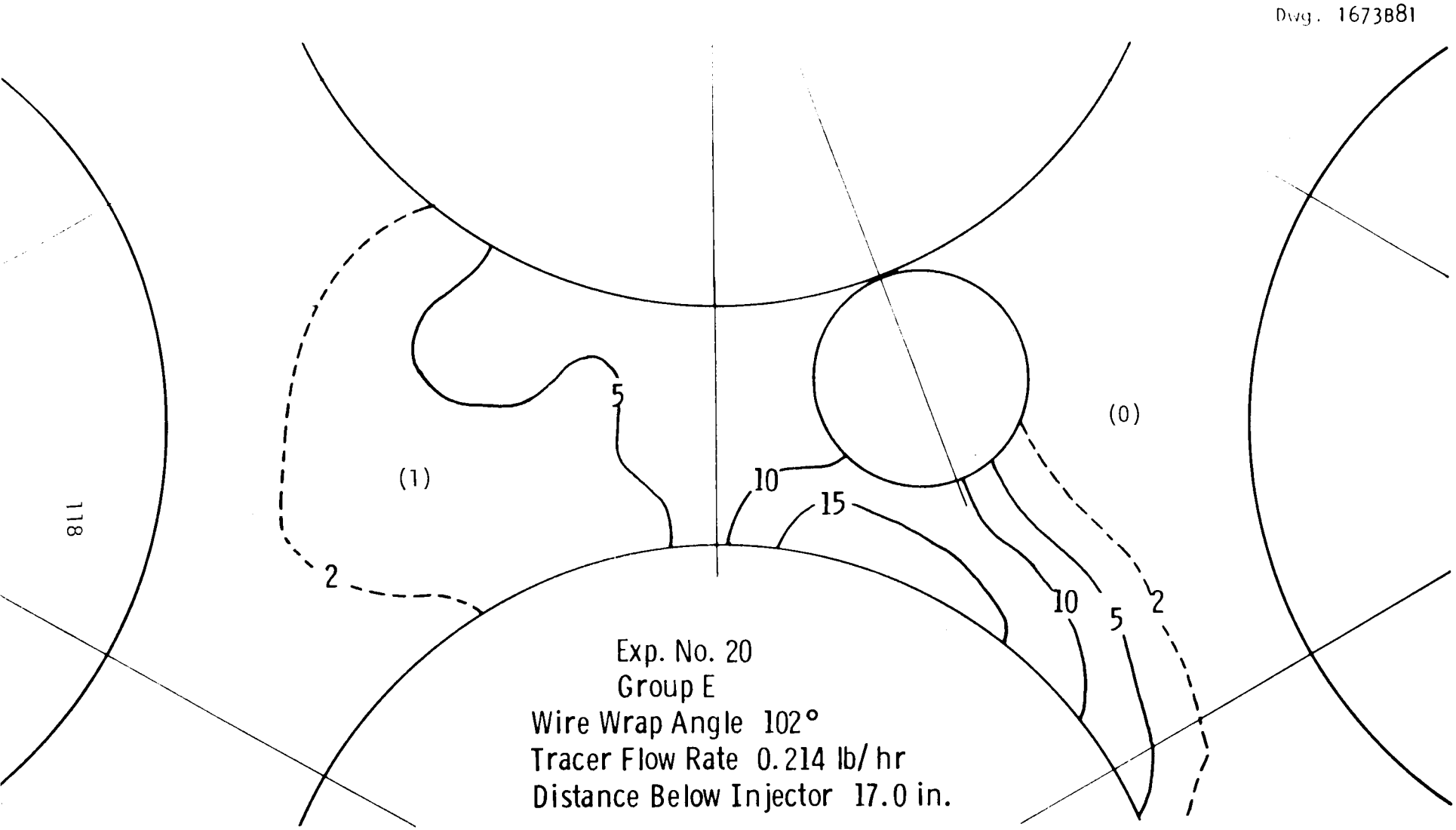

Fig. B-20—Tracer distribution no. 20

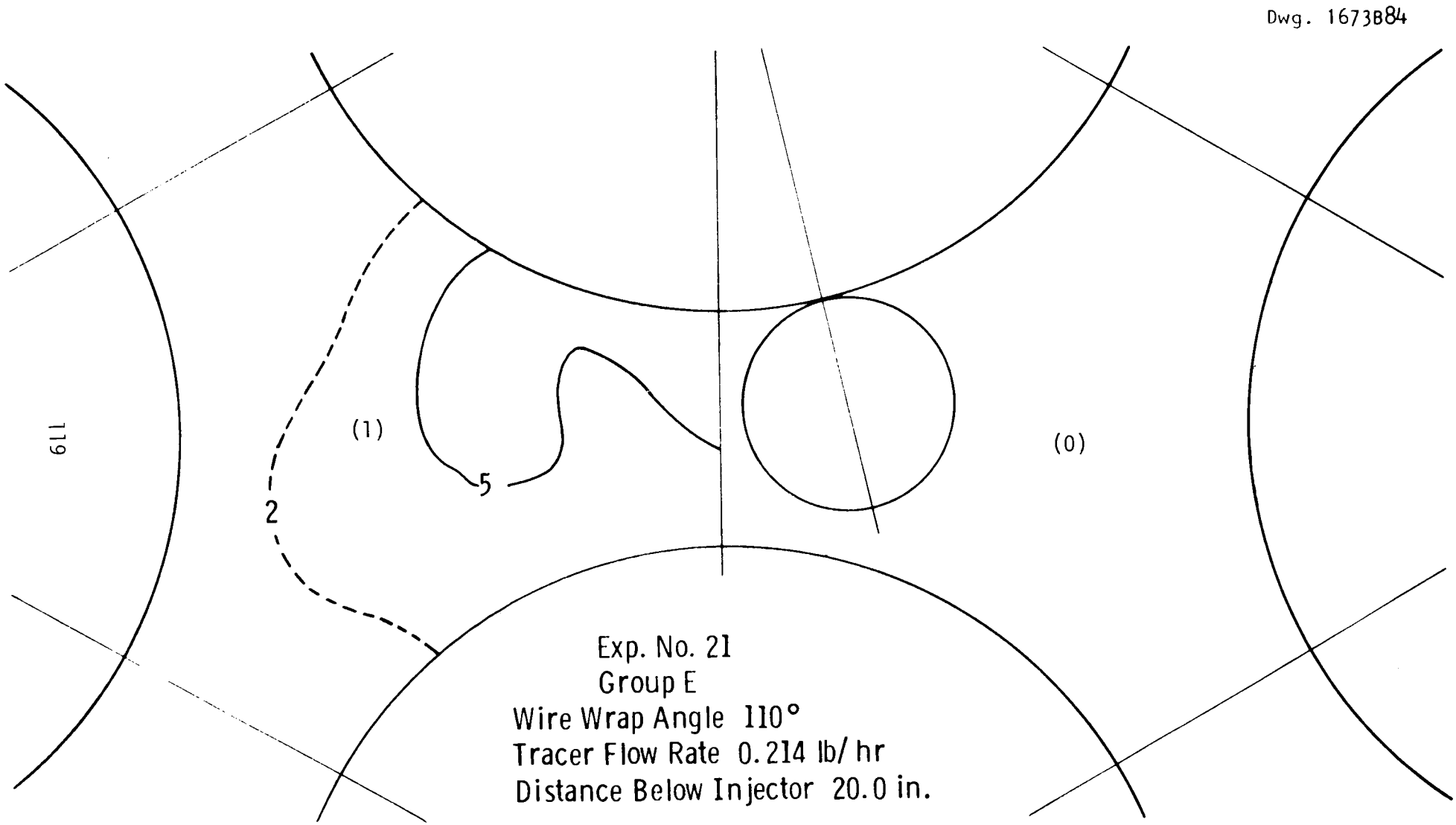

Fig. B-21—Tracer distribution no. 21

APPENDIX C

DERIVATION OF CONTINUITY OF MASS CORRELATION FOR GAP CROSSFLOW (Equation 15)

PROBLEM: To prove the continuity of mass correlation

$$\overline{\phi}(\alpha + 120) = \overline{\phi}(\alpha + 60) - \overline{\phi}(\alpha)$$

as it applies to the interior subchannels of a wire wrapped bundle.

ASSUMPTIONS:

1) Conservation of mass in subchannel (0) (see Figure C-1)
2) Constant fluid density, ρ
3) Constant average axial flow, $\overline{u}$
4) Uniform gap widths
5) The wire wrap has zero cross-sectional area and displaces zero volumn

CONVENTIONS:

1) Crossflow $\overline{V}$ out of subchannel (0) is positive
2) Crossflow $\overline{V}$ into subchannel (0) is negative
3) Angles α and α' are measured clockwise from base direction $\overline{DE}$ (see Figure C-1)
4) Subscripts refer to gaps in Figure C-1
5) θ equals the constant angle of the wire wrap centerline with respect to the rod axis

DERIVATION:

$$\rho\overline{V}_C(\alpha') + \rho\overline{V}_V(\alpha') + \rho\overline{V}_A(\alpha) = 0 \qquad \text{Conservation of Mass}$$

This statement relies on the simplifying assumptions of no volumetric displacement of fluid by the wire wrap and an average axial velocity constant at all axial locations.

$$\bar{\phi}_C(\alpha') + \bar{\phi}_V(\alpha') + \bar{\phi}_A(\alpha) = 0 \qquad \text{Divide by } \rho\bar{U}\tan\theta$$

or $$\bar{\phi}_C(\alpha') = -[\bar{\phi}_B(\alpha') + \bar{\phi}_A(\alpha)]$$

$$\bar{\phi}_C(\alpha') = -\bar{\phi}_A(\alpha - 120°) \qquad \text{Geometric Symmetry}$$

$$\bar{\phi}_B(\alpha') = -\bar{\phi}_A(\alpha - 60°) \qquad \text{Geometric Symmetry}$$

These last two statements simply describe the relative orientation of the three gaps in terms of wire wrap angular displacement.

$$\bar{\phi}(\alpha - 120°) = \bar{\phi}(\alpha - 60°) - \bar{\phi}(\alpha) \qquad \text{Substitution and Dropping of Subscript}$$

$$\bar{\phi}(\alpha) = -\bar{\phi}(\alpha + 180°) \qquad \text{Geometric Symmetry}$$

$$-\bar{\phi}(\alpha + 60°) = -\bar{\phi}(\alpha + 120°) - \bar{\phi}(\alpha) \qquad \text{Substitution}$$

or $$\bar{\phi}(\alpha + 120°) = \bar{\phi}(\alpha + 60°) - \bar{\phi}(\alpha) \qquad \text{Q.E.D.}$$

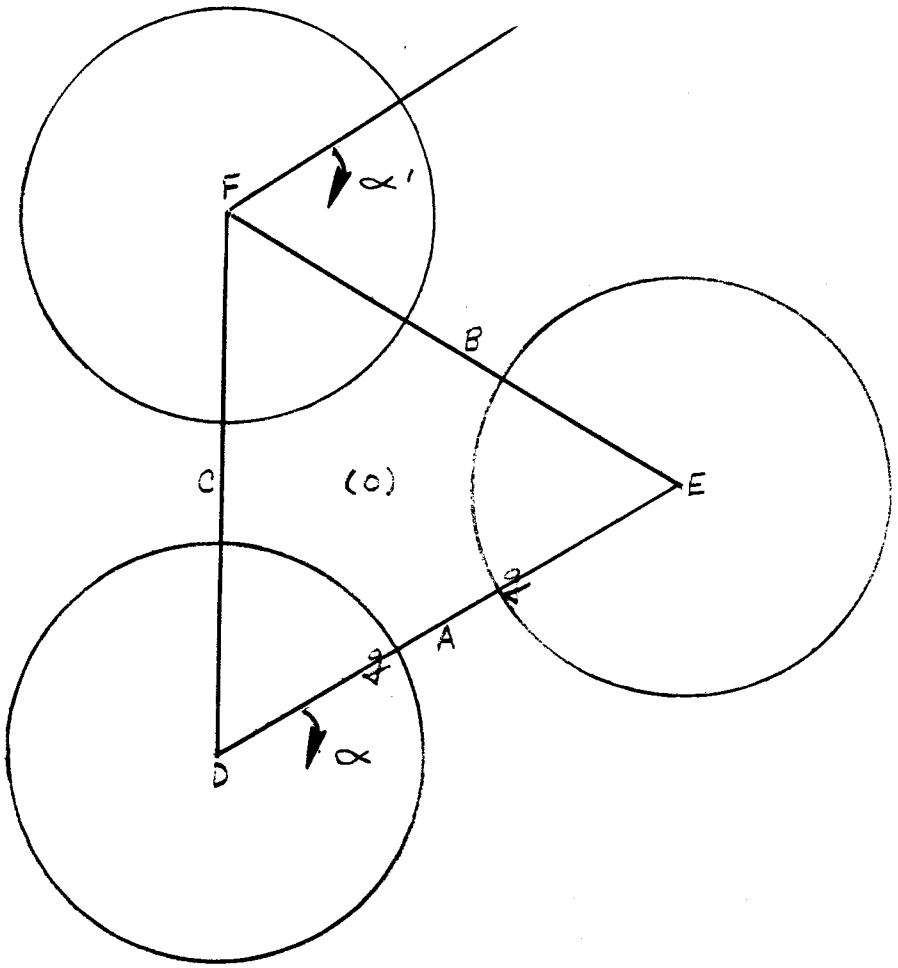

FIGURE C-1

SUBCHANNEL CONFIGURATION

APPENDIX D

GAP CROSSFLOW PROFILES

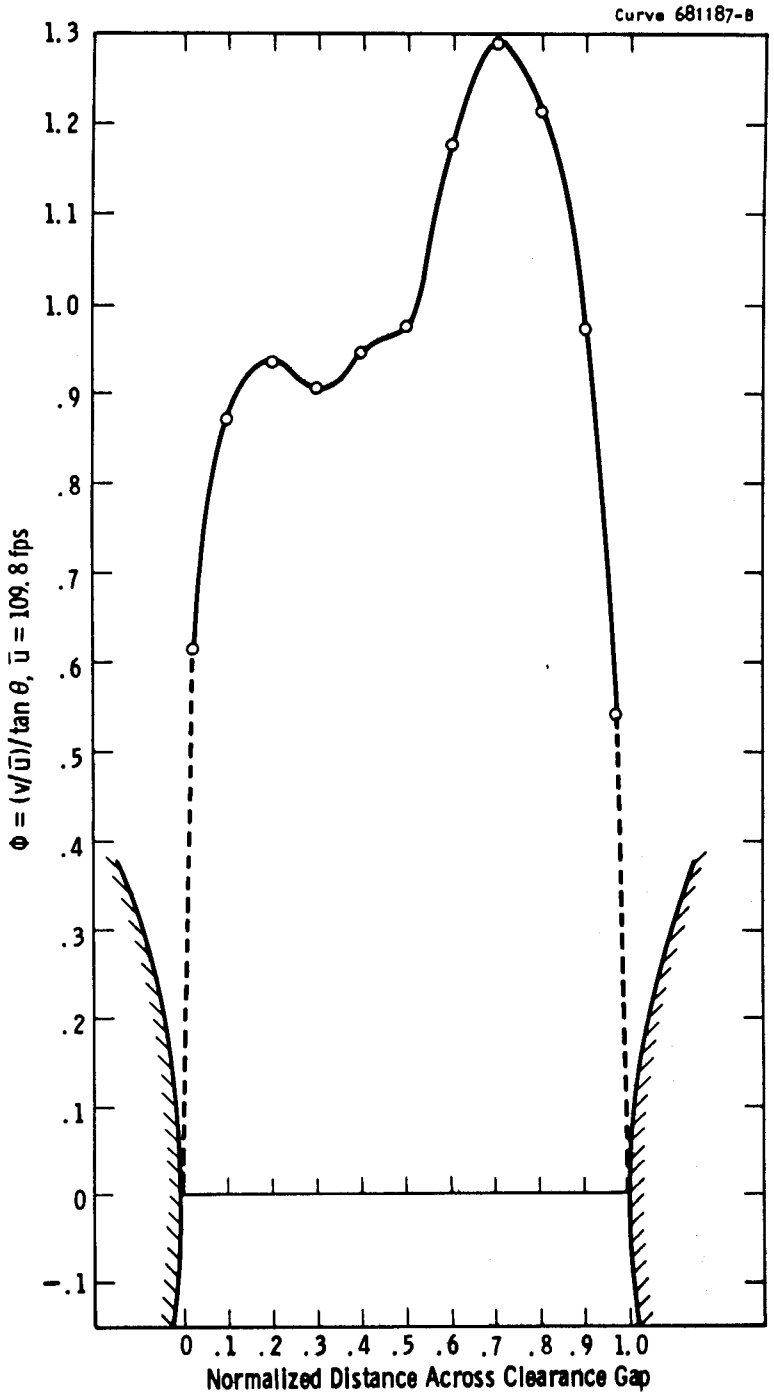

FIG. D-1 ϕ - PROFILE AT α = 10°

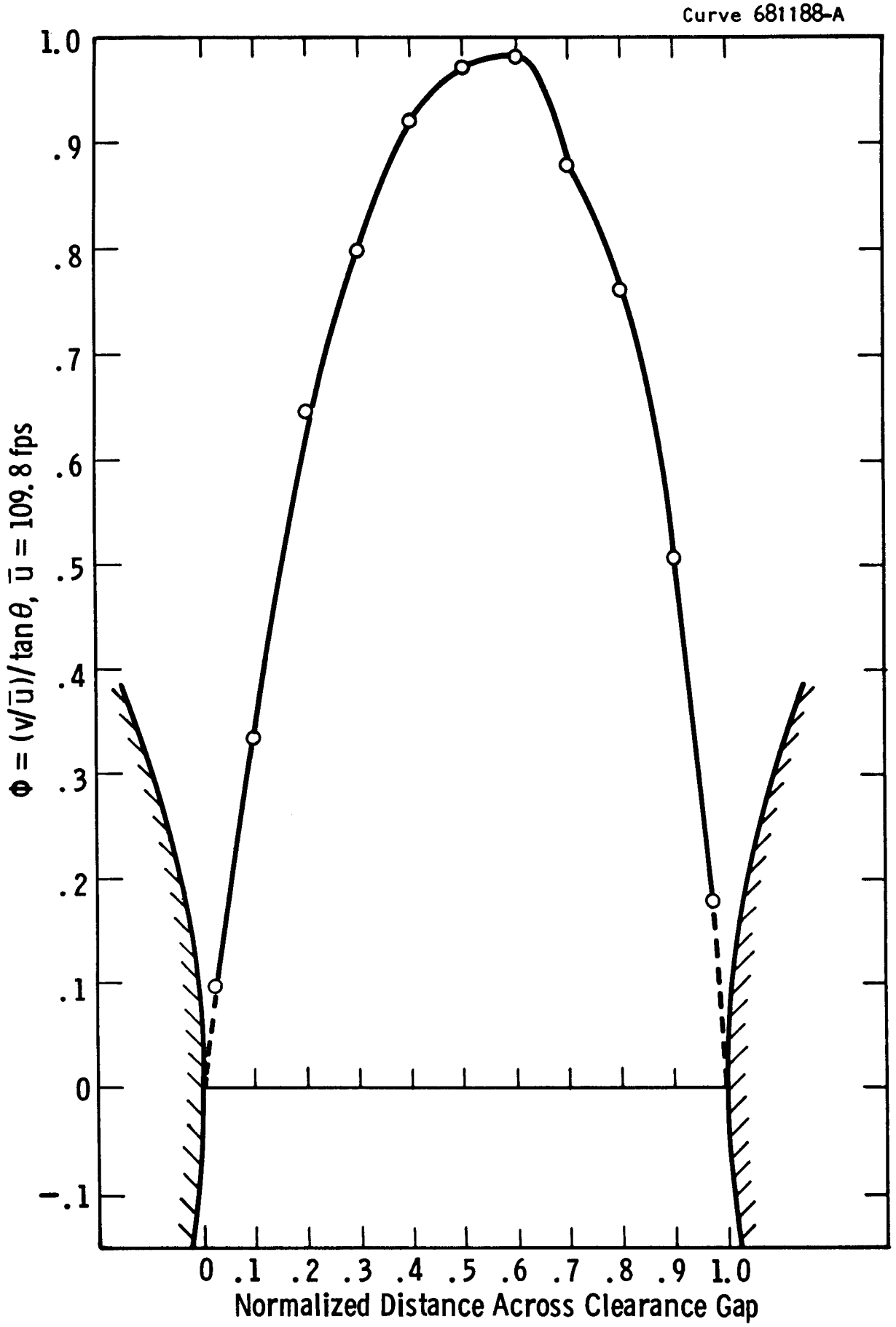

FIG. D-2 ϕ-PROFILE AT α = 16°

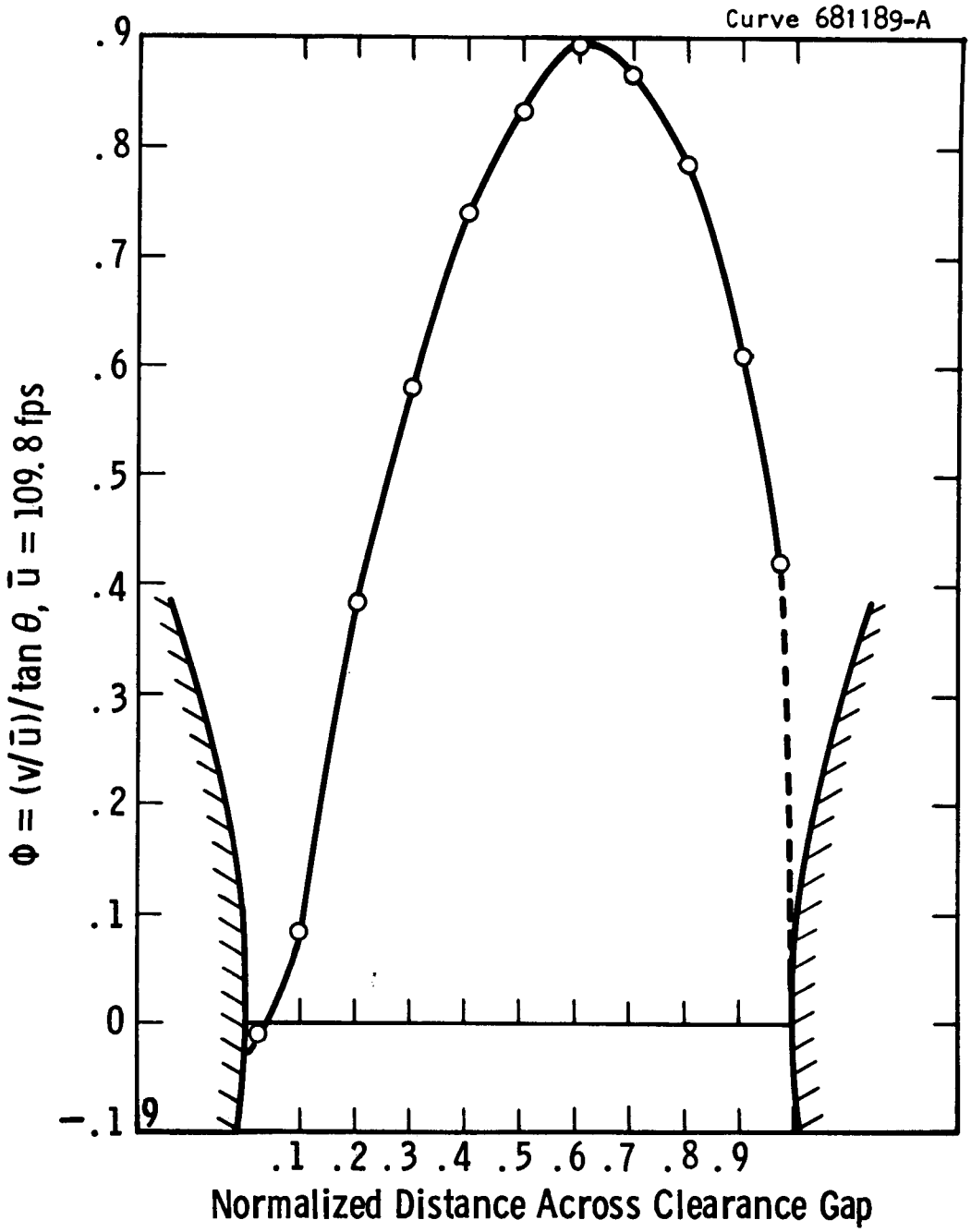

FIG. D-3 ϕ-PROFILE AT $\alpha = 24°$

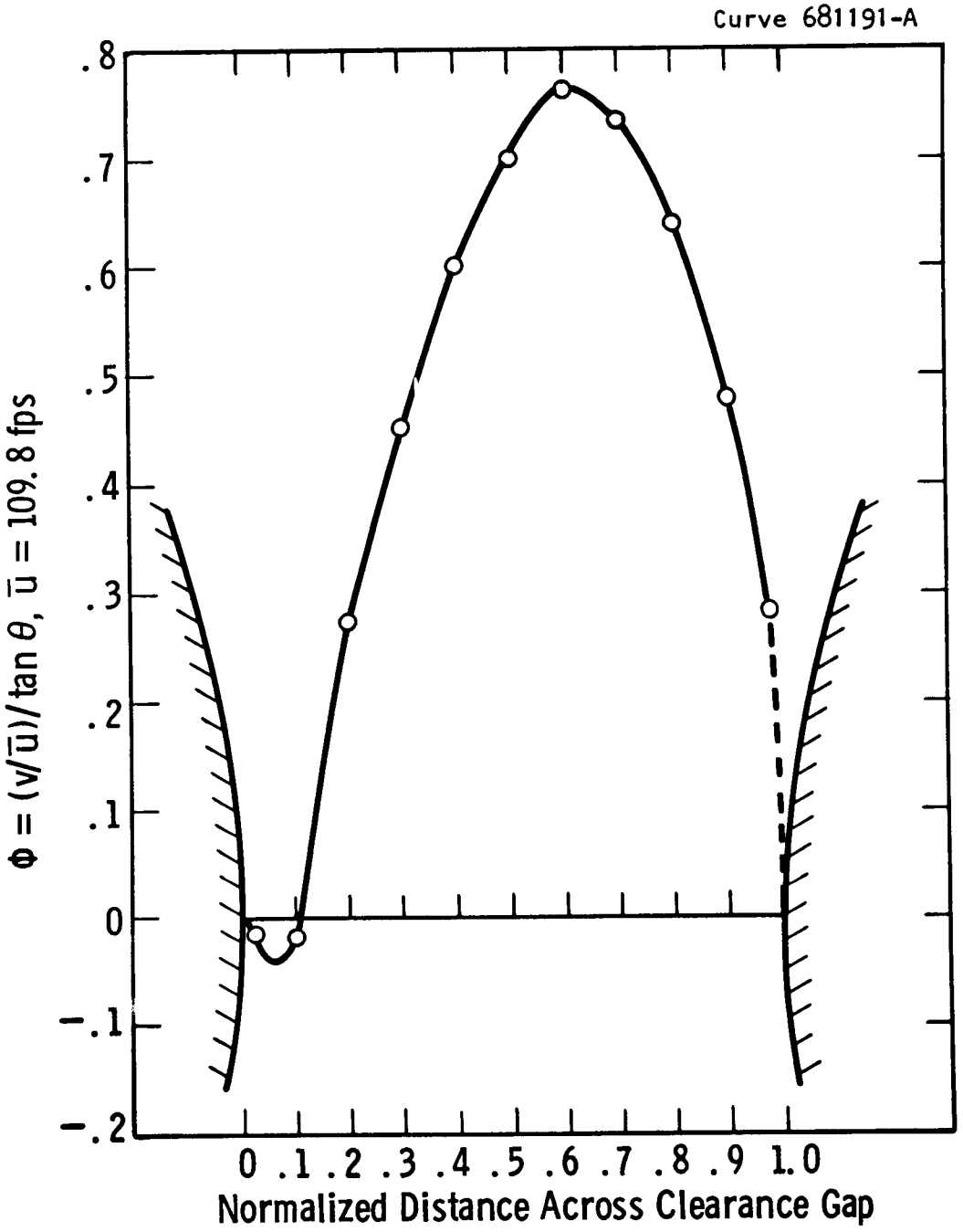

FIG. D-4 ϕ-PROFILE AT α = 32°

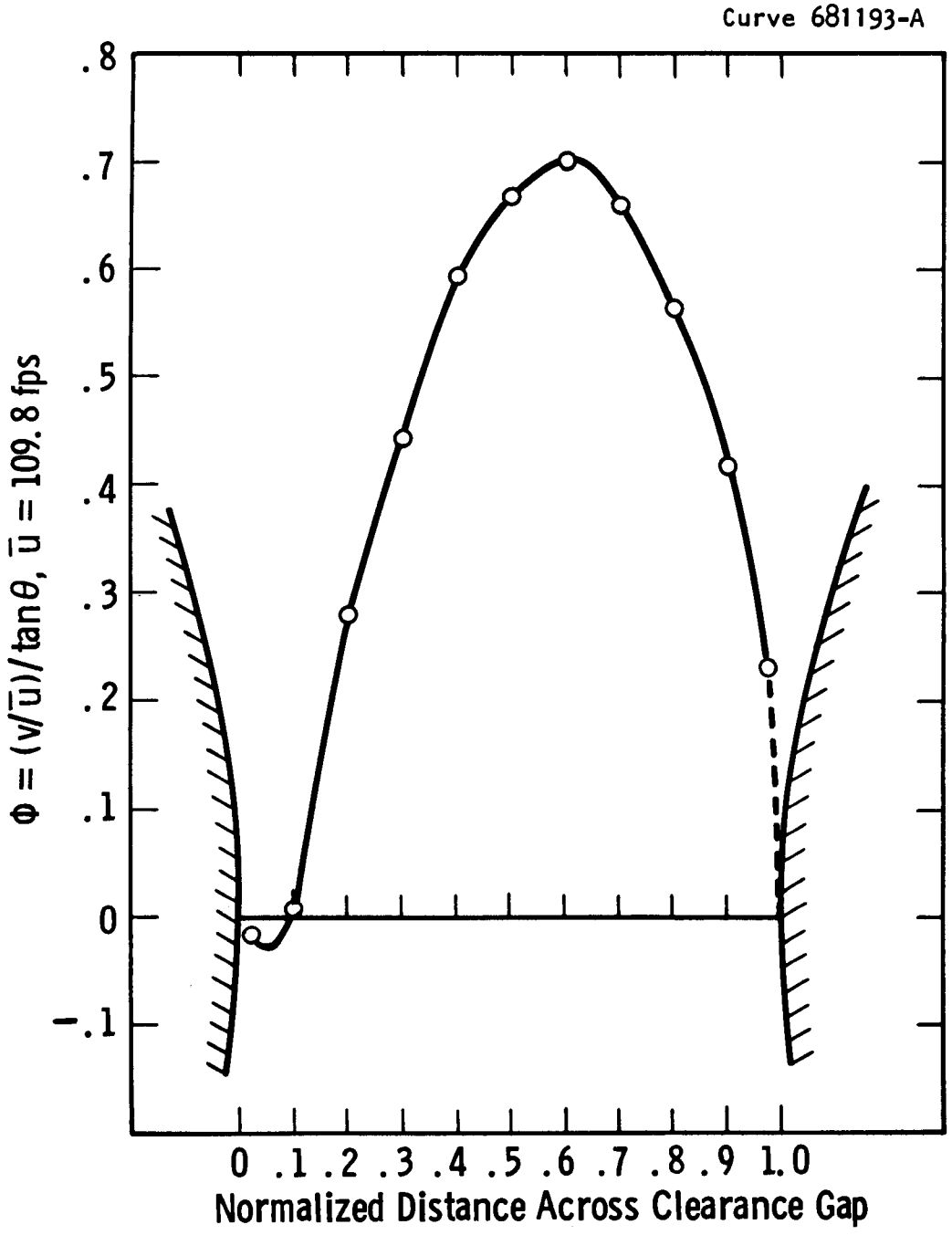

FIG. D-5 ϕ-PROFILE AT α = 40°

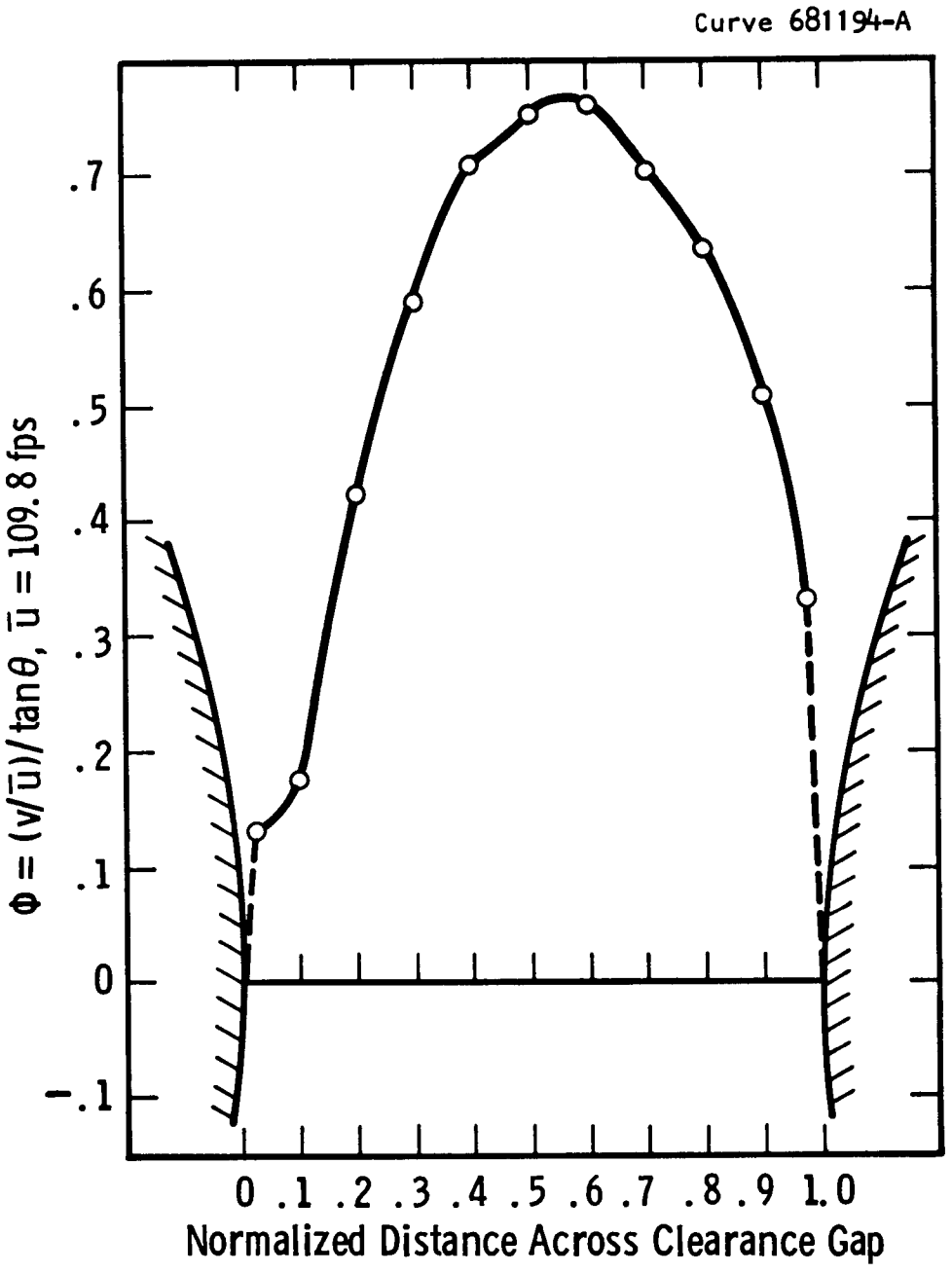

FIG. D-6 ϕ-PROFILE AT α =48°

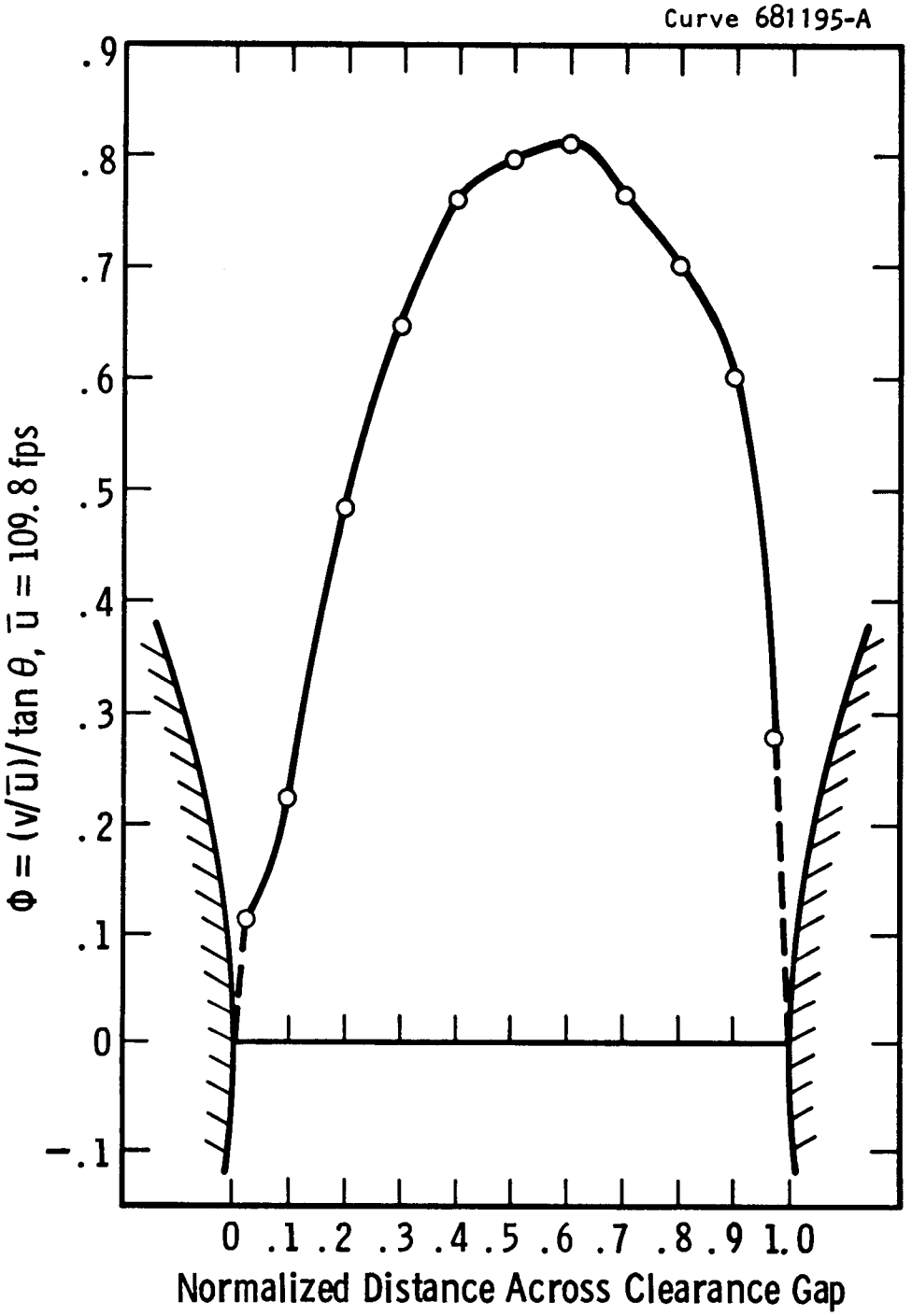

FIG. D-7 ϕ-PROFILE AT $\alpha = 56°$

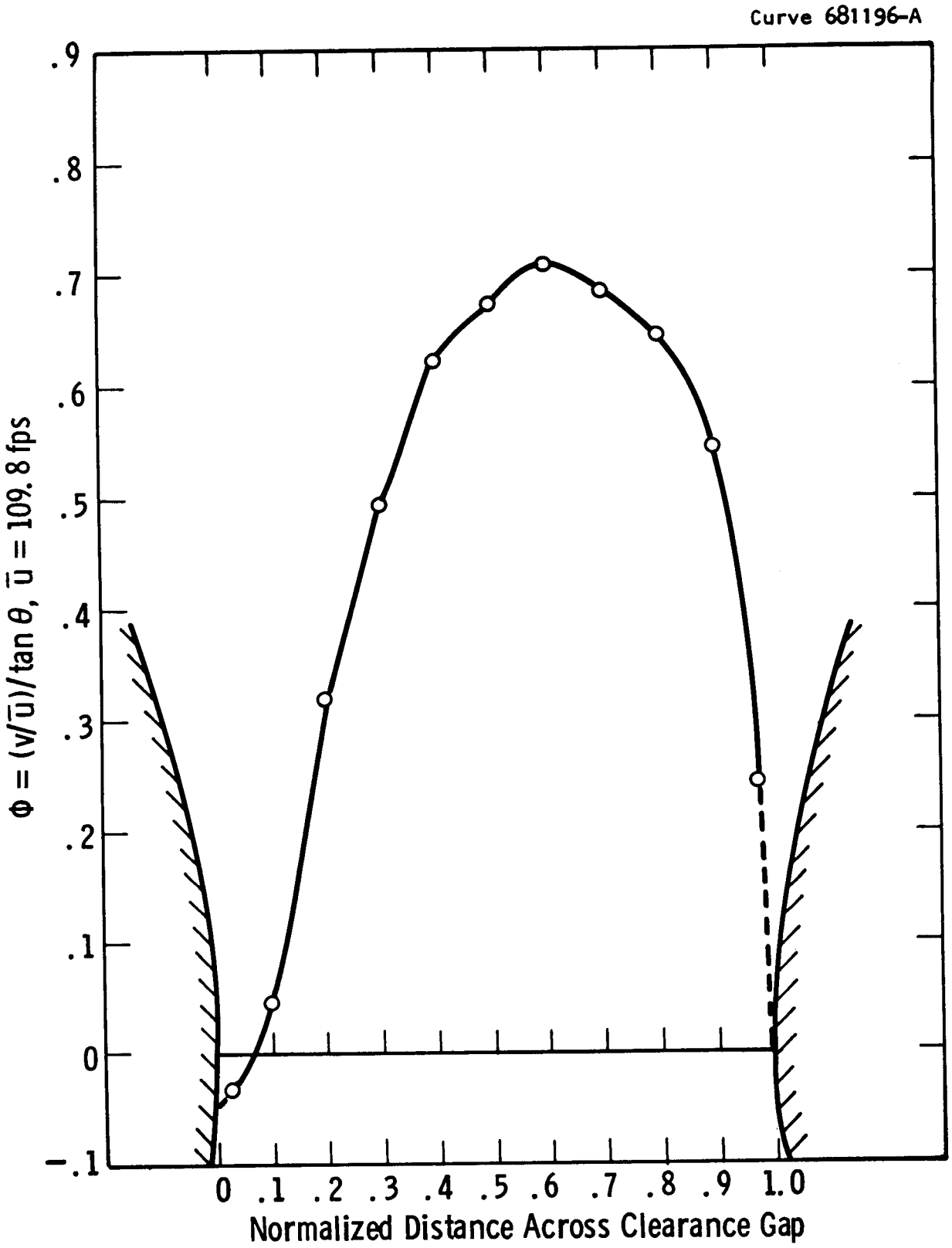

FIG. D-8 ϕ-PROFILE AT $\alpha = 64°$

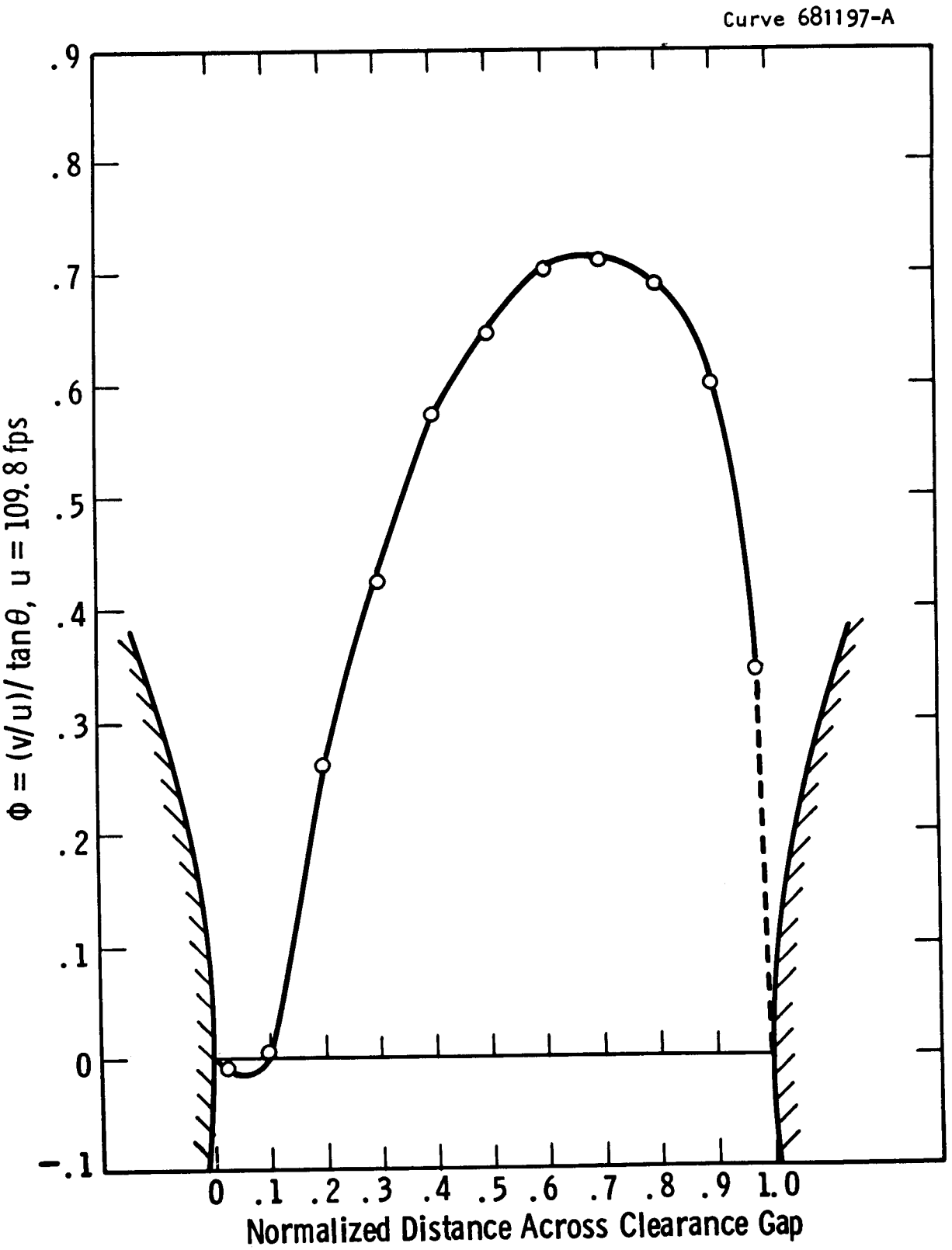

FIG. D-9 ϕ-PROFILE AT α =72°

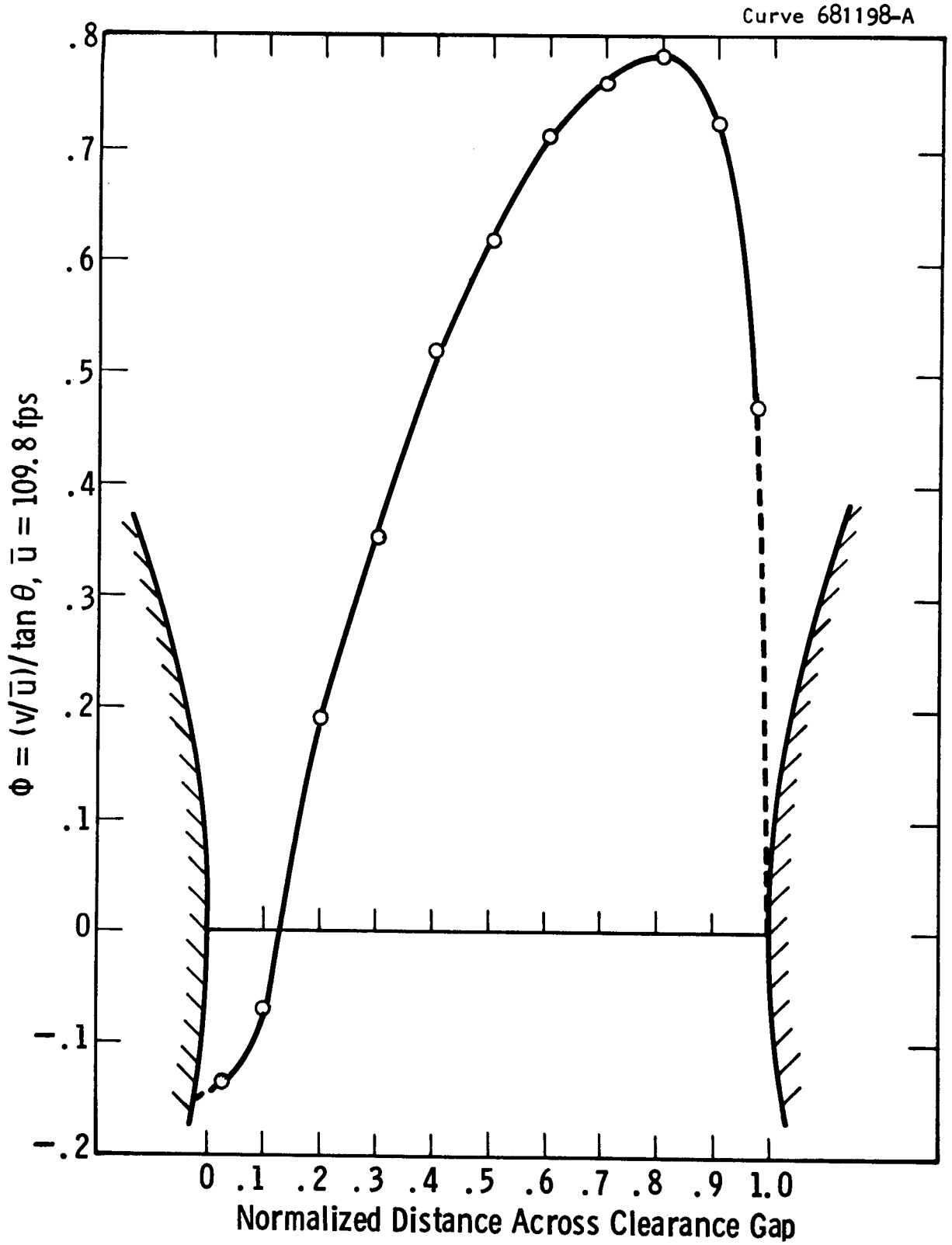

FIG. D-10 ϕ-PROFILE AT α = 80°

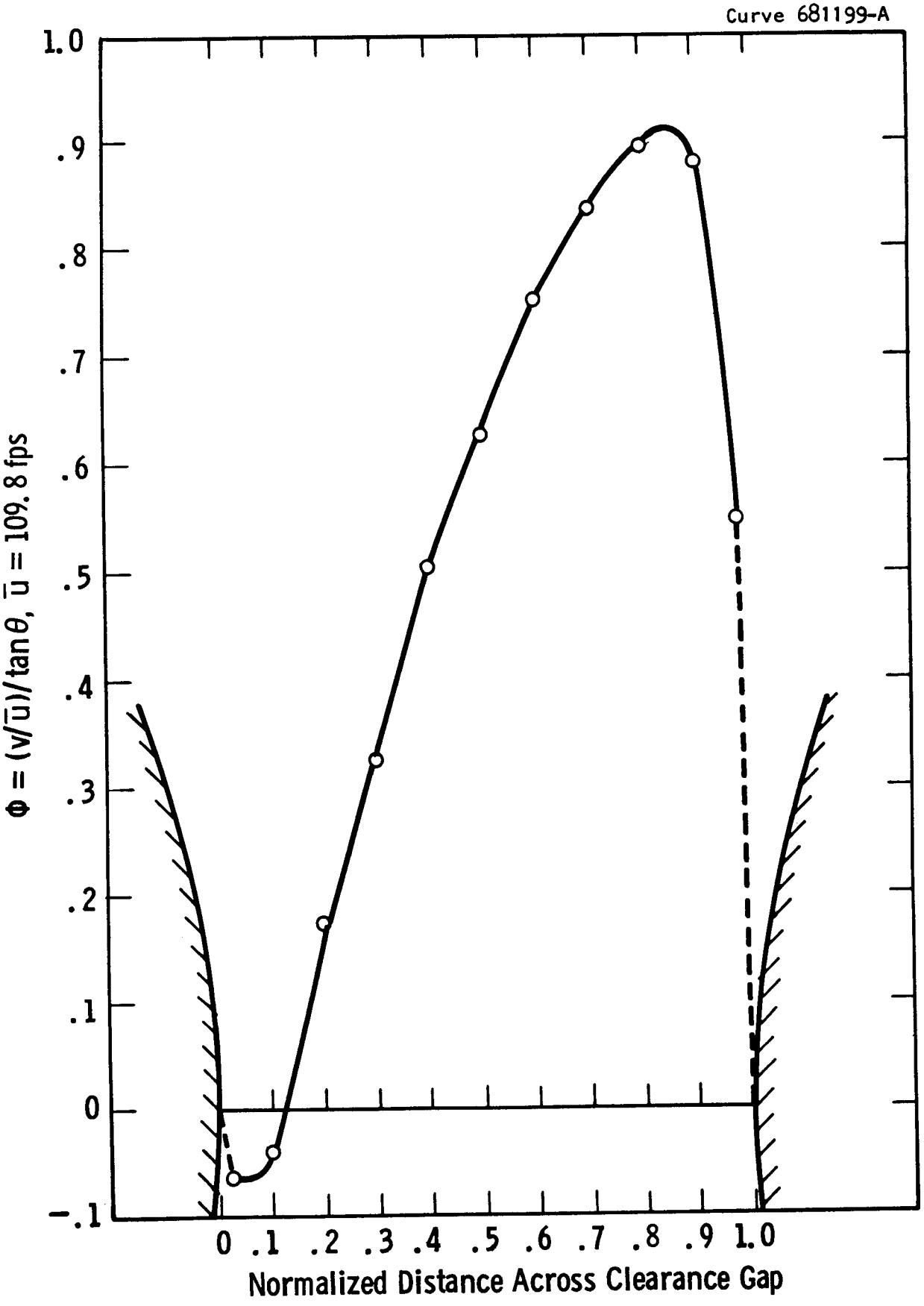

FIG. D-11 ϕ-PROFILE AT α = 88°

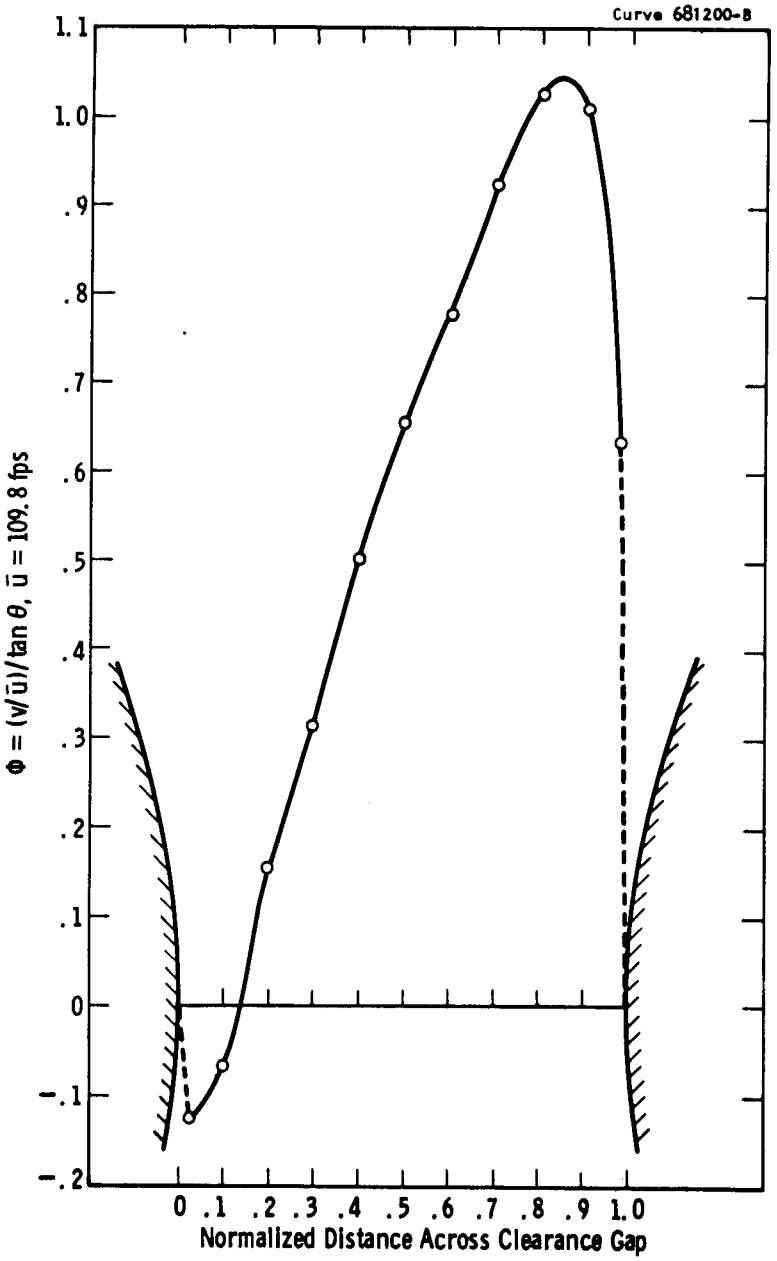

FIG. D-12 Φ-PROFILE AT α = 96°

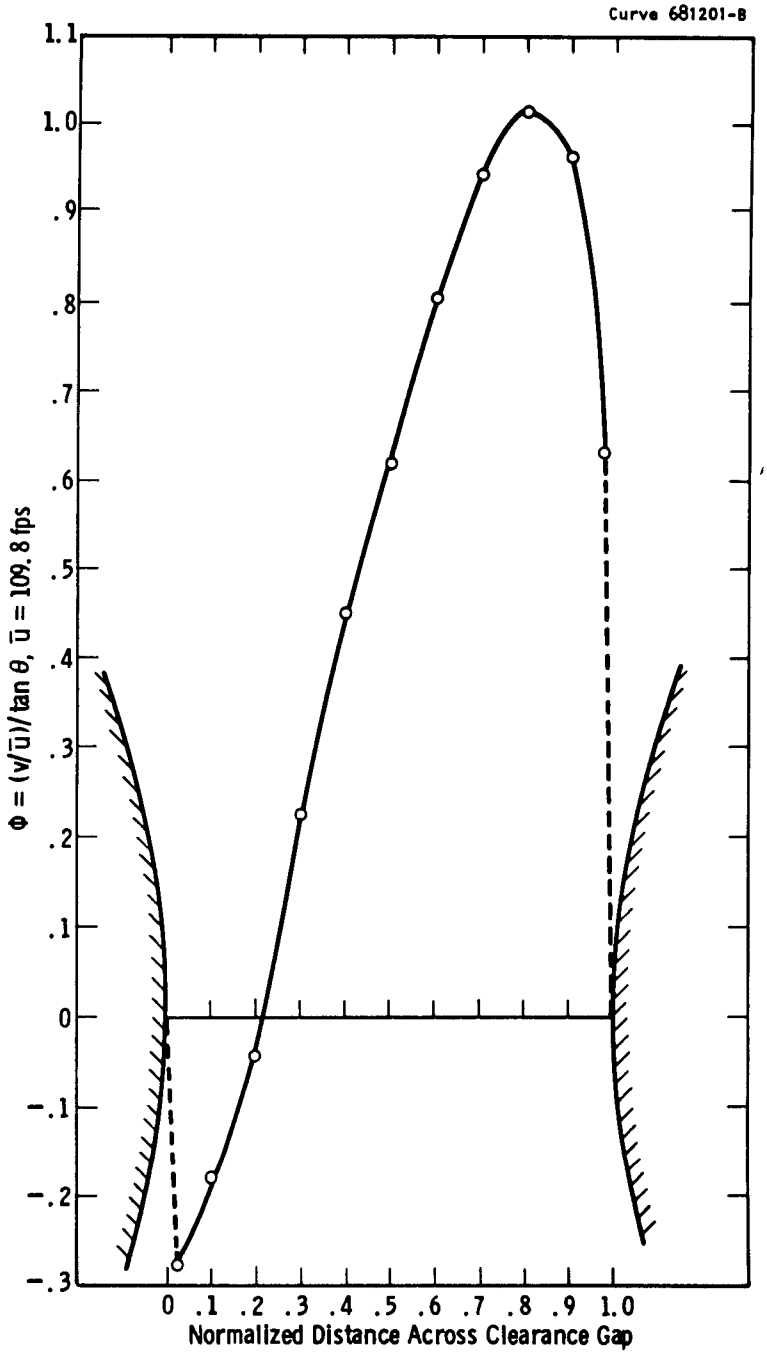

FIG. D-13 ϕ-PROFILE AT α = 104°

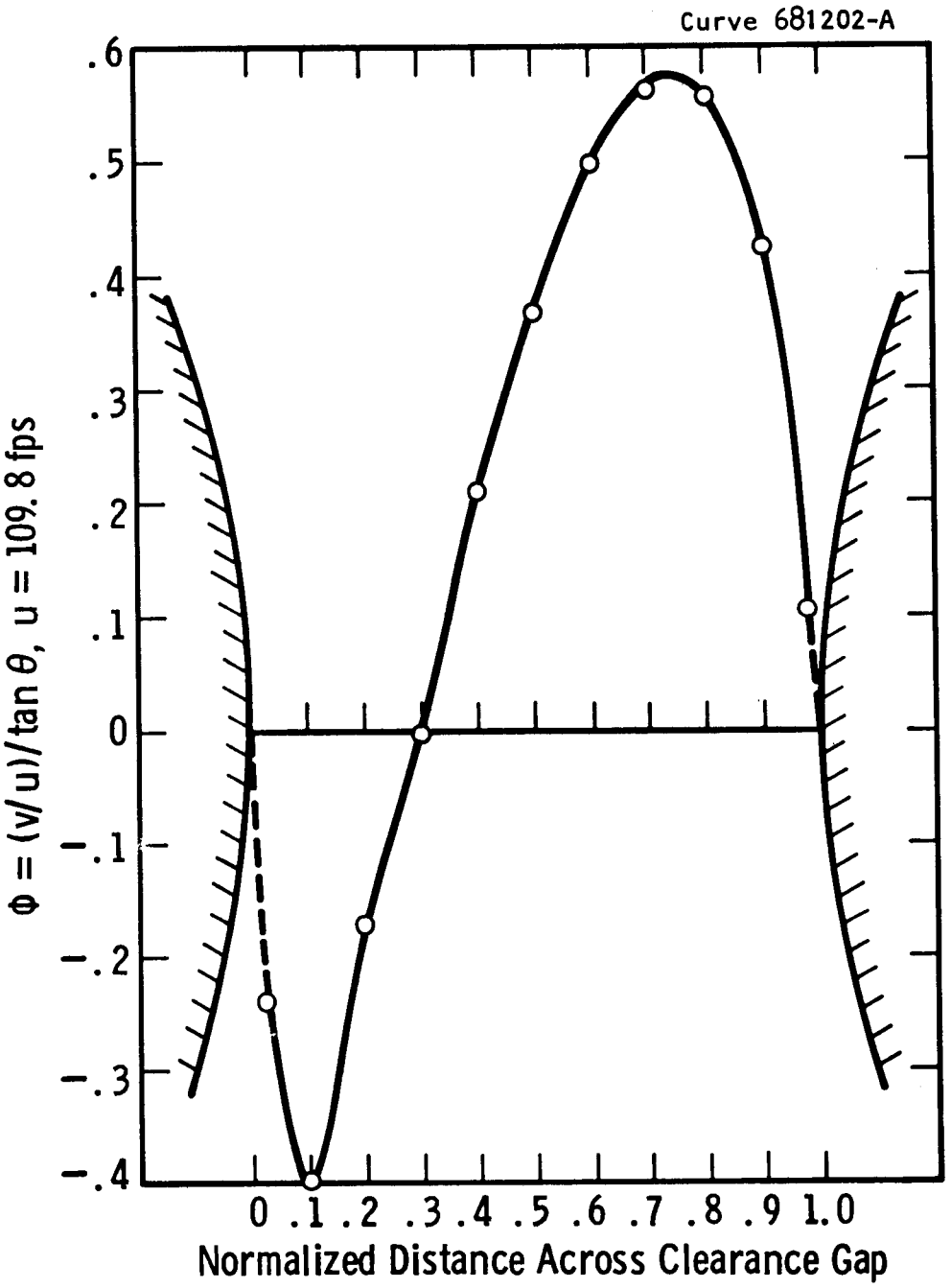

FIG. D-14 ϕ-PROFILE AT $\alpha = 112°$

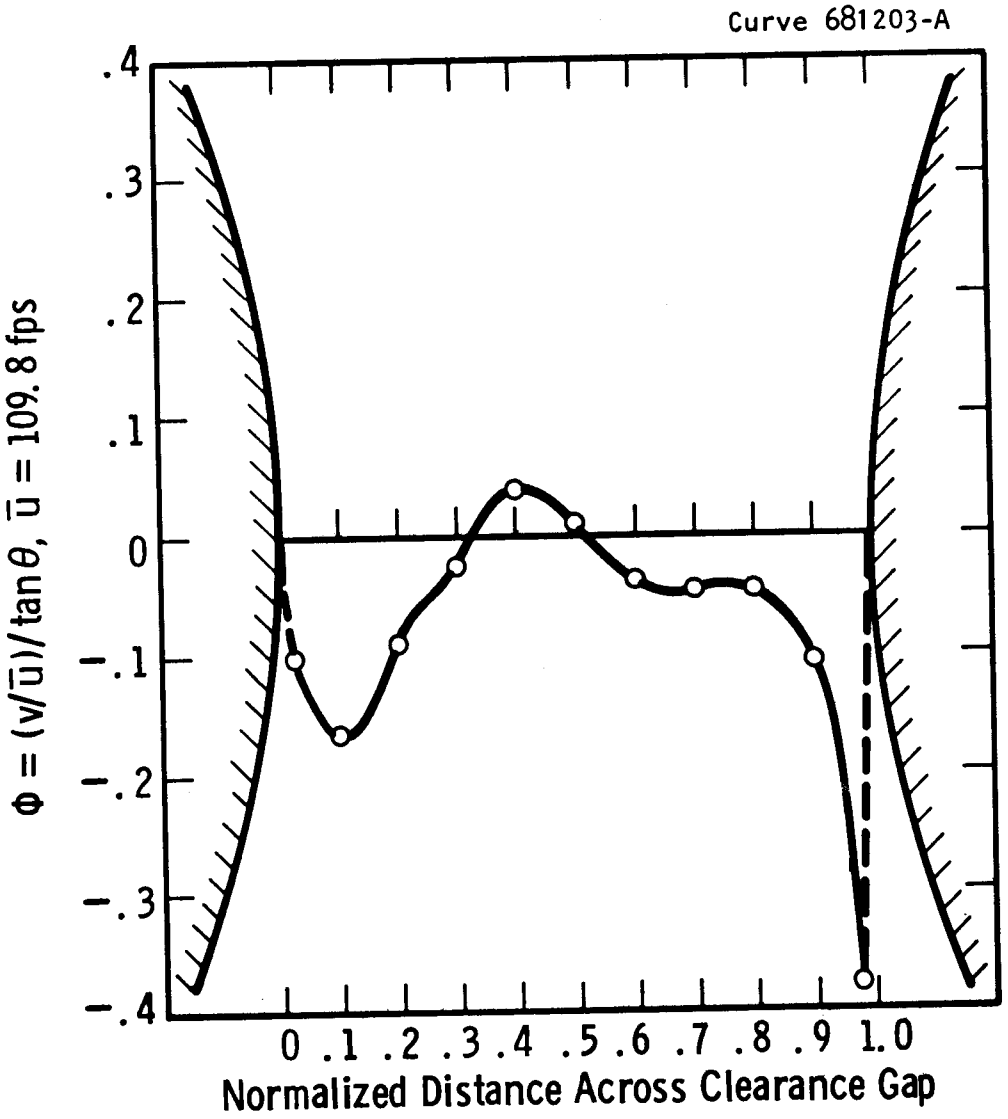

FIG. D-15 ϕ-PROFILE AT α = 117°

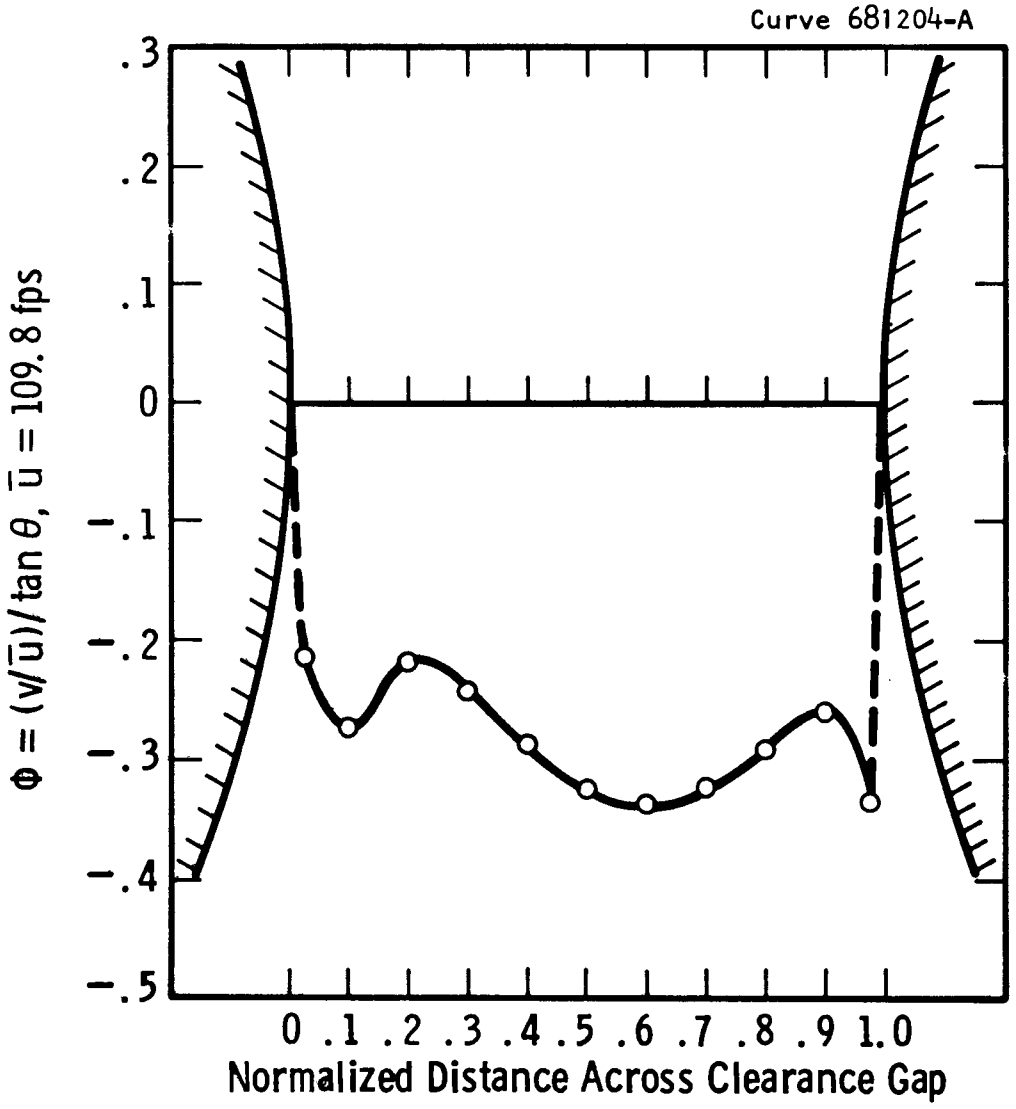

FIG. D-16 ϕ-PROFILE AT α = 120°

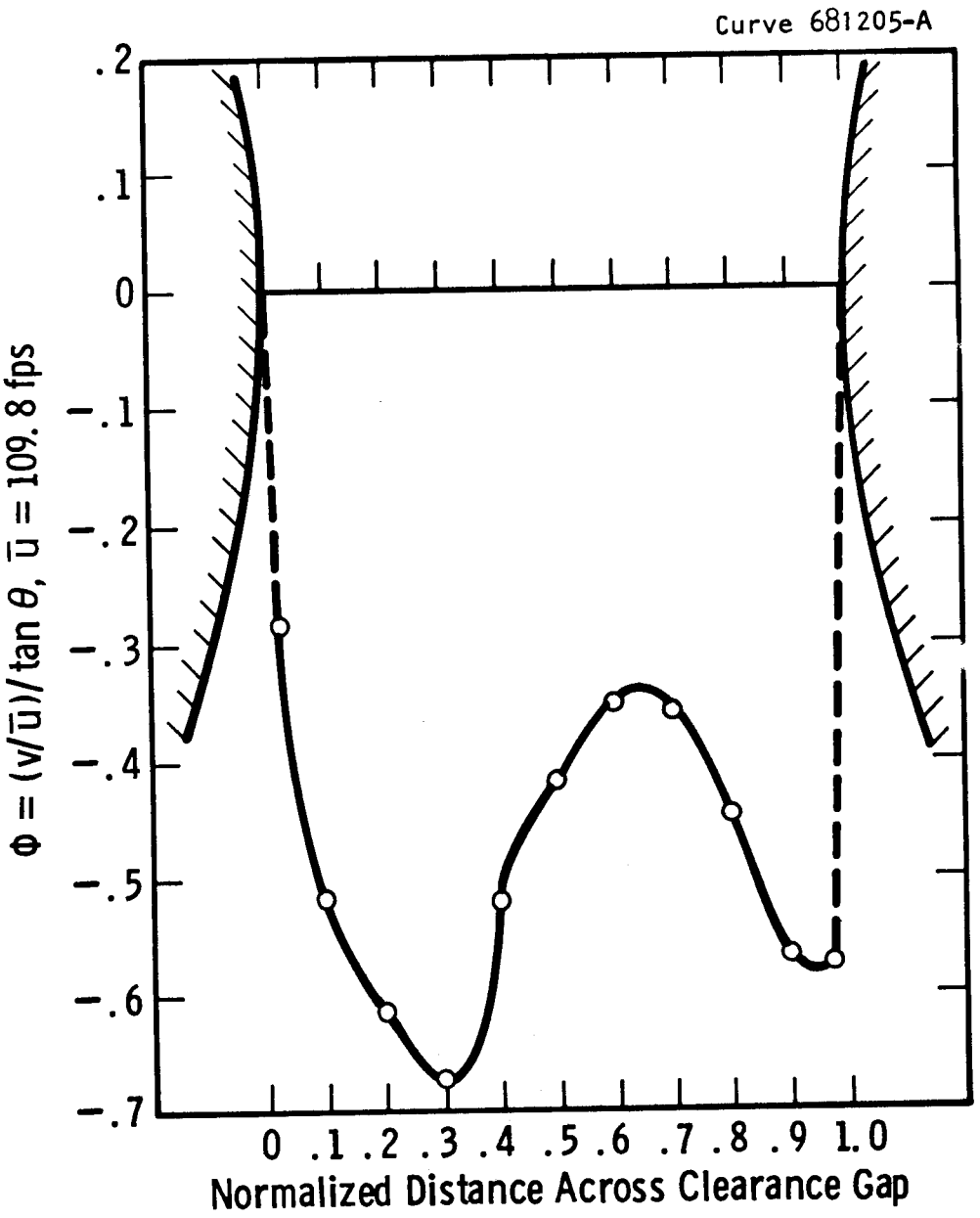

FIG. D-17 ϕ-PROFILE AT α = 128°

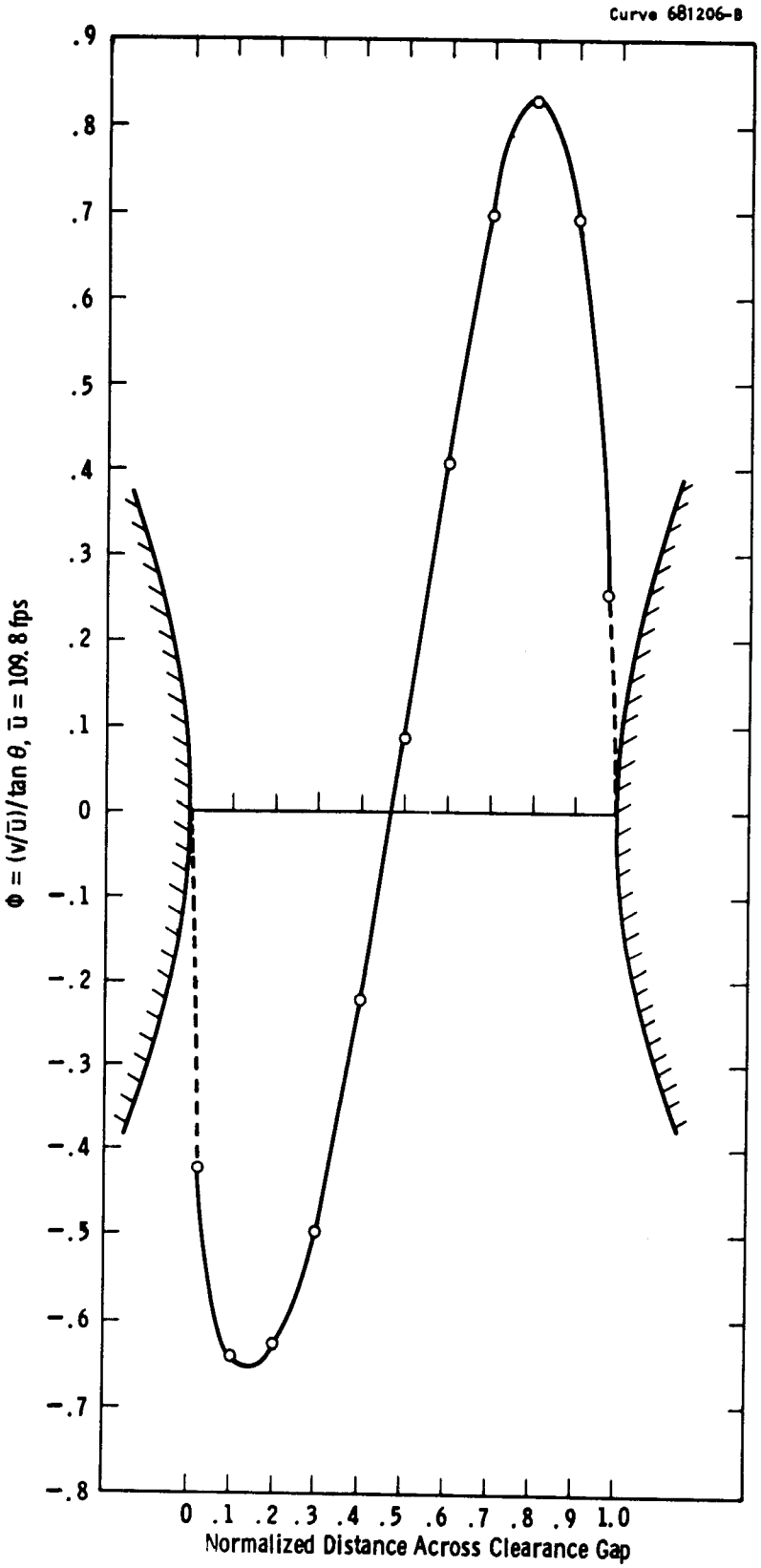

FIG. D-18 Φ-PROFILE AT α =136°

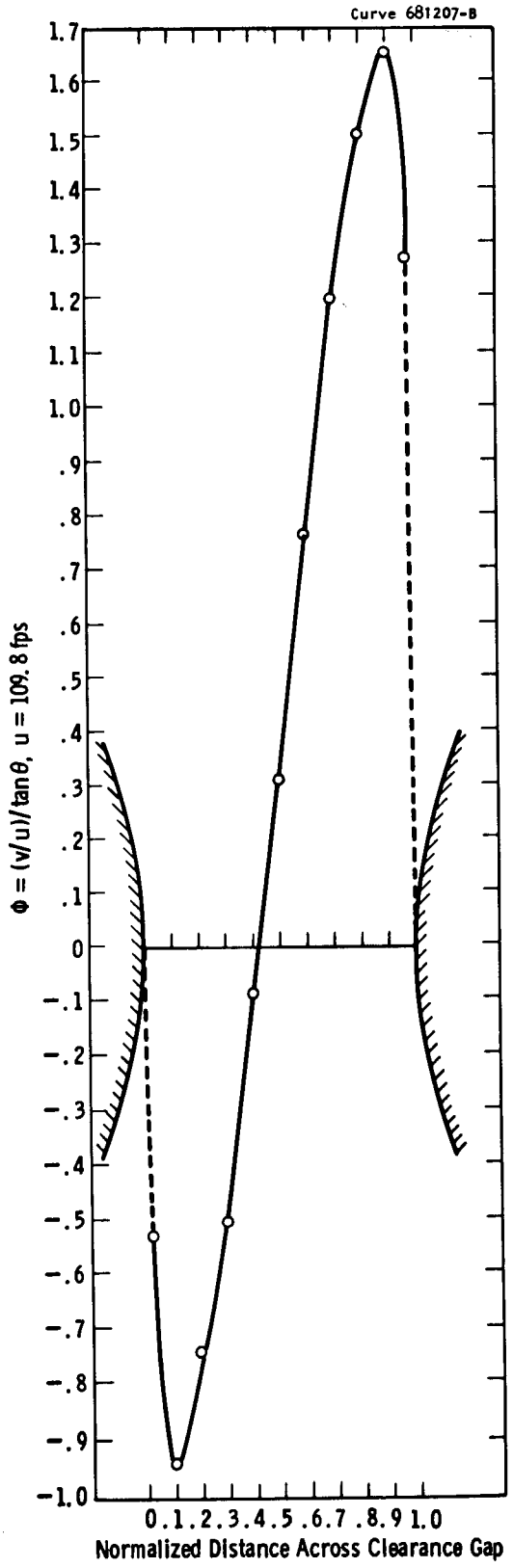

FIG. D-19 Φ-PROFILE AT α = 144°

APPENDIX E

DERIVATION OF AXIAL FLOW RELATIONSHIP AS A FUNCTION OF GAP CROSSFLOW (Equation 16)

PROBLEM: To derive the following empirical relationship of axial flow and gap crossflow data:

$$U(\alpha) = \frac{1}{A_c(\alpha)} \{C + \frac{P\tan\theta}{2\pi} \int_0^{\alpha} [\sum_{j=1}^{3} \overset{\sim}{\phi}_j(\alpha)\ Sgj(\alpha)]d\alpha\}$$

where α = angular displacement of wire wrap, radians

$U(\alpha)$ = normalized axial flow in average subchannel

$u(\alpha)$ = axial flow in average subchannel

$A_c(\alpha)$ = cross-sectional area of average subchannel, in^2

C = constant of integration

P = wire wrap lead, in.

θ = constant angle of wire wrap centerline from rod bundle axis, 4.33°

$\overset{\sim}{\phi}_j(\alpha)$ = as-measured gap crossflow in j^{th} gap, dimensionless

$Sgj(\alpha)$ = unobstructed gap width of j^{th} gap.

ASSUMPTIONS:

1) Conservation of mass in an axial increment dx of an average interior subchannel.
2) Constant fluid density, ρ.
3) Uniform gap widths, wire wrap diameters, rod diameters, wire wrap pitch.

CONVENTIONS:

1) The function $\overset{\sim}{\phi}_j(\alpha)$ for measured gap crossflow in the j^{th} gap is determined by replotting the curve of Figure 5-4 <u>through</u> the data points to account for fluid displacement and gap obstruction by the phased wire wraps and are adjusted for a local $\bar{u}$ = 104.5 ft/sec rather than 109.8 ft/sec. The functions $\overset{\sim}{\phi}_j(\alpha)$ are the same curve for each gap but phased according to the passage of wire wraps through the gap.

2) The function $Sgj(\alpha)$ for unobstructed gap width of the j^{th} gap is similarly phased for each gap according to passage of wire wraps through the gap.

3) Initial location ($\alpha = 0$) of the in-phase wire wraps is chosen so that one wire wrap is centered in one gap of the subchannel.

4) Configuration of the axial increment of the subchannel is as shown in Figure E-1.

5) The gap crossflow $\bar{v}_{gj}(\alpha)$ in ft/sec is calculated from $\tilde{\phi}_j(\alpha)$ by the relationship

$$\tilde{\phi}_j(\alpha) = \frac{\bar{v}_{gj}(\alpha)\tan\theta}{\bar{u}}$$

for $\bar{u} = 104.5$ ft/sec.

DERIVATION:

$$d[\rho u(\alpha)A_c(\alpha)] = [\sum_{j=1}^{3} \rho\, \bar{v}_{gj}(\alpha)\, Sgj(\alpha)]\, dx \qquad \text{Conservation of Mass.}$$

$$dx = (P/2\pi)\, d\alpha \qquad \text{Pitch of Wire Wrap.}$$

$$d[u(\alpha)A_c(\alpha)] = (P/2\pi)[\sum_{j=1}^{3} \bar{v}_{gj}(\alpha)Sgj(\alpha)]\, d\alpha \qquad \text{Substitution and Division by Constant } \rho.$$

$$\bar{v}_{gj}(\alpha) = \bar{u}\tan\theta\, \tilde{\phi}_j(\alpha) \qquad \text{Convention 5.}$$

$$d[u(\alpha)A_c(\alpha)] = \frac{\bar{u}\,P\tan\theta}{2\pi}[\sum_{j=1}^{3} \tilde{\phi}_j(\alpha)Sgj(\alpha)]d\alpha \qquad \text{Substitution.}$$

$$u(\alpha)A_c(\alpha) = C' + \frac{\bar{u}\,P\tan\theta}{2\pi}\int_o^{\alpha}[\sum_{j=1}^{3} \tilde{\phi}_j(\alpha)Sgj(\alpha)]d\alpha \qquad \text{Integration.}$$

$$U(\alpha) = \frac{u(\alpha)}{\bar{u}} = \frac{1}{A_c(\alpha)}\{C + \frac{P\tan\theta}{2\pi}\int_o^{\alpha}[\sum_{j=1}^{3} \tilde{\phi}_j(\alpha)Sgj(\alpha)]d\alpha\} \qquad \text{Division by } \bar{u}A_c(\alpha).$$

The constant C is determined by selecting the value for C which makes

$$\frac{1}{2\pi} \int_0^{2\pi} U(\alpha)\, d\alpha = 1.0.$$

Using the average dimensions of the measured subchannels for rod diameter, gap width, and wire wrap diameter, C is evaluated as 1.648 in^2 or 90.5% of the maximum subchannel cross-sectional area.

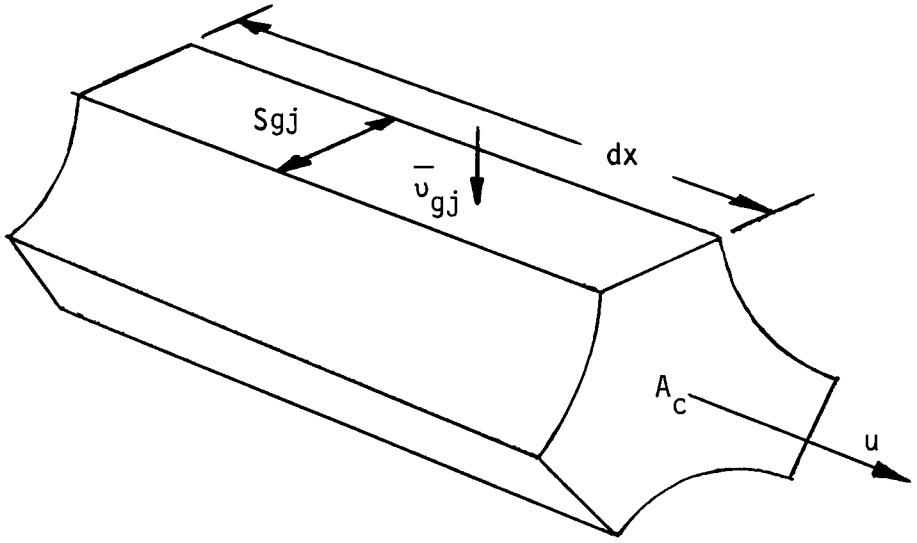

FIGURE E-1

AXIAL INCREMENT OF INTERIOR SUBCHANNEL

(Wire Wrap Not Shown)